Computational Studies of Heterogeneous and Homogeneous Catalysis by Late Transition Metals

Thesis by

Jeremy Kua

In Partial Fulfillment of the Requirements

For the Degree of

Doctor of Philosophy

California Institute of Technology

Pasadena, California

2001

(Submitted December 1, 2000)

Acknowledgement

I would like to thank my wife Aileen, my parents, and my siblings for their constant support and encouragement throughout my graduate school career. I also thank my advisor, Prof. William A. Goddard III, for his support, encouragement, being an excellent source of good ideas, and his infectious enthusiasm in both teaching and research. I thank members of the Goddard group who have helped me be a better scientist through good discussions, in particular, Dr. Vaidehi Nagarajan and Dr. Francesco Faglioni. Thanks also to Darryl Willick, the most efficient systems administrator I think I will ever meet, who kept machines up and running. Last but not least I would like to thank the many friends I have gotten to know since coming to Pasadena, who have helped contribute to graduate school being an overall enjoyable experience! After all, when I look back, my best memories come from the friendship I have shared with people in the Goddard group, the Caltech Christian Fellowship graduate bible study group, Aileen's friends, the Malaysian/Singaporean lunch group, and Timothy Cheng who gets me into the most interesting discussions.

Abstract

To design new catalysts that meet the environmental, materials and energy concerns of modern society, it is vital to understand the fundamental mechanisms involved in catalytic reactions. This thesis focuses on using quantum mechanical methods to determine the mechanisms for several critical catalytic processes in chemical industry.

Late transition metals are widely used as heterogeneous catalysts involving organic substrates. To lay a foundation for developing an orbital view useful for reasoning about surface reactions, we have developed the interstitial electron model (IEM) for bonding in platinum described in Chapter 1. To test the validity of the model cluster chosen to represent the surface, we studied the chemistry of C_1 and C_2 hydrocarbons, for which the most single-crystal experimental data is available, as described in Chapter 2.

In Chapter 3, we extend this model to the second and third row Group VIII transition metals (Ir, Os, Pd, Rh, Ru) and develop a thermochemical group additivity framework for hydrocarbons on metal surfaces similar to the Benson scheme so useful for gas phase hydrocarbons. This provides a potentially powerful technique for deriving a mechanistic understanding on complex hydrocarbon reactions on catalytic surfaces, applicable to hydrocarbon reforming processes.

An advantage of direct methanol fuel cells (DMFCs) over the internal combustion engines is to avoid the environmental damage caused by the latter. Chapter 4 describes our studies on electrocatalysis of methanol oxidation in direct methanol fuel cells. In particular, we focus on the role of different metals at the anode as alloys and as promoters for various aspects of the reaction converting methanol and water to CO_2 and energy.

One of the most important challenges is to find ways to utilize the enormous resources in methane around the world as the fundamental feedstock for the chemical and energy industries. Perhaps the most promising progress in developing low-temperature highly selective homogeneous catalysts have been the Hg and $PtCl_2$ catalysts from Catalytica. Chapter 5 reports our studies on the stability, thermodynamics, and reaction mechanism of the $PtCl_2$ catalysts, with suggestions of possible modifications necessary to make this process economic.

Contents

List of Figures

List of Tables

Chapter 1: Chemisorption on Platinum Clusters: Bonding in Platinum Clusters and the Interstitial Electron Model

Abstract

Using first principles quantum mechanics (nonlocal density functional theory), we studied the bonding and electronic states for clusters of Pt atoms. These calculations suggest the interstitial electron model (IEM) in which (i) the 6s valence orbitals from the four atoms of a tetrahedron combine to form an interstitial bonding orbital at the center of the tetrahedron that is occupied by two electrons to form the interstitial bond orbital (IBO), (ii) the 5d valence orbitals from each atom form a band of bonding and anti-bonding states sufficiently dense that the optimum occupation is high spin (Hund's rule) or nearly so, and (iii) bonds of organics to the Pt surface lead to covalent σ bonds to d orbitals localized on individual Pt atoms. This simple model explains the bonding and lowest electronic state of essentially all clusters studied. The IEM suggests that the bonding in three-dimensional face-centered cubic (fcc) systems has two electrons from each atom in the IBOs, leaving the remaining eight valence electrons in d-like orbitals. For bulk platinum, this leads to a $6s^2 5d^8$ effective electronic configuration. The IEM suggests that the (111) surface of Pt would have a $6s^1 5d^9$ effective electronic configuration. This suggests that to model the chemistry of Pt(111) surface we should use clusters leading to the $6s^1 5d^9$ configuration. The simple planar cluster with eight atoms serves to model the chemistry of the Pt(111) surface.

1-1. Introduction

In recent decades, there has been enormous progress toward a fundamental understanding of the nature of reactivity in organic reactions (e.g., the Woodward-Hoffmann rules) and in organometallic systems where the nature of the atomic and molecular orbitals can be used directly in explaining the reactivity. There has also been enormous progress in the characterization of chemisorption and reactions on metal surfaces (mostly based on surface science experiments). However, there has been little advance in how the orbitals of the surface control the reactions on metal surfaces. Instead, most discussions treat the metal atoms as round balls with little regard for the character of the orbitals. Such a view may be rationalized in terms of the delocalization of the molecular orbitals into bands of states where the atomic character may not be obvious. However, we believe the evidence is that chemical reactions involve localized sets of orbitals, even on metal surfaces.

To lay a foundation for developing an orbital view useful for chemical reasoning about reactions on metals surfaces, we initiated a research program examining the properties of small metal clusters and the bonding of organics to these clusters. Previous calculations on metal clusters have focused on equilibrium structures and adsorption of small molecules. Feng and Lin chose planar clusters containing from 7 to 12 Pt atoms of appropriate symmetry to bind CH_x fragments using DV-Xα methods.[1] Fahmi and van Santen used the local density approximation (LDA) of density functional theory (DFT) to study the interaction of water and ammonia with Pt_4 and Pt_6 clusters.[2] Higher levels of theory have been applied to similar problems over the past two years. The chemisorption of CO to Pt(111) has been the subject of much theoretical investigation. Illas and co-

workers[3] used complete active space self-consistent field (CASSCF) methods to study CO adsorption on the Pt_4 tetrahedron. Dumesic and co-workers[4] have used the B3LYP flavor of DFT to study single and multiple CO adsorption to a Pt_{10} tetrahedron, with application to Pt clusters supported in L-zeolite. Adsorption of atomic oxygen to similar Pt_{10} tetrahedral clusters has been studied using nonlocal DFT.[5] A theoretical study of CH_4 photodissociation has also been carried out using a Pt_n (n = 1, 4, 6, 7, 10) cluster model both by DFT and state-averaged CASSCF.[6] It has been suggested by theoretical studies on Pt_n clusters that when the number of Pt in the cluster reaches seven atoms, the electronic structure of the cluster becomes more metallic.[7] Smaller clusters ($n < 7$) on the other hand show vastly different electronic properties from bulk metallic platinum.

The concept of interstitial bonds in metallic bonding was suggested by McAdon and Goddard[8] based on generalized valence bond (GVB) calculations of M_n (M = Li, Na, Cu, Ag, Au). They found that, for one-dimensional systems, singly occupied orbitals are localized at each bond midpoint to form one-electron bonds. Two-dimensional systems have orbitals localized at the centers of equilateral triangles in the interior and at bond midpoints at the edge regions. They suggest that infinite systems have interstitial electrons at the center of the tetrahedra.

Our focus in studying metal clusters is to extract an orbital view of the electronic states. This led to the interstitial electron model (IEM) for the states of the metal clusters. On the basis of the IEM from metal clusters, we deduced the orbital nature expected for the infinite crystal and reasoned about the nature of the atoms on the surface of the bulk metal. This led to the idea that the surface atoms for bulk Pt prefer to have a $6s^1 5d^9$ electronic configuration. This suggested a strategy by which small clusters could be

constructed whose surface chemistry would mimic the properties of the bulk surface. We then used our model cluster to study the chemisorption and reactions on the Pt(111) surface (Chapter 2). These concepts have been extended to other metals including Ir, Os, Pd, Rh, and Ru (Chapters 3 and 4).

1-2. Platinum Clusters

We optimized the structures for clusters with up to 10 Pt atoms and carried out single-point calculations for those and additional 9-10 atom clusters. In each case, we determined the optimum spin. The energetic results are given in Table 1, and the optimum structures are shown in Figure 1. We see that the average bond distance increases gradually from 2.36 Å with Pt_2 to 2.77 Å for the central part of Pt_{10}. This compares with the experimental bond distance of 2.775 Å for bulk Pt, suggesting that the central atoms of these small clusters already have character similar to the bulk system.

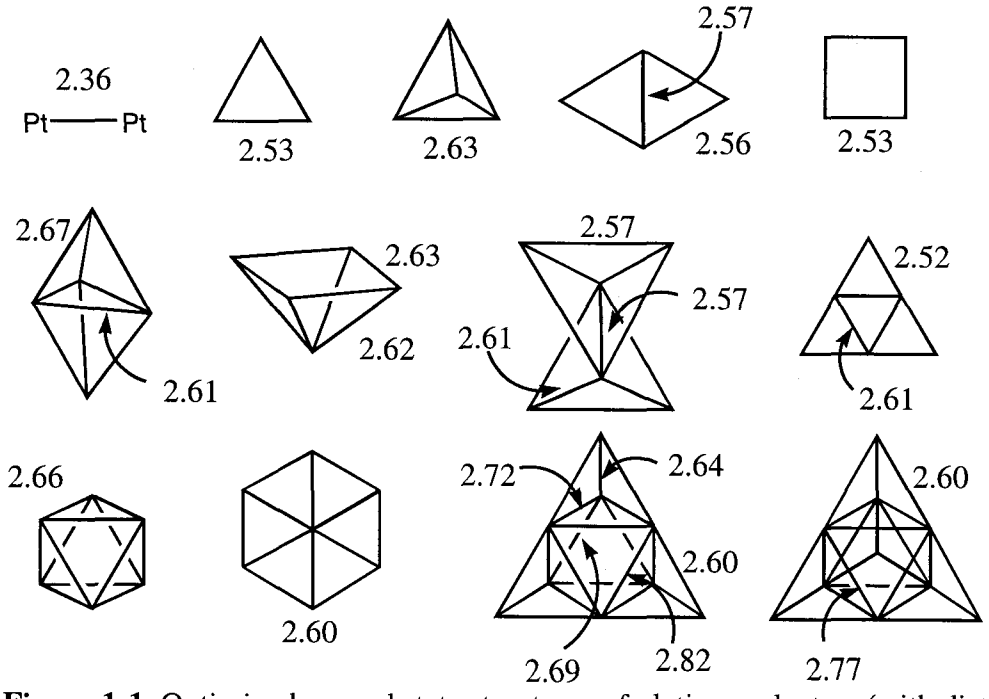

Figure 1-1. Optimized ground state structures of platinum clusters (with distances in Å).

Pt_n	Geometry (Symmetry)	Absolute ground state energy (hartrees)	Spin	Excited state energy (kcal/mol)	Total binding energy (kcal/mol)	Binding energy/n-1 (kcal/mol)	IBOs
2	linear ($D_{\infty h}$)	-238.36032	0	21.38	83.62	83.62	1
			1	0			
3	triangle (D_{3h})	-357.60474	0	3.27	165.76	82.88	1
			1	0			
4	tetrahedron (T_d)	-476.84339	3	22.12	244.27	81.42	1
			0	9.32			
			2	4.21			
			1	0			
4	rhombus (D_{2h})	-476.83092	1	7.59	236.45	78.82	2
			0	3.77			
			2	0			
4	square (D_{4h})	-476.82843	2	18.35	234.77	78.26	1
			0	1.45			
			1	0			
5	face-shared tetrahedron (D_{3h})	-596.10039	0	11.65	334.31	83.55	2
			1	7.05			
			2	0			
5	square pyramid (C_{4v})	-596.08737	4	18.42	328.24	82.06	3
			0	8.93			
			2	3.96			
			1	2.75			
			3	0			
6	edge-shared tetrahedra (D_{2h})	-715.34644	0	15.42	417.47	83.50	2
			3	5.81			
			1	2.33			
			2	0			
6	triangle (D_{3h})	-715.33936	4	46.97	413.02	82.60	3
			0	29.11			
			1	11.86			
			2	10.62			
			3	0			
6	octahedron (O_h)	-715.33970	1	3.68	413.24	82.34	4
			0	3.10			
			2	2.88			
			4	0.09			
			3	0			
7	hexagon (D_{6h})	-834.56554	0	24.60	483.91	80.65	3
			1	3.78			
			3	2.66			
			2	0			
9	bilayer (6.3) (C_{3v})	-1073.15779	4	13.30	712.88	89.11	4
			3	0			
10	trilayer (6.3.1) (T_d)	-1192.42902	5	22.54	811.81	90.20	4
			2	12.46			
			4	0.85			
			3	0			

Table 1-1. Calculated energetics of geometry-optimized platinum clusters with NLDA-GGAII.

A remarkable result here is that the net cohesive energy of the Pt_n cluster is

$$E_{cohesive} \approx (n - 1)85 \text{ kcal/mol} \quad (1\text{-}1)$$

where n is the number of Pt atoms. This suggests that each additional atom (after the first) adds the same amount to the cohesion of the system. The calculated bond energy of 83.6 kcal/mol for Pt_2 is in the range of experimental results, 65-86 kcal/mol.[9] The experimental cohesive energy for bulk Pt is 134.9 kcal/mol.[10]

For Pt_4, we find (DFT/NLDA-GGAII) the ground state to be the tetrahedron with the rhombus being 7.8 kcal/mol higher and the square 9.5 kcal/mol higher. There is no experimental data to compare with. Using the CASSCF method, Dai[11] reports the rhombus to be more stable than the tetrahedron by 1.1 kcal/mol. With DFT/LDA, Yang[12] reports the rhombus to be more stable than the tetrahedron by 1.1 kcal/mol. Using DV-Xα methods, Ellis[13] found the square to be most stable (by 10 kcal/mol over the rhombus). On the basis of extended Huckel calculations, Bigot[14] reported the tetrahedron to be most stable (10.4 kcal/mol below the rhombus). Of these previous calculations, only Dai and Ellis seem to have optimized the spin.

For Pt_6, we find that the edge-shared tetrahedron is lowest (4.45 kcal/mol better than the planar structure and 4.23 kcal/mol better than the octahedron). No previous predictions seem to have considered this structure. For Pt_{10} we find a stable three-layer structure (6 + 3 + 1 atoms per layer), which is a super tetrahedron with six closest packed atoms on each face.

Pt_n	Geometry (Symmetry)	Absolute ground state energy (hartrees)	Spin	Excited state energy (kcal/mol)	IBOs
2	linear ($D_{\infty h}$)	-238.22101	0	20.41	1
			1	0	
3	triangle (D_{3h})	-357.40522	0	2.05	1
			1	0	
4	tetrahedron (T_d)	-476.59198	0	14.55	1
			2	7.63	
			1	0	
4	rhombus (D_{2h})	-476.55484	0	2.40	2
			1	0.54	
			2	0	
4	square (D_{4h})	-476.54821	2	12.18	1
			1	2.92	
			0	0	
5	face-shared tetrahedron (D_{3h})	-595.77021	3	13.02	2
			1	5.56	
			2	0	
5	square pyramid (C_{4v})	-595.76839	4	27.65	3
			2	3.51	
			3	0	
6	edge-shared tetrahedra (D_{2h})	-714.93613	0	17.64	2
			1	5.34	
			3	4.17	
			2	0	
6	triangle (D_{3h})	-714.91209	4	34.02	3
			2	10.41	
			3	0	
6	octahedron (O_h)	-715.93219	5	40.41	4
			2	7.46	
			3	4.79	
			4	0	
7	hexagon (D_{6h})	-834.08903	1	28.32	3
			4	25.11	
			2	21.68	
			3	0	
9	bilayer (6.3) (C_{3v})	-1072.50763	5	30.97	4
			2	11.58	
			3	0.40	
			4	0	
10	trilayer (6.3.1) (T_d)	-1191.69744	5	11.61	4
			3	10.09	
			4	0	

Table 1-2. Single-point energy calculations of platinum clusters at bulk distances with B3LYP.

Pt_n	Geometry (Symmetry)	Absolute ground state energy (hartrees)	Spin	Excited state energy (kcal/mol)	IBOs
2	linear ($D_{\infty h}$)	-238.23892	0	20.69	1
			1	0	
3	triangle (D_{3h})	-357.57361	0	4.79	1
			1	0	
4	tetrahedron (T_d)	-476.82586	0	10.06	1
			2	7.31	
			1	0	
4	rhombus (D_{2h})	-476.79616	1	7.49	2
			0	4.15	
			2	0	
4	square (D_{4h})	-476.77974	0	6.40	1
			2	1.47	
			1	0	
5	face-shared tetrahedron (D_{3h})	-596.08482	0	14.70	2
			1	5.97	
			2	0	
5	square pyramid (C_{4v})	-596.07140	4	18.49	3
			2	2.59	
			3	0	
6	edge-shared tetrahedra (D_{2h})	-715.32132	0	12.68	2
			3	4.66	
			1	2.14	
			2	0	
6	triangle (D_{3h})	-715.30276	4	37.86	3
			2	12.53	
			3	0	
6	octahedron (O_h)	-715.32098	5	40.92	4
			2	1.26	
			4	0.46	
			3	0	
7	hexagon (D_{6h})	-834.52555	1	15.14	3
			4	11.38	
			2	8.82	
			3	0	
9	bilayer (6.3) (C_{3v})	-1073.12261	5	25.07	4
			2	9.88	
			3	0.01	
			4	0	
10	trilayer (6.3.1) (T_d)	-1192.39952	5	27.49	4
			3	10.01	
			4	0	

Table 1-3. Single-point energy calculations of platinum clusters at bulk distances with NLDA-GGAII.

1-2-1. The Interstitial Electron Model (IEM)

For linear Pt_2, the ground state has two electrons in a symmetric (bonding) combination of 6s orbitals and 20 – 2 = 18 electrons distributed among the ten 5d-like orbitals, leading to an S=1 state. The two anti-bonding combinations of the 6s orbitals are much higher, as are various combinations of 6p orbitals. This is shown in Figure 1-2.

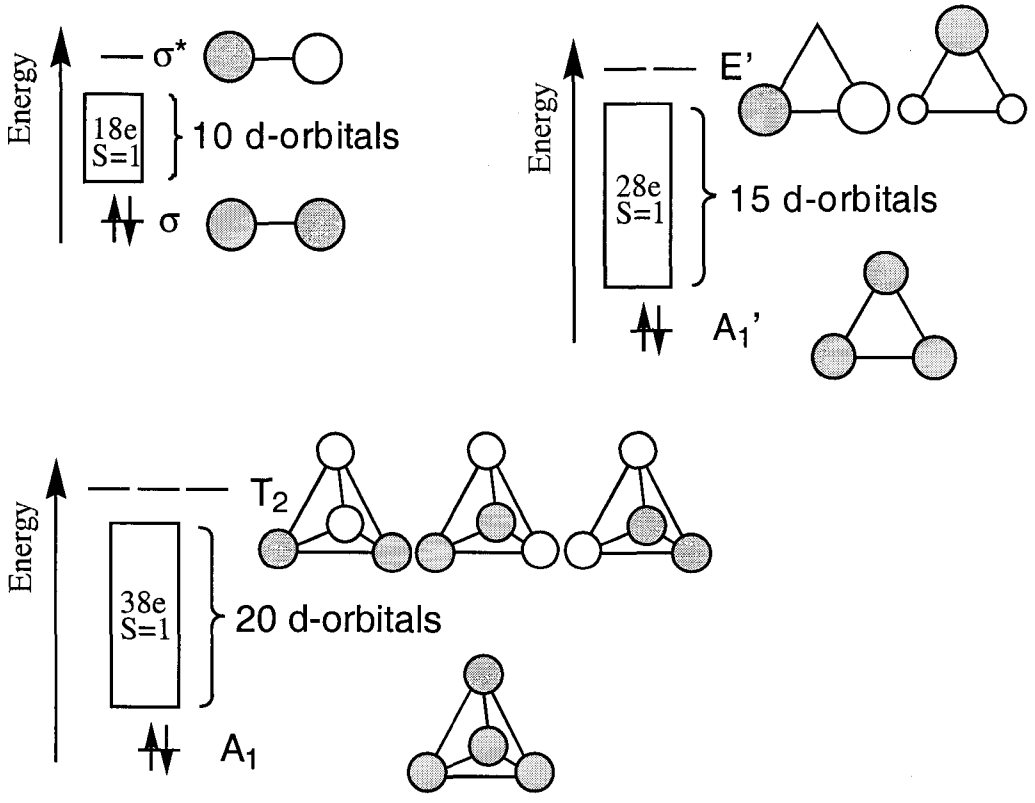

Figure 1-2. Molecular orbital diagrams of Pt_2, Pt_3, and Pt_4.

Similarly, for triangular Pt_3, the ground state has two electrons in a symmetric (bonding) combination of three 6s orbitals and 30 – 2 = 28 electrons distributed among the fifteen 5d-like orbitals, leading to an S=1 state. The two anti-bonding combinations of the 6s orbitals are much higher, as are various combinations of 6p orbitals.

We see the same trend for tetrahedral Pt_4. The ground state has two electrons in a symmetric (bonding) combination of four 6s orbitals and 40 – 2 = 38 electrons distributed among the twenty 5d-like orbitals, leading to an S=1 state. The three anti-bonding combinations of the 6s orbitals and various combinations of 6p orbitals are much higher in energy.

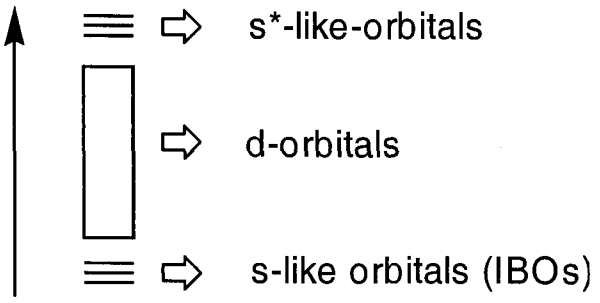

Figure 1-3. Schematic energy diagram for platinum clusters.

These results are summarized in Figure 1-3. It is because 6s orbitals on adjacent Pt atoms have much higher overlap than do 5d orbitals that the anti-bonding combinations of 6s orbitals are so much higher than the anti-bonding 5d orbitals. Because these clusters are being used to model the extended Pt(111) surface, we calculated the energies of different spin states of these clusters at the bulk platinum distance (Pt-Pt 2.775 Å) using DFT/B3LYP (Table 1-2). For comparison, the DFT/NLDA-GGAII energies at bulk platinum distance are tabulated in Table 1-3. Differences between the levels of theory and between single-point and geometry-optimized clusters are discussed in the appendix to this chapter.

For the larger Pt_n clusters, we find similar interstitial bond orbitals (IBOs) formed from symmetric combinations of 6s orbitals of tetrahedra or triangles to dominate the bonding, leaving the remaining ($10n - 2 \times$ IBO) electrons to be sprinkled over the $5n$ d

orbitals. The maximum number of unpaired spins for such a system is 2 × IBO, leading to a net spin of S = IBO. Usually we find this maximum spin case to be the ground state (Hund's rule). Figure 1-4 shows the location of IBOs for the various calculated clusters. Here, we see that the IBOs tend not to occupy adjacent triangles or tetrahedra. This is because the Pauli Principle, requiring that the orbitals be orthogonal, would force the IBO to incorporate 5d or 6p character.

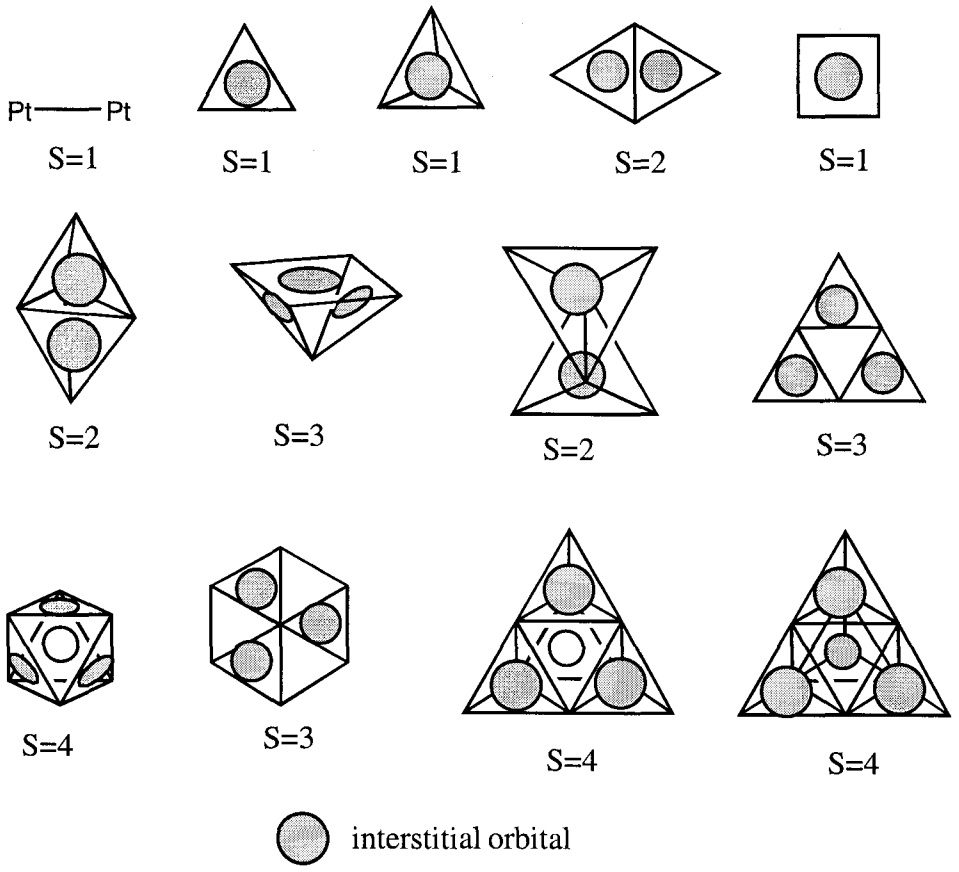

Figure 1-4. IBO location and S values predicted by the IEM for Pt clusters.

These results suggest a simple procedure for predicting the ground-state spin of a cluster.

1. Determine the number of IBOs in the cluster.
2. Occupy each IBO with two electrons.

3. Since the anti-bonding combination of s orbitals is left unoccupied, the remaining electrons are filled into d orbitals.
4. Using the simple assumption that the d orbitals are close in energy, we can apply Hund's rule to determine the predicted ground spin state.

A brief discussion of the number and location of IBOs is in order, since this determines the ground-state spin of the cluster.

The Pt_4 rhombus has two equivalent triangles each containing an IBO; this leads to S=2. The Pt_4 square has one IBO in its center, which leads to S=1.

For Pt_5 with face-shared tetrahedra, there is an IBO in each of the two equivalent tetrahedra, leading to S=2. The Pt_5 square pyramid has three IBOs, one located on the square face and two located in the two alternate triangular faces.

In the Pt_6 triangle, we find one IBO in each of the edge triangles, leading to S=3. The central triangle does not have an IBO. This cluster illustrates the feature of alternation of IBO that we will find in the larger clusters. The edge-shared tetrahedra Pt_6 cluster has two equivalent tetrahedra, and consequently there are two IBOs (S=2). The octahedron has four IBOs in alternate triangular faces, leading to S=4.

The Pt_7 hexagon also shows alternation. It has three IBOs in alternate triangles, leading to S=3. An equivalent structure has the three IBOs in the *other* three triangles (see discussion in the next section).

The Pt_9 (6.3 bilayer) has an S=4 ground state. IBOs are located in three of the tetrahedra. The fourth IBO is associated with the face of the octahedron, satisfying the alternating pattern (on the three-atom face).

The Pt_{10} tetrahedron has four IBOs located in the four tetrahedra that are arranged at the alternate faces of the central octahedron, and S=4 as expected.

On the whole, the S values calculated for these clusters from quantum mechanics match remarkably well with the S values predicted form the IEM.

The only case that does not is the Pt_4 square. Here, the IEM suggests S=1, whereas the value calculated using B3LYP is S=0 (with S=1 higher by 2.9 kcal/mol). [NLDA-GGAII gives a ground state with S=1 a expected from IEM.] However, we find that the orbitals for S=0 and S=1 are essentially the same (with one IBO), indicating that the S=0 arises from spin pairing of the d electrons in the two highest d-like orbitals of the S=1 state (Hund's rule is not quite satisfied). We expect this effect to be more apparent at shorter distances where it becomes more favorable to spin-pair electrons in the high-lying d orbitals. Such violations of Hund's rule are expected to occur more in larger clusters. A general schematic of this is shown in Figure 1-5. A comparison of different levels of theory, and a comparison of energetics for optimized versus single-point cluster calculations is discussed in the Appendix.

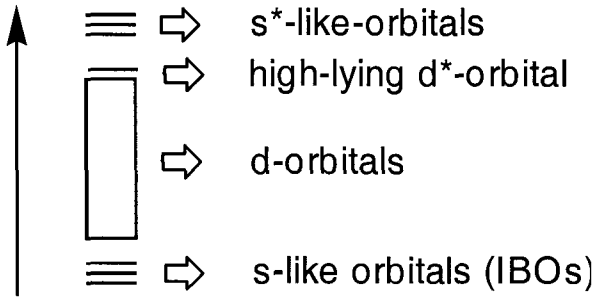

Figure 1-5. Schematic energy diagram showing pairing of electrons to leave high-lying d* orbitals unoccupied.

1-2-2. Implications of the IEM for Bulk Pt

We wish to extrapolate the results from the cluster calculations to predict the bonding in bulk and surface platinum. Platinum crystal has a closed-cubic-packed (ccp) structure with a face-centered-cubic (fcc) unit cell. Each unit cell consists of four platinum atoms, eight tetrahedra and four octahedra. Figure 1-6 shows the fcc unit cell and a view of the central octahedron (white spheres) which has each of its eight triangular faces capped (with black spheres) to form the eight tetrahedra. The remaining space of the cube is taken up by three octahedra formed by half-octahedra on each of the six faces of the cube.

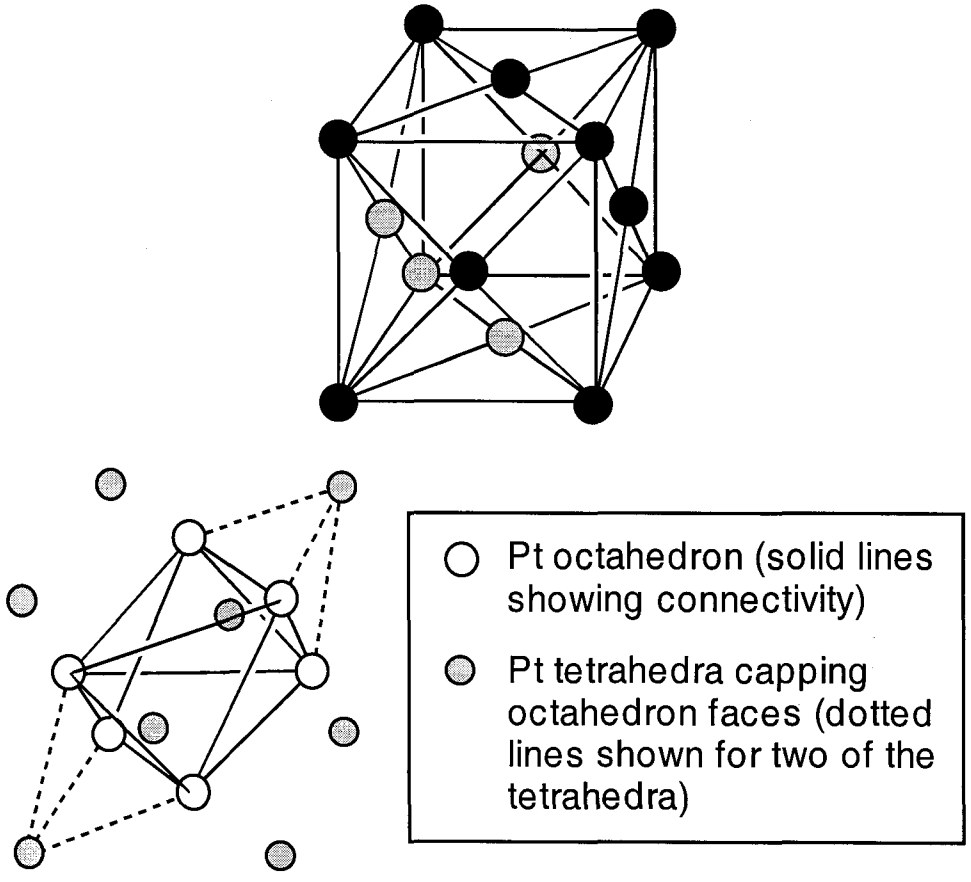

Figure 1-6. Unit cell of platinum (fcc) showing face-shared octahedra and tetrahedra.

Since the crystal is made up of face-sharing octahedra and tetrahedra, an IBO has four possible locations: (a) in the center of a formal Pt-Pt bond, (b) in the center of a triangular face, (c) in the center of a tetrahedron, or (d) in the center of an octahedron. Our calculations suggest that for bulk Pt there would be doubly occupied IBOs *located in half the tetrahedra.*[15] The Pt_6 triangle and octahedron, and the Pt_7 hexagon, show alternation of the IBOs. The Pt_9 and Pt_{10} clusters (along with Pt_4 tetrahedron) suggest that the IBOs are located in tetrahedra rather than octahedra. To confirm the validity of our suggestion, we did single point energy calculations to determine the ground spin states for three larger clusters (see Figure 1-7 and Table 1-4) at the Pt-Pt 2.6875 Å (the average of 2.60 and 2.775 Å, the distances in optimized Pt_{10} tetrahedron).

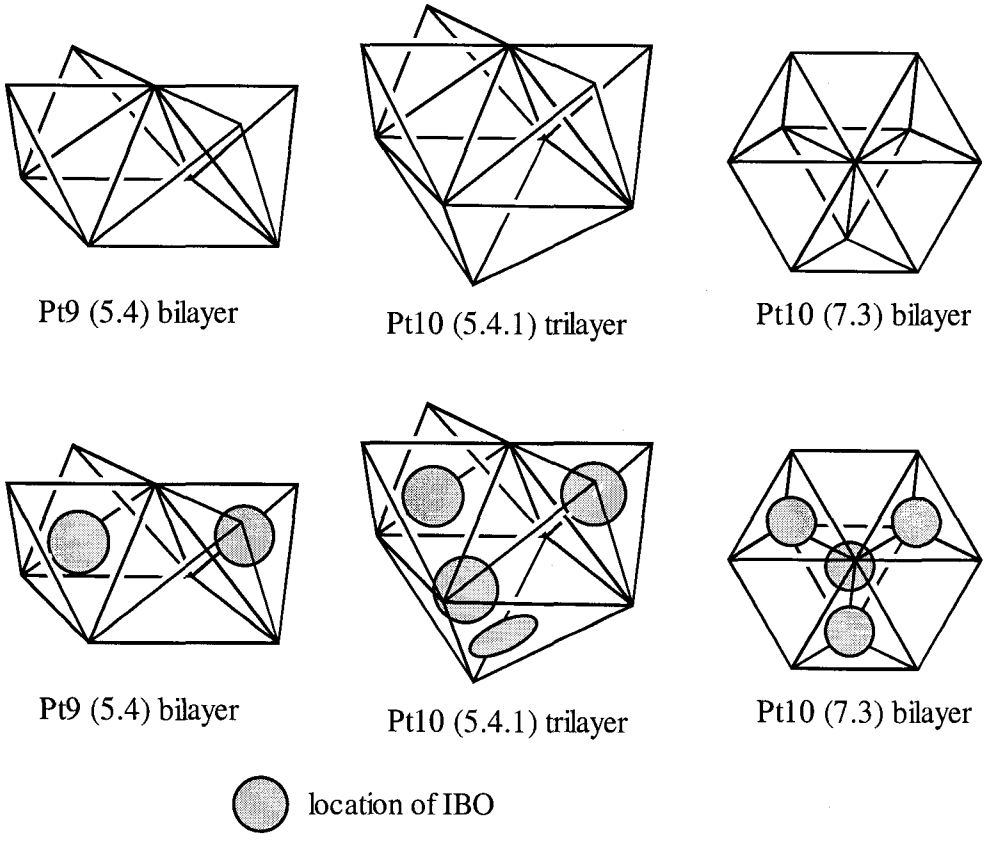

Figure 1-7. Geometries and location of IBOs for three larger Pt_9 and Pt_{10} clusters.

Pt_n	Geometry (Symmetry)	Absolute ground state energy (hartrees)	Spin	Excited state energy (kcal/mol)	IBOs
9	bilayer (5.4) (C_{4v})	-1073.09244	3	10.68	2
			1	6.49	
			2	0	
10	bilayer (7.3) (C_{3v})	-1192.34780	5	15.39	4
			2	2.55	
			3	0.90	
			4	0	
10	trilayer (5.4.1) (C_{4v})	-1192.34646	5	11.35	4
			3	3.51	
			4	0	

Table 1-4. Single-point Energy calculations of platinum clusters at Pt-Pt 2.6875 Å with NLDA-GGAII.

The first of these is a Pt_9 (5.4) bilayer cluster that is half of the fcc unit cell. The five-atom face forms the top layer and the second layer has four atoms. Geometrically, this structure is a half-octahedron with four tetahedra capping the four adjacent triangular faces. The calculated ground state of this cluster is S=2; i.e., two IBOs are present and located in two of the four tetrahedra.

The second cluster is a Pt_{10} (5.4.1) trilayer, which differs from the first cluster by having an additional atom in the third layer to complete the octahedron. From our small cluster calculations, we predicted that this adds two IBOs on two of the triangular faces of the bottom half of the octahedron. Indeed, calculations give us S=4 as the ground state, indicating that this cluster has four IBOs.

The third cluster, the Pt_{10} (6.3) bilayer, has a hexagonal layer of seven atoms with three additional atoms in the second layer to form three tetrahedra (and three half octahedra). If the IBOs are located in the tetrahedra, we expect to find an IBO in each of the three outer tetrahedra plus one in the central tetrahedra. If instead they are in the half-octahedra, we would expect to find six IBOs (two for each of the half-octahedra). Our

cluster calculation gives S=4, i.e., three IBOs are located in the outer tetrahedra and one in the inner tetrahedra. Thus, the IBOs prefer tetrahedra.

We now return to the unit cell of platinum. Each unit cell has four platinum atoms and eight tetrahedra. Therefore, each platinum atom is associated with two tetrahedra. Since there are IBOs in half the tetrahedra, each platinum atom has one IBO associated with it. We previously showed that IBOs are doubly-occupied and represent the in-phase combination of s orbitals. Since platinum has ten valence electrons, the model predicts that *bulk* platinum has a $6s^2 5d^8$ electronic configuration.

The band structure of platinum has been determined by angle-resolved ultraviolet photoemission spectroscopy (ARUPS) with general agreement with fully relativistic self-consistent calculations.[16] The lowest valence band (mostly s character) does not cross the Fermi level, suggesting an electronic configuration close to $s^2 d^8$, in agreement with IEM predictions. However, calculations of the d occupancy vary significantly. Linear augmented Slater-type orbital methods suggest that $d^{n-1}s^2$ configurations predominate in the 5d row.[17] Platinum is calculated to have a d occupancy of 8.1-8.3. A recent Compton profile study with calculations based on the renormalized free-atom (RFA) model yielded a d occupancy of 9.2 for platinum.[18]

1-2-3. Implication of the IEM for the (111) Surface of Bulk Pt

We will consider the Pt(111) surface, since the most experimental data is available for this surface. Forming the (111) surface for the crystal involves cleaving one tetrahedra per surface atom (Figure 1-8). [Each surface atom of the two new surfaces is shared by four tetrahedra that are cleaved, each of which is counted four times.] Since IBOs are

located in half the tetrahedra, then the surface atoms each must accommodate one additional electron in the d shell. This leads to the $6s^1 5d^9$ electronic configuration, with the s electron involved in IBOs in half the tetrahedra involving the subsurface tetrahedra. This is illustrated in Figure 1-9. As a result, the IEM suggests that each platinum atom on the (111) surface has the $6s^1 5d^9$ configuration.

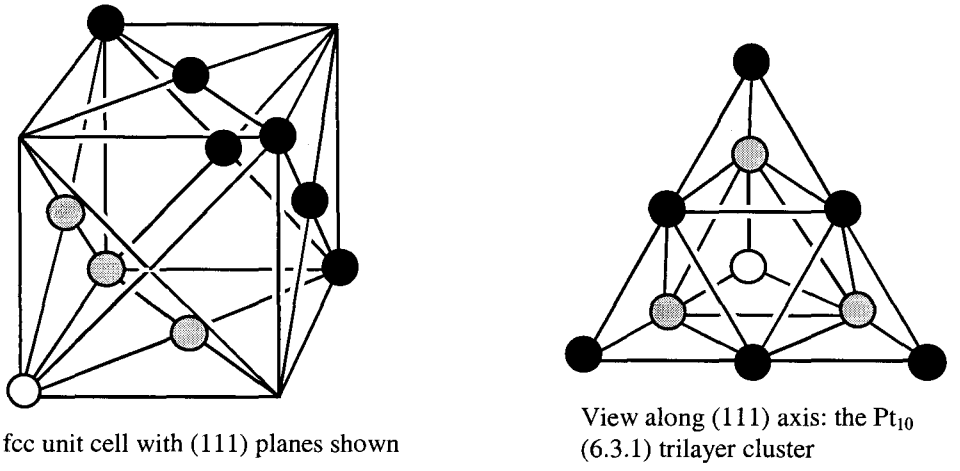

fcc unit cell with (111) planes shown

View along (111) axis: the Pt_{10} (6.3.1) trilayer cluster

Figure 1-8. Unit cell of platinum illustrating derivation of clusters corresponding to the Pt(111) plane.

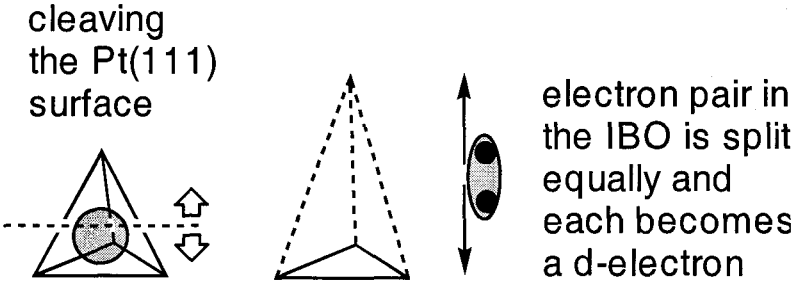

Figure 1-9. Illustration showing breaking of an IBO when a tetrahedron is cleaved.

The IEM suggests an explanation for the site preference of a hydrogen atom adsorbed on Pt(111). High-resolution electron energy loss spectroscopy (HREELS) experiments have shown that H-atom binds to the fcc sites of Pt(111) with a binding energy of 60

kcal/mol (at high coverage).[19] The (111) surface is composed of two different types of triangles depending on the location of the atoms in the second layer. If there is an atom directly below the triangle, this means that the triangle is a tetrahedral face and hence a hcp site. If instead there is no atom in the second layer directly below the triangle, then it is an octahedral face and hence a fcc site. This is illustrated by the Pt_9 cluster shown in Figure 1-10.

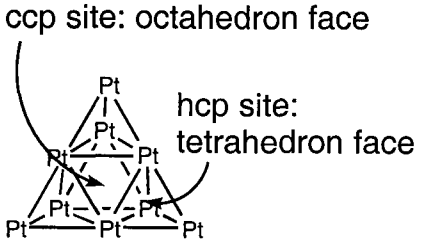

Figure 1-10. Pt_9 (6.3) bilayer cluster illustrating fcc and hcp sites.

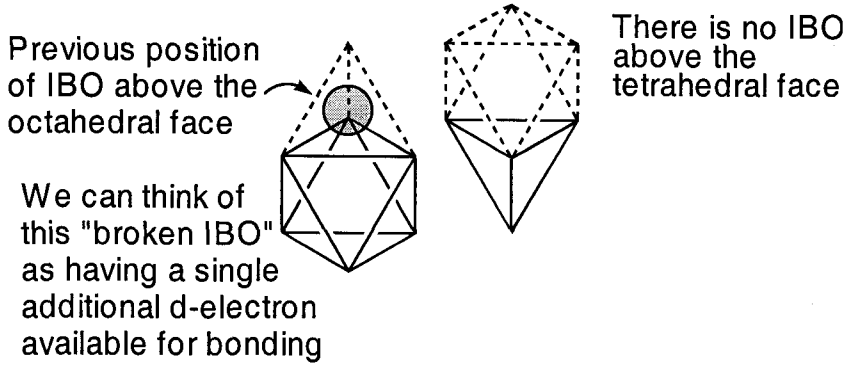

Figure 1-11. Illustration of *previous* location of IBOs above fcc and hcp sites.

Consider what *previously* occupied these two sites. Before cleaving the surface at the (111) plane, there used to be a tetrahedron sitting above an octahedral face, and an octahedron sitting above a tetrahedral face (see Figure 1-11). Above the octahedral face (fcc site), there used to be an IBO, which has now been cleaved leaving an additional d electron available for adsorbate binding at this site. The tetrahedral face (hcp site) does

not have this, since an octahedron used to be above this site. This predicts that hydrogen, with a single electron in its spherical 1s orbital, will bind preferentially at fcc sites over hcp sites.

1-2-4. Clusters to Model the (111) Surface

The above analysis suggests criteria for clusters to serve as good models for Pt(111). First, the clusters should have an electronic configuration close to the predicted $6s^1 5d^9$ electronic configuration. This criteria is met by clusters having half the number of IBOs as there are atoms in the cluster. Second, the cluster should be able to model two types of triangular faces. This criteria is met by clusters having at least two inequivalent triangles on a surface (the Pt_7 hexagon has all equivalent triangles that would not work). The planar Pt_6 triangle meets these criteria but does not provide an adequate site for on-top binding. Thus, we consider the Pt_8 planar cluster to be the smallest cluster suitable for examining the chemistry of the fcc surfaces. This is the smallest cluster showing all types of surface sites to be probed. Figure 1-12 shows this cluster and the calculated relative energies at the bulk Pt-Pt distance. The S=3 state is calculated (B3LYP) to be 1.4 kcal/mol lower in energy than the S=4 state. This is due to spin-pairing of d orbitals, which leaves the highest-lying d-orbital unoccupied.

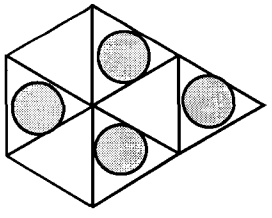

B3LYP	NLDA-GGAII
S=4 1.41 kcal/mol	S=3 2.29 kcal/mol
S=3 0 (ref)	S=4 0 (ref)
Energy of ground state:	Energy of ground state:
-953.25726 hartrees	-953.77987 hartrees

Figure 1-12. Pt_8 cluster proposed as a model for Pt(111).

1-2-5. Planar and Bilayer Clusters: an IEM View

In this section, we present an IEM view in understanding for some biases inherent in using planar and bilayer clusters. The theory presented here uses binding of a hydrogen atom to platinum clusters as the prototype. Our calculations of H-Pt clusters support the IEM view, and are presented in Chapter 2.

The smallest cluster that represents a 3-fold site is the Pt_3 triangle. We expect the H 1s orbital to overlap well with the IBO in the center of the triangle. This is the most simplified case of H binding to an "fcc-like" site (see Figure 1-11). The reason it is "fcc-like" is because it only approximates the fcc site, as we shall see later in the explanation. Our calculations show that H binds stably to Pt_3 at the cap (3-fold) site. However, H does not bind to the cap site of the Pt_4 tetrahedron. This is because the IBO is no longer on a triangular face, but is now located in the center of the tetrahedron. Figure 1-13 illustrates that adding the fourth atom to the Pt_3 triangle results in the IBO "sinking" below the surface plane. There is now poor overlap between a H 1s orbital and the IBO. As we have discussed in the previous section, tetrahedral faces represent hcp sites, and so these sites are not favorable for H-binding.

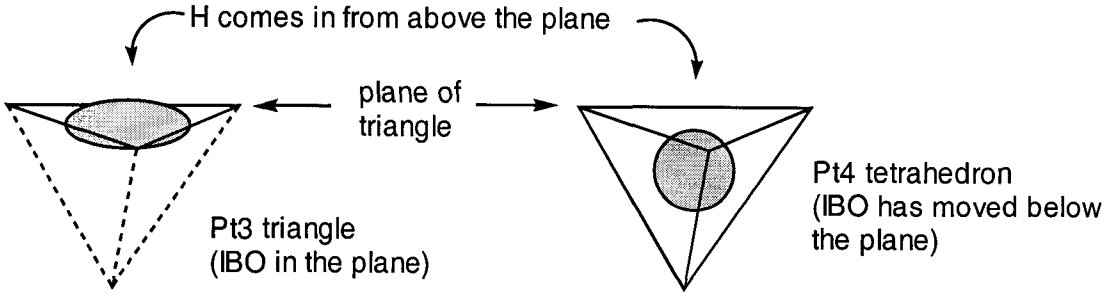

Figure 1-13. Position of the IBO in the Pt_3 triangle and Pt_4 tetrahedron.

Consider now the Pt_6 planar triangle that meets the two important criteria for a cluster modeling the (111) surface (that is it has two different types of 3-fold sites and a net $6s^1 5d^9$ electronic configuration). The four lowest orbitals of this cluster are shown in Figure 1-14. The three lowest orbitals (A_1' and E') have more s character while the higher energy A_1' orbital has more d character. The three IBOs are also located in the three outer triangles. Notice that the d-like A_1' orbital would also overlap with a H 1s orbital in the 3-fold site of the central triangle (and indeed we find this in our calculations).

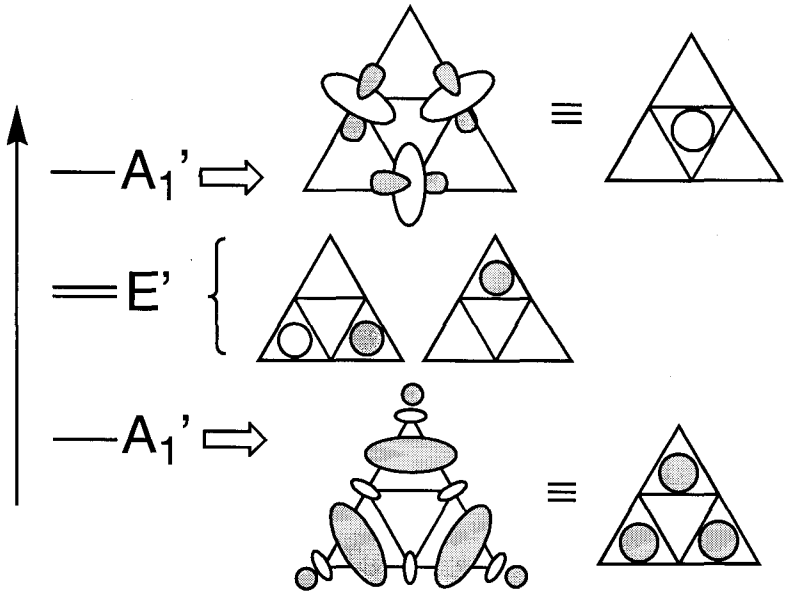

Figure 1-14. Lowest valence orbitals of the Pt_6 planar cluster.

If we were now to add three Pt atoms to form a second layer by placing them directly underneath the three outer triangles to form three tetrahedra, this would be the Pt_9 (6.3) bilayer cluster. The three IBOs in the outer triangles would now "sink below the surface" in the same way that adding an additional Pt atom to Pt_3 triangle to form a tetrahedron causes the IBO to move to the middle of the tetrahedron. Adding this second layer has no

effect on the d character orbital in the central triangle (an octahedral face), which will still have good overlap with a H 1s orbital at the surface. This is why the octahedral face (fcc site) is still favorable for H-binding.

Figure 1-9 seems to suggest that the fcc sites are favorable for binding H because a broken IBO from a cleaved tetrahedron above this site results in an additional unpaired electron available for bonding. The same argument can be used to favor an on-top site (see Figure 1-15). When a tetrahedron and its corresponding IBO are cleaved, the electron pair is split homolytically between the two new "surfaces." One is associated with an on-top site and the other is associated with a 3-fold site. This is probably not significant on the extended surface where you end up having an average of one additional unpaired electron per surface atom. However, in a cluster, it is something that we need to be concerned about. We will now proceed to explain that the on-top site has a favorable bias in a planar cluster.

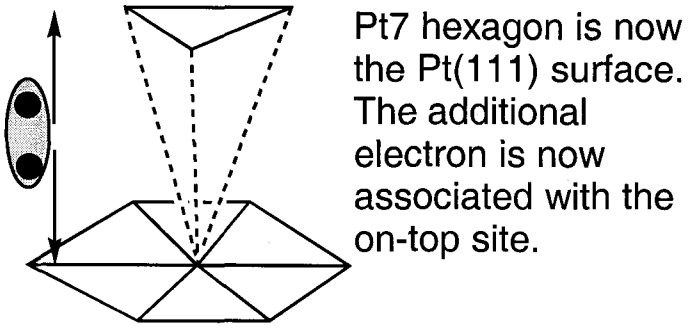

Figure 1-15. Cleaving of a tetrahedron favoring the on-top site.

Consider the Pt_9 (6.3) bilayer cluster (see Figure 1-16). The orientation of the tetrahedra containing the IBOs is fixed in this cluster. The result of this is that the two opposite 3-fold faces of the central octahedron, which both model fcc sites, are not the

same. If we consider two imaginary tetrahedra that would have previously occupied these two different faces, the model predicts, since half the tetrahedra are occupied by IBOs, that there *was* an IBO in the bottom tetrahedron but not in the top one. This predicts that the fcc site formed by the three-atom surface (the bottom surface of the bilayer cluster) is favorable for H binding. The fcc site on the six-atom face is not favorable. Upon examining the orbitals, we see that both the fcc sites have potentially good overlap with a H 1s orbital. The significant difference is that overlap with the bottom face would be with orbitals of mostly s character; overlap with the top face would be with orbitals of mostly d character (see Figure 1-17). Our calculations of H at these two positions (presented in Chapter 2) are in agreement with this analysis.

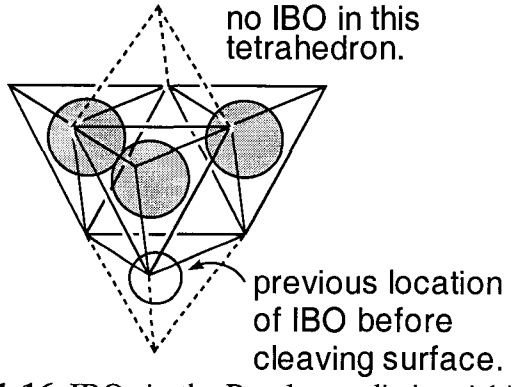

Figure 1-16. IBOs in the Pt_9 cluster distinguishing the two fcc sites.

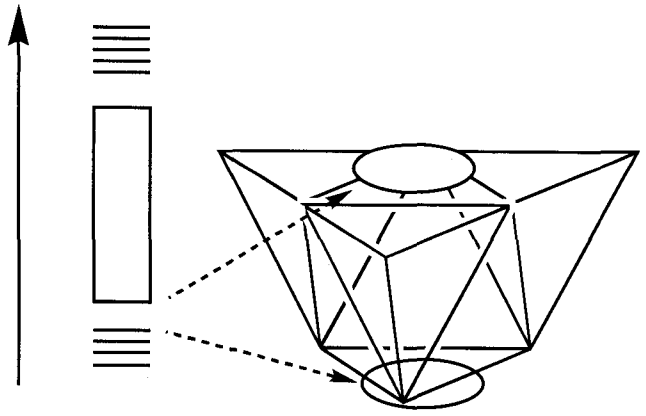

Figure 1-17. Schematic of valence orbitals in Pt_9 showing the different character of the orbitals at the fcc sites.

Next, consider the octahedron in the center of the Pt_9 bilayer cluster. If we look down on the face of the six-atom surface, we see that the IBOs are located underneath triangular faces. If instead we look up on the three-atom surface, we see that the IBOs are now located underneath atom centers and not triangle centers. In a planar cluster, the IBOs are located in the center of triangles. Hence, the fcc sites which do *not* have IBOs are more like the fcc sites of the six-atom face of the Pt_9 cluster rather than the three-atom face. A planar cluster biases for the on-top site because, in having its IBOs located in triangles, it presumes the orientation of tetrahedra containing IBOs to be facing in such a way that the "points" of the tetrahedra point below the surface into the bulk. Hence, atom centers rather than 3-fold sites would have the additional associated electron from bonding after cleaving an IBO. The situation in the planar cluster therefore resembles the situation in Figure 1-15 rather than Figure 1-9, and we expect a bias in favor of the on-top site. Our calculations with H (in Chapter 2) do indeed show a small bias for the on-top site.

This leads to the conclusion that the planar clusters have two different kinds of triangles that do not quite model the fcc and hcp sites respectively. Rather they model two different kinds of fcc sites, one that allows overlap with the "s-like" orbitals, and the other with "d-like" orbitals. The bilayer clusters are also similarly biased because of the fixed orientation of the tetrahedra inherent in such a cluster. Although we have these biases, our subsequent calculations show that the Pt_8 cluster seems quite adequate in describing the binding of hydrocarbon species to Pt(111) and the small size of the cluster is well compromised by the high level of theory used in the calculation.

In small three-dimensional clusters such as the Pt_4 tetrahedron and the Pt_6 edge-shared tetrahedra, the IBO are located in the center of tetrahedra. Each of these tetrahedral IBOs is doubly occupied. If we consider the two-dimensional high symmetry Pt_7 hexagon which has three IBOs, following the same rules we would assign doubly occupied IBOs to alternate triangles. However, an equivalent "resonance" structure is also present whereby the *other* three alternate triangles are occupied. This model would suggest six singly occupied interstitital orbitals, one in each of the triangles, echoing the model proposed by McAdon and Goddard.[8] This is equivalent to having three doubly occupied IBOs in two resonant structures. The electron configuration remains unchanged, since the number of electrons in IBOs remains the same in both pictures.

In our model Pt_8 cluster, there are four IBOs formed from orbitals of predominantly s character (Figure 1-18). The first two d-like orbitals are also shown for comparison. The four s-like orbitals distinctly show electron density in the interstitial positions, a feature absent in the d-like orbitals. A Pipek-Mezey localization[20] of these orbitals is shown in Figure 1-19. The three orbitals in the hexagon part of the cluster are delocalized over two triangles each, just like the resonance structures of the Pt_7 hexagon. The fourth IBO in the outer triangle is doubly occupied. In total, there are still eight IBO electrons (s-like), giving rise to the desired s^1d^9 configuration. Figure 1-20 shows the five localized IBOs in the Pt_{12} (8.4) bilayer cluster. Four of the doubly occupied IBOs are located in the four tetrahedra of the same orientation. The last IBO is delocalized over the octahedron and the remaining tetrahedra. The electron configuration of this cluster is $s^{0.83}d^{9.17}$ since there are ten s-like electrons in a 12-atom cluster.

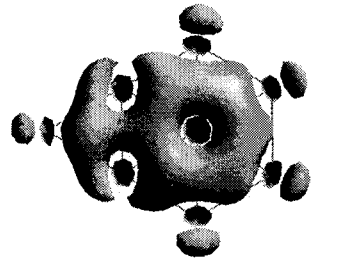

A_1 (IBO, s-like)

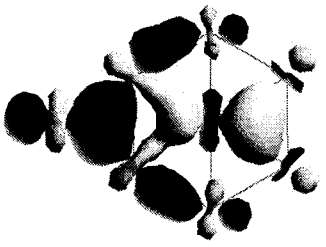

A_1 (IBO, s-like)

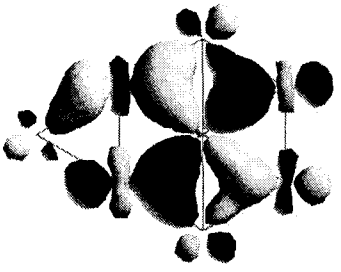

B_2 (IBO, s-like)

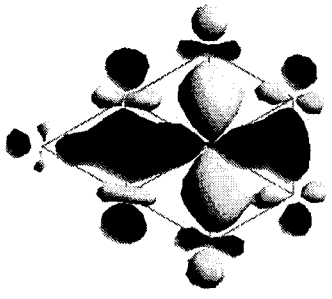

A_1 (IBO, s-like)

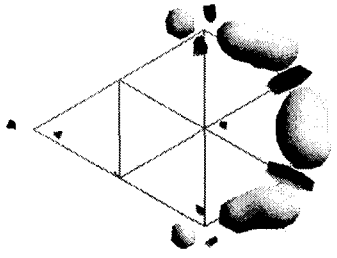

A_1 (non-IBO, d-like)

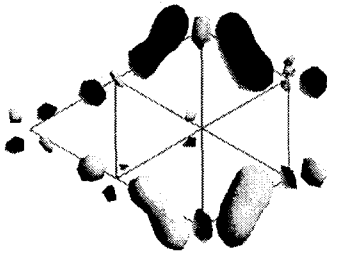

B_2 (non-IBO, d-like)

Figure 1-18. Six lowest valence occupied orbitals of Pt_8.

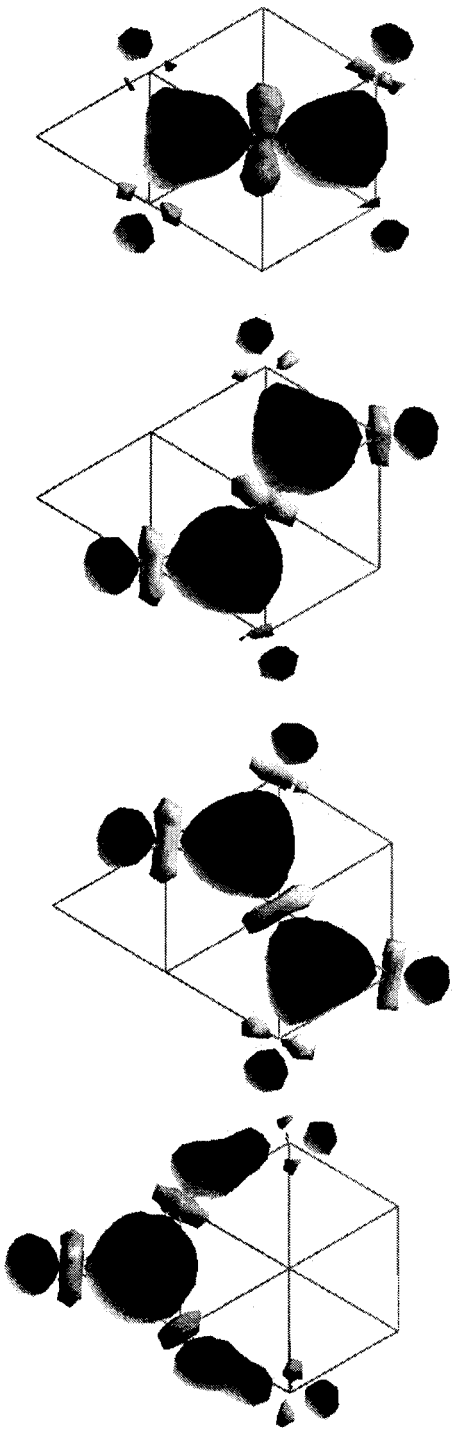

Figure 1-19. Pipek-Mezey localization of Pt_8 IBOs.

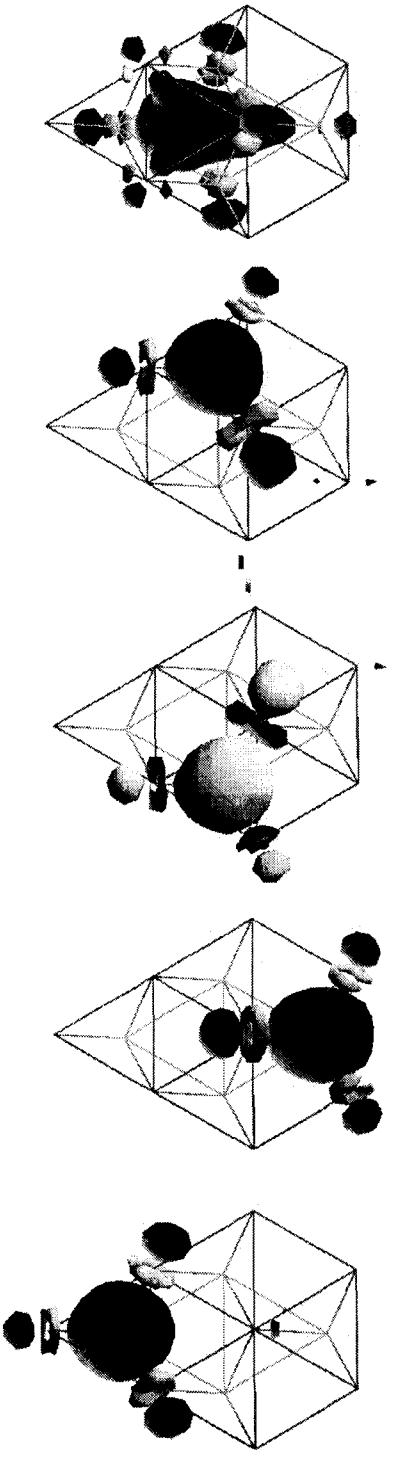

Figure 1-20. Pipek-Mezey localization of Pt_{12} (8.4) IBOs.

1-3. Conclusion

We have studied the bonding in platinum clusters using non-local density functional methods employing a relativistic effective core potential. The ground state spin of the clusters can be explained using the IEM. The essence of the model is the presence of low-lying IBOs formed from the in-phase combination of the 6s-orbitals. The corresponding out-of-phase combinations are very high in energy and left unoccupied. These two sets of orbitals sandwich a band of d orbitals. Our cluster calculations suggest that IBOs are located in half the tetrahedra in platinum. Thus, the IEM predicts that bulk platinum has a $6s^2 5d^8$ electronic configuration and surface platinum on Pt(111) has a $6s^1 5d^9$ electronic configuration. The IEM also provides an explanation for the adsorption preference of H for the 3-fold fcc sites over the hcp sites. We propose the use of a Pt_8 planar cluster to model chemical reactions on Pt(111) based on its electronic configuration and ability to model the necessary sites corresponding to the (111) surface. Inherent biases in the planar and bilayer clusters are explained by the IEM. However, our computational results of chemisorption (Chapter 2), in good agreement with experimental results, suggest that the small size of this cluster is compensated by the high level of theory used in our calculations.

1-4. Computational Methods

Calculations were carried out with nonlocal density functional theory (DFT) using the NLDA-GGAII method, which uses the Slater local exchange functional[21] and the Perdew-Wang local correlation functional with Perdew-Wang generalized gradient approximation (GGA-II) nonlocal correlation functionals.[22] The choice of this nonhybrid

Three clusters show a difference in the ordering of the spin states. The Pt_4 square has S=1 as the ground state (as predicted by IEM) using NLDA-GGAII. With B3LYP, the S=1 state is 2.92 kcal/mol higher in energy than the S=0 state. An examination of the orbitals shows that the S=0 state leaves the highest d-like anti-bonding orbital (an A_{2g} state) unoccupied. The lowest bonding valence orbital is the only one with dominant s-like bonding character, with the IBOs located in the center of the square. The Pt_6 octahedron using NLDA-GGAII has S=4 a mere 0.46 kcal/mol above the S=3 state. Again, this is due to the pairing up of d electrons to unoccupy high-lying d orbitals.

Tables 1-1 and 1-3 show the results of geometry-optimized clusters compared to the single-point energy clusters at bulk Pt distances using NLDA-GGAII; we see good agreement again between these two sets of values. A notable exception is the Pt_7 hexagon where S=2 is the calculated ground state of the optimized cluster. The shorter Pt-PT distances in the geometry-optimized cluster make it more favorable to pair up two of the electrons occupying high-lying d-orbitals. We expect more pairing of d orbitals for larger more bulk-like clusters. As fewer of the atoms are at *corners*, it becomes more favorable to pair up the spins (see Figure 1-5).

Similar results are obtained for the octahedral-based clusters, Pt_6 octahedron, Pt_9 (6.3) bilayer, and Pt_{10} (6.3.1) trilayer. S=3 is the calculated ground state for the geometry-optimized clusters. The IEM predicts S=4 to be the ground state of these clusters. In the high-symmetry Pt_6 octahedron and Pt_{10} tetrahedron, the S=4 state lies less than 1 kcal/mol higher in energy. For geometry-optimized Pt_9 (6.3) bilayer, the S=4 state is 13.30 kcal/mol higher in energy than the S=3 state. However, the octahedron is distorted in this cluster because of the lowered symmetry. From single-point energy calculations

for this cluster (both B3LYP and NLDA-GGAII), we find that the gap between the S=3 and S=4 states is less than 1 kcal/mol. The very small gap (less than 1 kcal/mol) indicates the metallic character of the clusters as we go to larger clusters.[7]

Acknowledgement

The content of this chapter was adapted from reference 29. This research was funded by the NSF (CHE 95-22179). Some calculations were carried out at the NCSA, University of Illinois.

References

1. Feng, K. A.; Lin, Z. D. *Appl. Surf. Sci.*, **1993**, *72*, 139.
2. Fahmi, A.; van Santen, R. A. *Z. Phys. Chem.*, **1996**, *197*, 203.
3. Illas, F.; Zurita, S.; Marquez, A. M.; Rubio, J. *Surf. Sci.*, **1997**, *376*, 279.
4. Watwe, R. M.; Spiewak, B. E.; Cortright, R. D.; Dumesic, J. A. *Catal. Lett.*, **1998**, *51*, 139.
5. Chen, M.; Bates, S. P.; van Santen, R. A.; Friend, C. M. *J. Phys. Chem. B*, **1997**, *101*, 10051.
6. Akinaga, Y.; Taketsugu, T.; Hirao, K. *J. Chem. Phys.*, **1997**, *107*, 415.
7. Xu, W.; Schierbaum, K. D.; Goepel, W. *Int. J. Quant. Chem.*, **1997**, *62*, 427.
8. McAdon, M. H.; Goddard III, W. A. *Phys. Rev. Lett.*, **1985**, *55*, 2563.
9. Gupta, S. K.; Nappi, B. M.; Gingerich, K. A. *Inorg. Chem.*, **1981**, *20*, 966.
10. Lide, D. R. *Handbook of Chemistry and Physics*, 71st ed.; CRC Press: Boca-Raton, 1990-1991.
11. Dai, D.; Balasubramaniam, K. J. *J. Chem. Phys.*, **1987**, *103*, 648.
12. Yang, S. H.; Drabold, D. A.; Adams, J. B.; Ordejon, P.; Glassford, K. *J. Phys. Cond. Matter*, **1997**, *9*, L39.
13. Ellis, D. E.; Guo, J.; Cheng, H. P.; Low, J. J. *Adv. Quant. Chem.*, **1991**, *22*, 125.
14. Bigot, B.; Minot, C. *J. Am. Chem. Soc.*, **1984**, *106*, 6601.

15. An equivalent resonance structure would have doubly occupied IBOs in the *other* half of the tetrahedra. Another picture of this could be to have singly occupied tetrahedral interstitial orbitals in all the tetrahedra. We have chosen to formulate the model in terms of one resonant structure, since the electron configuration remains unaffected.
16. Leschik, G.; Courths, R.; Wern, H.; Hufner, S.; Eckardt, H.; Noffke, J. *Sol. Stae. Commun.*, **1984**, *52*, 221.
17. Davenport, J. W.; Watson, R. E.; Weinert, M. *Phys. Rev. B*, **1985**, *32*, 4883.
18. Pandya, R. K.; Joshi, K. B.; Jain, R.; Ahuja, B. L.; Sharma, B. K. *Phys. Status Solidi B*, **1997**, *200*, 137.
19. Richter, L. J.; Ho, W. *Phys. Rev. B*, **1987**, *36*, 9797.
20. Pipek, J.; Mezey, P. G. *J. Chem. Phys.*, **1989**, *90*, 4916.
21. Slater, J. C. "Quantum Theory of Molecules and Solids" Vol. 4: *The Self-Consistent Field for Molecules and Solids*, McGraw-Hill, New York (1974).
22. Perdew, J. P.; Chevary, J. A.; Vosko, S. H.; Jackson, K. A.; Pederson, M. R.; Singh, D. J.; Fiolhals, C. *Phys. Rev. B*, **1992**, *46*, 6671.
23. Moore, C. E. *Atomic Energy Levels*, Volume III; National Bureau of Standards: Washington, DC, 1971.
24. Jaguar 3.0, Schrodinger, Inc., Portland, Oregon,1997; PS-GVB v2.3, Schrodinger, Inc., Portland, Oregon, 1996.
25. Hay, P. J.; Wadt, W. R. *J. Phys. Chem.*, **1985**, *82*, 299.
26. Becke, A. D. *Phys. Rev. A*, **1988**, *38*, 3098.
27. Vosko, S. H.; Wilk, L.; Nusair, M. *Can. J. Phys.*, **1980**, *58*, 1200.
28. Lee, C.; Yang, W.; Parr, R. G. *Phys. Rev. B*, **1988**, *37*, 785.
29. Kua, J.; Goddard III, W. A. *J. Phys. Chem. B*, **1998**, *102*, 9481.

Chapter 2: Chemisorption on Platinum Clusters: Chemisorption of C_2H_x, CH_x and H on Pt(111)

Abstract

Using the model cluster developed in the previous chapter, we examined the structrues and energetics of a number of organic fragments on Pt(111). Using nonlocal density functional methods (B3LYP) we find that organics covalently bond to the Pt(111) surface with localized σ bonds to the surface Pt atoms, leading to tetrahedral hybridization of each carbon bonded to the surface. Thus, (i) CH_3 prefers an on-top site (a bond energy of ~54 kcal/mol), (ii) CH_2 prefers a 2-fold bridge site (a bond energy of ~104 kcal/mol), and (iii) CH prefers the 3-fold fcc cap site (a bond energy of ~167 kcal/mol). Similarly C_2H_4 forms a strong (36 kcal/mol) di-σ bond, while CCH_3 forms three σ bonds to the cap site. The results for C_2H_x/Pt_8 are in good agreement with available experimental results on Pt(111). These results are used to obtain heats of formation (ΔH_f) for chemisorbed intermediates useful in estimating the energetics of various hydrocarbon intermediates on Pt surfaces. The application of these ΔH_f values is illustrated by considering ethylene hydrogenation and decomposition on Pt(111).

2-1. Introduction

Supported platinum clusters catalyze a wide variety of hydrocarbon conversion reactions[1] involving C-C and C-H activation and are ubiquitous in the catalytic cracking and reforming processes used in the petrochemical industry. The chemistry of C_1 and C_2 hydrocarbons is fundamental to understanding this class of reactions. However, despite a

great deal of progress on characterizing these systems,[2] there remain a number of uncertainties concerning the energetics, barriers, and mechanisms of even such simple reactions as hydrogenation/dehydrogenation.[3] Our objective is to establish a framework useful for understanding the various reaction steps involved with hydrocarbon rearrangements on Pt surfaces.

In the previous chapter, we developed the IEM for describing the bonding in platinum clusters. In that work, we concluded that the planar Pt_8 cluster in Figure 1-12 should serve as a good model for the structures and energies for hydrocarbons on Pt(111) surfaces.

Many important catalytic processes use highly dispersed Pt catalysts with clusters as small as 10 atoms. However, the best characterized systems involve studies on single crystal surfaces such as Pt(111). We will use clusters to examine both systems. The advantage of using clusters is that it allows one to zoom in directly on the details of a chemical reaction. For a bulk metal, the surface orbitals mix into bands, making it difficult to isolate which orbitals are essential to interactions with the adsorbate orbitals.

The strong interactions between nonmetal adsorbates and the metal surface generally split out a set of orbitals that can be regarded as localized in the vicinity of the adsorption site. We model this *localized vicinity* with a cluster chosen to have an effective configuration similar to the infinite surface. This enables us to focus directly on the interaction between orbitals of the metal surface and the adsorbate.

We have examined all CH_x and C_2H_x intermediates. This allows us to consider the hydrogenation and decomposition pathways of ethylene on Pt(111). These calculations

on Pt_8 lead to geometries and energetics of ethylene and ethylidyne in good agreement with available experimental results.

2-2. Methane Chemistry on Pt(111)

2-2-1. Structures and Energetics

To establish the preferences of hydrocarbons for various sites on the Pt(111) surface, we calculated the optimum geometry of CH_3, CH_2, and CH in the top, bridge and cap sites of Pt_8 (for the non-optimal sites geometric constraints were applied). All calculations used the planar Pt_8 cluster fixed at the Pt-Pt bulk distance of 2.775 Å to represent the surface. The optimized structures are shown in Figure 2-1 and Figure 2-2. Table 2-1 gives the binding energies and Pt-C bond lengths of all these species.

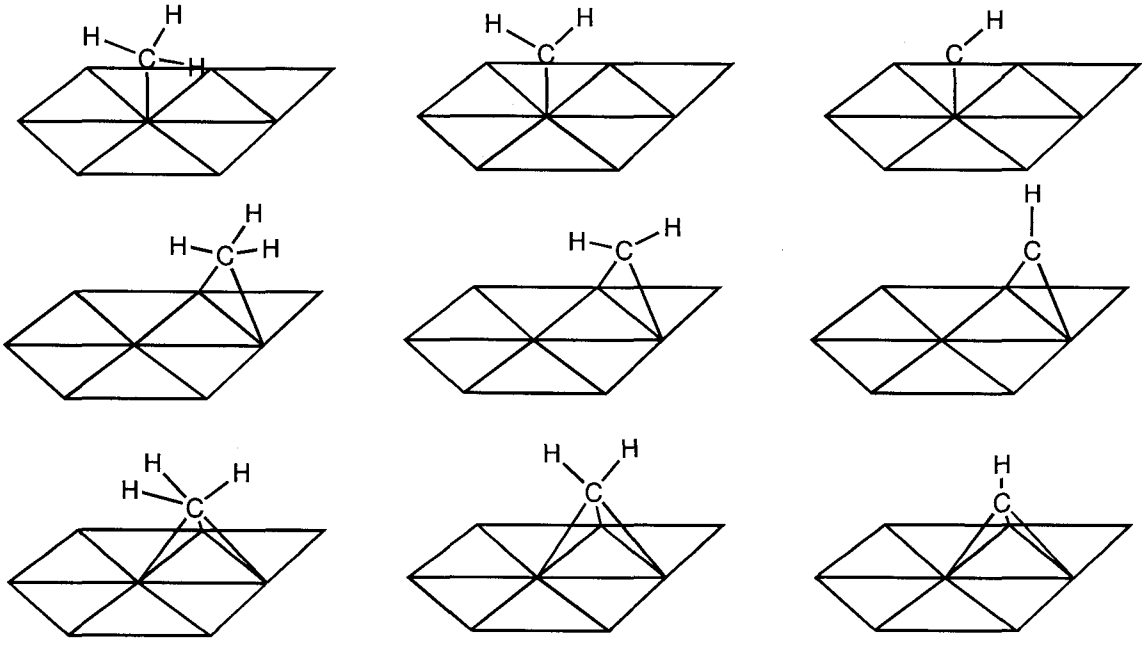

Figure 2-1. CH_x adsorbed at different sites on Pt_8.

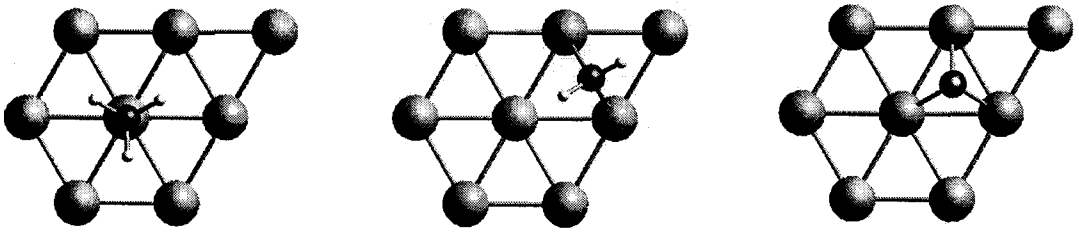

Pt_8-CH_3 (top site) Pt_8-CH_2 (bridge site) Pt_8-CH (cap site)

Figure 2-2. Top view of best binding structures of CH_x on Pt_8.

site	CH_3	CH_2	CH
		Binding Energy (kcal/mol)	
top	53.77	78.07	80.93
bridge	26.87	104.28	149.37
cap	22.52	80.54	166.60
		Pt-C bond length (Å)	
top	2.07	1.84	1.88
bridge	2.41	2.01	1.86
cap	2.63	2.11	1.95

Table 2-1. Binding energies and Pt-C distances of CH_x/Pt_8.

In each case, the preferred binding site is the one that allows carbon to make four σ bonds. Thus, the most stable structures are CH_3 in the on-top site (binding energy of 53.8 kcal/mol), CH_2 in the 2-fold bridge site (binding energy of $104.3 = 2 \times 52.2$ kcal/mol), CH in the 3-fold cap site (binding energy of $166.6 = 3 \times 55.5$ kcal/mol). In addition, the total bond energy to the surface is proportional to the number of Pt-C bonds (53 ± 3 kcal/mol per bond). The Pt-C bond lengths are 2.07 (CH_3), 2.01 (CH_2) and 1.95 Å (CH). We find that atomic C also binds to the cap site (binding energy of 152.0 kcal/mol, Pt-C 1.90 Å).

Each adsorbate was allowed to optimize freely, and only the lowest energy (strongest binding) structures are reported. The spin state of the cluster chosen is the one lowest in

energy (ground state). The calculated ground state of Pt_8 is S=3, which is our reference state. The ground state for CH_3/Pt_8 is S=5/2, which arises from spin pairing the dangling bond electron of CH_3 with an unpaired spin of Pt_8. The ground sate for CH_2/Pt_8 is S=2. Since the ground state of CH_2 is S=1, its two unpaired electrons spin pair with two of the unpaired spins on Pt_8. For CH/Pt_8, we find a net spin of S=5/2. Since the ground state of CH is S=1/2, this would be expected by spin pairing rules (the low-spin coupling of Pt_8 with S=3 and CH with S=1/2 would be S=5/2).

Table 2-2a summarizes the spin states used and the calculated absolute energy and heats of formation for each of these species. Table 2-2b shows the optimized energies and ground spin states of the fragments.

adsorbate on Pt_8	site	S	absolute energy (hartrees)	heat of formation (kcal/mol)
CH_3 (+1H)	top	5/2	-993.18432	-24.43
CH_2 (+2H)	bridge	2	-992.57507	-23.27
CH (+3H)	cap	5/2	-992.00222	-44.96
C (+4H)	cap	3	-991.34425	-13.23
H	cap	5/2	-953.86467	-11.38

Table 2-2a. Calculated energies, heats of formation, and spin states of CH_x/Pt_8 clusters and H/Pt_8.

fragment	S	Absolute energy (hartrees)
CH_4	0	-40.52405
CH_3	1/2	-39.84137
CH_2	1	-39.15163
CH	1/2	-38.47947
C	3	-37.84474
Pt_8	5/2	-953.25726

Table 2-2b. Optimized CH_x and Pt_8 energies and ground spin states.

2-2-2. Comparison with Experiment

There is kinetic and spectroscopic evidence for methyl (CH_3), methylene (CH_2), and methylidyne (CH) moieties on Pt(111).[4] However, neither the energetics nor the structures of CH_x species adsorbed on Pt(111) have been sufficiently characterized experimentally to provide a test for calculations.

Low energy-electron irradiation of CH_4 on Pt(111) shows evidence of C-H bond cleavage to form chemisorbed methyl and chemisorbed hydrogen atoms.[5] Molecular beam surface scattering experiments find that the dissociative chemisorption of methane is enhanced by increasing both the translational energy of methane and the surface temperature.[6]

Generating methyl adsorbed on Pt(111) via gas-phase pyrolysis of azomethane allows the study of its chemistry by temperature-programmed desorption (TPD) and reflection-adsorption infrared spectroscopy (RAIRS).[7] The surface chemistry of methyl is characterized by a competition between hydrogenation (to produce methane) and dehydrogenation (which ultimately leads to the production of surface carbon). An early TPD and RAIRS study using methyl iodide as a precursor to form chemisorbed methyl on Pt(111) concluded, from deuterium exchange reactions, that the final hydrogenation step to form methane is preceded by multiple exchange reactions.

It has been suggested that CH_2/Pt is much more reactive than CH_3/Pt and undergoes reversible conversion to CH before finally fully hydrogenating to methane.[8]

Considering the various CH_x species adsorbed on a Pt_8 planar cluster, we find CH to be the thermodynamic sink. The binding energies for each of these species (still unavailable from experiment) are in Table 2-1.

2-2-3. Heats of Formation

To study the energetics of hydrogenation/dehydrogenation reactions involving the chemisorbed CH_x species, it is useful to obtain the heats of formation for each chemisorbed species. We calculated the lowest energy structures of all intermediates bound to the Pt_8 cluster. The calculated energetics for the various intermediates are shown in Figure 2-3. We have converted these energetics to heats of formation by using appropriate reference compounds.

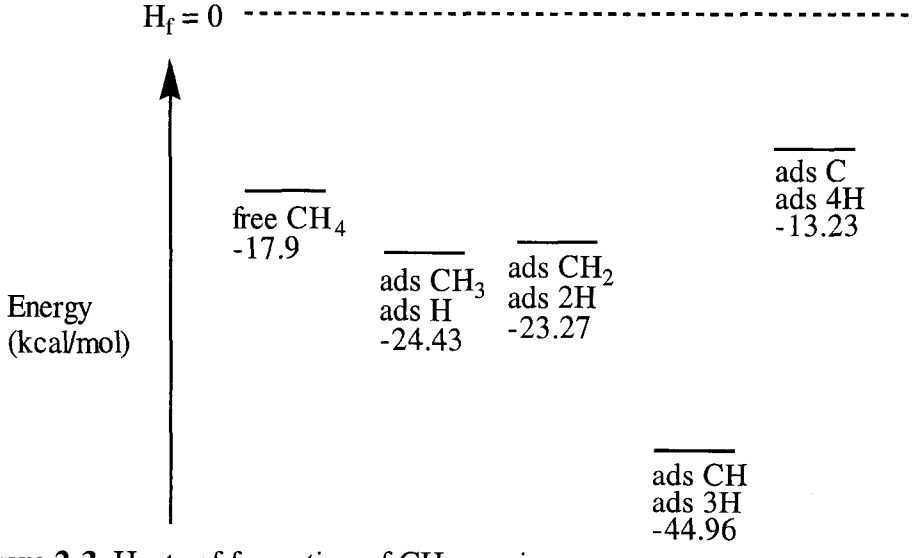

Figure 2-3. Heats of formation of CH_x species.

To calculate heats of formation, we must choose an appropriate ensemble of reference compounds (one for each element). We have chosen the following as the reference compounds: (a) Pt_8 (since all our calculations use this cluster) in the S=3 ground state, which is assigned $\Delta H_f (Pt_8) = 0$, (b) free gas-phase H_2, which is assigned $\Delta H_f (H_2) = 0$, and (c) free gas-phase methane, which is assigned $\Delta H_f (CH_4) = -17.9$ kcal/mol = -0.02852 hartrees.

Reference compound	Absolute energy (hartrees)	Experimental heat of formation (kcal/mol)	Corrections (hartrees)
Pt_8	-953.25726	0	$E(Pt_8)$ = -953.25726
H_2	-1.17853	0	$E(H_2)$ = -1.17854
CH_2CH_2	-78.59379	+12.5	E(C) = -38.12832
CH_4	-40.52405	-17.9	E(C) = -38.13845

Table 2-3. Calculated energies and assigned heats of formation of reference compounds.

The calculated energies of the reference compounds are shown in Table 2-3. Heats of formation for ethylene and methane are taken from gas-phase experimental values.[9] The method used to calculate heats of formation is as follows: Since ΔH_f (Pt_8) and ΔH_f (H_2) are both zero, the *reference energy* for a hydrogen, E(H) will be –0.58927 hartrees (half the calculated value for free H_2). The *reference energy* for carbon, E(C) is derived from

$$C + 2H_2 \rightarrow CH_4 \qquad (2.1)$$

which leads to

$$E(CH_4) = -40.52405 = -0.02852 \text{ hartrees} + E(C) + 4E(H)$$

where E(C) is –38.13845 hartrees. The *reference energy* for Pt_8 is $E(Pt_8)$ = -953.25726 hartrees.

To calculate the heat of formation of C_xH_y/Pt_8 clusters, we used the formula

$$\Delta H_f(C_xH_y/Pt_8) = \{E(C_xH_y) - E(Pt_8) - xE(C) - yE(H)\} \times 627.5096 \qquad (2.2)$$

For example, the heat of formation of methyl is

$$\Delta H_f(CH_3/Pt_8) = \{-993.18432 + 953.25726 + 2(38.13845) + 3(0.58927)\}$$

$$\times 627.5096 = -13.05 \text{ kcal/mol}$$

In comparing C_xH_y clusters with various numbers of H atoms, we assume low coverage conditions in which excess H atoms go onto the Pt surface in locations well separated

from the carbon-containing species. Thus, in examining rearranged structures starting with CH_4, we consider the ΔH_f to be

$$\Delta H_f (CH_x/Pt_8) + (4 - x)\, \Delta H_f (H/Pt_8) \qquad (2.3)$$

Thus, one methyl (x = 3) has one hydrogen less than methane, leading to (4 – x) = 1. Therefore, we add one increment of ΔH_f (H/Pt_8) to account for the heat of formation for the chemisorbed H. From Table 2-2a, ΔH_f (H/Pt_8) = -11.38 kcal/mol. Hence,

$$\Delta H_f (CH_3)_{ads} + \Delta H_f (H)_{ads} = -13.05 - 11.38 = -24.43 \text{ kcal/mol}$$

The heats of formation shown in Tables 2-2a and 2-4a have all been calculated and corrected using this scheme.

Table 2-2a shows these values with the necessary corrections for adsorbed hydrogen. Table 2-2b shows the optimized energies and ground spin states of the fragments. The reference compounds chosen are Pt_8, H_2 and methane. The procedure used is similar for the C_2H_x compounds with the exception that E(C) is –38.12832 since ethylene is used as the reference hydrocarbon instead of methane. [The corresponding tables are Table 2-4a and 2-4b.]

From Figure 2-3 we see that CH is the thermodynamic sink. The dissociative chemisorption of methane to CH_3 and H is downhill by 6.5 kcal/mol. Breaking the second C-H bond to form CH_2 adsorbed on the surface is only 1.2 kcal/mol uphill. Forming CH adsorbed is then downhill by 21.7 kcal/mol. In order to determine a complete reaction profile, it is necessary to include activation energy barriers. Estimated transition state geometries and reaction barriers can be found in the Appendix.

2-3. Ethylene Chemistry on Pt(111)

The chemistry of ethylene on Pt(111) has been studied extensively because it is a model reaction for understanding two major mechanisms in heterogeneous catalysis of hydrocarbon reactions: (1) hydrogenation to form ethane and (2) decomposition to finally deposit coke on the platinum surface. A barrage of experimental techniques has been used to study the mechanisms of these reactions, characterize the stable species and identify the intermediates involved. However, only three species have been well-characterized: di-σ bonded ethylene, π-bonded ethylene, and ethylidyne (CCH_3). The most stable species at low temperature is CCH_3. A consensus has not yet been reached for the mechanisms of catalytic hydrogenation and decomposition reactions.[3]

Recent studies using modern surface sensitive techniques have made it possible to study and characterize a few of the C_2H_x species on Pt(111). The two important pieces of information are structural information (bond lengths and angles) and adsorption or binding energy. Ethylene has been found to bind in two different modes, di-σ and π.

2-3.1. π bonded Ethylene

Ultraviolet photoemission spectroscopy (UPS) shows that ethylene adsorbs through its π bonding orbital on clean Pt(111) below 52K.[10] Reflection-adsorption infrared spectroscopy (RAIRS) concludes that the C=C bond is parallel to the surface and that the binding energy of this species is 9.6±2.4 kcal/mol.[11] Our calculated structure of π bonded ethylene at an on-top site on a Pt_8 planar cluster is in very good agreement with these results (see Figure 2-4). We calculate a binding energy of 8.49 kcal/mol and a C-C

distance of 1.35 Å. The C=C bond is parallel to the surface and the molecular plane is slightly tilted (92°). The Pt-C distances are calculated to be 2.70 Å.

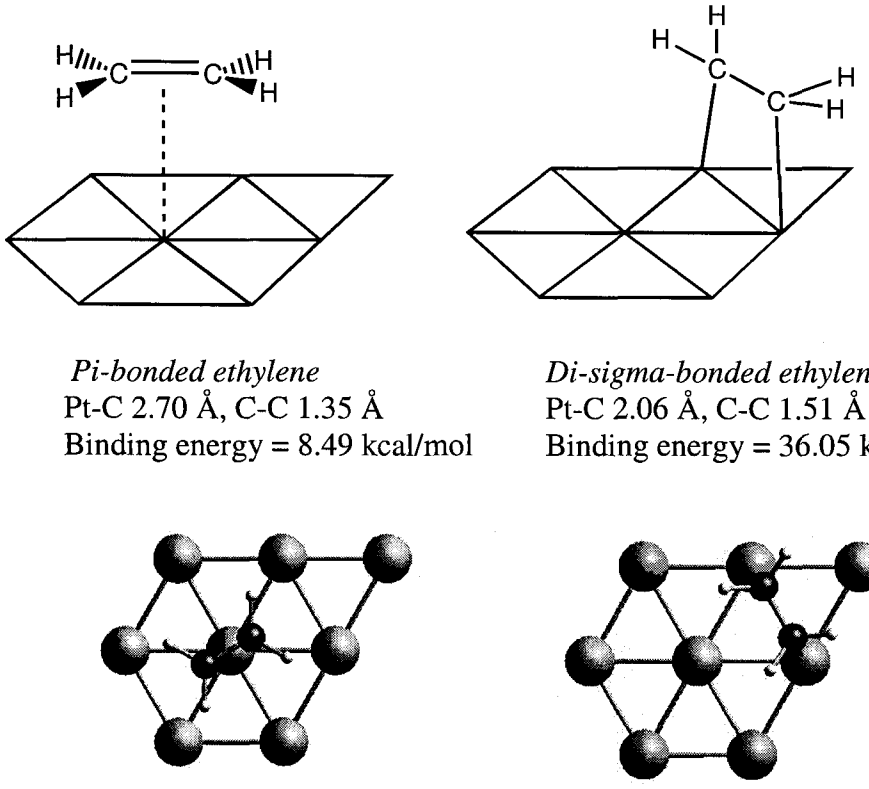

Figure 2-4. π and di-σ bonded ethylene on Pt_8.

2-3-2. Di-σ bonded Ethylene

The more stable mode of ethylene is the di-σ bonding mode. When heated above 52 K, the π bond breaks and each carbon forms a single bond to a platinum atom. The C-C bond is parallel to and found above a Pt-Pt bridge. The molecular plane is tilted. This is suggested on the basis of high resolution electron energy-loss spectroscopy (HREELS),[12] UPS,[13] and near-edge X-ray absorption fine structure (NEXAFS) studies.[14] The C-C

bond measured from NEXAFS is 1.49 ± 0.04 Å. Initial TPD experiments measured the adsorption energy to be 17 kcal/mol.[15] However, recent measurements by collision-induced desorption (CID)[16] suggest that this value is too small and that TPD does not accurately measure the binding energy of this species. Both CID and microcalorimetry[17] measure an adsorption energy ranging from 29.6 to 41.6 kcal/mol at low coverage. We calculate a binding energy of 36.05 kcal/mol and a C-C bond length of 1.51 Å. The C-C bond is at the bridged position, parallel to the surface and the tilt of the molecular plane is now much larger (115-116°). The Pt-C bond length is 2.06 Å (see Figure 2-4).

2-3-3. Ethylene Hydrogenation

The hydrogenation reaction is thought to proceed via direct hydrogenation of ethylene to form an ethyl radical. Further hydrogenation of the ethyl radical leads to ethane desorbed from the platinum surface (see Figure 2-5). This mechanism was first proposed by Horiuti and Polanyi in the 1930s.[18] Recent evidence to support this mechanism comes from experiments using ultrahigh vacuum (UHV) techniques,[19] carbon-14-labeling studies,[20] and deuterium-labeling experiments.[21] These studies conclude that the stable ethylidyne species is *not* an intermediate in the reaction, but rather the hydrogenation incorporation occurs stepwise directly on the ethylene species. The ethyl radical is not a stable intermediate but readily undergoes β-H elimination to yield ethylene.[22] Structural and energetic information is not yet available on the transient ethyl species experimentally. Our calculations show that that ethyl binds most stably at an on-top site with a binding energy of 48.60 kcal/mol (see Figure 2-6). The Pt-C bond length is 2.13 Å and the C-C bond length is 1.50 Å.

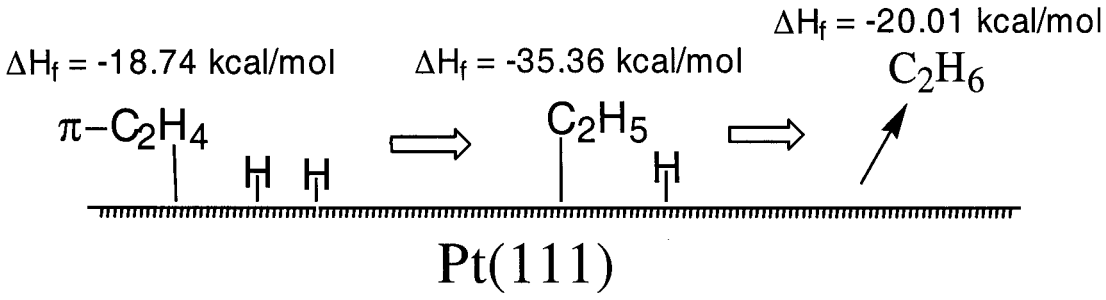

ΔH_f values in kcal/mol

	adsorbed C_xH_y	adsorbed H	total
π-C_2H_4	+4.02	2*(-11.38)	-18.74
C_2H_5	-23.56	-11.38	-35.36

Figure 2-5. Horiuti-Polanyi mechanism for hydrogenation of ethylene.

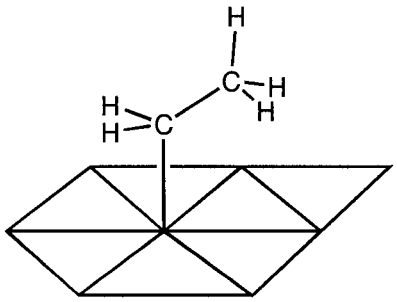

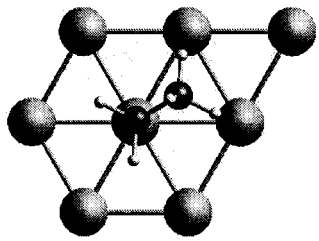

Ethyl
Pt-C 2.13 Å, C-C 1.51 Å
Binding energy = 48.60 kcal/mol

Top view

Figure 2-6. Ethyl (C_2H_5) on Pt_8.

2-3-4. Ethylene Decomposition

The pathway for ethylene decomposition remains controversial. It is agreed that ethylidyne is the most stable of the C_2H_x species on Pt(111). Ethylene loses a net one hydrogen to form ethylidyne, which then eventually fully dehydrogenates at higher temperatures to deposit coke. Low-energy electron diffraction (LEED) studies show that ethylidyne occupies a three-fold fcc site.[23] The C-C bond is perpendicular to the

platinum surface and the bond length is 1.50±0.05 Å. The Pt-C bond length is measured to be 2.00±0.05 Å. Our calculation of ethylidyne in the fcc site (see Figure 2-7) has the same geometry with an optimized C-C bond length of 1.49 Å. We further calculate a Pt-C bond length of 1.96 Å and a binding energy of 154.73 kcal/mol.

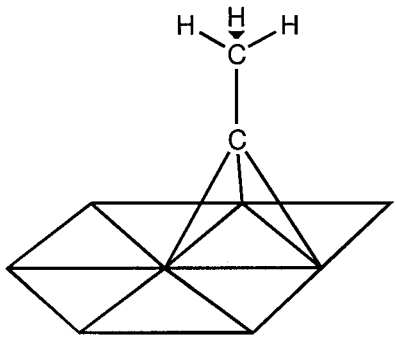

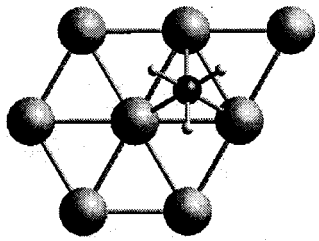

Ethylidyne
Pt-C 1.96 Å, C-C 1.49 Å
Binding energy = 154.73 kcal/mol

Top view

Figure 2-7. Ethylidyne (CCH_3) on Pt_8.

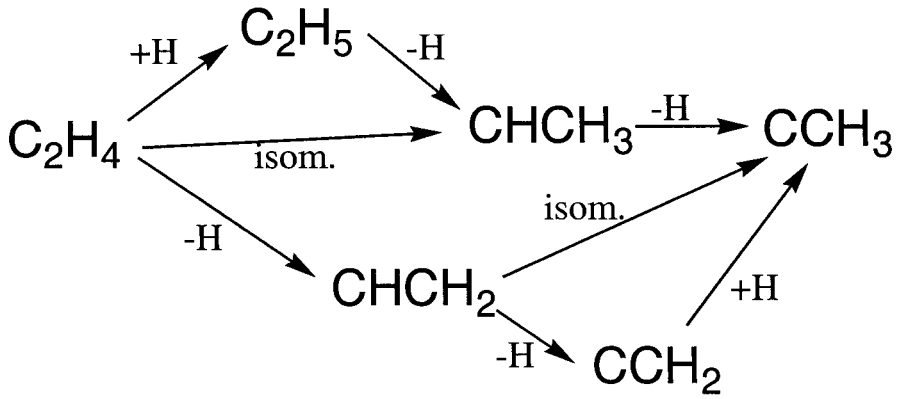

Somorjai:	$C_2H_4 \rightarrow C_2H_5 \rightarrow CHCH_3 \rightarrow CCH_3$
Windham/Koel:	$C_2H_4 \rightarrow CHCH_3 \rightarrow CCH_3$
Zaera:	$C_2H_4 \rightarrow CHCH_2 \rightarrow CCH_3$
Kang/Anderson:	$C_2H_4 \rightarrow CHCH_2 \rightarrow CCH_2 \rightarrow CCH_3$

Figure 2-8. Four pathways for ethylene conversion to ethylidyne.

Four different pathways have been suggested for the conversion of ethylene to ethylidyne (see Figure 2-8). Two of these pathways (the middle two) are two-step reactions involving an isomerization step and a dehydrogenation step. They differ in which step comes first. The Windham/Koel pathway[15] proposes that ethylene first isomerizes to ethylidene ($CHCH_3$) and then undergoes α-H elimination to form ethylidyne. In the Zaera pathway,[21] dehydrogenation is the first step to form vinyl ($CHCH_2$), followed by isomerization to ethylidyne. The two other pathways that only have hydrogenation and dehydrogenation reactions are the Somorjai pathway,[24] which goes through the ethyl intermediate, and the Kang/Anderson pathway,[25] which includes vinylidene (CCH_2) as an intermediate. These latter two pathways are unlikely because ethyl readily undergoes β-H elimination and vinylidene transforms to ethylene at temperatures as low as 170 K.[3] It is suggested that ethylidyne undergoes successive dehydrogenation until coke is finally deposited on the platinum surface. At this point, no experiments clearly identify the intermediates in this reaction. Our calculated thermodynamics favor the Zaera pathway that goes through $CHCH_2$ as an intermediate.

2-3-5. Comparison to Previous Theory

Previous computational work on ethylene chemistry on Pt(111) has been limited to less accurate or semi-empirical methods. Anderson and co-workers have used extended Huckel theory with empirical two-body atom-atom corrections [the atom superposition electron delocalization molecular orbital (ASED-MO) method] in conjunction with a Pt_{15} planar cluster to calculate adsorption energies and reaction barriers.[26] The geometries show overly long bond lengths for the adsorbed species. For example, the C-C bond

lengths of adsorbed CCH_3, di-σ C_2H_4, and C_2H_5 were calculated to be 1.70, 1.77 and 1.73 Å respectively (15-20% too large). The energetics do not agree. ASED-MO leads to a binding energy of ~90 kcal/mol for H to Pt(111), whereas the experimental value is ~60 kcal/mol.

Another method of making predictions is to estimate the thermochemistry by calculating the heats of formation for the adsorbed species of all the intermediates involved.[27] This method involves (a) using electronic excitation energies, electron affinities, or ionization potentials to calculate a heat of formation for a gas phase species that resembles the electronic state of an adsorbed molecule, (b) using measured heats of adsorption, and (c) using *ab initio* calculations to predict the heat of formation of adsorbed species. This method depends on the accuracy of the measured heats of formation of adsorbed species. Thus, some experimental numbers used[27] are now thought to be incorrect. For example, the 17 kcal/mol TPD value[15] for the binding energy of ethylene was used, whereas recent experiments[16-17] suggest the correct value to be 30-42 kcal/mol.

2-3-6. Analysis of Energetics for C_2H_4 Conversion

Structures and binding energies of the strongest binding species for the other C_2H_x species are shown in Figure 2-9. From the heat of formation values for each of the clusters, with the appropriate corrections (Tables 2-4a and 2-4b), we can consider the thermodynamics of all the C_2H_x species adsorbed on Pt(111). Figure 2-10 provides information to consider the pathways for ethylene conversion on Pt(111).

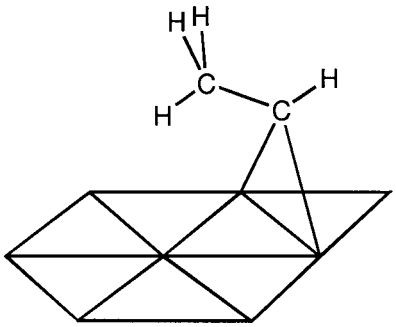

Ethylidene
Pt-C 2.04 Å, C-C 1.51 Å
Binding energy = 98.05 kcal/mol

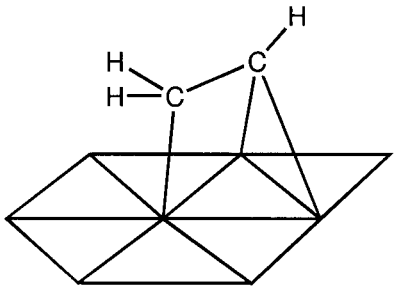

Vinyl
Pt-C 1.99-2.03 Å, C-C 1.50 Å
Binding energy = 94.63 kcal/mol

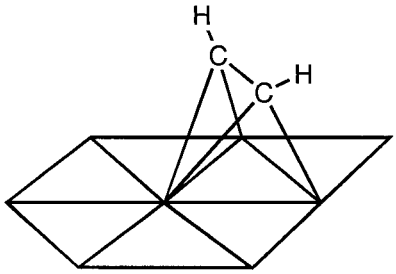

Acetylene
Pt-C 1.94-2.12 Å, C-C 1.42 Å
Binding energy = 78.83 kcal/mol

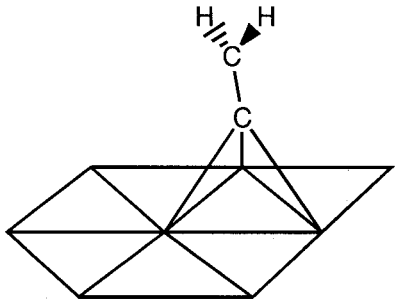

Vinylidene
Pt-C 1.95-2.04 Å, C-C 1.39 Å
Binding energy = 96.49 kcal/mol

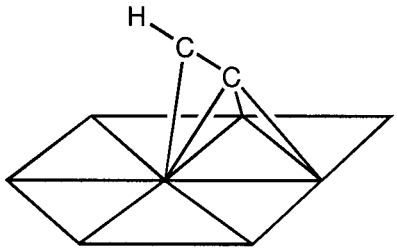

Ethynyl
Pt-C 1.91-2.29 Å, C-C 1.35 Å
Binding energy = +94.54 kcal/mol

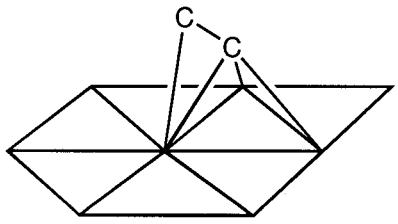

Dicarbon
Pt-C 1.89-2.13 Å, C-C 1.41 Å
Binding energy = +143.90 kcal/mol

Figure 2-9a. Geometries and binding energies of intermediates in the ethylene decomposition reaction (schematic view).

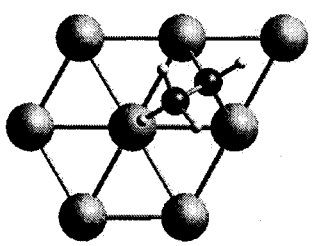

Ethylidene

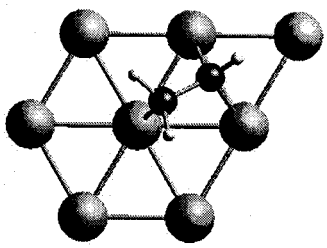

Vinyl

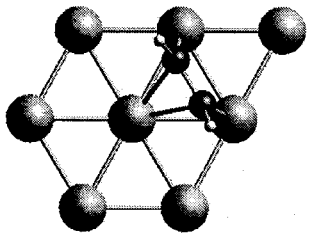

Acetylene

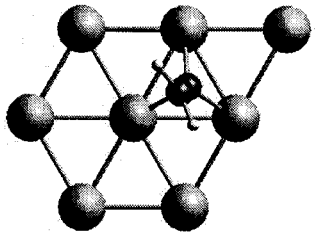

Vinylidene

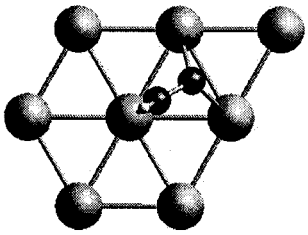

Ethnyl

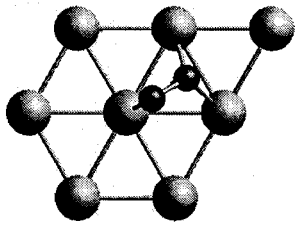

Dicarbon

Figure 2-9b. Top view of intermediates in the ethylene decomposition reaction.

adsorbate on Pt_8	site	S	Absolute energy (hartrees)	ΔH_f (kcal/mol)
CH_2CH_3 (-1H)	top	5/2	-1032.49839	-12.55
CH_2CH_2 (di-σ)	bridge	2	-1031.90852	-23.56
$H_2C{=}CH_2$ (π)	top	3	-1031.86458	+4.02
$CHCH_3$	bridge	2	-1031.89164	-12.96
CCH_3 (+1H)	cap	5/2	-1031.33096	-42.28
$CHCH_2$ (+1H)	cap	5/2	-1031.31067	-29.55
HC=CH (+2H)	cap	2	-1030.71021	-33.91
$C{=}CH_2$ (+2H)	cap	3	-1030.67134	-9.52
C=CH (+3H)	cap-top	5/2	-1030.00967	+24.53
C=C (+4H)	cap-top	2	-1029.36672	+46.84

Table 2-4a. Calculated energetics, ΔH_f, and spin states of C_2H_x/Pt_8 clusters.

fragment	S	Absolute energy (hartrees)
CH_2CH_3	1/2	-79.16369
CH_2CH_2	0	-78.59380
$CHCH_3$	1	-78.48001
CCH_3	1/2	-77.82713
$CHCH_2$	1/2	-77.90486
HCCH	0	-77.32960
CCH_2	0	-77.26338
CCH	1/2	-75.88241
CC	1	-75.86790

Table 2-4b. Optimized C_2H_x energies and ground spin states.

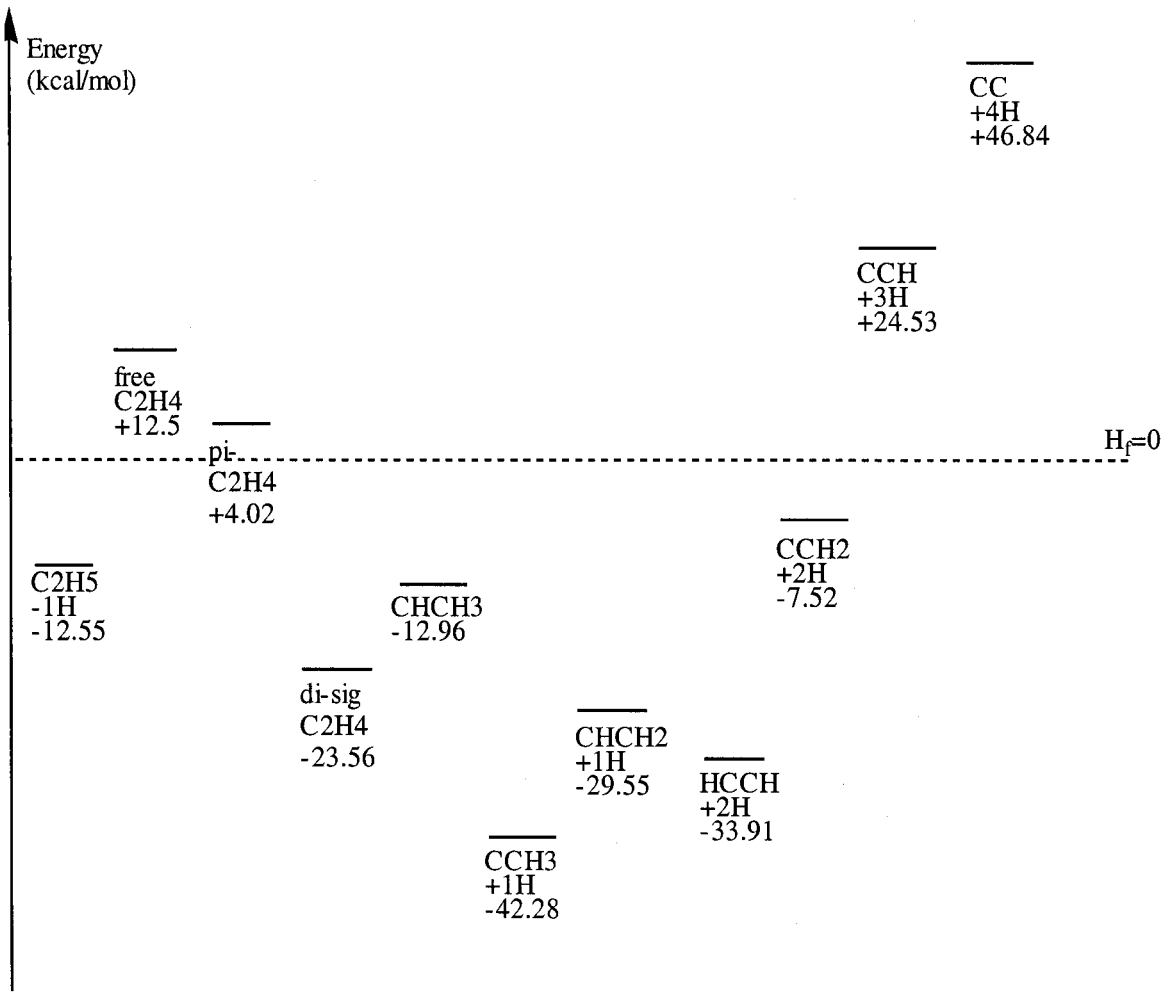

Figure 2-10. Heats of formation of C_2H_x species chemisorbed on Pt(111).

The heat of formation of ethane (not shown in Figure 2-10) is –20.0 kcal/mol.[9] For the first step of ethylene hydrogenation, thermodynamics favors the conversion of ethyl to ethylene. Although not calculated in these studies, we expect the barrier to this reaction to be small. Experimental evidence supports rapid β-H elimination. Ethylidyne is the thermodynamic sink for the C_2H_x species in our calculations. This is in agreement with experimental evidence that it does not participate as an intermediate in ethylene hydrogenation. Our calculations also suggest that the hydrogenation of π bonded ethylene to ethyl is exothermic. Activation barriers need to be determined, but at this point, our calculations are in favor of the Horiuti-Polanyi mechanism.

For the conversion of ethylene to ethylidyne, the energetics rule out the Kang/Anderson pathway. The conversion of $CHCH_2$ to CCH_2 is almost 20 kcal/mol uphill. It seems more likely that $CHCH_2$ isomerizes to form ethylidyne, according to the Zaera pathway. The Somorjai pathway is thermodynamically only slightly less favorable than the Windham/Koel pathway. However, the barrier to hydrogenation will need to be compared to the barrier to isomerization for a more complete comparison. When the two pathways that include an isomerization step are compared, the Zaera pathway seems to be more favorable since $CHCH_2$ is 6 kcal/mol downhill from ethylene, while $CHCH_3$ is 10 kcal/mol uphill from ethylene.

2-3-7. Comparison of CH_x and C_2H_x

The C_2H_x compounds are closely related to the CH_x compounds on Pt(111). Interconversion between these two classes of compounds takes place via C-C bond breaking or C-C coupling reactions. Platinum metal is known to catalyze both these

processes, of which isomerization of the carbon backbone in hydrocarbons is a good example. These reactions are expected to occur with higher activation energies compared to reactions that involve C-H bond forming and breaking. This is due to the directionality of the R_3C fragment orbital, which destabilizes the transition state where a metal-carbon (M-C) bond is being converted to a C-C or C-H bond and vice versa. The spherical H 1s orbital can form multicenter bonds easily, and so the barrier for converting C-H bonds to metal-hydrogen (M-H) bonds and vice versa is much lower than that for converting C-C bonds.[28]

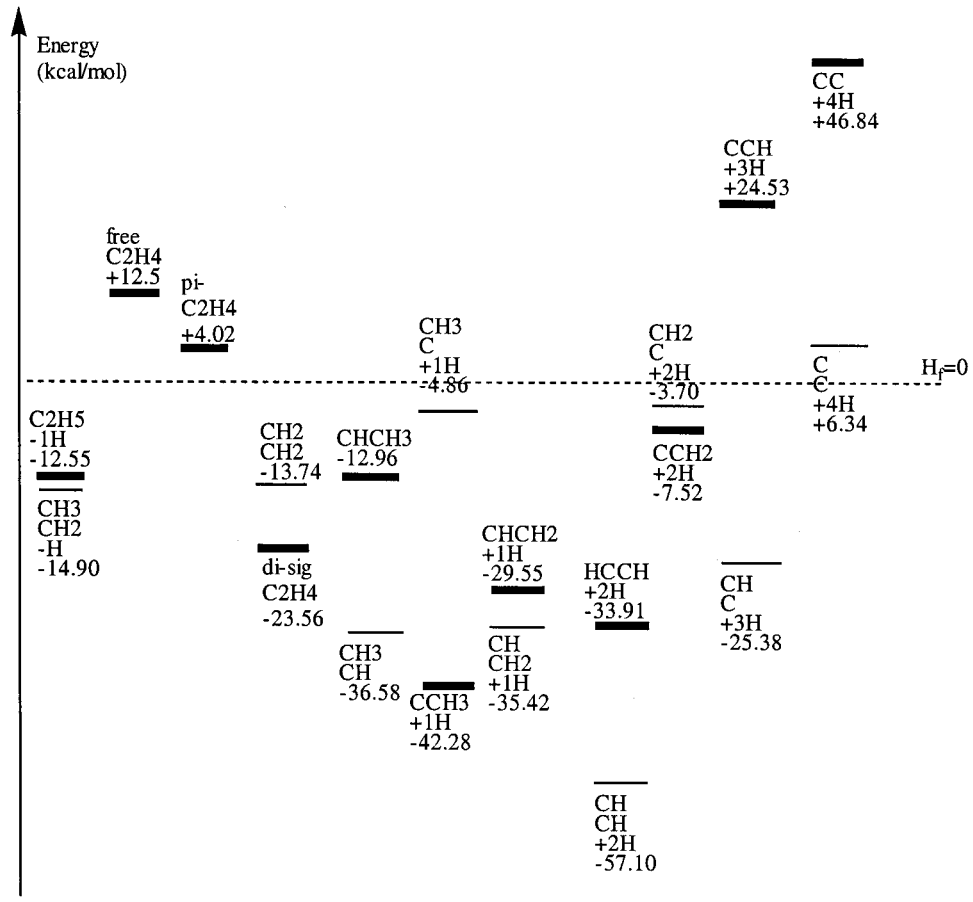

Figure 2-11. Heats of formation of C_2H_x and CH_x species.

Using Pt_8, H_2, and ethylene as reference compounds, we can examine the thermodynamics for the fragmentation reactions (see Figure 2-11). In general, the C_2H_x compounds on the right side have fragments that are lower in energy, while compounds on the left side have higher energy fragments. This is largely due to the stability of the CH fragment. The thicker energy level lines correspond to the C_2H_x compounds (Figure 2-10).

2-4. Hydrogen Chemisorption on Pt(111)

Extensive work has been done on the chemisorption of hydrogen on metals.[29] This is not surprising since hydrogenation and dehydrogenation reactions are among the most fundamental in industrial processes. The hydrogen molecule undergoes dissociative chemisorption on Pt(111) to form two separate hydrogen atoms. The development of HREELS has made it possible to study hydrogen adsorption on Pt(111). H is found to be most stable in the fcc site with a binding energy of 60 kcal/mol.[30]

In the computational area, periodic linearized augmented plane wave (LAPW) calculations of a H monolayer on Pt(111) has H in the fcc sites with a Pt-H bond length of 1.86 Å,[31] for a bond energy of 61 kcal/mol. One-electron pseudo-potential calculations[32] on Pt-H and Pt_2-H lead to binding energies that are too low (62 and 35 kcal/mol respectively). Very extensive calculations have been done on Pt-H and Pt_2-H using high level configuration interactions (CI) and spin-orbit coupling methods.[33] These lead to binding energies of 72 and 59 kcal/mol respectively. Our computational results on these same clusters using DFT NLDA-GGAII on Pt-H and Pt_2-H are in agreement with these results.

For the Pt-H molecule, we calculate an optimum bond length of 1.52 Å and a binding energy of 68.77 kcal/mol. For Pt_2-H, we find that H is bridge-bound with Pt-H bond lengths of 1.57 Å, a Pt-Pt distance of 2.50 Å, and a binding energy of 58.80 kcal/mol. Other studies on H binding to platinum clusters were concerned with studying the saturation of H on these clusters.[34-35] These do not directly utilize the cluster as a model for the platinum surface.

Our calculations of H in the capped site of different platinum clusters have Pt-H bond lengths of 1.86 Å and binding energies ranging from 56 to 60 kcal/mol, in good agreement with experimental results (60 kcal/mol). Full geometry optimized structures were calculated for Pt_3-H and Pt_6-H with H in the cap site. Pt_3 is a triangle, and for Pt_6, both the triangle and octahedron were calculated. The clusters are shown in Figure 2-12. Bond lengths and binding energies are reported in Table 2-5. An IEM explanation for the binding of H to these small clusters has been explained in the previous chapter.

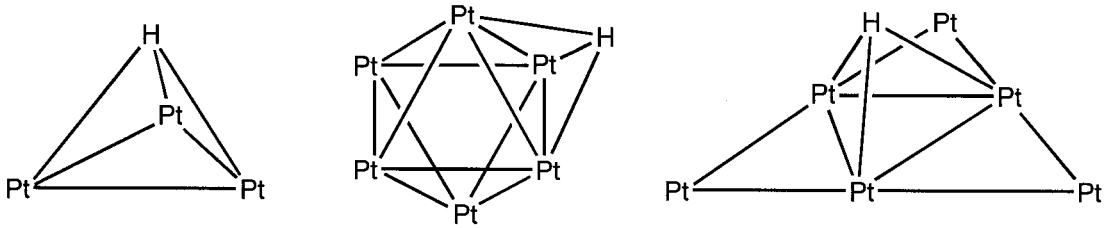

Figure 2-12. Optimized clusters of H adsorbed in the 3-fold sites of Pt_3 and Pt_6 clusters.

	H-Pt_3 (triangle)	H-Pt_6 (octahedron)	H-Pt_6 (triangle)
Pt-Pt (Å)	2.59	2.71 [9], 2.78 [3]	2.52 [6], 2.75 [3]
Pt-H (Å)	1.86	1.86	1.87
Binding energy (kcal/mol)	59.04	59.64	56.06

Table 2-5. Bond lengths and binding energies of H capped in Pt_3 and Pt_6. [Number in brackets indicates number of bonds with same length.]

Attempts to optimize H in the capped site of a Pt_4 tetrahedron were unsuccessful. H either moves to a bridge site or an η^1 site on the cluster. In the bridge site, the Pt-H bond length is 1.71 Å and the binding energy of H is 68.49 kcal/mol. The Pt-Pt bond lengths in this cluster range from 2.63-2.65 Å. The η^1-bound H has a Pt-H bond length of 1.56 Å and a binding energy of 70.97 kcal/mol. The higher binding energies are not surprising because these structures correspond to binding at defect (edge or corner) sites. It is also not surprising that the capped site of the tetrahedron is unstable for H adsorption, since the triangular faces of the tetrahedron represent hcp sites. Compare this to the octahedron where the faces represent fcc sites where H adsorbs with a binding energy of 56.6 kcal/mol. These results are well explained by the IEM (Chapter 1).

Constrained optimizations of H/Pt_8 were calculated using the B3LYP method (see Figure 2-13) since the C_xH_y/Pt_8 clusters were calculated using this hybrid method. The results are shown in Table 2-6. Once again, H in the cap site has the largest binding energy, in agreement with experiment. Hydrogens adsorbed in the top and bridge sites are only 0.5 and 1.8 kcal/mol less strongly bound. This suggests facile diffusion of H on the Pt(111) surface.

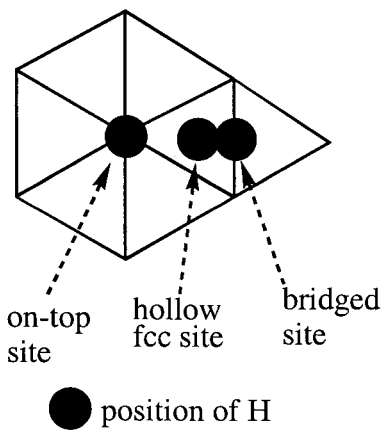

Figure 2-13. H adsorbed at different sites on Pt_8.

site	spin state	Pt-H (Å)	absolute energy (hartrees)	binding energy (kcal/mol)
top	7/2	1.51	-953.86381	66.69
bridge	2	1.74	-953.86196	65.62
cap	5/2	1.86	-953.86457	67.23
Reference energies: Pt_8 (S=3): -953.25726 hartrees; H (S=1/2): -0.50027 hartrees.				

Table 2-6. B3LYP constrained optimizations of H/Pt_8.

We also did B3LYP constrained optimizations of H adsorbed on the Pt_{12} (8.4) bilayer cluster (shown in Figure 2-14). Note that this cluster does not have a s^1d^9 electronic configuration. Pt-H bond lengths and binding energies are shown in Table 2-7. The ground spin state of the naked platinum cluster is S=5. This is also the state predicted by the IEM (four IBOs in the four tetrahedra, and an additional IBO associated with the fcc face of the octahedron on the four-atom face). The spin state used for the Pt_{12}-H clusters is therefore S=9/2. There is now a larger discrimination in the energies of different sites on the eight-atom face. Bias for the on-top site is expected to be larger (from IEM) because of the fixed orientation of the tetrahedra with the tips pointing down. This is indeed the case from our calculations. More important is the comparison between the binding of H to the fcc sites on the eight-atom and four-atom faces. IEM predicts that the four-atom face fcc site has orbitals of mostly s character while the eight-atom face fcc site has orbitals of mostly d character. Hence, we expect stronger binding to the four-atom face fcc site, because of better overlap between the H 1s orbital and the orbitals of s character. From our calculations, the binding energy is lower at the eight-atom face fcc site (52.22 kcal/mol) compared to the four-fold atom face fcc site (59.08) kcal/mol. The latter binding energy is also very close to the experimental binding energy of 60 kcal/mol.

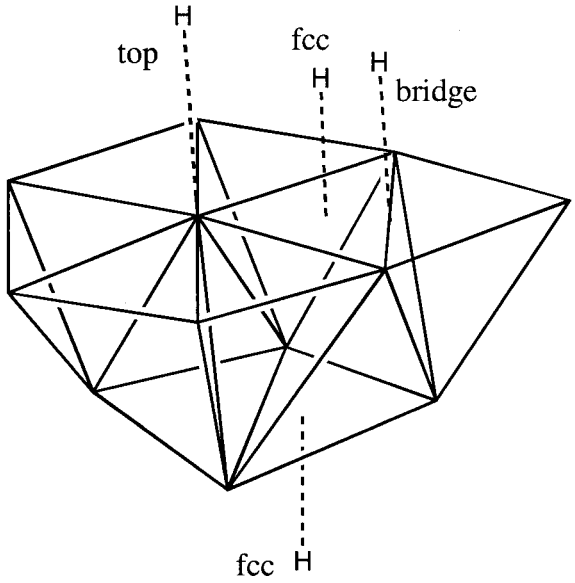

Figure 2-14. H adsorbed at different site on the Pt_{12} (8.4) bilayer cluster.

site	spin state	Pt-H (Å)	absolute energy (hartrees)	binding energy (kcal/mol)
Top (8-atom face)	9/2	1.55	-1430.66546	64.90
Bridge (8-atom face)	9/2	1.73	-1430.65287	57.00
Cap (8-atom face)	9/2	1.85	-1430.64525	52.22
Cap (4-atom face)	9/2	1.87	-1430.65618	59.08
Reference energies: Pt_{12} (S=5): -1430.06176 hartrees, H (S=1/2): -0.50027 hartrees The excited states of Pt_{12} are S=6 at 5.13 kcal/mol and S=7 at 11.84 kcal/mol.				

Table 2-7. B3LYP constrained optimizations of H/Pt_{12}.

2-5. Chemisorption of CH_3 on Selected Platinum Clusters

It has been suggested that the use of naked metal clusters in calculating good chemisorption energies of adsorbates requires the cluster to be in a *prepared* bonding state.[36] The argument is that the excitations to higher states are involved in the *preparation*. For the infinite surface, this value is close to zero, but for a small cluster, the required excitation energy should be added to the calculated chemisorption energy of the

ground state of the cluster. Using this rule, accurate chemisorption energies were calculated for H adsorbed to appropriate Ni clusters representing the Ni(111) and Ni(110) surfaces. More recently, this idea has been used to calculate the surface chemisorption of acetylene to cluster models of the copper (110, (110), and (111) surfaces.[37] In di-σ bonded ethylene, for example, there are two triplet states, a local triplet surface state and a triplet adsorbate state, which are coupled to produce a net singlet state for the two M-C bonds. Chemisorbed ethylene, which is no longer planar, is akin to ethane in structure and bonding.

Our view is that one should choose the metal clusters so that the *ground state* has the same configuration as the semi-infinite metal surface. This should yield accurate chemisorption energies. The IEM suggests that Pt(111) has an s^1d^9 electronic configuration and hence only clusters with this configuration are suitable.

cluster	S_{pred} from IEM of naked cluster	predicted electronic configuration	calculated binding energy (kcal/mol)
Pt atom		s^1d^9 (expt.)	66.98
Pt_4 tetrahedron	1	$s^{0.5}d^{9.5}$	56.16
Pt_8 planar (C_{2v})	4	s^1d^9	53.77
Pt_{12} planar (D_{3h})	6	s^1d^9	52.23
Pt_7 hexagon	3	$s^{0.86}d^{9.14}$	43.47
Pt_{12} (8.4) bilayer	5	$s^{0.83}d^{9.17}$	41.39

Table 2-8. Binding energy of selected CH_3/Pt_n clusters.

To test this concept, we studied CH_3 chemisorption for several Pt clusters, as shown in Table 2-8. The Pt atom has a s^1d^9 configuration, but it has a significantly larger binding energy. This is not surprising, since unlike the other s^1d^9 clusters (and the extended surface), the atom has net two unpaired electrons rather than one. Pt_4 tetrahedron represents the smallest bilayer cluster that models binding to an on-top site. The binding

energy is decreased significantly from that of the Pt atom. The other two s^1d^9 clusters, planar Pt_8 and Pt_{12}, have roughly similar binding energies. There is a slight decrease in binding energy from Pt_8 to Pt_{12}. The effect of adding more neighbors in different positions does not change binding significantly. Although the Pt_7 hexagon is very similar to planar Pt_8 (C_{2v}) in structure (the additional Pt atom not being connected to the central Pt that forms the Pt-C bond), the binding energies are 10 kcal/mol different. Indeed, the Pt_7 hexagon does *not* have the desired s^1d^9 configuration. The Pt_{12} (8.4) bilayer cluster has an electronic configuration close to Pt_7, leading to a binding energy in the same range. These results suggest that the electronic configuration of the cluster has a dominant effect on these calculations.

2-6. Conclusions

On the basis of the IEM, we chose a Pt_8 planar cluster to study adsorption and reaction pathways for chemisorption of C_1 and C_2 hydrocarbons on Pt(111). Using density functional methods with gradient corrections, we find geometries and energetics of C_2H_x/Pt_8 clusters in good agreement with experimental results (where available). The calculated energetics are in agreement with the Horiuti-Polanyi mechanism for hydrogenation to ethane. For the conversion of ethylene to ethylidyne, our results support the Zaera pathway (which goes through chemisorbed $CHCH_2$ as an intermediate). However, the Windham/Koel pathway (going through chemisorbed $CHCH_3$) cannot be discounted.

These calculations show that for chemisorbed hydrocarbon fragments the most stable sites have four σ bonds to each fragment carbon. The calculated binding energies for H in

the fcc site on small Pt clusters are in good agreement with experiment. On the planar cluster, the on-top site is slightly more favorable for H adsorption, a bias explained by the IEM.

These results suggest that relatively small clusters can be used to obtain accurate data for chemisorption *if* the clusters are properly chosen.

2-7. Computational Methods

Calculations were carried out with non-local density functional theory (DFT) using two major methods. The first method is NLDA-GGAII which uses the Slater local exchange functional[38] and Perdew-Wang local correlation functional with the Perdew-Wang generalized gradient approximation (GGA-II) non-local correlation functionals.[39] This method is used for the study of the platinum clusters (in Chapter 1) and hydrogen chemisorption on these clusters.

The second method is B3LYP which uses the exact Hartree-Fock (HF) and Slater local exchange functional for the exchange terms using the Becke 3-parameter method,[40] the Becke non-local gradient correction,[41] the Vosko-Wilk-Nusair exchange functional,[42] and the Lee-Yang-Parr local and non-local functional.[43] This method has been proven to be particularly good for calculating hydrocarbon species, and is used in our calculations of CH_x and C_2H_x on platinum clusters.

All *ab initio* calculations were done using the PS-GVB (v2.35) and JAGUAR programs.[44] The basis set used for platinum is the Hay and Wadt 18-electron relativistic effective-core potential.[45] For carbon and hydrogen, the 6-31G** basis set was used.

Appendix

Optimizing transition states on fixed metal clusters is more difficult than finding stable configurations of adsorbed species, hence we are less confident in the accuracy of our transition structures and activation barriers.

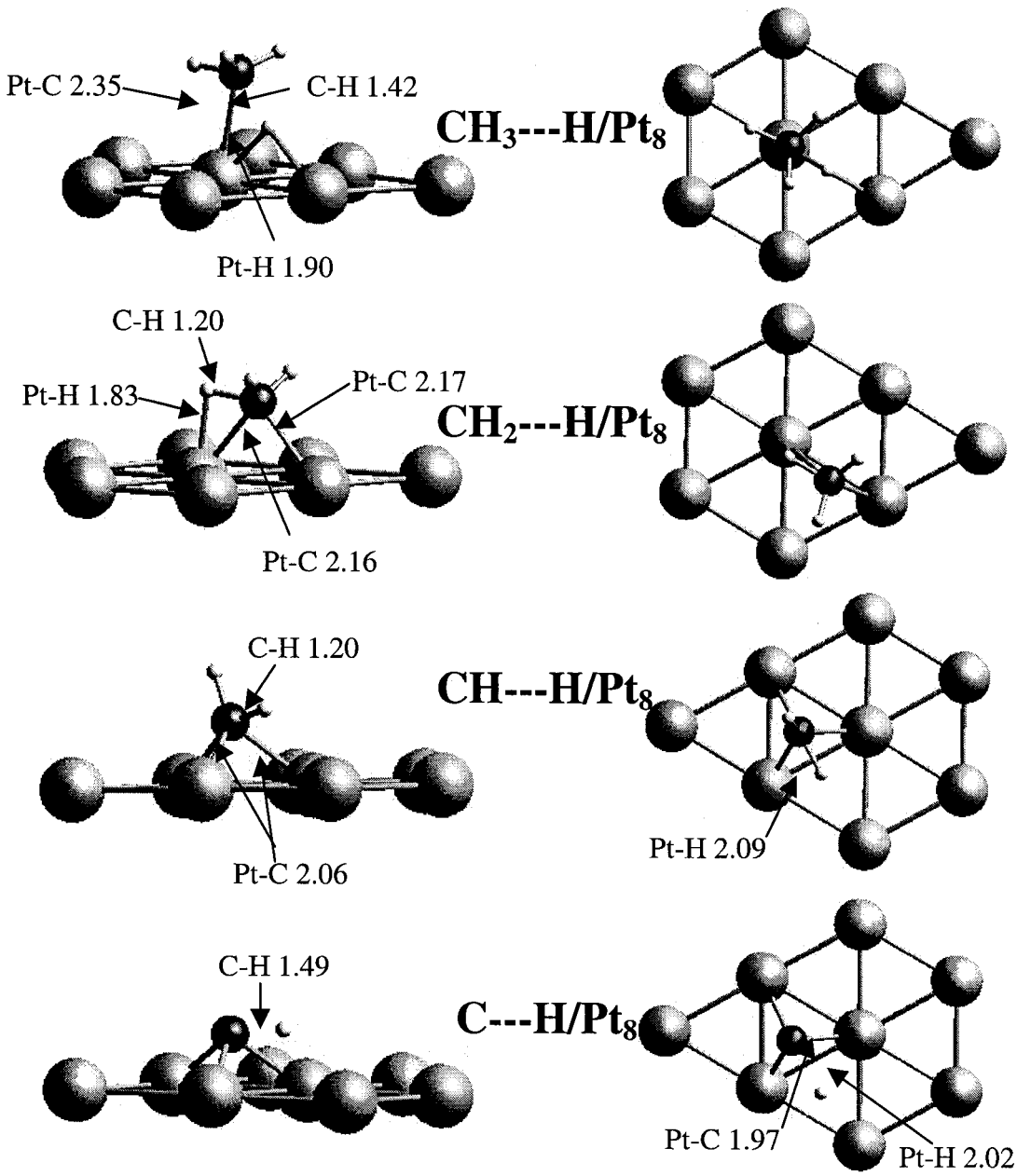

Figure 2-15. Transition state structures for CH_x dehydrogenation on Pt_8.

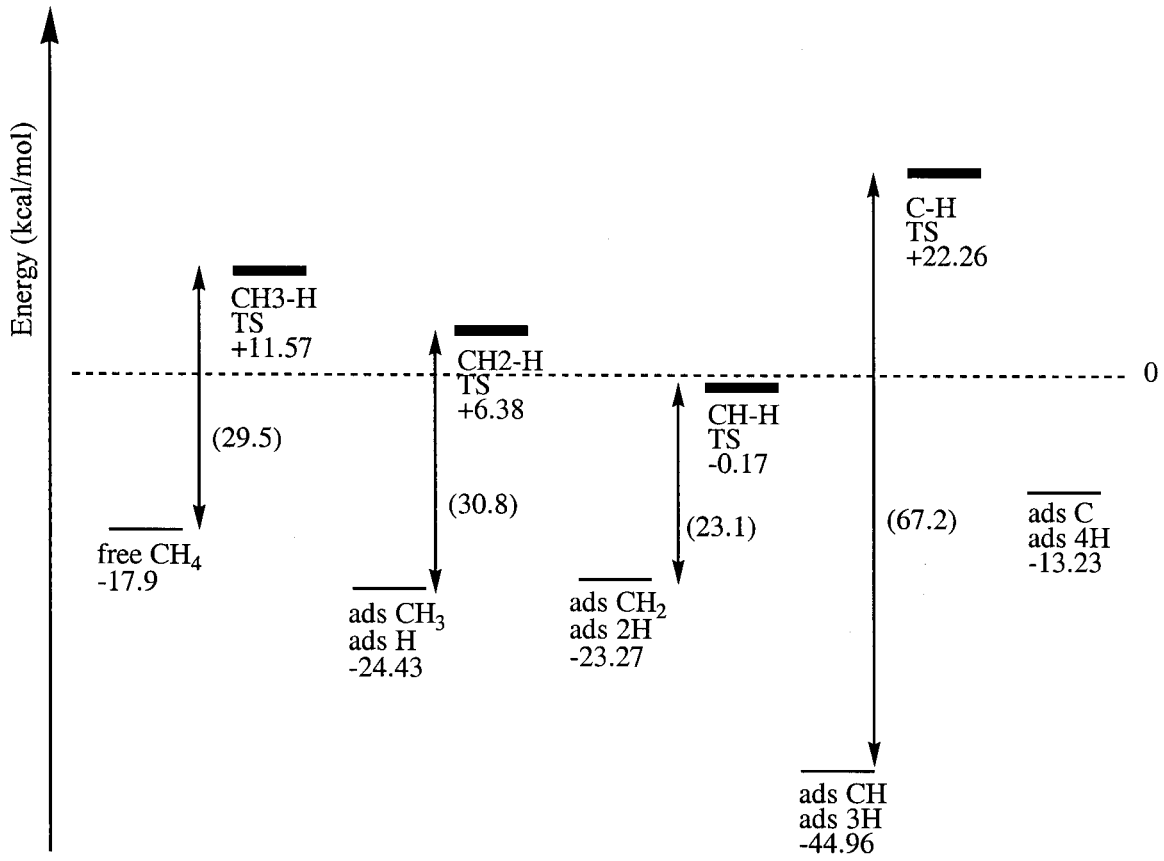

Figure 2-16. Estimated activation barriers for CH_x dehydrogenation on Pt_8.

Transition state structures for CH_x dehydrogenation are shown in Figure 2-15 and calculated barriers in Figure 2-16.

We find that breaking the first C-H bond of methane takes place over an on-top site via a three-center (Pt-C-H) transition state. The bond lengths (Pt-C 2.35, C-H 1.42, Pt-H 1.90 Å) are similar to those found in organometallic C-H activation three-center transition state structures. H initially is adsorbed in the bridged position that contains the Pt involved in the activation before diffusing to its preferred cap position since the methyl group, which prefers the on-top site, does not change positions. The activation barrier is calculated to be ~29.5 kcal/mol. For comparison, we calculate the activation barrier to break the first C-H bond in ethane (not shown) to be ~24.5 kcal/mol.

To break the second C-H bond leads to methylene on the surface. Since methylene prefers the bridge site for adsorption, the methyl group moves over from the on-top site to the bridge site. This costs ~26.9 kcal/mol (see Table 2-1). The overall calculated barrier is just slightly higher, ~30.8 kcal/mol. The transition state is also three-centered; however, the geometries are just slightly stretched from methyl adsorbed in the bridge site. H initially occupies an on-top site before diffusion to the cap site.

To form methylidyne on the surface, CH_2 moves into the cap site. The C-H bond now breaks over a Pt-Pt bridge position as shown in Figure 2-15. The calculated barrier of ~23.1 kcal/mol is the lowest in the reaction profile. Methylidyne is expected to be stable on the surface at low temperatures. To form coke (carbon) on the surface requires heating, and as expected there is a large barrier to break the last C-H bond. The C-H bond in methylidyne, which starts off perpendicular to the surface, has to bend until almost parallel to the surface. The structure of the transition state is very similar to breaking the C-H bond in methylene except the C-H bond distance is stretched to 1.49 Å.

Acknowledgements

The content of this chapter was adapted from reference 46. This research was funded by the NSF (CHE 95-22179). Some calculations were carried out at NCSA, University of Illinois.

References

1. Davis, S. M.; Somorjai, G. A. *Hydrocarbon Conversion over Metal Catalysts* in *The Chemical Physics of Solid Surfaces and Heterogeneous Catalysis*, Volume 4, p217; eds. King, D. A.; Woodruff, D. P.; Elsevier, New York, 1982.

2. Somorjai, G. A. *Chem. Rev.*, **1996**, *96*, 1223.
3. Zaera, F. *Langmuir*, **1996**, *12*, 88.
4. Zaera, F. *Langmuir*, **1991**, *7*, 1998.
5. Alberas-Sloan, D. J.; White, J. M. *Surf. Sci.*, **1996**, *365*, 212.
6. Valden, M.; Xiang, N.; Pere, J.; Pessa, M. *Appl. Surf. Sci.*, **1996**, *99*, 83.
7. Fairbrother, H. D.; Peng, X. D.; Trenary, M.; Stair, P. C. *J. Chem. Soc. Farad. Trans.*, **1995**, *91*, 3619.
8. Kemball, C. *Catal. Rev.*, **1971**, *5*, 33.
9. Chase, M. W., Jr.; Davies, C. A.; Downey, J. R., Jr.; Frurip, D. J.; McDonald, R. A.; Syverud, A. N. *J. Phys. Chem. Ref. Data, Suppl. 1*, **1985**, *14*, 1.
10. Cassuto, A.; Kiss J.; White, J. M. *Surf. Sci.*, **1991**, *255*, 289.
11. Kubota, J.; Ichihara, S.; Kondo, J. N.; Domen, K.; Hirose, C. *Surf. Sci.*, **1996**, *357-358*, 634.
12. Steininger, H.; Ibach, H.; Lehwald, S. *Surf. Sci.*, **1982**, *117*, 685.
13. Felter, T. E.; Weinberg, W. H. *Surf. Sci.*, **1981**, *103*, 265.
14. Stohr, J.; Sette, F.; Johnson, A. L. *Phys. Rev. Lett.*, **1984**, *53*, 1684.
15. Windham, R. G.; Bartram, M. E.; Koel, B. E. *J. Phys. Chem.*, **1988**, *92*, 2862.
16. Szulczewski, G.; Levis, R. J. *J. Am. Chem. Soc.*, **1996**, *118*, 3251.
17. Yeo, Y. Y.; Stuck, A.; Wartnaby, C. E.; King, D. A. *Chem. Phys. Lett.*, **1996**, *259*, 28.
18. Horiuti, J.; Polanyi, M. *Trans. Faraday Soc.*, **1934**, *30*, 1164.
19. Cremer, P. S.; Su, X.; Shen, Y. R.; Somorjai, G. A. *J. Am. Chem. Soc.*, **1996**, *118*, 2942.
20. Davis, S. M.; Zaera, F.; Gordon, B.; Somorjai, G. A. *J. Catal.*, **1985**, *92*, 250.
21. Zaera, F. *J. Phys. Chem.*, **1990**, *94*, 5090.
22. Zaera, F. *J. Am. Chem. Soc.*, **1989**, *111*, 8744.
23. Starke, U.; Barbieri, A.; Materer, N.; van Hove, M. A.; Somorjai, G. A. *Surf. Sci.*, **1993**, *286*, 1.
24. Somorjai, G. A.; Van Hove, M. A.; Bent, B. E. *J. Phys. Chem.*, **1988**, *92*, 973.
25. Kang, D. B.; Anderson, A. B. *Surf. Sci.*, **1985**, *155*, 639.
26. Anderson, A. B.; Choe, S. J. *J. Phys. Chem.*, **1989**, *93*, 6145.
27. Carter, E. A.; Koel, B. E. *Surf. Sci.*, **1990**, *226*, 339.

28. Low, J. J.; Goddard, W. A., III *Organometallics*, **1986**, *5*, 609.

29. Christmann, K. *Surf. Sci. Reports*, **1988**, 9, 1.

30. Richter, L. J.; Ho, W. *Phys. Rev. B*, **1987**, *36*, 9797.

31. Feibelman, P. J.; Hamann, D. R. *Surf. Sci.*, **1987**, *182*, 41.

32. Zurita, S.; Rubio, J.; Illas, F.; Barthelate, J. C. *J. Chem. Phys.*, **1996**, *104*, 8500.

33. Balasubramaniam, K.; Feng, P. Y. *J. Chem. Phys.*, **1990**, *92*, 541.

34. Watari, N.; Ohnishi, S. *J. Chem. Phys.*, **1997**, *106*, 7531.

35. Minot, C.; Bigot, B.; Hariti, A. *J. Am. Chem. Soc.*, **1996**, *108*, 196.

36. Panas, I.; Schule, J.; Siegbahn, P.; Wahlgren, U. *Chem. Phys. Lett.*, **1988**, *149*, 265.

37. Triguero, L.; Pettersson, L. G. M.; Minaev, B.; Agren, H. *J. Chem. Phys.*, **1988**, *108*, 1193.

38. Slater, J. C. "Quantum Theory of Molecules and Solids" Vol. 4: *The Self-Consistent Field for Molecules and Solids*, McGraw-Hill; New York, 1974.

39. Perdew, J. P.; Chevary, J. A.; Vosko, S. H.; Jackson, K. A.; Pederson, M. R.; Singh, D. J.; Fiolhals, C. *Phys. Rev. B*, **1992**, *46*, 6671.

40. Becke, A. D. *J. Chem. Phys.*, **1993**, *98*, 5648.

41. Becke, A. D. *Phys. Rev. A*, **1988**, *38*, 3098.

42. Vosko, S. H.; Wilk, L.; Nusair, M. *Can. J. Phys.*, **1980**, *58*, 1200.

43. Lee, C.; Yang, W.; Parr, R. G. *Phys. Rev. B*, **1988**, *37*, 785.

44. Jaguar 3.0, Schrodinger, Inc.; Portland, Oregon, 1997. PS-GVB v2.3, Schrodinger, Inc.; Portland, Oregon, 1996.

45. Hay, P. J.; Wadt, W. R. *J. Phys. Chem.*, **1985**, *82*, 299.

46. Kua, J.; Goddard III, W. A. *J. Phys. Chem. B*, **1998**, *102*, 9492.

Chapter 3: Thermochemistry for Hydrocarbon Intermediates Chemisorbed on Second and Third Row Group VIII Transition Metals

Abstract

To provide insight and understanding of the thermochemistry underlying hydrocarbon rearrangements on transition metal surfaces, we report systematic studies of hydrocarbon radicals chemisorbed on metal clusters representing the closest packed surfaces of the six second and third row Group VIII transition metals. Using first principles quantum mechanics [nonlocal density functional theory with exact HF exchange (B3LYP)], we find that (i) $CH_{3-m}(CH_3)_m$ forms one bond to the surface, preferring the on-top site (η^1), (ii) $CH_{2-m}(CH_3)_m$ forms two bonds to the surface, preferring the bridge site (η^2), and (iii) $CH_{1-m}(CH_3)_m$ forms three bonds to the surface, preferring the fcc 3-fold site (η^3). For all six metals, the adiabatic bond energy is nearly proportional to the number of bonds to the surface, but there are dramatic decreases in the bond energy with successive methyl substitution. Thus from CH_3 to CH_2CH_3, $CH(CH_3)_2$, $C(CH_3)_3$ the binding energy decreases by 6, 14, and 23 kcal/mol respectively (out of ~50). From CH_2 to $CHCH_3$ and $C(CH_3)_2$, the binding energy decreases by 8 and 22 kcal/mol respectively (out of ~100). These decreases due to methyl substitution can be understood in terms of steric repulsion with the electrons of the metal surface. For CH to $C(CH_3)$ the bond energy decreases by 13 kcal/mol (out of ~160), which is due to electronic promotion energies. These results are cast in terms of a thermochemical group additivity framework for hydrocarbons on metal surfaces similar to the Benson scheme so useful for gas phase hydrocarbons. This is used to predict the chemisorption energies of more complex adsorbates.

3-1. Introduction

Hydrocarbon reactions and rearrangements catalyzed by transition metal surfaces underlie the chemical processes at the core of the petrochemical and polymer industries. These include:[1]

(1) hydrogenation of unsaturated hydrocarbons,

(2) double-bond isomerization of olefins,

(3) dehydrogenation and dehydro-isomerization to aromatics,

(4) isomerization of alkanes,

(5) dehydro-cyclization, and

(6) hydrogenolysis.

The fundamental reactions in these processes involve the breaking and forming of C-C, C-H, M-C and M-H bonds on catalysts usually involving the late transition metals (Group VIII), particularly Pt, Pd and Ni. Yet, despite intensive experimental study there remain major gaps in our understanding of mechanism and energetics of these essential industrial processes.

Although molecular orbital and valence bond theories have helped explain the nature of reactivity in organic and single metal center organometallic reactions, there has been little progress in understanding how the orbitals control reactions on metal surfaces. Thus the extensive experimental work on skeletal isomerization on platinum[2] provided valuable information about cyclic and bond-shift mechanisms but little understanding of the role of the metal. Surface science experiments helped characterize some intermediates in chemisorption and reactions on metal surfaces.[3-5] However, little or nothing is known about most potential intermediates and, with the exception of work by

Carter,[6-7] there is little in the way of thermochemical concepts about chemisorbed intermediates.

In order to lay the foundation for developing both the thermochemical data needed for design and control process and the mechanistic information useful for chemical reasoning about reactions on metals surfaces, we carried out systematic calculations on the structures and energetics for $CH_{n-m}(CH_3)_m$ fragments with n=1,2,3 and m≤n at on-top, bridging, and cap sites of the second and third row Group VIII transition metals (Pt, Ir, Os, Pd, Rh, and Ru). Such systematic studies allow us to examine group additivity and substituent effects for prototypical hydrocarbon intermediates chemisorbed on a range of metal surfaces. This allows us to estimate the steric and electronic contributions affecting binding and reactivity. We expect that such semi-quantitative concepts could become a powerful tool in understanding and predicting the reactions of larger and more complex hydrocarbons on metal surfaces. We would hope that thermochemical concepts on the stability of various intermediates would lead to the predictive power contained in Benson group additivities so useful in understanding mechanisms of organic reactions.[8-9]

In order to study such an enormous range of systems at a consistent level of accuracy, we have modeled the metal surface as a closest packed but planar cluster with 8 metal atoms. This is based on the IEM developed from studies of the bonding in platinum clusters (Chapter 1). We have used this cluster to examine all CH_x and C_2H_x intermediates on platinum (Chapter 2). These calculations lead to geometries and energetics in good agreement with available experimental results on bulk Pt (111) surfaces, suggesting that it is an accurate model.

3-2. Chemistry of Chemisorbed CH_x

3-2-1. Structures and Energetics

To examine the preference of hydrocarbons for various sites on the closest-packed surfaces of the six metals, we calculated the optimum geometries of CH_3, CH_2 and CH in the top, bridge and cap (hollow fcc) sites. The optimized structures are shown in Figure 3-1. Table 3-1 lists the total energy and spin states, Table 3-2 lists the binding energies, and Table 3-3 lists the M-C bond distances of all these species. [The values for CH_x/Pt_8 are similar to those in Chapter 2]. The binding energies and M-C bond distances for the most stable sites form the diagonal and are highlighted in bold.

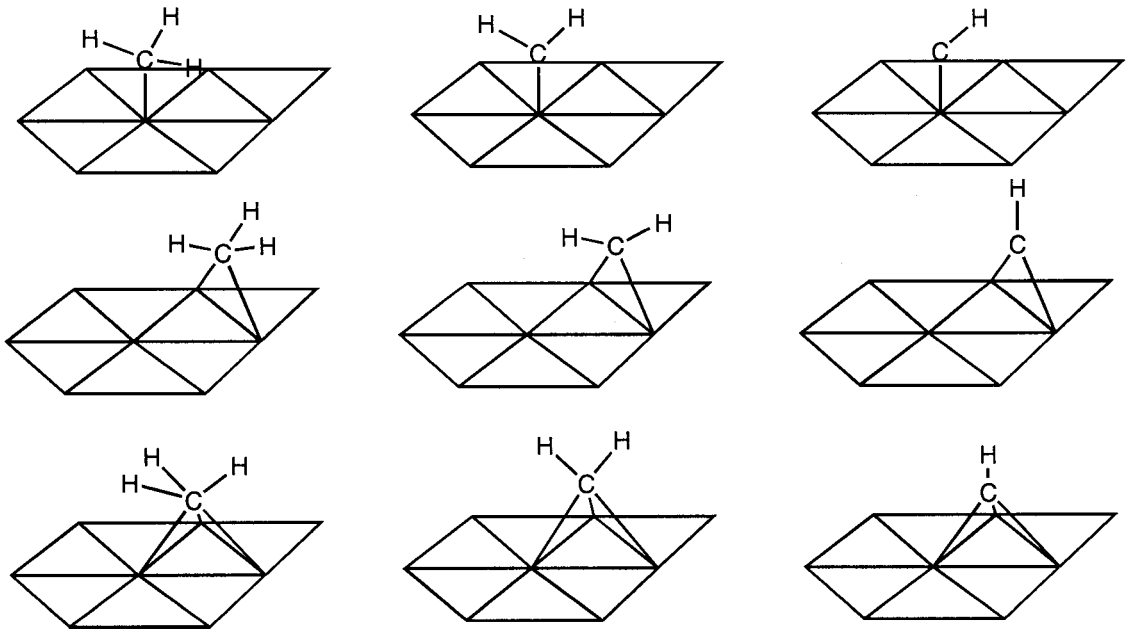

Figure 3-1a. CH_x adsorbed at different sites on M_8.

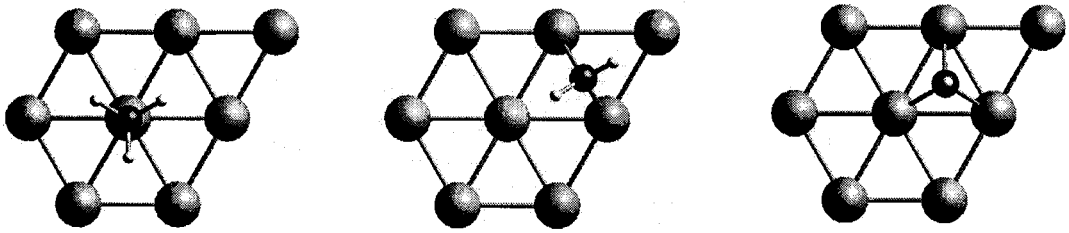

Pt_8-CH_3 (top site) Pt_8-CH_2 (bridge site) Pt_8-CH (cap site)

Figure 3-1b. Top view of best binding structures of CH_x on M_8.

	M	CH_3	CH_2	CH	C	none
Total Energy (hartree)	Pt	-993.18432	-992.57507	-992.00222	-991.34424	-953.25726
	Ir	-877.32844	-876.71914	-876.14272	-875.49444	-837.40601
	Os	-767.92530	-767.31425	-766.73710	-766.09668	-728.00941
	Pd	-1053.90674	-1053.29631	-1052.71078	-1052.08202	-1013.98567
	Rh	-915.90760	-915.29500	-914.71593	-914.07860	-875.98723
	Ru	-790.74033	-790.12999	-789.54508	-788.90809	-750.83465
Total Spin	Pt	5/2	2	5/2	3	3
	Ir	13/2	6	11/2	7	8
	Os	19/2	10	19/2	10	10
	Pd	3/2	2	3/2	2	1
	Rh	13/2	6	11/2	6	7
	Ru	21/2	10	21/2	11	11

Table 3-1. Spin state and total energies (hartrees) for CH_x/M_8.

Pt	CH_3	CH_2	CH	**Pd**	CH_3	CH_2	CH
Top	**53.77**	78.07	80.93	Top	**50.01**	70.94	85.35
Bridge	26.87	**104.28**	149.37	Bridge	41.54	**99.79**	137.85
Cap	22.52	80.54	**166.60**	Cap	32.41	91.53	**154.14**
Ir	CH_3	CH_2	CH	**Rh**	CH_3	CH_2	CH
Top	**50.87**	78.26	82.96	Top	**49.58**	83.32	91.89
Bridge	24.72	**101.34**	152.80	Bridge	35.04	**97.98**	137.97
Cap	17.36	77.20	**161.42**	Cap	25.27	84.21	**151.43**
Os	CH_3	CH_2	CH	**Ru**	CH_3	CH_2	CH
Top	**46.76**	74.81	94.19	Top	**40.36**	65.84	94.15
Bridge	17.59	**96.14**	142.99	Bridge	25.20	**90.18**	132.78
Cap	14.67	78.70	**155.76**	Cap	20.54	77.07	**144.93**

Table 3-2. Adiabatic binding energies (kcal/mol) for CH_x/M_8.

For each fragment on all six metals, the preferred binding site is the one allowing carbon to form four σ bonds. Thus, the most stable binding site for CH_3 is the top site (η^1 bound), CH_2 the bridge site (η^2 bound), and CH the cap site (η^3 bound).

The adiabatic binding energies are also roughly additive, i.e., the total bond energy to the surface is roughly 50 kcal/mol times the number of M-C bonds. Table 3-4 lists the average M-C σ bond strength based on the adiabatic binding energy. In nearly every case, the average M-C bonds are within 3 kcal/mol of each other. Exceptions are that CH_3/Os_8 is 5.2 kcal/mol weaker than the average from CH/Os_8 and CH_3/Ru_8 is 4.7 and 7.9 kcal/mol weaker than the average from CH_2/Ru_8 and CH/Ru_8, respectively.

For the fcc metals (Pt, Pd, Ir, Rh), the M-C bond of CH_3/M_8 is slightly stronger than the average M-C bond of CH_2/M_8, but this is reversed for the hcp metals (Os, Ru). For all six metals, the most significant trend is that the average M-C bond strengths of CH/M_8 are all ~3 kcal/mol higher than the average M-C bond strengths of CH_2/M_8, suggesting that there may be added stability associated with the 3-fold site.

Pt	CH_3	CH_2	CH	**Pd**	CH_3	CH_2	CH
Top	**2.07**	1.84	1.88	Top	**2.01**	1.83	1.77
Bridge	2.41	**2.01**	1.86	Bridge	2.28	**1.98**	1.85
Cap	2.63	2.11	**1.95**	Cap	2.37	2.06	**1.93**
Ir	CH_3	CH_2	CH	**Rh**	CH_3	CH_2	CH
Top	**2.09**	1.84	1.69	Top	**2.04**	1.82	1.79
Bridge	2.31	**2.06**	1.88	Bridge	2.26	**2.01**	1.87
Cap	2.65	2.11	**1.98**	Cap	2.35	2.05	**1.95**
Os	CH_3	CH_2	CH	**Ru**	CH_3	CH_2	CH
Top	**2.12**	1.87	1.71	Top	**2.10**	1.85	1.78
Bridge	2.40	**2.08**	1.92	Bridge	2.32	**2.03**	1.91
Cap	2.44	2.17	**2.02**	Cap	2.45	2.12	**1.98**

Table 3-3. M-C bond lengths (Å) of CH_x/M_8.

Metal	CH_3	CH_2	CH
Pt	53.8	52.1	55.5
Ir	50.9	50.7	53.8
Os	46.7	48.1	51.9
Pd	50.0	49.9	51.4
Rh	49.6	49.0	52.1
Ru	40.4	45.1	48.3

Table 3-4. Average M-C σ bond strength (kcal/mol).

The adiabatic binding energies *increase across the row* (Os < Ir < Pt for the third row; Ru < Rh < Pd for the second row) and *down the columns* (Pd < Pt; Rh < Ir; Ru < Os) of the periodic table. The anomalous case is CH/Pd_8, which has a slightly weaker binding energy than CH/Rh_8 (difference of 2.3 kcal/mol). For CH_2 and CH_3, the bond to Pd is slightly stronger than to Rh (differences are 0.4 and 1.8 kcal/mol, respectively). This arises from the strong stabilization for Pd atom of the d^{10} configuration over the s^1d^9 configuration, which causes Pd to not follow the IEM rules as well as the other five metals. The Pt-C bond is the strongest (~54 kcal/mol) and Ru-C is the weakest (~45 kcal/mol).

The M-*C bond lengths decrease across the row and increase down the column* reflecting the normal changes in atomic size.

3-2-2. Quantum Mechanical (QM) Heats of Formation

To study the energetics of hydrogenation/dehydrogenation reactions involving chemisorbed CH_x species, we converted our calculated energies into heats of formation for each chemisorbed species.

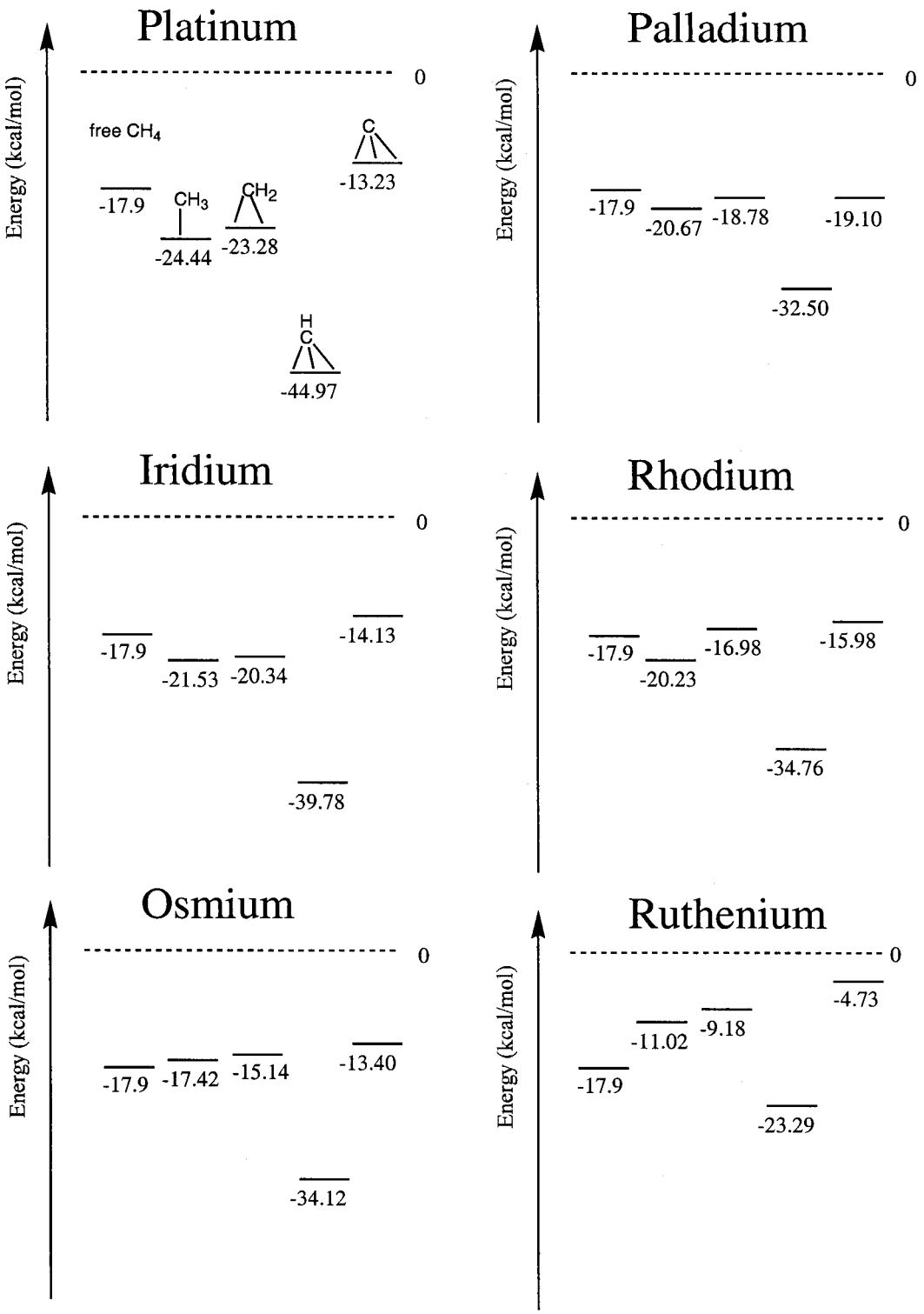

Figure 3-2. Heats of formation of CH_x/M_8 (adsorbed H not shown).

We chose as reference compounds:

- the M_8 metal cluster ($\Delta H_f = 0$),
- gas phase CH_4 (ΔH_f = -17.9 kcal/mol) and
- gas phase H_2 ($\Delta H_f = 0$).

A thorough example was worked out for CH_x/Pt_8 in the previous chapter, and we apply this same method to CH_x/M_8 of all the metals studied here.

Based on HREELS experiments, it is known that H atom prefers binding to the cap site on Pt(111).[10] We find the binding energy for H in the cap site to be 67.2 kcal/mol. Using the same method, the calculated desorption enthalpy to obtain gas phase H_2 is 11.38 kcal/mol per adsorbed H. This compares with 10.6 kcal/mol obtained from thermal desorption spectroscopy (TDS).[11] Similar experimental techniques yield desorption enthalpies (per adsorbed H) of 12.6 kcal/mol for Ir(111),[12] 10.6 kcal/mol for Pd(111),[13] 10.1 kcal/mol for Rh(111),[14] and 9.5 kcal/mol for Ru(0001).[15] In order to simplify the comparison of bond energies of different adsorbates on these various metals, we used the same value of -11.38 kcal/mol (calculated for Pt) for all the metals.

The heats of formation for the most stable CH_x species are shown in Figure 3-2 for all six metals. The total energies and spin states are given in Table 3-1. We find the following trends:

(1) $(CH)_{ads}$ is the thermodynamic sink for all six metals,

(2) The first dehydrogenation to form $(CH_3)_{ads} + H_{ads}$ from gas phase methane is downhill for the fcc metals (Pt, Ir, Pd, Rh) and uphill for the hcp metals (Os, Ru).

(3) The second dehydrogenation step converting $(CH_3)_{ads}$ to $(CH_2)_{ads} + H_{ads}$ is slightly uphill for all six metals,

(4) The final dehydrogenation step to form adsorbed C is quite uphill for all six metals,

(5) Thermodynamically, Pt is the most favorable towards methane dehydrogenation while Ru is the least favorable.

For simplicity in comparing a large number of adsorbates on a number of metals and sites, we reference our calculated energetics for the minimized structures to experimental heats of formation of organics at room temperature and assign the naked metal cluster a heat of formation of zero. This provides an implicit first order correction for zero point energy and changes in the enthalpy to room temperature to the calculated heats of formation, but is not rigorous. A more accurate method would be to calculate zero point energies and room temperature enthalpy changes directly for every cluster and molecule as a direct correction. This difference may lead to changes in the final heat of formation of a few kcal/mol. In Section 3-6-4, we compare the implicit to explicit calculations for H/Pt_8. However, our interest here is to provide a simple method to predict the relative stability of a large number of adsorbates. Since these changes are expected to be nearly the same for adsorbates at the same site of the various metals, implying a constant correction to the current results, we choose to neglect these corrections herein. Section 3-4 contains examples of using such bond additivities to predict bond energies and heats of formation of various other chemisorbed molecules.

3-2-3. Comparison with Previous Experimental and Computational Studies

Platinum. There is kinetic and spectroscopic evidence for methyl, methylidene (CH_2) and methylidyne (CH) moieties on Pt(111).[16] However, neither the energetics nor

the structures of CH_x species adsorbed on Pt(111) have been sufficiently characterized experimentally to provide a test of the calculations.

Low energy electron irradiation of CH_4 on Pt(111) shows evidence of C-H bond cleavage to form chemisorbed methyl and chemisorbed hydrogen atoms.[17] Molecular beam surface scattering experiments find that the dissociative chemisorption of methane is enhanced by increasing both the translational energy of methane and the surface temperature.[18] Adsorbed methyl species has also been generated via gas-phase pyrolysis of azomethane.[19]

Microcalorimetric studies suggest that intrinsic Pt-C bond energies on Pt(111) are in the range of 54-64 kcal/mol,[20] in agreement with our calculations.

DFT (B3LYP) quantum calculations of CH_x on a Pt_{10} (6.3.1) tri-layer cluster with a basis set similar to ours yielded results[21] in agreement with ours. They find that CH_3 prefers an on-top site, CH_2 a bridge site, and CH a cap site (bond energy data was not provided). The cluster chosen for these calculations does not have the s^1d^9 configuration and spin was not optimized.

CH_4 activation has also been studied on small clusters of Pt and Pd ranging from 1 to 3 atoms.[22-23] Essentially these clusters model edge-sites rather than terraces of an extended metal and concentrate only on the first step of C-H activation.

Akinaga *et al.* used B3LYP density functional theory with small Pt clusters to study the photodissociation of methane on the Pt(111) surface.[24] Their study was motivated by the experimental work of Watanabe *et al.*[25] They find that the Rydberg-type first excited state of methane strongly interacts with Pt_n unoccupied states, resulting in a charge-transfer state that finally leads to the dissociation of methane. Their calculations indicate

that the excitation energy to the Rydberg state of methane interacting with Pt decreases by ~3 eV compared to isolated methane. This is consistent with the experimental observation that irradiation with 193 nm photons of methane over Pt(111) surface leads to photodissociation.

Feng *et al.* computed CH_3, CH_2 and CH on small planar Pt clusters using DV-Xα methods (DFT but without gradient or exact exchange corrections) with similar results.[26] They find binding energies of 56.7, 93.4 and 149.2 kcal/mol to the top, bridge and cap sites of Pt_7, Pt_{10}, and Pt_{12} planar clusters (chosen to match the symmetry of the adsorbate). This compares to our values of 53.8, 104.3, and 166.6 kcal/mol, respectively.

Iridium. A study of the dissociative chemisorption of methane on Ir(111), found two distinct pathways:[27] (i) a trapping-mediated pathway with a lower activation energy (12.6 kcal/mol), and (ii) a direct pathway with a higher activation energy (17.4 kcal/mol). This study did not investigate subsequent CH_x adsorbed species on the Ir(111) surface.

Osmium. We know of no publications investigating CH_4 dissociation on Os(0001).

Palladium. Paul and Sautet[28] calculated CH_x on Pd(111) using gradient-corrected DFT calculations on two- and three-layer slabs with periodic boundary conditions. The GGA PW91 functional was used for structural optimization and calculation of binding energies. The basis set was of double-ζ quality [a combination of Slater-type orbitals (STO) and natural atomic orbitals (NAO)] and included an 18-electron effective core potential for Pd. The calculated coverage was 1/3 monolayer. The site preference is in agreement with our results: CH_3 on-top, CH_2 bridge, and CH cap. Their calculated binding energies of 39.4, 84.4 and 136.1 kcal/mol respectively are 10 to 18 kcal/mol lower than our values of 50.0, 99.8 and 154.1. Their Pd-C bond lengths of 2.05, 2.03 and

1.95 Å, respectively, are 0.02 to 0.05 Å larger than our values of 2.01, 1.98 and 1.93. The lower binding energies found in these slab calculations may arise from the difference between a full monolayer and the low coverage limit. Thus, in microcalorimetric studies, Yeo[20] found a 12 kcal/mol decrease in the heat of reaction of ethylene on Pt(111) as the coverage increased from zero concentration to 0.2 monolayers. Differences in basis set and density functionals might also account for a few kcal/mol of the discrepancy. In addition, it might be that cluster calculations would give a higher binding energy than a slab at very low coverage. Unfortunately, there does not yet seem to be a direct comparison between cluster and slab calculations using the same basis sets and density functionals.

Rhodium. Extended Huckel calculations using empirical two-body energy corrections (ASED-MO) on Rh(111)[29] lead to the same site preferences we find: CH_3 on-top, CH_2 bridge, and CH cap. The binding energies of 68.0, 106.3, and 151.7 kcal/mol, respectively, are somewhat larger than our values of 49.6, 97.8 and 151.4, respectively.

Ruthenium. On Ru(0001), HREELS experiments have identified a stable CH (methylidyne) species located in the cap site.[30] The assignment of the C-H peak comes from comparison to the $Ru_3(\mu_3\text{-}CH)(CO)_9$ organometallic complex.[31] On the basis of analogy to similar organometallic complexes of various metals, the HREELS results on Rh(111), Pd(111) and Pt(111) have been interpreted in terms of chemisorbed CH.[30] These observations are compatible with our calculations showing that CH is the most stable CH_x species on all of these surfaces.

3-3. Methyl Substitution on CR_x/M_8

3-3-1. Structures and Energetics

The general effect of successive methyl substitution is to decrease the adiabatic binding energy. The final substitution to form a "quaternary" carbon shows the largest decrease. The M-C bond lengths also increase with increasing substitution. This effect is very pronounced in the CR_3 series, less so in the CR_2 series, and not observable in the CR series. For the partially methylated species, there is some tilting of the adsorbed species due to sterics. For example, $CH(CH_3)_2$ tilts so that the two CH_3 groups move away from the surface while the H "group" moves towards the surface (C-C-Pt and H-C-Pt bond angles of 112° and 95° respectively, compared to H-C-Pt bond angle in CH_3/Pt_8 of 106°). Structures are shown in Figure 3-3. [Total energies are reported in Table 3-5.] Adiabatic binding energies are reported in Table 3-6 and corresponding M-C bond lengths are reported in Table 3-7. The ground spin states of CR_x/M_8 are the same as for CH_x/M_8 with the exception of CCH_3/Ir_8, where the ground spin state is S=13/2 rather than 11/2.

	CH_2CH_3	$CH(CH_3)_2$	$C(CH_3)_3$	$CHCH_3$	$C(CH_3)_2$	CCH_3
Pt	-1032.49839	-1071.80954	-1111.11617	-1031.89164	-1071.20037	-1031.33096
Ir	-916.64302	-955.95392	-995.25715	-916.03085	-955.33819	-915.47231
Os	-807.23593	-846.55005	-885.85999	-806.62775	-845.93076	-806.06282
Pd	-1093.21839	-1132.52640	-1171.83550	-1092.61241	-1131.91807	-1092.04037
Rh	-955.22059	-994.53353	-1033.84255	-954.60839	-993.92358	-954.04178
Ru	-830.05143	-869.36167	-908.66618	-829.44516	-868.75116	-828.87045

Table 3-5. Total energies (in hartrees) of C_2, C_3, C_4 species on M_8.

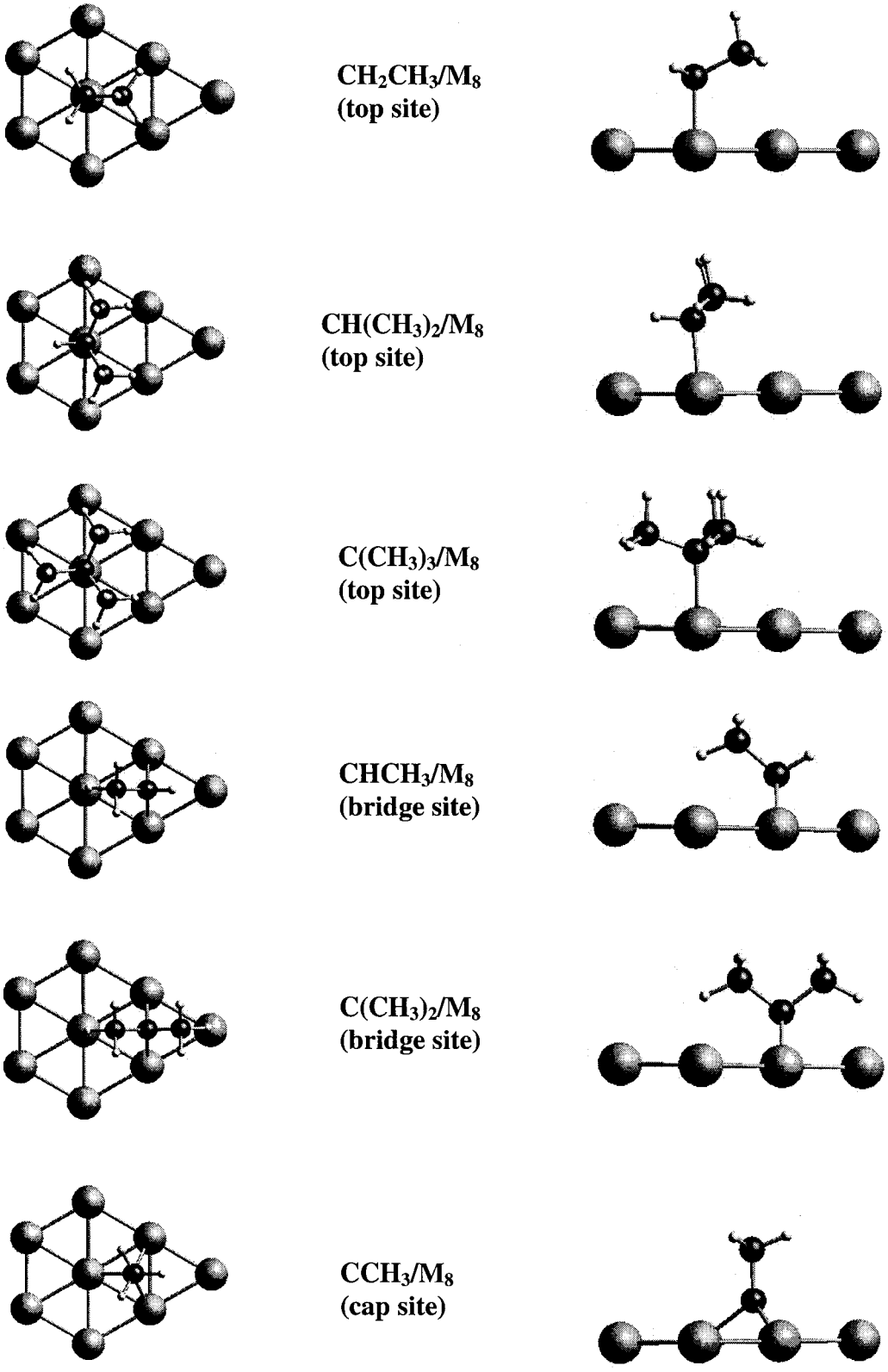

Figure 3-3. CR_x adsorbed on M_8.

Numbers in parentheses indicate the difference in binding energy with respect to CH_3.

CR_3 series

Metal	CH_3	CH_2CH_3	$CH(CH_3)_2$	$C(CH_3)_3$
Pt	53.8	48.6 (-5.2)	41.1 (-12.7)	31.0 (-22.8)
Ir	50.9	46.0 (-4.9)	38.4 (-12.5)	26.1 (-24.8)
Os	46.7	39.4 (-7.3)	33.8 (-13.1)	25.8 (-20.9)
Pd	50.0	43.3 (-6.7)	33.9 (-16.1)	25.3 (-24.7)
Rh	49.6	43.7 (-5.9)	37.4 (-12.2)	28.8 (-20.8)
Ru	40.4	33.3 (-7.1)	25.3 (-15.1)	13.8 (-26.6)
Average difference		(-6.2 ± 1.3)	(-13.6 ± 2.5)	(-23.4 ± 3.2)

CR_2 series

Metal	CH_2	$CHCH_3$	$C(CH_3)_2$
Pt	104.3	98.1 (-6.2)	84.8 (-19.5)
Ir	101.3	92.0 (-9.3)	78.0 (-23.3)
Os	96.1	86.8 (-9.3)	71.2 (-24.9)
Pd	99.8	92.1 (-6.7)	78.1 (-21.7)
Rh	98.0	88.6 (-9.4)	80.6 (-17.4)
Ru	90.2	81.9 (-8.3)	68.2 (-22.0)
Average difference		(-8.2 ± 2.0)	(-21.5 ± 3.4)

CR series

Metal	CH	CCH_3
Pt	166.6	154.7 (-11.9)
Ir	161.4	150.1 (-11.3)
Os	155.8	142.0 (-13.8)
Pd	154.1	142.8 (-11.3)
Rh	156.4	142.7 (-13.7)
Ru	144.9	130.9 (-14.0)
Average difference		(-12.7 ± 1.4)

Table 3-6. Adiabatic binding energies of CR_x/M_8 (in kcal/mol).

CR_3 series

Metal	CH_3	CH_2CH_3	$CH(CH_3)_2$	$C(CH_3)_3$
Pt	2.07	2.13	2.21	2.37
Ir	2.09	2.12	2.16	2.25
Os	2.12	2.14	2.18	2.24
Pd	2.01	2.05	2.08	2.14
Rh	2.04	2.08	2.08	2.12
Ru	2.10	2.12	2.16	2.24

CR_2 series

Metal	CH_2	$CHCH_3$	$C(CH_3)_2$
Pt	2.01	2.04	2.08
Ir	2.06	2.08	2.09
Os	2.08	2.10	2.15
Pd	1.98	2.00	2.07
Rh	2.01	2.03	2.05
Ru	2.03	2.05	2.10

CR series

Metal	CH	CCH_3
Pt	1.95	1.96
Ir	1.98	1.99
Os	2.02	2.03
Pd	1.93	1.94
Rh	1.95	1.97
Ru	1.98	2.00

Table 3-7a. Bond lengths for CR_x/M_8.

		Pt	Ir	Os	Pd	Rh	Ru
CH_3	MCH	106	108	110	107	109	109
	HCH	112	111	109	112	109	109
CH_2Me	MCH	101	104	106	103	106	104
	MCC	116	117	117	115	116	118
$CHMe_2$	MCH	95	99	102	101	102	100
	MCC	113	114	115	110	113	115
CMe_3	MCC	108	111	111	109	111	111
	CC_MC	111	108	108	110	108	107
CH_2	MCM	88	83	83	88	85	84
	XCH	125	125	127	125	126	126
CHMe	MCM	87	83	81	87	83	82
	XCH	116	118	117	114	118	116
	XCC	137	136	137	139	135	138
CMe_2	MCM	84	81	79	83	82	80
	CC_MC	104	106	104	105	106	104
CH	MCH	125	128	129	124	127	128
	MCM	91	87	85	91	87	86
CMe	MCC	125	128	129	126	128	130
	MCM	90	87	85	90	86	85

X is the point on the metal surface such that C-X is perpendicular to the surface plane.

Table 3-7b. Selected bond angles for CR_x/M_8.

CR_3 series. For the series $CH_3 \rightarrow CH_2CH_3 \rightarrow CH(CH_3)_2 \rightarrow C(CH_3)_3$, the adiabatic binding energy decreases by an average (over all six metals) of 6.2, 13.6 and 23.4 kcal/mol compared to CH_3/M_8. This is very significant since the average M-C bond energy of CH_3/M_8 is only 48.6 kcal/mol. The dominant effect here is the steric interaction of the hydrocarbon to the surface, that is, the nonbonded or Pauli repulsion between the electrons in the CH_3 substituent with the surface. Based on $C(CH_3)_3$, the cost is ~7.8 kcal/mol per CH_3. The value for $CH_2(CH_3)$ is smaller by 1.6 kcal/mol while the value per CH_3 for $CH(CH_3)_2$ is smaller by 2.0 kcal/mol. The smaller value for the first and second methyl groups arises because steric repulsions can be decreased by

increasing the C-C-M angle while compensating with a decrease in H-C-M angle. This compensation cannot occur in the trimethyl case.

These steric effects are also apparent in the M-C bond lengths. There is a significant increase in the M-C bond lengths for Pt from 2.08 → 2.13 → 2.21 → 2.37 Å for adding CH_3 groups. For the six metals, the average successive increase in M-C bond length is 0.035, 0.038, and 0.082 Å. For $C(CH_3)_3$, lengthening the M-C bond is the only method to relieve steric repulsion.

CR_2 series. For the series CH_2 → $CHCH_3$ → $C(CH_3)_2$, the average decrease in binding energy is 8.2 and 21.5 kcal/mol, respectively, compared to CH_2/M_8. The steric interactions for the fully methyl-substituted adsorbate is 10.8 kcal/mol per CH_3, substantially larger than for CR_3/M_8. This is because CR_2 adsorbs in a bridge site, putting the methyl groups closer to the surface. For example, CH_2/Pt_8 has a Pt-C bond length of 2.01 Å, leading to a surface to carbon distance of 1.45 Å (compared to 2.07 Å for CH_3). However, because the CR_2 total bond energy is twice as large, the decrease in bond energy for the fully substituted case is only 28% of the total bond energy for CR_2 but 48% for CR_3 .

The steric effect for the singly substituted case, $CHCH_3$, is 2.6 kcal/mol smaller than the average for CR_2 since the methyl group can tilt away from the surface (the opposite H has little steric repulsion with the surface). Substituting the first methyl increases M-C by 0.022 Å and the second methyl by 0.040 Å, much less than in the CR_3 series.

CR series. There is an average 12.7 kcal/mol decrease in binding energy for the series CH → CCH_3. This might seem strange since the methyl substituent is far from the surface, leading to very little steric interaction. In fact this decrease arises from an

electronic effect. In order for the CR adsorbate to form three bonds in the cap site, the CR fragment needs to have 3 unpaired spins. This corresponds to the S=3/2 state of CR, but for both CH and CCH_3 the ground state is the S=1/2 state. Thus, the process of bonding CR to the surface requires promoting CR from the doublet to quartet state, reducing the bond energy by this amount. Indeed, the doublet to quartet excitation energies are calculated to be 19.7 and 32.4 kcal/mol for CH and CCH_3 respectively. This difference in excitation energy of 12.7 kcal/mol is expected to cause CCH_3 to have a bond energy 12.7 kcal/mol smaller than for CH, in exact agreement with the calculated number.

The average M-C bond length increases by only 0.013 Å between the two species, as expected from the similar bonding.

3-3-2. Charge Transfer Effects

To estimate the effect of methyl substitution on charge transfer to the cluster, we calculated the Mulliken charges. Table 3-8 lists the Mulliken charges for four groups of atoms in CR_x/Pt_8:

(1) R groups,

(2) C atom in M-C bond,

(3) M atoms involved in direct M-C bonding, and

(4) M atoms not directly involved in M-C bonds.

The sum of these four groups is the overall charge of the cluster (zero since all the metal-adsorbate clusters are overall neutral). The other metals show qualitatively similar trends to Pt.

The total charge on the metal (sum of rows 3 and 4 of Table 3-8) becomes increasingly negative with increasing methyl substitution, indicating that C→M charge transfer occurs. This increased charge transfer from the hydrocarbon to the metal with increasing number of methyl groups is interpreted in terms of methyl inductive effects (electron donation) just as observed in organic compounds.

CR_3 series

	CH_3	CH_2CH_3	$CH(CH_3)_2$	$C(CH_3)_3$
R group (Organic ligands to C)	+0.56	+0.51	+0.47	+0.48
C atom in M-C bond	-0.25	-0.12	+0.01	+0.11
M atom in M-C bond	-0.42	-0.39	-0.34	-0.05
M atoms not in M-C bond	+0.11	+0.00	-0.14	-0.54

CR_2 series

	CH_2	$CHCH_3$	$C(CH_3)_2$
R group (Organic ligands to C)	+0.41	+0.38	+0.41
C atom in M-C bond	-0.34	-0.27	-0.08
M atoms in M-C bond	+0.08	+0.06	-0.01
M atoms not in M-C bond	-0.15	-0.17	-0.32

CR series

	CH	CCH_3
R group (Organic ligands to C)	+0.18	+0.18
C atom in M-C bond	-0.41	-0.34
M atoms in M-C bond	+0.12	+0.09
M atoms not in M-C bond	+0.11	+0.07

Table 3-8. Mulliken charges for CR_x/Pt_8.

The charge on the C atom involved in the M-C bond (row 2) becomes increasingly positive with CH_3 substitution. We interpret this in terms of methyl group stabilization just as observed in the stabilization of organic tertiary carbocations over secondary and primary.

Methyl substitution also tends to favor the planar form of CR_3 with respect to pyramidal. This leads to a significant increase in M-C bond lengths across the CR_3/M_8 species. Thus, CH_3/Pt_8 has a C-Pt bond of 2.07 A while $C(CH_3)_3/Pt_8$ has a C-Pt bond length of 2.37A.

3-3-3. Snap Chemisorption Energies

The snap chemisorption energy is defined as the difference in energy between the adsorbate-metal cluster and the metal cluster infinitely separated from the adsorbate, but for which the structure of the adsorbate and metal cluster are frozen both at the geometry and spin state of the complex. That is, the adsorbate is not permitted to relax as the M-C bonds are broken. The snap bond energies of CR_x/Pt_8 are reported in Table 3-9 along with the corresponding adiabatic binding energies. The other metals show similar trends to Pt. The spin state of frozen CR_3 species is S=1/2. CR_2 species are frozen at a spin state of S=1 since two unpaired electrons are required to form two M-C bonds. CR species are frozen at a spin state of S=3/2 since three unpaired electrons are required to form three M-C bonds. This includes the effect of the doublet-quartet excitation on the bond energy, discussed in Section 3-3-1.

Whereas adiabatic binding energies are additive with the number of M-C bonds (Table 3-4), snap bond energies do *not* show this trend. The average M-C snap bond energies for CH_3, CH_2, and CH on Pt_8 are 57.4, 54.2 and 62.1 kcal/mol.

The difference between the snap bond energies of CH_3 and CH_2 can be attributed to strain energy in the Pt-C-Pt ring of the bridged CH_2/Pt_8 system. For CH_2/Pt_8 the Pt-C-Pt bond angle is 90° while for CH_3/Pt_8 the Pt-C-H bond angles are 106°, closer to

tetrahedral. This strain might well decrease the average bond energy by 3 kcal/mol for CH_2/Pt_8.

Numbers in parentheses indicate the difference between one row/column and the next row/column.

CR_3/Pt_8	Adiabatic		Snap
CH_3	53.8	(+3.6)	57.4
	(-5.2)		(-4.2)
CH_2CH_3	48.6	(+4.6)	53.2
	(-6.5)		(-6.5)
$CH(CH_3)_2$	41.1	(+5.6)	46.7
	(-10.1)		(-9.0)
$C(CH_3)_3$	31.0	(+6.7)	37.7
CR_2/Pt_8	Adiabatic		Snap
CH_2	104.3	(+4.0)	108.3
	(-6.2)		(-2.7)
$CHCH_3$	98.1	(+7.5)	105.6
	(-13.3)		(-12.5)
$C(CH_3)_2$	84.8	(+8.3)	93.1
CR/Pt_8	Adiabatic		Snap
CH	166.6	(+19.7)	186.3
	(-11.9)		(+0.8)
CCH_3	154.7	(+31.4)	187.1

Table 3-9. Comparison of adiabatic and snap bond energies (in kcal/mol).

Increasing methyl substitution leads to decreasing snap bond energy for the CR_3 and CR_2 species, similar to the trend observed in adiabatic binding energies. There are some differences quantitatively; for example, the snap bond energy does not decrease as much as the adiabatic binding energy across the series. The lack of a direct steric effect on the snap bond energy for CR is plausible since the R group is far from the surface. However, CH in the cap position has an average M-C snap bond energy 4.7 kcal/mol higher than for CH_3. For CR there is essentially no difference between the snap bond energy of CH and CCH_3, the full effect being accounted for by the doublet to quartet excitation energy (vide supra).

We believe that the increased bond strength of CR to cap sites is due to additional flexibility of the Pt orbitals to bind species to the cap site. In addition to the d-orbitals localized on each Pt atom, the cap site can utilize the interstitial s-like orbital located in the triangle of the cap site (mixing with the d-orbitals to create s-d hybrid orbitals). The added flexibility in the bond orbitals could be responsible for the increased Pt-C snap bond energy.

Experimental results confirm that methylidyne (CH) and ethylidyne (CCH_3) are the stable thermodynamic sinks at low temperature for C_1 and C_2 adsorbates on metals. This is most firmly established experimentally for ethylidyne on Pt(111).[32-33] Ethylidyne occupies a 3-fold fcc site and the C-C bond is perpendicular to the platinum surface. The experimental C-C and Pt-C bond lengths are 1.50±0.05 and 2.00±0.05 Å respectively. Our calculations have the same geometry with optimized C-C and Pt-C bond lengths of 1.49 and 1.96 Å respectively. Studies on other closed packed surfaces relevant to our study include Ir(111),[34] Pd(111),[35] Rh(111),[36] and Ru(0001).[37]

3-4. Thermochemical Computations

We will now consider how to use the bond energies from QM calculations to estimate the bond energies and heats of formation of more complex chemisorbed species. Experimental heats of formation and bond energies quoted here were obtained from reference 38.

3-4-1. Group Additivity Values

Based on the heats of formation calculated from QM for the $CH_m(CH_3)_n$ species, we can assign group values in a scheme analogous to Benson group additivities. The heats of formation are calculated using three reference compounds:

- the M_8 metal cluster ($\Delta H_f = 0$),
- gas phase CH_4 (ΔH_f = -17.9 kcal/mol) and
- gas phase C_2H_6 (ΔH_f = -20.0 kcal/mol).

This yields atomic ΔH_f values required to convert from QM data (in hartree) to thermochemical data referenced to standard states [E(C) = -38.12718 and E(H) = -0.59209 hartrees]. This provides implicit first order corrections for zero point energy and enthalpy changes at room temperature (discussed in Section 3-2-1). CH_4 and C_2H_6 were chosen, rather than CH_4 and H_2, because they are expected to provide a better implicit correction in the case of adsorbates containing C-C bonds. We would expect that the QM results would have systematic errors proportional to the number of bonds; however, we make no such empirical corrections here. The resulting group values are shown in Table 3-10a.

	Pt	Ir	Os	Pd	Rh	Ru
C-M(H)$_3$	-14.82	-11.91	-7.81	-11.06	-10.62	-1.40
C-M(C)(H)$_2$	-6.32	-3.73	+2.85	-1.04	-1.44	+8.96
C-M(C)$_2$(H)	+4.02	+6.76	+11.32	+11.26	+7.77	+19.86
C-M(C)$_3$	+17.18	+22.06	+22.41	+22.88	+19.44	+34.36
C-M$_2$(H)$_2$	-4.05	-1.11	+4.09	+0.45	+2.25	+10.05
C-M$_2$(C)(H)	+2.88	+8.87	+12.95	+7.61	+11.18	+17.86
C-M$_2$(C)$_2$	+14.73	+21.59	+28.39	+21.45	+18.98	+31.43
C-M$_3$(H)	-16.12	-10.94	-5.28	-3.66	-5.92	+5.55
C-M$_3$(C)	-16.83	-12.18	-4.09	-4.90	-4.81	+6.96

Table 3-10a. Group values (kcal/mol) for C-$M_k(C)_n(H)_{4-k-n}$ (see Section 3-4-1).

	Pt	Ir	Os	Pd	Rh	Ru
C-M(C_M)(H_2)	-10.57	-7.82	-2.48	-6.05	-6.03	+3.78
C-M(C_M)(C)(H)	-1.15	+1.52	+7.09	+5.11	+3.17	+14.41
C-M(C_M)(C_2)	+10.60	+14.41	+16.87	+17.07	+13.61	+27.11

Table 3-10b. Group values (kcal/mol) for C-M(C_M)$(C)_{n-1}(H)_{3-n}$ (see Section 3-4-3).

C-$(C)(H)_3$	-10.20
C-$(C)_2(H)_2$	-4.93
C-$(C)_3$(H)	-1.90

Table 3-10c. Group values (kcal/mol) for C-$(C)_n(H)_{4-n}$ from ref 6 (see Sections 3-4-1, 3-4-3, 3-4-4).

An example of how these are assigned is as follows. The calculated heat of formation of CH_3 on Pt_8 can be written in terms of two group contributions:

-14.82 kcal/mol = [C-(Pt)$(H)_3$] + [Pt-(C)]

We will take

[Pt-(C)] = 0

so that

[C-(Pt)$(H)_3$] = -14.82 kcal/mol[39]

The calculated heat of formation of CH_2CH_3 on Pt_8 is written as

-16.52 kcal/mol = [C-(Pt)(C)$(H)_2$] + [C-(C)$(H)_3$]

Since [C-(C)$(H)_3$] = -10.20 (used by Benson[8]), we obtain

[C-(Pt)(C)$(H)_2$] = -6.32 kcal/mol.

Table 3-10 allows one to predict the relative stability of surface hydrocarbons. For example, considering the isopropyl and n-propyl isomers, the heats of formation predicted from Group Additivities are

ΔH_f (i-C_3H_7/Pt) = [C-(Pt)$(C)_2$(H)] + 2 [C-(C)$(H)_3$] = 4.02 + 2(-10.20)

= -16.38 kcal/mol

ΔH_f (n-C_3H_7/Pt) = [C-(Pt)(C)$(H)_2$] + [C-$(C)_2(H)_2$] + [C-(C)$(H)_3$]

= -6.32 + (-4.93) + (-10.20) = -21.45 kcal/mol

Here we use the Benson group values for groups that do not involve the metal. Thus we predict that n-C_3H_7 chemisorbs more strongly to Pt than i-C_3H_7 by 5.1 kcal/mol. Indeed, we carried out QM calculations for these two species (on Pt_8) and find an energy difference of 6.4 kcal/mol (within 1.3 kcal/mol of the group additivity value). These results are summarized in Table 3-11, along with predictions of the relative energies for various butyl radicals chemisorbed on Pt to illustrate further the process.

	Grp. Add. Prediction		**QM Calculation**	
	ΔH_f	**Substituent Effect**	**ΔH_f**	**Substituent Effect**
i-C_3H_7/Pt	-16.38	5.1	-16.38	6.4
n-C_3H_7/Pt	-21.45	0.0	-22.82	0.0
t-C_4H_9/Pt	-13.42	13.0		
i-C_4H_9/Pt	-21.31	5.1		
n-C_4H_9/Pt	-26.38	0.0		

Table 3-11. Group additivity predictions (kcal/mol) for propyl and butyl adsorbed on Pt.

3-4-2. Bond Additivities of di-σ Adsorbed Species

In this section, we use only calculated values with no zero point or room temperature enthalpy corrections. This provides a comparison to the next section on group additivities (Section 3-4-3) where implicit first order corrections have been included into the heats of formation.

The di-σ bond of ethylene to the surface. The process of converting ethane to ethylene can be written as

$$H_3C\text{-}CH_3 \rightarrow H + H_2C\text{-}CH_3 \rightarrow 2H + H_2C{=}CH_2 \rightarrow H_2 + H_2C{=}CH_2$$

$$D(C\text{-}H) \qquad D(C\text{-}H) - \pi \qquad -D(H\text{-}H)$$

Thus the heat of reaction is

$$\Delta H_{rxn} = 2\,D(C\text{-}H) - \pi - D(H\text{-}H) \tag{3.1}$$

where π is the energy of the C=C π bond. From QM we calculate ΔH_{rxn} = +41.7 kcal/mol. Using the QM values of D(C-H) = 109.7, and D(H-H) = 111.7 leads to

$$\pi^{qm} = 2D(C\text{-}H) - D(H\text{-}H) - \Delta H_{rxn} = 219.4 - 111.7 - 41.7 = 66.0 \text{ kcal/mol}$$

as the QM value π bond strength for C_2H_4.

Using instead the experimental numbers of ΔH_f (C_2H_6) = -20.02, ΔH_f (C_2H_4) = +12.55, D(C-H) = 100.5, D(H-H) = 104.20, would lead to the thermochemical value of

$$\pi^{tc} = 2D(C\text{-}H) - D(H\text{-}H) - \Delta H_{rxn} = 201.0 - 104.2 - 32.5 = 64.3 \text{ kcal/mol}$$

Both numbers are quite close to the experimental rotational barrier in ethylene of π^{exp} = 65 kcal/mol.[40]

Consider now the di-σ bond of ethylene to the metal surface. We can *predict* this number in an analogous fashion as

$$M\text{-}CH_2\text{-}CH_2\text{-}M \rightarrow M + CH_2\text{-}CH_2\text{-}M \rightarrow 2M + H_2C{=}CH_2 \rightarrow M_2 + H_2C{=}CH_2$$

$$D(M\text{-}C) \qquad D(MC) - \pi \qquad -D(M\text{-}M)$$

This time we write

$$\Delta H_{rxn} = 2\,D(M\text{-}C) - \pi - D(M\text{-}M) \tag{3.3}$$

The question now is which value to use for D(M-C) for the $M\text{-}CH_2CH_2\text{-}M$ system. We have two choices. Electronically D($M\text{-}CH_2CH_3$) is more similar to the D(M-

CH_2CH_2M) system since C in the M-C bond also has an additional C-C bond. Sterically $D(M\text{-}CH_3)$ is more similar to $D(M\text{-}CH_2CH_2M)$ since after forming the second bond to the surface, neither C causes steric repulsion with the surface. The most rigorous approach would be to carry out a series of calculations to separate the steric and electronic contributions due to methyl substitution.

A simple alternative, which we use here, is to use the average value. Hence for C_2H_4/Pt_8, we use

$$D(M\text{-}C) = [\, D(Pt\text{-}CH_3) + D(Pt\text{-}CH_2\text{-}CH_3) \,]/2$$

$$= (53.8 + 48.6)/2 = 51.2 \text{ kcal/mol}$$

Using this value for D(M-C),

$$BE(H_2C{=}CH_2/Pt_8) = 2*51.2 - 66.0 - D(M\text{-}M) = 36.4 - D(M\text{-}M)$$

The calculated QM binding energy is 36.1 kcal/mol. Thus we obtain D(M-M) = +0.3 kcal/mol (see Table 3-12). Coverage-dependent microcalorimetry measures an adsorption energy ranging from 30-48 kcal/mol.[20] The C-C bond is parallel to and found above a Pt-Pt bridge. The molecular plane of C_2H_4 is tilted and the C-C bond length measured from NEXAFS is 1.49±0.04 Å.[41] This compares to our calculated C-C bond length of 1.51 Å.

adsorbate	Total Energy (hartree)	BE[a]	Selected bond distances (Å)	$\pi^{QM,b}$	D(M-C)[b]	D(M-M)[c]
C_2H_4	-1031.90852	36.1	Pt-C 2.06, C-C 1.52	66.0	51.2	+0.3
cis-C_4H_8	-1110.53844	30.1	Pt-C 2.10, C-C 1.53	57.4	44.9	+2.3
$C_2(CH_3)_4$	-1189.15174	16.4	Pt-C 2.14, C-C 1.58	50.0	36.1	+5.8

[a] Values in kcal/mol. Calculated from E(cis-butene) = -157.23323 hartree and E(2,3-dimethylbut-2-ene) = -235.86839 hartree.
[b] Values in kcal/mol calculated from Table 3-6 using averages as discussed in Section 3-4-2.
[c] Calculated as described in Section 4.2 using QM results.

Table 3-12. Results from QM calculations of ethylene, cis-butene, and 2,3-dimethylbut-2-ene on Pt_8.

For all six metals, Table 3-13 compares the di-σ bond of ethylene predicted using these bond additivity concepts (assuming π^{qm} = 66.0 kcal/mol) with the QM value (we report the value of D(M-M) required to make the two consistent). The average value is D(M-M) = -2.3 kcal/mol. Thus we take the average strain for the M_2C_2 cyclobutane to be -2.3 kcal/mol. Using this average value we would have predicted the di-σ bond energies for all six metals to within ~3 kcal/mol of the QM result.

M	Total Energy (hartree)	Selected distances (Å)	QM BE[a]	D(M-C)[b]	Bond Add. BE[c]	D(M-M)[d]
Pt	-1031.90852	Pt-C 2.06; C-C 1.52	36.1	51.2	36.4	+0.3
Ir	-916.05391	Ir-C 2.08; C-C 1.53	34.0	48.5	31.0	-3.0
Os	-806.63625	Os-C 2.14; C-C 1.52	20.7	43.1	20.2	-0.5
Pd	-1092.63192	Pd-C 2.07; C-C 1.46	32.9	46.7	27.4	-5.5
Rh	-954.62570	Rh-C 2.05; C-C 1.51	28.0	46.7	27.4	-0.6
Ru	-829.44775	Ru-C 2.11; C-C 1.50	12.2	36.9	7.8	-4.4

[a] Values in kcal/mol calculated from QM using E(C_2H_4) = -78.59380 hartree and E(M) from last column of Table 3-1.
[b] Values in kcal/mol calculated using [D(M-CH_3) + D(M-C_2H_5)]/2 from Table 3-6.
[c] Values in kcal/mol calculated as described in Section 4.2.1 using π^{qm} = 66.0 kcal/mol.
[d] Values in kcal/mol. Average value for D(M-M) is -2.3 kcal/mol.

Table 3-13. QM and bond additivity calculations of C_2H_4/M_8.

The di-σ bond of cis-butene to Pt surface. As a second example, consider the bond energy of cis-2-butene to Pt surface. The process of converting n-butane to cis-2-butene can be written as

$$n\text{-}C_4H_{10} \rightarrow H + CH(CH_3)(C_2H_5) \rightarrow 2H + cis\text{-}C_4H_8 \rightarrow H_2 + cis\text{-}C_4H_8$$

$$D(C\text{-}H) \qquad D(C\text{-}H) - \pi \qquad -D(H\text{-}H)$$

Using the QM values of ΔH_{rxn} = +32.1, D(C-H) = 100.6, and D(H-H) = 111.7 leads to

$$\pi^{qm} = 2D(C\text{-}H) - D(H\text{-}H) + \Delta H_{rxn} = 2*100.6 - 111.7 - 32.1 = 57.4 \text{ kcal/mol}$$

which is 8.6 kcal/mol weaker than in ethylene.

Consider now the bonding of cis-butene to the metal surface. Following the same reasoning as for ethylene, we consider that

$$BE[cis\text{-}(CH_3)HC{=}CH(CH_3)/M_8] = 2\,D(M\text{-}C) - \pi - D(M\text{-}M)$$

Since $D(Pt\text{-}C_2H_5) = 48.6$ and $D(Pt\text{-}C_3H_7) = 41.1$, we assign D(M-C) = 44.9 kcal/mol (average of the two), and obtain

$$BE[cis\text{-}(CH_3)HC{=}CH(CH_3)/M_8] = 2*44.9 - 57.4 - D(M\text{-}M) = 32.4 - D(M\text{-}M)$$

The calculated QM binding energy is 30.1 kcal/mol (Table 3-12). Thus we obtain D(M-M) = +2.3 kcal/mol, which is 2.0 kcal/mol higher than for C_2H_4. Thus, bond additivity predicts a small increase in strain in the cyclic M_2C_2 unit.

	Cis-butene			2,3-dimethylbut-2-ene		
	D(M-M)[a]	**D(M-C)[b]**	**BE[c]**	**D(M-M)[d]**	**D(M-C)[e]**	**BE[f]**
Pt	+2.3	44.9	30.1	+5.8	36.1	16.4
Ir	-1.0	42.2	28.0	+2.5	32.3	12.1
Os	+1.5	36.6	14.3	+5.0	29.8	4.6
Pd	-3.5	38.6	23.3	+0.0	29.6	9.2
Rh	+1.4	40.6	22.4	+4.9	33.1	11.3
Ru	-2.4	29.3	3.6	+1.1	19.6	-9.7

[a] Predicted from QM results for Pt by adding 2.0 kcal/mol to D(M-M) in Table 3-13.
[b] Calculated using [$D(M\text{-}C_2H_5) + D(M\text{-}C_3H_7)$]/2 in Table 3-6.
[c] Calculated using predicted D(M-M), $\pi^{qm} = 57.4$ in Table 3-13, and corrected D(M-C).
[d] Predicted from QM results for Pt by adding 5.5 kcal/mol to D(M-M) in Table 3-13.
[e] Calculated using [$D(M\text{-}C_3H_7) + D(M\text{-}C_4H_9)$]/2 in Table 3-6.
[f] Calculated using predicted D(M-M), $\pi^{qm} = 50.0$ in Table 3-13, and corrected D(M-C).

Table 3-14. Predicted adiabatic binding energies (kcal/mol) from bond additivity of cis-butene and 2,3-dimethylbut-2-ene.

Assuming this increase of strain by 2.0 kcal/mol, we can estimate the D(M-M) for the other five metals. This leads then to predictions of the di-σ bond energies for bonding cis-2-butene to the other metals using

$$BE[cis\text{-}(CH_3)HC{=}CH(CH_3)/M_8] = 2*D(M\text{-}C) - \pi^{qm} - D(M\text{-}M)$$

where D(M-C) is calculated from the average of M-C_2H_5 and M-C_3H_7 binding energies. These results are summarized in Table 3-14. Noteworthy here is that cis-butene is predicted to bind quite weakly to Ru.

The di-σ bond of 2,3-dimethylbut-2-ene (tetramethylethylene) to Pt surface. As a third example, consider the bond energy of 2,3-dimethylbut-2-ene [$(CH_3)_2C=C(CH_3)_2$] to the Pt surface. The process of converting 2,3-dimethylbutane [$(CH_3)_2HC-CH(CH_3)_2$] to $(CH_3)_2C=C(CH_3)_2$ can be written as

$$[(CH_3)_2HC\text{-}CH(CH_3)_2] \rightarrow H + [(CH_3)_2C\text{-}CH(CH_3)_2] \rightarrow 2H + (CH_3)_2C=C(CH_3)_2$$

$$D(C\text{-}H) \qquad D(C\text{-}H) - \pi \qquad \downarrow D(H\text{-}H)$$

$$H_2 + (CH_3)_2C=C(CH_3)_2$$

Using the QM values of ΔH_{rxn} = +27.5, D(C-H) = 94.6, and D(H-H) = 111.7 leads to

$$\pi^{qm} = 2D(C\text{-}H) - D(H\text{-}H) + \Delta H_{rxn} = 2*94.6 - 111.7 - 27.5 = 50.0 \text{ kcal/mol}$$

which is 7.4 kcal/mol weaker than in cis-butene and 16.0 kcal/mol weaker than in ethylene.

Consider now the bonding of $(CH_3)_2C=C(CH_3)_2$ to the metal surface. We write

$$BE[(CH_3)_2C=C(CH_3)_2/M_8] = 2\,D(M\text{-}C) - \pi - D(M\text{-}M)$$

Since D(Pt-C_3H_7) = 41.1 and D(Pt-C_4H_9) = 31.0, we assign D(M-C) = 36.1 kcal/mol, leading to

$$BE[(CH_3)_2C=C(CH_3)_2/M_8] = 2*36.1 - 50.0 - D(M\text{-}M) = 22.2 - D(M\text{-}M)$$

The calculated QM binding energy is 16.4 kcal/mol (Table 3-12). Hence, D(M-M) = +5.8 kcal/mol which is 3.5 kcal/mol larger than for cis-butene and 5.5 kcal/mol larger than for ethylene.

Assuming this increase of strain by 5.5 kcal/mol from ethylene, we can estimate the D(M-M) for the other five metals. Again D(M-C) is calculated as the average of M-C_3H_7 and M-C_4H_9 binding. Using the same equation

$$BE[(CH_3)_2C=C(CH_3)_2/M_8] = 2*D(M-C) - \pi^{qm} - D(M-M)$$

we can predict the binding energy of $(CH_3)_2C=C(CH_3)_2$ to the other five metals. The results, summarized in Table 3-14, predict that $(CH_3)_2C=C(CH_3)_2$ binds weakly to Os and does not bind to Ru.

Comparing the strain of di-σ bonds for ethylene, cis-2-butene, and 2,3-dimethylbut-2-ene, we find the strain associated with the M_2C_2 unit increases slightly from +0.3 to +2.3 to +5.8 kcal/mol.

3-4-3. Modified Group Additivities to Predict di-σ Chemisorbed Species on Metals

The discussions in Sections 3-4-1 and 3-4-2 suggest that for bonding olefins to metal surfaces the group function [C-MC_nH_{3-n}] be modified to the form [C-$MC_MC_{n-1}H_{3-n}$] to reflect the decreased steric effects for adding the second bond to the surface. Effectively we can calculate these values as

$$[C\text{-}MC_MC_{n-1}H_{3-n}] = \{ [C\text{-}MC_nH_{3-n}] + [C\text{-}MC_{n+1}H_{2-n}] \}/2$$

where the [C-MC_nH_{3-n}] and [C-$MC_{n+1}H_{2-n}$] values are from Table 3-10a. Thus,

$$[C\text{-}M(C_M)(H)_2] = (-14.82 - 6.32)/2 = -10.57 \text{ kcal/mol}$$

$$[C\text{-}M(C_M)(C)(H)] \ (-6.32 + 4.02)/2 = -1.15 \text{ kcal/mol}$$

$$[C\text{-}M(C_M)(C)_2] = (4.02 + 17.18)/2 = +10.60 \text{ kcal/mol}$$

These terms are tabulated in Table 3-10b.

Using these group additivities we can predict the heat of formation of ethylene bonded to Pt (di-sigma) to form a M_2C_2 four-membered ring on the metal surface.

$$\Delta H_f\ (C_2H_4/Pt) = 2*[C\text{-}M(C_M)(H)_2] = 2*(-10.57) = -21.14\ \text{kcal/mol}$$

which compares to the QM value of -17.9 kcal/mol. We interpret this reduction by 3.2 kcal/mol in the bonding to the surface as *strain energy* due to the M_2C_2 four-membered ring unit.

Similarly, the heat of formation of chemisorbed cis-$(CH_3)HC{=}CH(CH_3)$ is predicted to be

$$\Delta H_f\ [\text{cis-}(CH_3)HC{=}CH(CH_3)/Pt] = 2*[C\text{-}M(C_M)(C)(H)_2] - 2*[C\text{-}C(H)_3]$$
$$= 2*(-1.15) - 2*(-10.20) = -22.70\ \text{kcal/mol}$$

which compares to the QM value of -22.4 kcal/mol. Thus the strain energy due to the M_2C_2 unit is 0.3 kcal/mol.

For $(CH_3)_2C{=}C(CH_3)_2/Pt$, we predict the heat of formation of chemisorbed $(CH_3)_2C{=}C(CH_3)_2/M_8$ to be

$$\Delta H_f\ [(CH_3)_2C{=}C(CH_3)_2/Pt] = 2*[C\text{-}M(C_M)(C)_2(H)] - 4*[C\text{-}C(H)_3]$$
$$= 2*(10.60) - 4*(-10.20) = -19.60\ \text{kcal/mol}$$

which compares to the QM value of -16.5 kcal/mol. Thus we assign the strain energy due to the M_2C_2 unit as 3.1 kcal/mol.

These results suggest that there is little increase in strain energy in the M_2C_2 unit due to substitution of methyl groups. The average strain energy is 2.2 kcal/mol. The results are summarized in Table 3-15. This differs from the D(M-M) values calculated in Section 3-4-2 where the apparent strain increases with substitution. The difference in these two approaches is that the group values in this section include implicitly zero point energy

and enthalpy corrections to room temperature. Since larger adsorbates have a larger zero point energy correction, the binding energy is reduced. In this view the more flexible metal-carbon bonds can adjust to keep the strain energy low. This contrasts with cyclobutane C_4 units where stiff C-C bonds lead to a large strain energy and a Benson ring strain correction of 26 kcal/mol.

adsorbate	Group Add. ΔH_f (predicted)[a]	QM ΔH_f (calculated)	Strain energy[b,c]
C_2H_4	-21.1	-17.9	+3.2
cis-C_4H_8	-22.7	-22.4	+0.3
$C_2(CH_3)_4$	-19.6	-16.5	+3.1

[a] Calculated from Tables 9b-c.
[b] Strain energy = $\Delta H_f^{QM} - \Delta H_f^{GA}$.
[c] Average strain energy = +2.2 kcal/mol.

Table 3-15. Predicted ΔH_f, calculated ΔH_f, and strain energy of ethylene, cis-butene, and 2,3-dimethylbut-2-ene on Pt_8 (in kcal/mol).

Assuming similar strain energies as Pt (or an average of 2.2 kcal/mol) in the other five metals leads to predictions of the heat of formation for cis-butene and $(CH_3)_2C=C(CH_3)_2$ in a way analogous to predicting binding energies discussed in Section 3-4-2.

3-4-4. Use of Group Additivities to Predict Chemisorbed Cyclohexene on Pt

To investigate the applicability of strain energy concepts, consider chemisorption of cyclohexene (c-C_6H_{10}) in a 1,2-di-σ conformation to the Pt surface (see Figure 3-4). This adsorption geometry is similar to di-σ ethylene (also shown in Figure 3-4) and its methylated derivatives. The heat of formation of C_6H_{10}/Pt predicted using group additivity is

$$\Delta H_f\ (c\text{-}C_6H_{10}/Pt) = 2*[C\text{-}M(C_M)(C)(H)_2] + 4*[C\text{-}(C)_2(H)_2]$$

$$= 2*(-1.15) + 4*(-4.93) + \text{strain energy} = -22.02 + \text{strain energy}$$

The strain energy has two components. (1) The structure of the M_2C_2 unit of C_6H_{10}/Pt is similar to ethylene and its methyl-substituted derivatives. Hence, we can apply an average strain energy component of 2.2 kcal/mol calculated for C_2H_4/Pt_8 to this system. (2) On a flat surface the C_6 ring cannot have its favored chair form; instead it is promoted to the boat conformation (only slightly distorted from boat cyclohexane; see Figure 3-4). The boat to chair transition is ~6.0 kcal/mol giving an additional 6.0 kcal/mol of ring strain.

Thus, we expect

$$\Delta H_f\ (C_6H_{10}/Pt) = -22.0 + 6.0 + 2.2 = -13.8 \text{ kcal/mol}$$

The calculated QM value is -12.6 kcal/mol, only 1.2 kcal/mol different. Thus using group additivity, one can predict the heat of formation of chemisorbed intermediates within a few kcal/mol.

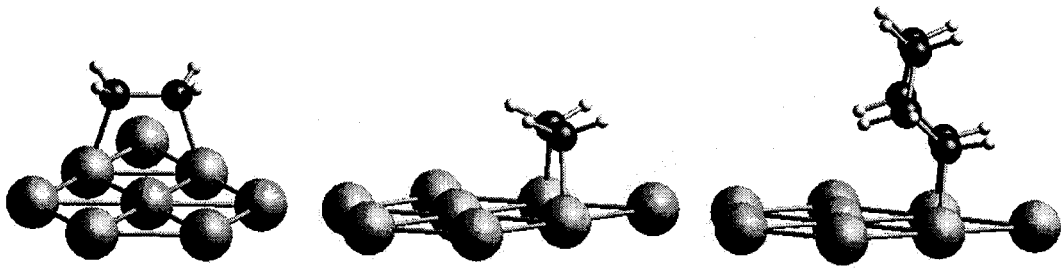

Figure 3-4. C_2H_4 and C_6H_{10} adsorbed on Pt_8.

3-4-5. How to Use These Values: A Recipe

The following steps summarize how to apply the derived group values to calculate the heat of formation for a hydrocarbon bound to a metal surface:

(1) Apply group values in Table 3-10 for carbons directly bound to the metal surface.

(2) Apply Benson group values for carbons *not* bound to the metal surface (some selected values are in Table 3-10c).

(3) Assume that the strain energy for an M_2C_2 unit is 2.2 kcal/mol (the average value from Table 3-15).

(4) Apply Benson strain energies for strain in any fully hydrocarbon ring. Also, additional strain energies due to non-ideal conformations (e.g., chair to boat) should be added here.

(5) Add the numbers from steps (1)-(4).

Relative comparison among purely organic molecules using Benson group values are good to within 1 kcal/mol. Our predictions of relative energies of adsorbed species have a slightly larger spread, in the range of 1.5 kcal/mol.

3-5. Conclusions

We find that the C bonded to the closest packed surface of Pt, Ir, Os, Pd, Rh, and Ru always prefers the site in which this C has four σ bonds. The adiabatic binding energies are roughly additive according to the number of M-C σ bonds formed and decrease with increasing methyl substitution for all CR_x. These effects due to substitution are similar for the various metals. The computed energetics are used to obtain a group additivity scheme for predicting binding energies of hydrocarbons chemisorbed to metal surfaces. We provide several examples to illustrate how nine new group values for M-C bonding can be combined with existing Benson group additivities to make useful predictions. This allows two types of estimates:

(i) predicting binding energies and heats of formation of larger and more complex hydrocarbons on the same metal and

(ii) predicting how changing the metal will change the energetics for the same organic fragments.

This provides a new powerful technique for deriving a mechanistic understanding of complex hydrocarbon reactions and rearrangements on catalytic surfaces.

3-6. Computational Approach

3-6-1. The M_8 Cluster Model

From studies on the six metals (Pt, Ir, Os, Pd, Rh, and Ru), we find that the M_8 cluster generally has the desired s^1d^{N-1} configuration. Since Pt, Ir, Pd, and Rh are fcc metals, this cluster models the (111) surface. For Os and Ru, which have hcp packing, the M_8 cluster models the (0001) surface.

Our calculations take the M-M bonds in each cluster to be the bond distance in the bulk crystal (see Table 3-16). This is because we consider that particles in the real catalyst are sufficiently large to enforce this structure. Slab calculations suggest that binding energies increase by 2-3 kcal/mol when the top layer of a slab is allowed to relax.[42]

Metal	M-M distance (Å)
Pt	2.775
Ir	2.714
Os	2.734
Pd	2.750
Rh	2.689
Ru	2.706

Table 3-16. Bulk M-M distances used in cluster calculations (ref 53).

For the optimal (most stable) binding sites, the chemisorbed organics were fully optimized on the cluster. For CH_x in non-optimal sites, we generally had to apply a constraint to keep the fragment in the non-optimal site. All methyl-substituted adsorbates were allowed to freely optimize but they were studied only in the optimal binding sites.

The M_8 cluster only models conditions close to the zero coverage limit. It is expected that at higher coverage, binding energies (and corresponding derived group values) may change. Modeling large complicated adsorbates that have steric interactions with a larger surface area of the metal would require a larger metal cluster. The group values derived in this paper may change systematically by a few kcal/mol for a different metal cluster with an s^1d^{N-1} configuration.

3-6-2. Details for QM Computations

Calculations were carried out using the restricted B3LYP flavor of density functional theory (DFT), which includes non-local corrections (generalized gradient approximation) and exact Hartree-Fock (HF) exchange operators with the Slater local exchange functional.[43] We use the parameters referred to as Becke3[44] with the Becke nonlocal gradient correction,[45] the Vosko-Wilk-Nusair exchange functional,[46] and the Lee-Yang-Parr local and nonlocal correlation functional.[47]

All calculations were carried out using the Jaguar program.[50-51] The metals were described using the Hay and Wadt core-valence relativistic effective-core potential (ECP) with 18 explicit electrons for Pt, Pd; 17 electrons for Ir, Rh; and 16 electrons for Os, Ru (denoted LACVP in Jaguar).[50] This is a non-local ECP using angular momentum

projection operators to enforce the Pauli Principle.[51-52] All electrons were considered for carbon and hydrogen using the 6-31G** basis set.

3-6-3. Spin States

The various spin states were calculated as pure spin states (not unrestricted DFT). The optimum spin of the metal-adsorbate complex is determined by separate calculations of all low-lying spins where in each case the geometric structure for each adsorbate on the metal surface was fully optimized (but M-M bonds kept fixed).

To ensure that we have the correct spin and occupation for each system, we went through an extensive procedure to determine the optimum orbital configuration for each spin and to consider all possible low lying spins. For example, consider Pt_8. We find that the ground state spin is S=3. In addition to low-lying excited states of S=3, the lowest energy S=4 state is higher by 1.4 kcal/mol. We consider each of these configurations in bonding various intermediates to the surface.

The IEM predicts that for small clusters, the low-lying s bonding orbitals are always doubly occupied, the high-lying s antibonding orbitals are always empty, and the d orbitals are filled in the high spin configuration. This is illustrated by the schematic in Figure 1-3. As the clusters get larger, it becomes more favorable to spin-pair electrons in the high-lying d-orbitals (Figure 1-5). This is what happens in Pt_8 where the high spin S=4 is less favorable than the lower spin S=3 state. Further examples of this can be found in Chapter 1.

Upon binding say CH_2 to the surface, we expect that the two unpaired electrons of triplet CH_2 will be paired with two electrons from the metal to form an S=2 ground state

for the CH_2/Pt_8 cluster. However, we calculated the energies of the S=1, S=2 and S=3 states. The result from the calculations is that S=2 is indeed the ground state. It is also necessary to check all low-lying orbital configurations for a given spin to ensure that the ground state energy is found. Depending on the initial guess, the wavefunction may converge to a state that is 2-3 kcal/mol higher than the ground state for a given spin. For example, the ground spin state of CH_2/Pt_8 is S=2, leading to 72 doubly-occupied d-orbitals and 4 singly-occupied d-orbitals. To ensure that this is indeed the ground state, the occupations of the lowest singly-occupied d-orbital and the highest doubly-occupied orbital are switched and the energy is recalculated. If the energy drops, then the switch occurs with the next doubly-occupied orbital until the energy no longer decreases. Although not exhaustive, this general procedure gives us reasonable confidence that the calculated energies are indeed the ground states.

The ground spin states and total energies of the six M_8 clusters are given in Table 3-1. In each case except Pd, the electronic structure is consistent with the IEM, which suggests s^1d^{N-1} character in the surface where N is the number of valence electrons. The ground spin states for the metal and metal-adsorbate clusters follow a coherent pattern based on the IEM. We ensured in each case that the optimum spin states are used in calculating the bond energies.

3-6-4. Comparison of Explicit and Implicit Corrections for H/Pt_8

Using our scheme of implictly correcting for zero point energy (ZPE) and enthalpy at room temperature, we calculate $\Delta H_f(H/Pt_8)$ = -11.38 kcal/mol (see Section 3-2). Instead we can explicitly compute these quantities.

The calculated non-ZPE corrected QM binding energy of H/Pt_8 is 67.2 kcal/mol. The three modes have frequencies summing to ~2000 cm^{-1}. Hence, the computed ZPE correction is ~1000 cm^{-1} in energy or 2.9 kcal/mol per H atom. Therefore, the ZPE-corrected binding energy of H/Pt_8 is 67.2 – 2.9 = 64.3 kcal/mol.

The calculated non-ZPE corrected QM bond strength of H-H is 111.7 kcal/mol. The calculated ZPE is 6.1 kcal/mol. Therefore, the ZPE-corrected bond energy is 111.7 – 6.1 = 105.6 kcal/mol.

Hence, $\Delta H_f(H/Pt_8) = 0.5 * (105.6 - 2*64.3) = -11.0$ kcal/mol. Enthalpy corrections to room temperature result in stabilizing the adsorbate by 1.2 kcal/mol. Therefore, the final computed number with explicit ZPE and thermal enthalpy corrections is $\Delta H_f (H/Pt_8) = -12.2$ kcal/mol. Using our scheme of implicit inclusion gives -11.4 kcal/mol, a difference of only 0.8 kcal/mol.

Acknowledgement

The content of this chapter was adapted from reference 54. This research was funded by the NSF (CHE 95-22179).

References

1. Davis, S. M.; Somorjai, G. A. *The Chemical Physics of Solid Surfaces and Heterogenous Catalysis*, eds. King, D. A.; Woodruff, D. P., Vol. 4, pp. 217-298, Elsevier, Amsterdam, 1982.
2. Gault, F. G. *Adv. Catal.*, **1981**, *30*, 1.
3. Albert, M. R.; Yates, J. T., Jr. *The Surface Scientists Guide to Organometallic Chemistry*; American Chemical Society, Washington, 1987.

4. Somorjai, G. A. *Introduction to surface chemistry and catalysis*, Wiley, New York, 1994.

5. Zaera, F. *Chem. Rev.*, **1995**, *95*, 2561.

6. Koel, B. E.; Blank, D. A.; Carter, E. A. *J. Mol. Cat A-CHEM*, **1998**, *131*, 39.

7. Carter, E. A.; Koel, B. E. *Surf. Sci.*, **1990**, *226*, 339.

8. Benson, S. W. *Thermochemical Kinetics*, Wiley, New York, 1968.

9. Cohen, N.; Benson, S. W. *Chem. Rev.*, **1993**, *93*, 2419.

10. Richter, L. J.; Ho, W. *Phys. Rev. B*, **1987**, *36*, 9797.

11. Christmann, K.; Ertl, G.; Pignet, T. *Surf. Sci.*, **1976**, *54*, 365.

12. Engstrom, J. R.; Tsai, W.; Weinberg, W. H. *J. Chem. Phys.*, **1987**, *87*, 3104.

13. Conrad, H.; Ertl, G.; Latta, E. E. *Surf. Sci.*, **1974**, *41*, 435.

14. Yates, J. T., Jr.; Thiel, P. A.; Weinberg, W. H. *Surf. Sci.*, **1979**, *84*, 427.

15. Feulner, R.; Menzel, D. *Surf. Sci.*, **1985**, *154*, 465.

16. Zaera, F. *Langmuir*, **1991**, *7*, 1998.

17. Alberas-Sloan, D. J.; White, J. M. *Surf. Sci.*, **1996**, *365*, 212.

18. Valden, M.; Xiang, N.; Pere, J.; Pessa, M. *Appl. Surf. Sci.*, **1996**, *99*, 83.

19. Fairbrother, H. D.; Peng, X. D.; Trenary, M.; Stair, P. C. *J. Chem. Soc. Faraday Trans.*, **1995**, *91*, 3619.

20. Yeo, Y. Y.; Stuck, A.; Wartnaby, C. E.; King, D. A. *Chem. Phys. Lett.*, **1996**, *259*, 28. The 30-48 kcal/mol microcalorimetry measurements are interpreted as ethylene adsorption in the smaller range, converting to ethylidyne in the larger range.

21. Watwe, R. M.; Speiewak, B. E.; Cortright, R. D.; Dumesic, J. A. *J. Catal.*, **1998**, *180*, 184.

22. Blomberg, M. R. A.; Siegbahn, P. E. M.; Svensson, M. *J. Phys. Chem.*, **1992**, *96*, 5783.

23. Cui, Q.; Musaev, D. G.; Morokuma, K. *J. Chem. Phys.*, **1998**, *108*, 8418.

24. Akinaga, Y.; Taketsugu, T.; Hirao, K. *J. Chem. Phys.*, **1997**, *107*, 415.

25. Watanabe, K.; Sawabe, K.; Matsumoto, Y. *Phys. Rev. Lett.*, **1996**, *76*, 1751.

26. Feng, K. A.; Lin, Z. D. *Appl. Surf. Sci.*, **1993**, *72*, 139.

27. Jachimowski, T. A.; Hagedorn, C. J.; Weinberg W. H. *Surf. Sci.*, **1997**, *393*, 126.

28. Paul, J.-F.; Sautet, P. *J. Phys. Chem. B*, **1998**, *102*, 1578.

29. De Koster, A.; Van Santen, R. A. *J. Catal.*, **1991**, *127*, 144.

30. Wu, M.-C.; Goodman, D. W. *J. Am. Chem. Soc.*, **1994**, *116*, 1364.

31. Oxton, I. A. *Spectrochim. Acta A*, **1982**, *38*, 181.

32. Kesmodel, L. L.; Dubois, L. H.; Somorjai, G. A. *J. Chem. Phys.*, **1979**, *70*, 2180.

33. Starke, U.; Barbieri, A.; Materer, N.; Van Hove, M. A.; Somorjai, G. A. *J. Phys. Chem.*, **1993**, *286*, 1.

34. Marinova, Ts. S.; Chakarov, D. V. *Surf. Sci.*, **1987**, *192*, 275.

35. Gates, J. A.; Kesmodel, L. L. *Surf. Sci.*, **1983**, *124*. 68.

36. Dubois, L. H.; Castner, D. G.; Somorjai, G. A. *J. Chem. Phys.*, **1980**, *72*, 5234.

37. Barteau, M. A.; Broughton, J. Q.; Menzel, D. *Appl. Surf. Sci.*, **1984**, *19*, 92.

38. Lide, D. R. *Handbook of Chemistry and Physics*, 74th ed.; CRC Press: Boca Raton, 1993-1994.

39. This value differs slightly from the one (-13.06) implicit in Figure 3 because the reference compounds are now CH_4 and C_2H_6. Using the derived value of E(H)=0.59209 yields ΔH_f [H_{ads}] = -9.62 kcal/mol. Hence, ΔH_f [$(CH_3)_{ads}$ + $(H)_{ads}$] = -14.82 - 9.62 = -24.44 kcal/mol. Section 2 (and Figure 3) use CH_4 and H_2 as reference compounds and hence the heat of formation of adsorbed CH_3 is -13.06 kcal/mol. However, now ΔH_f [H_{ads}] = -11.38 kcal/mol. Hence, ΔH_f [$(CH_3)_{ads}$ + $(H)_{ads}$] = -13.06 - 11.38 = -24.44 kcal/mol, the same value as using CH_4 and C_2H_6 as reference compounds.

40. Merer, A. J.; Mulliken, R. S. *Chem. Rev.*, **1969**, *69*, 639.

41. Stohr, J.; Setter, F.; Johnson, A. L. *Phys. Rev. Lett.*, **1984**, *53*, 1684.

42. Ge, Q.; King, D. A. *J. Chem. Phys.*, **1999**, *110*, 4699.

43. Slater, J. C. *Quantum Theory of Molecules and Solids*, Vol. 4: *The Self-Consistent Field for Molecules and Solids*, Mc-Graw Hill, New York, 1974.

44. Becke, A. D. *J. Chem. Phys.*, **1993**, *98*, 5648.

45. Becke, A. D. *Phys. Rev. A*, **1988**, *38*, 3098.

46. Vosko, S. H.; Wilk, L.; Nusair, M. *Can. J. Phys*, **1980**, *58*, 1200.

47. Lee, C.; Yang, W.; Parr, R. G. *Phys. Rev. B*, **1988**, *37*, 785.

48. Jaguar 3.5, Schrodinger, Inc., Portland, Oregon, 1998.

49. Greeley, B. H.; Russo, T. V.; Mainz, D. T.; Friesner, R. A.; Langlois, J.-M.; Goddard III, W. A.; Honig, B. *J. Am. Chem. Soc.*, **1994**, *116*, 11875.

50. Hay, P. J.; Wadt, W. R. *J. Phys. Chem.*, **1985**, *82*, 299.

51. Goddard III, W. A. *Phys. Rev.*, **1968**, *174*, 659.

52. Melius, C. F.; Olafson, B. O.; Goddard III, W. A. *Chem. Phys. Lett.*, **1974**, *28*, 457.

53. Winter, M.; *http://www.shef.ac.uk/chemistry/web-elements/*

54. Kua, J.; Faglioni, F.; Goddard III, W. A. *J. Am. Chem. Soc.*, **2000**, *122*, 2309.

Chapter 4: Oxidation of Methanol on Second and Third Row Group VIII Transition Metals: Application to Direct Methanol Fuel Cells

Abstract

Using first principles quantum mechanics [nonlocal density functional theory (B3LYP)], we calculated the 13 most likely intermediate species for methanol oxidation on clusters of all 2nd and 3rd row Group VIII transition metals for all three likely binding sites (top, bridge and cap). This comprehensive set of binding energies and structures allows a detailed analysis of possible reaction mechanisms and how they change for different metals. This illustrates the role that modern quantum chemical methods can be used to provide data for combinatorial strategies for discovering and designing new catalysts. We find that methanol dehydrogenation is most facile on Pt, with the hydrogens preferentially stripped off the carbon end. However, water dehydrogenation is most facile on Ru. These results support the bifunctional mechanism for methanol oxidation on Pt-Ru alloys in direct methanol fuel cells (DMFCs). We find that pure Os is capable of performing both functionalities without co-catalyst. Pathways to form the second C-O bond differ between the pure metals (Pt and Os) in which $(CO)_{ads}$ is probably activated by $(OH)_{ads}$ and the Pt-Ru binary system in which $(COH)_{ads}$ is probably activated by O_{ads}. For all cases we find that formation of $(COOH)_{ads}$ is an important precursor to the final dehydrogenation to desorb CO_2 from the surface.

4-1. Introduction

Fuel cells are electrochemical cells in which both fuel and oxidant are fed in a continuous supply to the electrodes. They are attractive sources of electrical power since the production of electrical energy can be maintained as long as the reactants are supplied to the electrodes. This concept was first proposed in 1839 by Sir W. R. Grove, and direct conversion of chemical to electric energy in a hydrogen/oxygen fuel cell was demonstrated. Although hydrogen/oxygen fuel cells are used in spaceships, wider applications in traction-based vehicles (for example, electric cars) are limited by unsolved problems such as transport and storage of hydrogen. Liquid fuels would solve this problem; however, extracting molecular hydrogen from a liquid fuel requires a reformer. This greatly increases the overall cost of the cell, reducing the fuel conversion efficiency.

An alternative to H_2 is the use of a liquid fuel such as methanol supplied directly to the anode and electro-oxidized to CO_2. Indeed, recent results for model direct methanol fuel cells (DMFCs) show that critical performance parameters for commercial use are now achievable with modern catalytic formulations and cell designs.[1] A simple schematic of the DMFC is shown in Figure 4-1. The fuel (methanol and water) is passed through the anode, and the oxidant (O_2 in air) flows through the cathode. The two electrodes are separated by a proton-exchange membrane such as Nafion. Platinum based electrodes demonstrate the highest catalytic activity and cleanest combustion products. Since engines operate at high temperatures, this whole system will be in an "oven-like" setting. The design and construction of high-performance DMFCs is already undergoing optimization.[1]

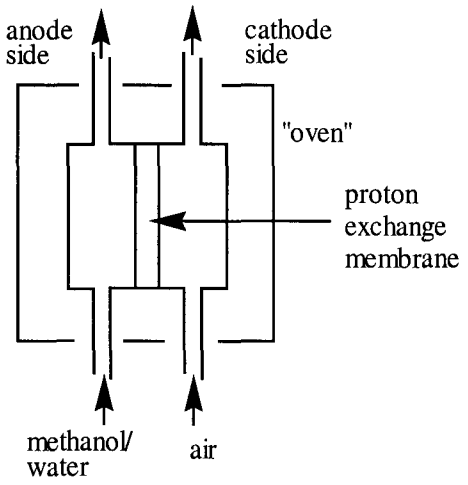

Figure 4-1. Schematic of a direct methanol fuel cell.

An obvious advantage of the DMFC over the internal combustion engines is to avoid the environmental damage caused by the latter. The alternative use of batteries could, in principle, operate a vehicle without unwanted emissions; however, current batteries also have environmental problems and require constant recharging. The DMFC, on the other hand, can provide a continuous supply of electrical energy as long as there is available fuel. Renewable liquid fuel alternatives such as methanol also allow use of the current infrastructure for petroleum.

However, the DMFC does have disadvantages, the primary problem being a low power density. High over-potentials at the anode catalyst combined with the necessity of using low temperatures severely reduce the conversion efficiency. Thus, high loading of noble-metals are required to enhance the performance of the anode, increasing costs. In addition, the membrane properties need to be improved with respect to water balance sensitivity (six protons at the anode produced per methanol molecule) and inhibition of methanol crossover. Diffusion of methanol across the membrane leads to depolarization of the cell and loss of activity.

Recently, advances have been made in two significant areas: (1) the use of solid polymer electrolyte (SPE) technology now allows increased operating temperatures, thereby improving efficiency,[2] and (2) improved electrocatalysts have been identified that increase reaction activity, allowing reduction of the noble metal loading. This decreases the cost and generates higher power densities. This paper will focus on the latter area.

The progress in developing improved DMFCs has been hindered by the lack of a detailed reaction mechanism. Relevant mechanistic were discussed by Leger and Lamy,[3] and recently reviewed by Hamnett,[4] while Parsons and VanderNoot[5] provide an earlier review of fuel cell research.

4-2. Review of Mechanistic Understanding for Direct Methanol Oxidation

There are several different plausible pathways for the oxidation of methanol. Water is required for the overall conversion of methanol to carbon dioxide (4.1)

$$CH_3OH + OH_2 \rightarrow CO_2 + 6H^+ + 6e^- \quad (4.1)$$

Methanol adsorbed on the electrode surface can undergo successive dehydrogenation, as indicated in steps (4.2) to (4.5). However, the exact structure of the adsorbed intermediates is unknown except for $(CO)_{ads}$.

$$(CH_3OH)_{ads} \rightarrow (CH_3O)_{ads} + H^+ + e^- \quad (4.2)$$

$$(CH_3O)_{ads} \rightarrow (CH_2O)_{ads} + H^+ + e^- \quad (4.3)$$

$$(CH_2O)_{ads} \rightarrow (CHO)_{ads} + H^+ + e^- \quad (4.4)$$

$$(CHO)_{ads} \rightarrow (CO)_{ads} + H^+ + e^- \quad (4.5)$$

Our computational results (vide infra) suggest which particular isomers are the adsorbed species. Water may also dehydrogenate successively to form adsorbed OH and O atom as in steps (4.6) to (4.7).

$$(OH_2)_{ads} \rightarrow (OH)_{ads} + H^+ + e^- \quad (4.6)$$

$$(OH)_{ads} \rightarrow (O)_{ads} + H^+ + e^- \quad (4.7)$$

Formation of a second C-O bond is then required to remove $(CO)_{ads}$ from the surface in the form of CO_2 as in (4.8a).

$$(CO)_{ads} + O_{ads} \rightarrow CO_2 \quad (4.8a)$$

Equation (4.8a) assumes complete dehydrogenation for both CH_3OH and H_2O takes place to form CO_{ads} and O_{ads}, which then forms CO_2, which desorbs from the surface. However, it is possible that partially dehydrogenated species could recombine and then dehydrogenate (either simultaneously or in a successive step) to form CO_2 as in (4.8b).

$$(CO)_{ads} + (OH)_{ads} \rightarrow (COOH)_{ads} \rightarrow CO_2 + H_{ads} \quad (4.8b)$$

The recombination of partially dehydrogenated species could also produce compounds such as HCOOH, $HCOOCH_3$ and $CH_2(OCH_3)_2$, all of which have been observed experimentally.[6]

4-2-1. Experimental Observations

It has long been known that Pt-Ru alloy electrodes increase the electrocatalytic activity compared to pure Pt electrodes.[7-8] Many recent advances in experimental techniques have contributed to elucidating the reaction mechanism. Recently on-line Fourier transform infrared (FTIR) spectroscopy[6] and real-time mass spectrometry[9] has been used to detect intermediates formed at higher operating temperatures. [Previous

studies had been performed only at room temperature.[10]] Low-energy ion scattering (LEIS), under ultrahigh vacuum (UHV) conditions, has been used to determine the surface compositions of various polycrystalline Pt-Ru bulk alloys[11] allowing kinetic studies as a function of temperature.[12] *In situ* X-ray absorption studies have been performed to characterize the Pt-Ru phases.[15] Differential electrochemical mass spectrometry (DEMS) has been used to compare the activity of Pt-Ru with pure Pt and pure Ru.[14] Structural effects and reactivity on different single crystal faces of platinum have been compared,[15] as have the effects of using bulk Pt, Pt particles, and carbon-black-supported Pt-Ru electrodes.[16]

It is known that methanol oxidation on platinum is structure-sensitive,[17] but the issue of size effects is unresolved. The Oxford group suggested an optimum diameter of 2nm;[18] however, other studies do not find evidence for size effects, even for particles as small as 1.4 nm.[19]

The confirmation that $(CO)_{ads}$ is the poisoning species [and not $(COH)_{ads}$ or $(CHO)_{ads}$] was made possible by electro-modulated infrared reflectance spectroscopy (EMIRS).[20] A chronological review of electro-oxidation of CO on polycrystalline Pt has been provided by Beden and Lamy.[21]

Recent experiments using combinatorial screening of electrochemical catalysts have identified ternary and quaternary alloys with higher activity than Pt-Ru.[22] The alloy with the best catalytic activity reported is $Pt_{0.44}Ru_{0.41}Os_{0.10}Ir_{0.05}$. The observation that Ir and Os can serve as promoters raises the question of what role is played by each different metal in the oxidation reaction.

4-2-2. Bifunctional Mechanism of Pt-Ru

The bifunctional mechanism of Pt-Ru was first presented by Watanabe and Motoo.[23] According to this mechanism, Pt is responsible for catalyzing the dehydrogenation of methanol. On pure Pt, this reaction is poisoned because of the formation of $(CO)_{ads}$ after complete dehydrogenation of methanol. The removal of CO is facilitated by Ru, which may act by weakening the Pt-CO bond, and/or by promoting the oxidation of CO to CO_2 via activation of water in an adjacent site to facilitate the formation of the second C-O bond. The onset potential of forming CO_2 on Pt-Ru (0.220 V versus RHE) is lower than that on Pt-black (0.325 vs RHE).[6] This has been attributed to the ability of Ru to adsorb OH at lower potentials.[24] Pure Pt decomposes water at a high potential of 0.8 V versus RHE; whereas, on pure Ru, the potential required is only 0.2 V versus RHE.[11]

4-2-3. Previous Computational Approaches

Semi-Empirical MO Calculations. Using semi-empirical molecular orbital calculations on cluster models, Anderson[25] has studied the interaction of $(CO)_{ads}$ and $(OH)_{ads}$ on Pt(111) using a bilayer Pt_{18} cluster to model two reactions: (1) the dehydrogenation of water to form $(OH)_{ads}$, and (2) the interaction of $(CO)_{ads}$ and $(OH)_{ads}$ to form the second C-O bond. These calculations used a modification of extended Huckel theory in which an empirical two-body nuclear-nuclear term is added to improve geometries and energetics. This is called Atom Superposition and Electron Delocalization Molecular Orbital (ASED-MO) theory. Their results suggest that reaction (4.8b) has a barrier of 22.6 kcal/mol. However, ASED-MO calculations yield binding energies that are far too high. For example, ASED-MO leads to a binding energy for

H_2O of 41.7 kcal/mol compared to 12 kcal/mol from experiment,[26] a binding energy for CO of 56.7 kcal/mol compared to 43 kcal/mol from experiment experiment,[27] and a binding energy for OH of 90.4 kcal/mol compared to 47 kcal/mol from experiment.[28] With binding energies too high by 30, 14, and 43 kcal/mol, it is doubtful that the calculated barriers are reliable. As discussed in Section 4-3, DFT B3LYP calculations lead to binding energies (kcal/mol) of 16.0 (H_2O), 41.9 (CO), and 40.8 (OH) which are off by 4, 1, and 6 kcal/mol off, respectively, from experiment.

A further study was done on mixed Pt-Ru clusters[29] suggesting that the adsorption of OH was stronger on Ru (binding energy of 122 kcal/mol) than Pt. The dehydrogenation of OH_2 was then studied on a series of $Pt_{17}M$ clusters for M atoms in periods 4-6 of the Periodic Table.[30] In these studies, only the on-top sites were considered for the adsorbed species. We show that bridging sites and cap sites also play a role.

First Principles Calculations. Recent studies using first principles gradient-corrected density function theory (DFT) (BP86) examined the chemisorption of CO on Pt-Pt, Pt-Ni, and Pt-Ru dimers.[31] They found binding energies (kcal/mol) of 33, 5, and -5, respectively, indicating that bridged CO binds weakest to Pt-Ru.

Other computational work focused on the binding of CO to Pt using a variety of computational approaches and different levels of theory. For example, restricted Hartree-Fock (RHF) on Pt_4 leads to a binding energy of 27.0 kcal/mol (on-top site) [complete active space self consistent field (CASSCF) on the same cluster gave the same structural parameters but the binding energy was not reported].[32] DFT-GGA on Pt_{10} leads to a binding energy for CO of 41.8 kcal/mol (on-top site),[33] and gradient corrected DFT on Pt with periodic boundary conditions leads to a binding energy of 33.4 kcal/mol (on-top

site).[34] Thus the various cluster calculations suggest an on-top site with energies of 16, 1, and 10 kcal/mol weaker than the experimental value of 43 kcal/mol. Our calculations (vide infra) lead to a cap site with a bond energy of 41.9 kcal/mol.

4-3. Results for Pt

We summarize in this section the results for Pt since all good DMFC catalysts involve Pt and since there is more experimental data with which to compare the theory. Section 4-4 will compare the results for all six metals. We consider separately three parts of the reaction:

(1) dehydrogenation of methanol,

(2) dehydrogenation of water, and

(3) formation of the second C-O bond.

For each of these reactions, we calculated the equilibrium structures of ~13 intermediates at each of the 3 sites on each of the six metals (Pt, Ir, Os, Pd, Rh, and Ru).

4-3-1. Calculation of Heats of Formation

For simplicity in comparing a large number of adsorbates on a number of metals and sites, we choose to reference our calculated energetics for the minimized structures with experimental heats of formation at room temperature. This is not rigorous. To compare energetics at room temperature, we should correct all calculated numbers for zero point energy and for changes in the enthalpy to room temperature. Such corrections will lead to changes in the final heat of formation of a few kcal/mol, which are expected to be nearly

the same for adsorbates at the same site of the various metals. Hence, in the interests of comprehensive results for many cases, we neglect these corrections here.

For convenience in considering the thermodynamics of these reactions, we convert the calculated metal-adsorbate energetics into heats of formation for each chemisorbed species. To calculate the heats of formation, we must choose an appropriate ensemble of reference compounds (one for each element). We chose the reference compounds as follows:

(1) M_8 in the ground state (S=3 for Pt_8)

(2) gas-phase H_2,

(3) gas-phase methane, and

(4) gas-phase water.

Reference	Absolute Energy (hartree)	Experimental ΔH_f (kcal/mol)	Reference energies (hartrees)
Pt_8 (S=3)	-953.25726	0	$E_0(Pt_8)$ = -953.25726
Ir_8 (S=8)	-837.40601	0	E_0 (Ir_8) = -837.40601
Os_8 (S=10)	-728.00941	0	E_0 (Os_8) = -728.00941
Pd_8 (S=1)	-1013.98567	0	E_0 (Pd_8) = -1013.98567
Rh_8 (S=7)	-875.98723	0	E_0 (Rh_8) = -875.98723
Ru_8 (S=11)	-750.83465	0	E_0 (Ru_8) = -750.83465
H_2	-1.17854	0	E_0 (H) = -0.58927
CH_4	-40.52405	-17.9	E_0 (C) = -38.13845
OH_2	-76.41973	-57.8	E_0 (O) = -75.14908

[a] Reference 35

Table 4-1. Reference energies and assigned heats of formation of reference compounds.

The calculated energies of the reference compounds are shown in Table 4-1. Heats of formation for methane and water are taken from gas-phase experimental values. The procedure used to calculate heats of formation is as follows:

- For the Pt cluster, since $H_f(Pt_8)$ =0 the *reference energy* for Pt_8 is $E_0(Pt_8)$ = -953.25726 hartrees.
- For H, since $H_f(H_2)$ =0 the *reference energy* is $E_0(H)$ = -0.58927 hartrees (half the calculated value for an isolated H_2 molecule).
- For C, the *reference energy*, $E_0(C)$, is derived from

$$C_{atom} + 2H_2 \rightarrow CH_4 \qquad (4.9)$$

Since[35] $\Delta H_f(CH_4)$ = -17.9 kcal/mol = -0.02852h, we obtain

$$E(CH_4) = -40.52405 = -0.02852 + E_0(C) + 4E_0(H) \qquad (4.10)$$

Thus, $E_0(C)$ = -38.13845 hartrees.

- For O, the *reference energy*, $E_0(O)$, is derived from

$$O_{atom} + H_2 \rightarrow OH_2 \qquad (4.11)$$

Since[35] $\Delta H_f(H_2O)$ = -57.8 kcal/mol = -0.09211h, we obtain

$$E(OH_2) = -76.41973 = -0.09211 + E_0(O) + 2E_0(H) \qquad (4.12)$$

Thus, $E_0(O)$ = -75.14908 hartrees.

Calculation of H_{ads}. Using Pt_8 we calculate binding energies of 67.2 kcal/mol for η_3-H/Pt_8 (cap site), 66.7 kcal/mol for η_2-H/Pt_8 (bridge site), and 65.5 kcal/mol for η_1-H/Pt_8 (on-top site). This suggests that H prefers the cap site on Pt (in agreement with experiment). The calculated desorption enthalpy to obtain gas phase H_2 is 11.38 kcal/mol per adsorbed H. This compares with 10.6 kcal/mol from low energy electron diffraction (LEED) and thermal desorption spectroscopy (TDS).[36] Similar techniques yield desorption enthalpies (per adsorbed H) of 12.6 kcal/mol for Ir(111),[37] 10.6 kcal/mol for Pd(111),[38] 10.1 kcal/mol for Rh(111),[39] and 9.5 kcal/mol for Ru(0001).[40] Since the variation of energy is small, we will use the same value of -11.38 kcal/mol calculated for

ΔH_f (H_{ads}) on Pt for all the metals. This simplifies the comparison of different adsorbates on these various metals.

To calculate the heat of formation of the CH_xO/M_8 clusters, we use the formula

$$\Delta H_f (CH_xOy/Pt_8) = \{E(CH_xO_y/M_8) - E_0(M_8) - E_0(C) - yE_0 (O) - xE_0(H)\}*627.5096 \quad (4.13)$$

For example, the heat of formation of CH_2OH_{ads} is

$$\Delta H_f (CH_2OH/Pt_8) = \{-1068.41374 + 953.25726 + 38.13845 + 75.14908 + 3(0.58927)\}*627.5096 = -63.47 \text{ kcal/mol}$$

In comparing CH_xO clusters with various numbers of H atoms, we assume low coverage conditions in which excess H atoms end up at sites of the Pt surface well separated from the carbon and oxygen containing species. Thus, in examining rearranged structures starting with CH_3OH, we consider the combined H_f to be

$$\Delta H_f (CH_xO/Pt_8) + (4 - x)\, \Delta H_f(H/Pt_8) \quad (4.14)$$

For example, CH_2OH (x = 3) has one hydrogen less than CH_3OH, leading to (4 – x) = 1. Therefore, we add one increment of ΔH_f (H/Pt_8) to account for the heat of formation for the chemisorbed H. For example, this leads to

$$\Delta H_f (CH_2OH) = \Delta H_f (CH_2OH)_{ads} + \Delta H_f (H_{ads}) = -63.47 - 11.38 = -74.85 \text{ kcal/mol}$$

4-3-2. Methanol Dehydrogenation on Pt

The complete dehydrogenation of methanol yields $(CO)_{ads}$ and four H_{ads}. We calculated the various likely intermediates in this reaction, obtaining the low energy structures shown in Figure 4-2 (with additional structural information in Table 4-2). The spin state, site preference, total energy and binding energy for each structure is listed in

Table 4-3. Binding energies were calculated with respect to the naked Pt_8 (S=3) cluster and the optimized fragments listed in Table 4-4.

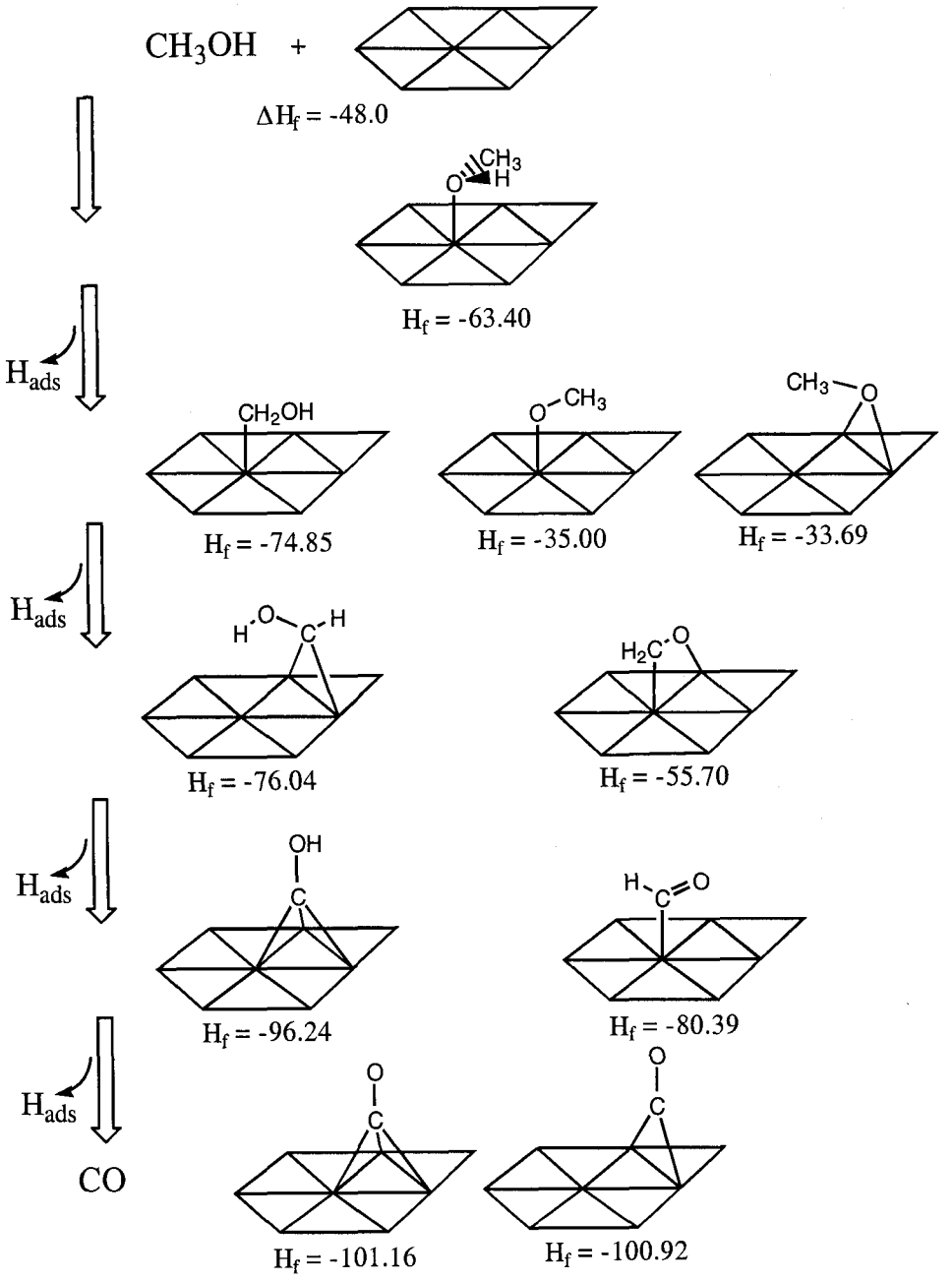

ΔH_f listed includes ΔH_f (H_{ads}) = -11.38 kcal/mol.

Figure 4-2. Low energy structures of CH_xO/Pt_8.

CH_3OH	CH_2OH	OCH_3 (top)	OCH_3 (bridge)
• Pt-O 2.36 Å • C-O 1.44 Å • C-O-Pt 119°	• Pt-C 2.13 Å • C-O 1.35 Å • O-C-Pt 113°	• Pt-O 1.99 Å • C-O-Pt plane 119°	• Pt-O 2.28 Å [2] • C-O-Pt plane 127°
CHOH	CH_2O	COH	CHO
• Pt-C 2.07 Å [2] • C-O 1.33 Å • O-C-Pt plane 120°	• Pt-C 2.06 Å • Pt-O 2.31 Å • C-O 1.35 Å • C-O bond twisted 28° to Pt-Pt bridge	• Pt-C 1.96 Å [3] • C-O 1.33 Å • H-O-C 110° (staggered)	• Pt-C 2.01 Å • C-O 1.18 Å • O-C-Pt 126° • H-C-Pt 107°
CO (cap)	CO (bridge)		
• Pt-C 2.09 Å [3] • C-O 1.18 Å	• Pt-C 2.00 Å [2] • C-O 1.17 Å		

[indicates number of equivalent bonds (all within 0.01 Å)]

Table 4-2. Selected geometric parameters of CH_xO/Pt_8.

Adsorbate on Pt_8	Spin	Site	Absolute Energy (hartree)	Binding Energy (kcal/mol)	δH_f (kcal/mol)
CH_3OH	3	top	-1069.00291	14.95	-63.40
OCH_3	7/2	top	-1068.35024	25.04	-23.62
OCH_3	7/2	bridge	-1068.34832	23.73	-22.31
CH_2OH	5/2	top	-1068.41374	65.65	-63.47
CH_2O	2	bridge	-1067.77583	9.62	-32.94
CHOH	2	bridge	-1067.80824	84.84	-53.28
CHO	5/2	top	-1067.20777	62.72	-46.25
COH	5/2	cap	-1067.23303	121.16	-62.10
CO	3	cap	-1066.63346	41.88	-55.64
CO	3	bridge	-1066.63308	41.64	-55.40
CO	3	top	-1066.60640	24.90	-38.66
H	5/2	cap	-953.86457	67.23	-11.38

Table 4-3. Calculated energies, heats of formation, and spin states of CH_xO/Pt_8.

Fragment	Spin	Absolute Energy (hartree)	Fragment	Spin	Absolute Energy (hartree)
CH_3OH	0	-115.72181	CHO	1/2	-113.85056
OCH_3	1/2	-115.05307	COH	1/2	-113.78269
CH_2OH (anti)	1/2	-115.05185	COH	3/2	-113.64311
CH_2O	0	-114.50324	CO	0	-113.30945
CHOH (trans)	0	-114.41578	H	1/2	-0.50027
CHOH (trans)	1	-114.37414			

Table 4-4. Optimized CH_xO ground spin states.

Figure 4-3 displays the heat of formation chart for this reaction. For Pt, in each step, dehydrogenation of methanol is exothermic all the way to formation of $(CO)_{ads}$. Indeed it is observed experimentally that CH_3OH rapidly dehydrogenates over Pt to form $(CO)_{ads}$.[16]

Stripping the hydrogens off the carbon leads to adsorbed intermediates that are more stable than losing the hydrogen off the oxygen. Thus, $(CH_2OH)_{ads}$ is more stable than $(OCH_3)_{ads}$, $(CHOH)_{ads}$ is more stable than $(CH_2O)_{ads}$, and $(COH)_{ads}$ is more stable than $(CHO)_{ads}$.

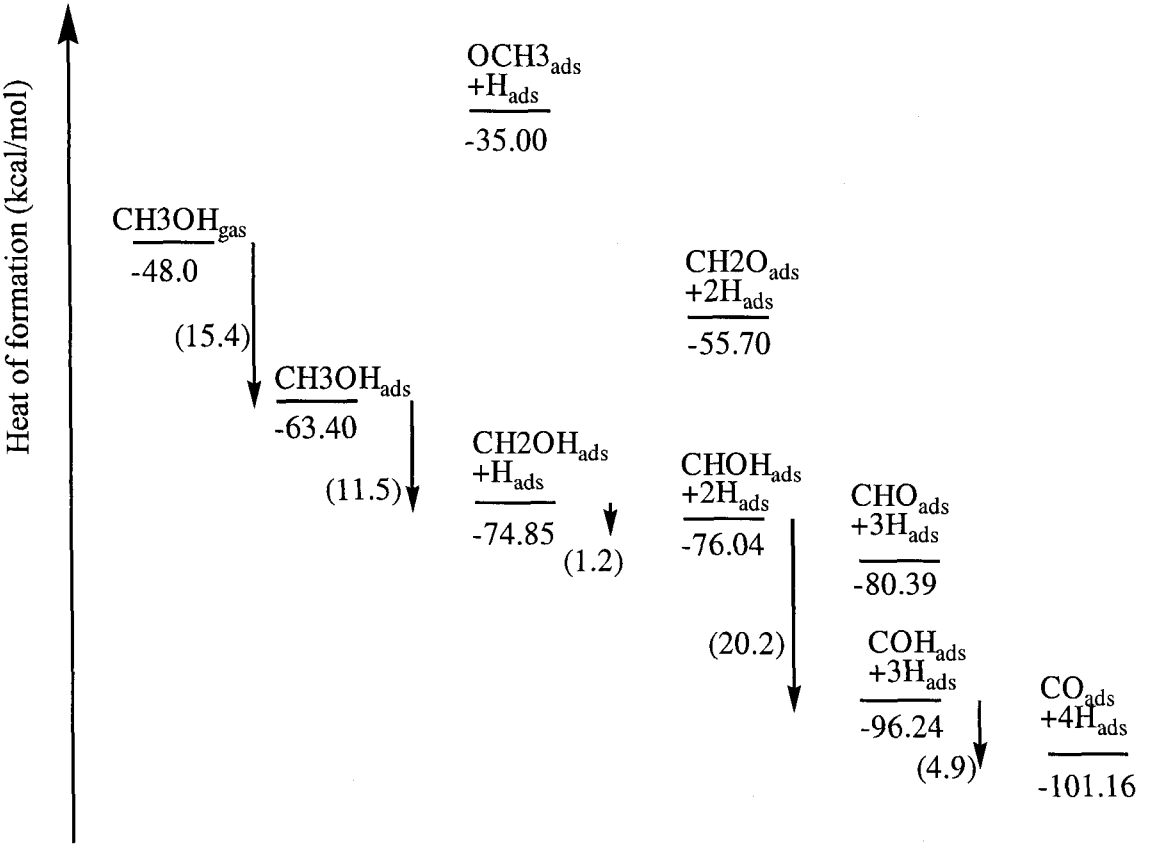

Figure 4-3. Heat of formation chart for methanol dehydrogenation on Pt.

We calculate that CH_3OH_{ads} prefers to bind to the on-top site via the oxygen lone pair of electrons. Thus, the COH plane is tilted by 61° from the perpendicular (a tetrahedral

lone pair would lead to 54.75°) and the Pt-O bond of 2.36 Å is longer than for $(OCH_3)_{ads}$, which is 1.99 Å. The calculated bond energy is 15.0 kcal/mol, which can be compared to the calculated bond energy of 16.0 kcal/mol for H_2O (same site). The experimental result for H_2O is 12 kcal/mol,[26] suggesting that our values are ~3 kcal/mol too strong (as expected by our neglect of zero point energy and vibrational enthalpy effects). The calculated energy leads to $\Delta H_f\ (CH_3OH)_{ads}$ = -63.40 kcal/mol.

We calculate that OCH_3 prefers the top site of Pt_8, leading to a covalent Pt-O bond length of 1.99 Å and a C-O-Pt angle of 119°. The bond energy is 25.04 kcal/mol, which is only 1.3 kcal/mol stronger than for the bridge site (which has a bond length 0.29 Å longer). The calculated energy leads to $\Delta H_f\ (OCH_3)_{ads}$ = -35.00 kcal/mol. This is 63.40 – 35.00 = 27.6 kcal/mol endothermic from $(CH_3OH)_{ads}$, making this an unlikely intermediate.

We calculate that CH_2OH has a bond energy of 65.7 kcal/mol to the on-top site with Pt-C 2.13 Å and a tilt angle to the surface of 68°. The Pt-C bond distance in $(CH_2OH)_{ads}$ is longer (2.13 Å) than in $(CH_3)_{ads}$ (2.07 Å), but the bond energy is 11.8 kcal/mol stronger. The increase in bond length might be due to steric interactions of the OH with the surface; we believe that the increase in bond strength must be an electronic effect (the OH polarizing the Pt-C bond to make it stronger). The energetics lead to $\Delta H_f\ (CH_2OH)_{ads}$ = -74.85 kcal/mol, making this process exothermic by 11.5 kcal/mol. Thus, forming $(CH_2OH)_{ads}$ is 40 kcal/mol more favorable than forming $(OCH_3)_{ads}$.

We have calculated the reaction path for dissociative chemisorption of CH_4 on Pt_8 to involve a transition state (see Appendix of Chapter 2) very similar to that found for CH_4

+ $Pt(PH_3)_2 \rightarrow Pt(CH_3)(H)(PH_3)_2$,[41] which leads to simultaneous formation of the Pt-H and Pt-C bonds. We believe that CH_3OH probably involves a similar transition state.

We calculate that CH_2O forms a di-σ bond to a bridge site with Pt-C 2.06 Å and Pt-O 2.01 Å. This is analogous to the di-σ bond of C_2H_4 to Pt_8. However, we find that di-σ CH_2O is bound by only 9.6 kcal/mol, whereas we find that di-σ $(C_2H_4)_{ads}$ binds by 36.1 kcal/mol, which is consistent with the most accurate experimental values ranging from 29.6 to 41.6 kcal/mol at low coverage using collision induced desorption (CID)[42] and microcalorimetry.[43] The weak bond of di-σ $(CH_2O)_{ads}$ is expected. Thus assuming a Pt-C bond strength of 48.6 kcal/mol (from C_2H_5/Pt_8, the calculated bond energy of 36.1 for di-σ $(C_2H_4)_{ads}$ suggests a C_2H_4 π bond of 2*48.6 – 36.1 = 61.1 kcal/mol, a plausible value (the rotational barrier in C_2H_4 is ~67 kcal/mol). Using bond energies of D_{Pt-C} = 65.7 (from CH_2OH/Pt_8) and D_{Pt-O} = 25.0 kcal/mol (from OCH_3/Pt_8), the di-σ $(CH_2O)_{ads}$ bond energy of 9.6 kcal/mol suggests a π bond for CH_2O of 65.7 + 25.0 – 9.6 = 81.1 kcal/mol, which is higher than the C_2H_4 π bond by 20 kcal/mol. These energetics lead to ΔH_f $(CH_2O)_{ads}$ = -55.70 kcal/mol, making this endothermic by 20 kcal/mol from $(CH_2OH)_{ads}$. However, CH_2O has been observed experimentally as one of the products of incomplete oxidation by *in situ* FTIR spectroscopy.[6]

We find that CHOH binds to a bridge site (just as for CH_2) leading to tetrahedral carbon. The calculated bond energy for $CHOH_{ads}$ is 20 kcal/mol more favorable than di-σ $(CH_2O)_{ads}$. The calculated Pt-C bond length is 2.07, which is 0.06 longer than for CH_2, a plausible steric effect of the OH. The CHOH plane is perpendicular to the surface. The calculated bond energy of 84.8 kcal/mol for $(CHOH)_{ads}$ is 19.5 kcal/mol weaker than for $(CH_2)_{ads}$. This might seem strange since replacing an H of $(CH_3)_{ads}$ with OH increased the

bond strength to the surface by 11.8 kcal/mol. However, the weaker CHOH bond is because the ground state of gas phase CHOH is the singlet state (a Fischer carbene) with a doubly occupied σ lone pair whereas the binding state to the surface requires the two singly occupied orbitals of the CHOH triplet state (which we calculate to be 26.1 kcal/mol above the gas phase singlet). Thus the bond energy of the triplet to the surface is 84.8 + 26.1 = 110.9 kcal/mol, which is 6.6 kcal/mol stronger than the bond energy of CH_2 (which has a triplet ground state). We refer to such a bond energy corrected to the proper dissociation product for forming the bond as a "snap bond energy." Here the geometry is optimized but the electronic state is fixed. This leads to $H_f(CHOH)_{ads}$ = 2*(-11.38) + 31.56 – 84.84 = -76.04 kcal/mol making formation of $(CHOH)_{ads}$ on the surface from $(CH_2OH)_{ads}$ exothermic by 1.19 kcal/mol.

We find that $(CHO)_{ads}$ prefers the on-top site, with a bond energy of 62.7 kcal/mol and a Pt-C bond length of 2.01 Å. Thus, ΔH_f $(CHO)_{ads}$ = -80.39 kcal/mol, which is 5 kcal/mol exothermic from $(CHOH)_{ads}$. We see below that forming $(COH)_{ads}$ is more exothermic by 21 kcal/mol. Even so, it is plausible that the O-H bond of $(CHOH)_{ads}$ might break first to form $(CHO)_{ads}$. This is because CHOH trans is structurally compatible with easy dehydrogenation from the oxygen, which might lead to a lower activation energy. Rearrangement to form the more stable $(COH)_{ads}$ could occur subsequently.

We find that COH binds to the cap site just as calculated for the analogous CH. The Pt-C bond lengths are similar, 1.96 and 1.95 Å respectively, showing the covalent character (the CO bond is perpendicular to the surface, just as is the CH bond). However, COH has a binding energy of 121.2 kcal/mol, much weaker than CH with binding energy

166.6 kcal/mol. This is expected since forming three covalent bonds to the Pt surface requires the three unpaired orbitals (σ, π_x, and π_y) of the quartet (S=3/2) state of CH or COH, whereas the ground state is the doublet state (S=1/2) with one unpaired π orbital. The adiabatic excitation energies from the S=1/2 to the S=3/2 states are calculated to be 87.6 (COH) and 19.7 kcal/mol (CH), respectively. This leads to a "snap" binding energy of 208.8 kcal/mol for COH and 186.3 kcal/mol for CH. Thus OH strengthens the surface bond of CX by 22.5 kcal/mol, compared to 6.8 for CHX and 11.8 for CH_2X. The calculated energy leads to $\Delta H_f\,(COH)_{ads}$ = -96.24 kcal/mol which is 21 kcal/mol exothermic from $(CHOH)_{ads}$, making $(COH)_{ads}$ a likely intermediate.

Our calculations indicate that CO binds strongest to the cap site with the bridge site only 2.4 kcal/mol higher. We calculate the binding energy for $(CO)_{ads}$ to be 41.9 kcal/mol which compares well with the best experimental values of 43 kcal/mol.[27] The Pt-C bond length is calculated to be 2.09 Å, compared to 1.96 Å for $(COH)_{ads}$. The CO bond distance of $(CO)_{ads}$ is 1.18 Å, which is 0.04 Å longer than for $(CO)_{gas}$ and 0.15 Å shorter than for $(COH)_{ads}$. Since $\Delta H_f\,(CO)_{ads}$ = -101.16 kcal/mol, losing the last H from $(COH)_{ads}$ is exothermic by 101.2 - 96.2 = 5.0 kcal/mol, making $(CO)_{ads}$ the thermodynamic sink in this reaction.

4-3-3. CO/M(111): Comparing Computational and Experimental Results

Early experiments for CO on Pt(111) using temperature programmed desorption (TPD)[44] reported a binding energy of 35 kcal/mol. Recent experiments using microcalorimetry[27] report a value of 43 kcal/mol for low coverage, which drops to a steady state value of 28 kcal/mol for half monolayer coverage, and finally to 16 kcal/mol

at high coverage. This low coverage value of 43 kcal/mol is in good agreement with the calculated value of 41.9 kcal/mol.

From slab calculations, Norskov and co-workers suggest the heat of adsorption of CO can be related to the position of the d-band of the Pt atop-atom relative to the Fermi energy.[34] Bonding arises from the interaction between the metal d states and the CO $2\pi^*$ and 5σ states. In addition, renormalization of the CO states arises via interaction between half-filled s-bands at the Pt(111) surface. The s^1d^9 configuration of our cluster also corresponds to a half-filled s-band. Our model suggests that the interstitial orbitals are very stable, and hence the density of electrons in the s-band is primarily at the base of the band. Although s-d mixing is present in our cluster, it does not form an s-band as diffuse as found in the slab calculations, which correspondingly changes the renormalization effect. It has been suggested that M_n clusters (where $n > 6$) show metallic character in the density of states. Dumesic and co-workers, studying CO binding to a Pt_{10} cluster, have compared the density of states to Norskov's slab calculations and concluded that the source of bonding is quite similar.

The differences in binding energies due to computational methodology (basis sets, density functionals, slab thickness, size of cluster) have not been directly compared. However, the two different experimental numbers for CO adsorption correspond well to the two different numbers obtained by the slab and cluster approaches. The TPD result (35 kcal/mol) corresponds to the high coverage situation of the $c(4 \times 2)$ unit cell. The calculated slab binding energy with a $p(2 \times 2)$ unit cell of 34 kcal/mol matches this number. The cluster calculations on the other hand match the low coverage value that comes from the initial heat of adsorption measured by microcalorimetry.

For CO/Pd(111) no microcalorimetry has been reported, but TPD data[45-47] lead to 30-35 kcal/mol. A very recent slab calculation[48] at two different coverages on Pd(111) gives 33 kcal/mol for the c(2 × 2) structure [higher coverage] and 46 kcal/mol for the c($\sqrt{3}$ × $\sqrt{3}$) structure [lower coverage]. Our calculated binding energy for CO/Pd_8 is 49 kcal/mol, in reasonable agreement with the low coverage value.

For CO/Rh(111) no microcalorimetry has been reported. However a very recent slab calculation,[49] at a lower coverage of p(3 × 3), gives 41 kcal/mol, close to our calculated cluster number of 39 kcal/mol. Here TPD data[47,50] lead to 31-32 kcal/mol.

We have not found microcalorimetry or slab calculations for the CO/Ru(0001) system. We do note that TPD[47,51] suggests a wide range of values from 28 to 38 kcal/mol. Our calculated number of 26 kcal/mol is at the lower end of this range, which may suggest that our bond energy for CO/Ru(0001) is too low by up to 10 kcal/mol. If our calculated numbers for Ru are on the low side (due to the basis set, the cluster, or the DFT functionals), this difference is expected to be *systematic* across all the Ru numbers. This will *not* change the conclusions since the relative numbers remain the same.

Summarizing, the experimental TPD numbers correspond to higher coverage conditions while our cluster numbers correspond to low coverage. Where available our results are confirmed by low coverage experiment or low coverage slab calculations.

Experimental studies of binding site have mainly used low energy electron diffraction (LEED),[52] infrared reflection absorption spectroscopy (IRAS),[53] scanning tunneling microscopy (STM),[54] and sum frequency generation.[55] These experiments are generally interpreted in terms of CO chemisorbed mainly at on-top sites at low coverage, and on

both on-top and bridge sites at higher coverages. However, there are no direct experimental results on the structure for the lowest coverages.

Slab calculations have only investigated bonding of CO to the on-top site. The difference we calculate between these sites (16.9 kcal/mol) seems rather large. Dumesic and co-workers also find a large difference (15.5 kcal/mol). Although the numbers match closely, their cluster does not have a net s^1d^9 configuration and is not optimized for spin. They have only investigated edge site terminal binding of CO. We could find no experimental evidence at low temperatures quantifying energetic site preference of CO on Pt(111), although it is commonly believed that the energy gap should be smaller. It would be useful to further investigate these effects by performing slab calculations with similar functionals and basis sets for direct comparison with the cluster calculations.

Using *in situ* FTIR and electrochemical mass spectrometry, Munk *et al.*[16] suggest that linearly bonded CO is formed initially at terrace sites on 15 nm Pt particles that subsequently migrate to edge or kink sites with increasing potential. The vacancies are then filled up by the transformation of singly bonded CO to triply bonded CO (in the threefold site). This migration was also observed on bulk polycrystalline metal, but with less pronounced effects since the relative terrace areas are larger.

We interpret these results as follows. At high coverage usually used in experimental studies of structure and specific binding site, packing effects lead to on-top binding of CO, but at low coverage the strongest bond is to cap sites (as in our calculations). Thus removing sufficient CO from a saturated terrace allows the remaining adsorbed CO to change from on-top to cap. (We calculate the bridge site to be 0.24 kcal/mol higher than the cap and the on-top site to be 16.9 kcal/mol higher.)

4-3-4. Dehydrogenation of Water on Pt

Complete dehydrogenation of water yields atomic O_{ads} and two H_{ads}. The adsorbate structures are shown in Figure 4-4 (selected geometric parameters in Table 4-5). The spin state, site preference, total energy and binding energy for each of the intermediates are listed in Table 4-6. Binding energies are calculated with respect to the naked Pt_8 (S=3) cluster and the optimized OH_x fragments listed in Table 4-7.

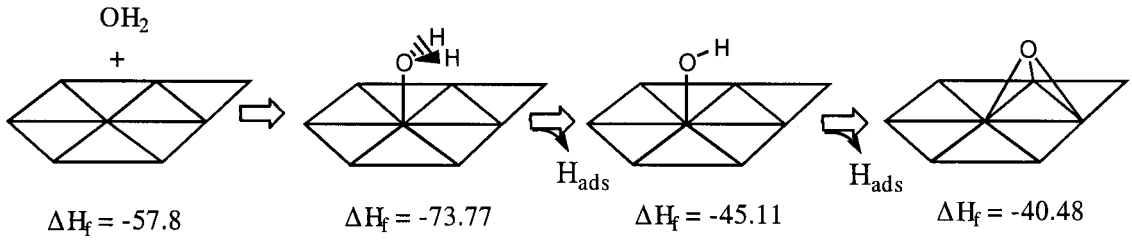

ΔH_f listed includes ΔH_f (H_{ads}) = -11.38 kcal/mol

Figure 4-4. Low energy structures of OH_x/Pt_8.

OH_2	OH	O
• Pt-O 2.35 Å • O-H 0.973 Å [2] • H-O-H 105° • tilt of H_2O plane to perpendicular 81°	• Pt-O 1.97 Å • O-H 0.975 Å • H-O-Pt 103°	• Pt-O 1.96 Å [3]

[indicates number of equivalent bonds (all within 0.01 Å)]

Table 4-5. Selected geometric parameters of OH_x/Pt_8.

Adsorbate on Pt_8	Spin	Site	Absolute Energy (hartree)	Binding Energy (kcal/mol)	ΔH_f (kcal/mol)
OH_2	3	top	-1029.70244	15.99	-73.77
OH	7/2	top	-1029.04937	40.79	-33.73
OH	7/2	bridge	-1029.04934	40.77	-33.71
O	2	cap	-1028.43458	74.56	-17.72

Table 4-6. Calculated energies, heats of formation, and spin states of OH_x/Pt_8.

Fragment	Spin	Absolute Energy (hartree)
OH_2	0	-76.41973
OH	1/2	-75.72712
O	1	-75.05850

Table 4-7. Optimized OH_x ground spin states.

The heat of formation for each of the Pt_8-OH_x clusters is calculated according to the same scheme as used above for the CH_xO adsorbates. The corrected heats of formation are given in Table 4-6. As above, we use ΔH_f (H_{ads}) = -11.38 kcal/mol. From the heat of formation chart (Figure 4-5), we see that dehydrogenation of water on Pt_8 is thermodynamically uphill by 28.7 kcal/mol for $(H_2O)_{ads} \rightarrow H_{ads} + (OH)_{ads}$. This is consistent with experiment since electrochemical experiments show that pure Pt decomposes water only at a high potential of 0.8 V versus RHE.

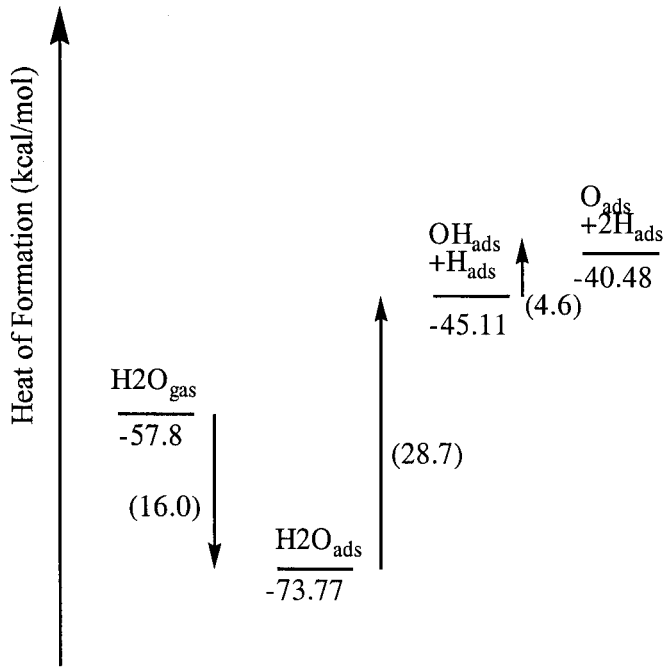

Figure 4-5. Heat of formation chart for water dehydrogenation on Pt.

We find that H_2O prefers the on-top site with a Pt-O bond length of 2.35 Å (cf. 2.36 Å for CH_3OH) and a tilt angle of 81° with respect to the vertical (cf. 61° for CH_3OH). Our calculated binding energy of 16.0 kcal/mol is comparable to the experimental adsorption energy of 12 kcal/mol.[26]

For Ru, we calculate the adsorption energy of H_2O to be 4 kcal/mol. This compares with the TPD experimental number of 12 kcal/mol.[53] This coincides with Pt where the TPD result is also 12 kcal/mol. We believe that the discrepancy for Ru may be because some amount of water dissociation takes place on Ru. Our calculations suggest that thermodynamics favors this by an additional 8 kcal/mol (see Section 4-4-2 and Figure 4-9). [This is not expected in Pt since the process is endothermic.] For high coverage conversion to multilayers of H_2O, TPD indicates a bond energy of 11.5 kcal/mol for Ru[53] and 12 kcal/mol for Pt.[26] We expect the multilayer ice peaks to appear in the same temperature range for both Ru and Pt. The energy should be ~12 kcal/mol since this is the heat of sublimation for normal ice.

We find that OH binds to the on-top site with a bond distance of 1.97 Å and a H-O-Pt angle of 103°. Our calculated binding energy is 40.8 kcal/mol, which compares to the experimental value of 47 kcal/mol.[28] Thus we calculate that forming $(OH)_{ads}$ from $(H_2O)_{ads}$ is endothermic by 28.7 kcal/mol.

We find that O binds to the cap site with a Pt-O bond distance of 1.96 Å. Our calculated binding energy is 74.6 kcal/mol, which compares to experimental values in the range of 40 to 110 kcal/mol.[56] Since OH bonds to Pt with a bond energy of 40.8 kcal/mol, one might expect O_{ads} to have a bond energy of 81.6 kcal/mol. However, as discussed by Harding and Goddard,[57] the first bond to an O atom is weakened by ~8

kcal/mol because of loss of intra-atomic exchange (e.g., The first bond of H to O is 111 kcal/mol whereas the second is 119 kcal/mol). Thus it is plausible that the O bond to Pt is 7 kcal/mol weaker than twice that of OH.

First principles computational work in this area includes studying the binding of these species on Pt_4 and Pt_6 clusters (using non-local DFT). The calculated binding energies of H_2O, OH and O are 8, 53 and 65 kcal/mol respectively in sites similar to our calculation.[58] Using non-local DFT with a triple-ζ basis set and a larger Pt_{10} cluster, O in the 3-fold site was calculated to have an adsorption energy of 66 kcal/mol.[59]

4-3-5. Other Intermediates

For the Pt_8 cluster, we find that COOH binds strongly (63.5 kcal/mol) but HCOOH weakly (8 kcal/mol through the oxygen lone pair), and no surface bond for CO_2. In Section 4-3-2, we find that bridged CHOH binds 19.5 kcal/mol weaker than bridged CH_2. Thus, the effect of replacing H with an OH substituent is to reduce the surface bond energy by ~20 kcal/mol. Comparing the binding of CH_2O and HCOOH, we would expect the binding energy of HCOOH to be ~20 kcal/mol weaker. Since the binding energy of di-σ CH_2O is 9.6 kcal/mol, di-σ HCOOH is not expected to bind.

We find that formic acid, HCOOH, bonds through the carbonyl oxygen at the on-top site (Pt-O 2.36 Å; C-O-Pt angle of 121°) by 8 kcal/mol. However, it does not form a π bond like $(CH_2O)_{ads}$. To make the π bond requires that the COO plane be parallel to the surface which apparently causes steric interactions of the OH with the surface that are too large given the small value (~10 kcal/mol) expected for the bond.

Removing the H from HCOOH leads to $(COOH)_{ads}$ which bonds by 63.5 kcal/mol with a Pt-C bond length of 2.06 Å. This can be compared to 62.7 kcal/mol and 2.01 Å for $(CHO)_{ads}$.

Another important intermediate is the carbene $C(OH)_2$ which bonds to the on-top site by 72.9 kcal/mol with a Pt-C bond length of 1.92 Å. The bridge bond (Pt-C 2.23 Å) is less stable by 9.7 kcal/mol. For $(CH_2)_{ads}$, the bridge site is favored over the on-top site by 104.3 – 78.1 = 26.2 kcal/mol. For $(CHOH)_{ads}$, the bridge site is favored by only 84.8 - 79.7 = 5.1 kcal/mol. Hence, the effect of replacing H with an OH substituent is to stabilize the on-top site by 21.1 kcal/mol with respect to the bridge site. Thus, for the carbene $[C(OH)_2]_{ads}$ we expect the on-top site to be favored over the bridge site since CHOH at the bridge site is only 5.1 kcal/mol favored over the on-top site.

The results for these species are tabulated in Tables 4-8a and 4-8b.

Adsorbate on Pt_8	Spin	Site	Absolute Energy (hartree)	Binding Energy (kcal/mol)	δH_f (kcal/mol)
HCOOH	3	top[a]	-1143.03171	7.65	-94.89
$C(OH)_2$	2	top	-1143.06235	72.85	-119.25
COOH	5/2	top	-1142.45250	63.49	-106.28
CO_2	3	top	-1141.83841[b]	0.00	-90.70

[a] Carbonyl oxygen to surface.

[b] Addition of calculated total energies of fragment and Pt_8 (S=3).

Table 4-8a. Calculated energies, heats of formation, and spin states of CO_2H_x/Pt_8.

Fragment	Spin	Absolute Energy (hartree)
HCOOH (H-trans)	0	-189.76227
COOH (trans)	1/2	-189.09406
CO_2	0	-188.58115
$C(OH)_2$	0	-189.68909

Table 4-8b. Optimized CO_2H_x ground spin states.

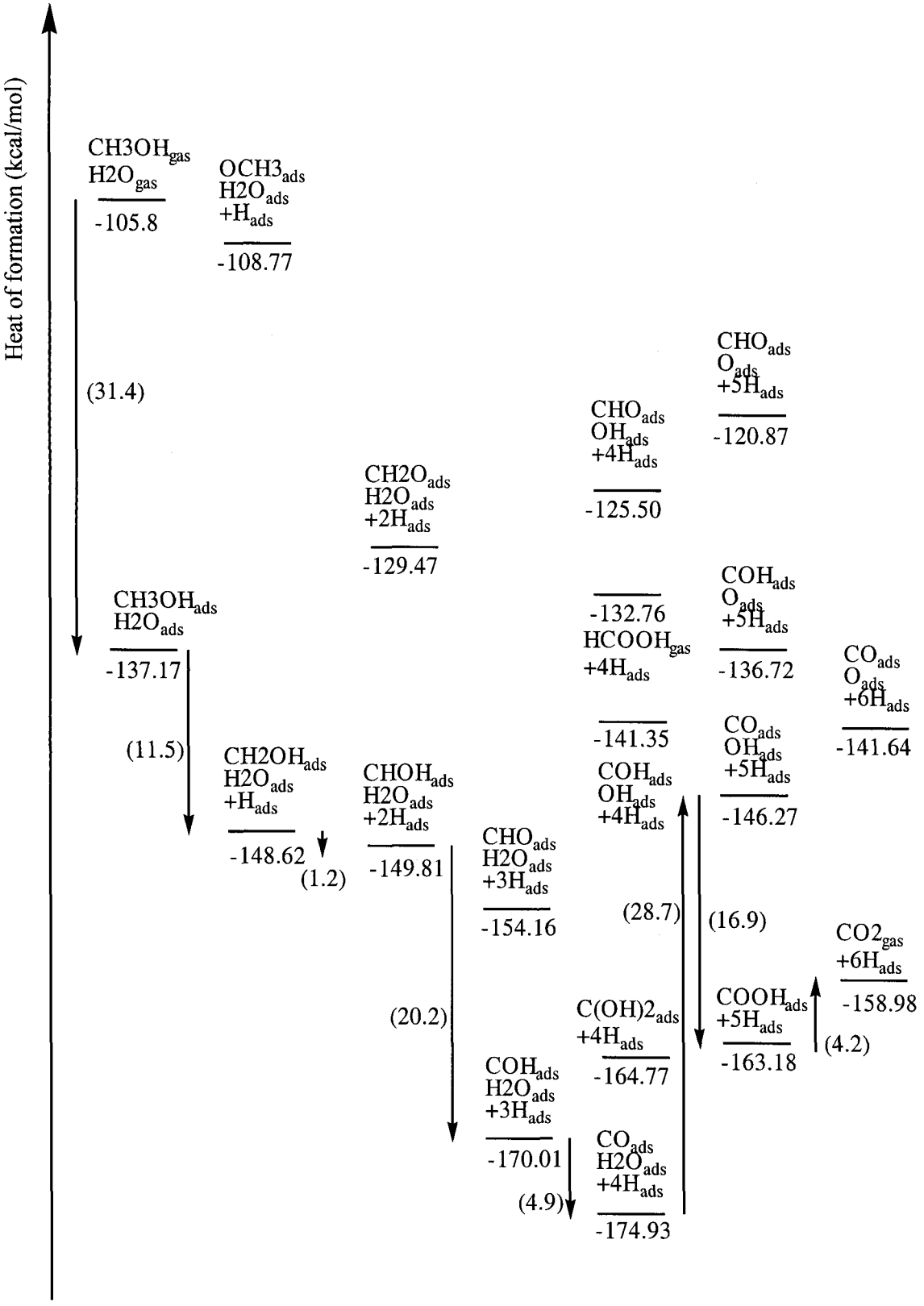

Figure 4-6. Combined heat of formation chart for methanol oxidation on Pt.

4-3-6. Combined Dehydrogenation and Oxidation on Pt

To examine the entire process, we combine the separate heat of formation charts (Figures 4-3 and 4-5) into one chart, with the addition of species that have formed the second C-O bond. Figure 4-6 shows the combined heat of formation chart. Compounds in the same *vertical column* are isomers.

The first half of the pathway in Figure 4-6 suggests facile dehydrogenation of CH_3OH from the carbon end to yield first $(COH)_{ads}$ and then $(CO)_{ads}$. In the second half, we see that dehydrogenating water from the thermodynamic sink of $(CO)_{ads} + (OH_2)_{ads} + 4H_{ads}$ (ΔH_f = -174.93 kcal/mol) to OH_{ads} is 28.7 kcal/mol uphill, and further dehydrogenation to O_{ads} requires another 4.6 kcal/mol. Directly transforming to $(COOH)_{ads} + 5H_{ads}$ (ΔH_f = -163.18 kcal/mol) from the thermodynamic sink via simultaneous dehydrogenation and C-O bond formation would be uphill 11.8 kcal/mol.

COOH
• Pt-C 2.06 Å
• C=O 1.19 Å, O-C-Pt 120°
• C-O 1.32 Å, O=C-Pt 115°

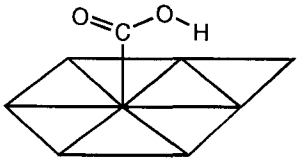

Figure 4-7. Structure of $COOH/Pt_8$.

Subsequent dehydrogenation of $(COOH)_{ads}$ to desorb CO_2 from the surface is expected to have a low barrier reaction because COOH is structurally compatible for the dehydrogenation (see Figure 4-7) [we calculate a barrier of 10 kcal/mol]. Thus, we conclude that $(CO)_{ads} + (OH)_{ads}$ would combine to form $(COOH)_{ads}$ in a reaction downhill by 16.9 kcal/mol. Consequently, we do not expect the reaction to go through both $(CO)_{ads} + O_{ads}$ species. Due to the high potential required to dehydrogenate water on platinum, it has been suggested that the oxygen-active species is "activated" water. Our results

suggest that this "active water" is $(OH)_{ads}$. This would subsequently form the second C-O bond which is less favorable thermodynamically than forming $(COOH)_{ads}$ directly from $(CO)_{ads}$ and $(OH_2)_{ads}$.

Forming the second C-O bond from $(COH)_{ads}$ and $(OH)_{ads}$ leads to $[C(OH)_2]_{ads}$ (ΔH_f = -164.77 kcal/mol). This species could then easily dehydrogenate to form $(COOH)_{ads}$ (ΔH_f = -163.18 kcal/mol) and H_{ads}, which is enothermic by 0.4 kcal/mol. However, starting from $(COH)_{ads}$ + $(H_2O)_{ads}$ the reaction has to go uphill 28.7 kcal/mol to first form $(COH)_{ads}$ + $(OH)_{ads}$ (ΔH_f = -141.35 kcal/mol) before forming $[C(OH)_2]_{ads}$. Since stripping of the hydrogens from methanol is facile on Pt, it is more likely that $(COH)_{ads}$ dehydrogenates to $(CO)_{ads}$ (downhill 4.9 kcal/mol) leading to the pathway discussed above that bypasses the formation of $[C(OH)_2]_{ads}$.

4-4. Methanol Oxidation on Second and Third Row Group VIII Transition Metals

The favorable methanol activation processes observed for transition metal alloys (both the familiar Pt-Ru and the recent ternary/quaternary systems involving Ir and Os) suggested that we investigate the various intermediates for methanol oxidation on Pt, Ir, Os, Pd, Rh, and Ru. Thus, we calculated the optimum structures and energetics of the intermediate species on a M_8 cluster using bulk M-M distances. As before, we considered three parts to the reaction: (1) methanol dehydrogenation, (2) water dehydrogenation, and (3) oxidation via formation of the second C-O bond. Heats of formation were calculated using the same scheme as for Pt using a uniform correction of ΔH_f (H_{ads}) = -11.38 kcal/mol. Heat of formation values for methanol dehydrogenation,

water dehydrogenation, and the combined values, for all six metals, are shown in Tables 4-9, 4-10 and 4-11 respectively.

The spin state, site preference, total energy and binding energy for each of the intermediates on the other five M_8 clusters is given in Tables 4-12 to 4-16. In general, there is not much difference in binding site across the metals except for $(CO)_{ads}$. We find that Pt, Pd, Rh, Ru prefer CO in the cap site, Ir in the bridge site, and Os in the top site. Our calculations find that HCOOH bonds only to Pt (7.95 kcal/mol), Ir (4.0 kcal/mol), and Rh (9.4 kcal/mol) while CO_2 does not bind to any of the metals. OCH_3 binds most strongly to the on-top site in all metals except Pd where it prefers the cap site. $(CH_3OH)_{ads} \rightarrow (CH_2O)_{ads} + 2H_{ads}$ is downhill by 10 kcal/mol for Os, 8 for Ir, and 4 for Ru, Rh, Pd, but uphill by 8 kcal/mol for Pt. Di-σ CH_2O is favorable over CHOH by 11 kcal/mol for Rh and 2 kcal/mol for Ru, but is disfavored by 20 kcal/mol for Pt.

Adsorbate	Pt_8	Ir_8	Os_8	Pd_8	Rh_8	Ru_8
CH_3OH	-63.40	-57.53	-51.69	-54.77	-63.72	-54.03
OCH_3	-35.00	-42.46	-46.11	-49.73	-45.13	-42.98
CH_2OH	-74.85	-65.17	-60.01	-60.08	-65.61	-56.29
CH_2O	-55.70	-65.47	-61.93	-57.92	-68.10	-58.24
CHOH	-76.04	-72.70	-64.03	-74.17	-57.01	-55.92
CHO	-80.39	-78.23	-72.25	-67.33	-82.14	-61.67
COH	-96.24	-88.98	-74.10	-75.18	-81.78	-71.45
CO	-101.16	-96.92	-93.81	-108.73	-99.23	-85.53

Table 4-9. Heats of formation (kcal/mol) for methanol dehydrogenation on all six metals.

Adsorbate	Pt_8	Ir_8	Os_8	Pd_8	Rh_8	Ru_8
OH_2	-73.77	-67.78	-63.56	-66.11	-69.47	-61.70
OH	-45.11	-42.99	-55.69	-51.22	-44.63	-53.63
O	-40.48	-57.59	-56.87	-52.50	-58.15	-69.92

Table 4-10. Heats of formation (kcal/mol) for water dehydrogenation on all six metals.

Adsorbate	Pt_8	Ir_8	Os_8	Pd_8	Rh_8	Ru_8
$[CH_3OH]_g + [OH_2]_g$	-105.8	-105.8	-105.8	-105.8	-105.8	-105.8
$CH_3OH + OH_2$	-137.17	-125.31	-115.25	-120.88	-133.19	-115.73
$OCH3 + OH_2 + H$	-108.77	-110.24	-109.67	-115.84	-114.60	-104.68
$CH_2OH + OH_2 + H$	-148.62	-132.95	-123.57	-126.19	-135.08	-117.99
$CH_2O + OH_2 + 2H$	-129.47	-133.25	-125.49	-124.03	-137.57	-119.94
$CHOH + OH_2 + 2H$	-149.81	-140.48	-127.59	-140.28	-126.48	-117.62
$CHO + OH_2 + 3H$	-154.16	-146.01	-135.81	-133.44	-151.61	-123.37
$COH + OH_2 + 3H$	-170.01	-156.76	-137.66	-141.29	-151.25	-133.15
$CHO + OH + 4H$	-125.50	-121.22	-127.94	-118.55	-126.77	-115.30
$[HCOOH]_g + 4H$	-136.72[a]	-136.72[a]	-132.76	-132.76	-132.76[a]	-132.76
$COH + OH + 4H$	-141.35	-131.97	-129.79	-126.40	-126.41	-125.08
$C(OH)_2 + 4H$	-164.77	-162.95	-159.16	-151.79	-151.83	-146.83
$CO + OH_2 + 4H$	-174.93	-164.70	-157.37	-174.84	-168.70	-147.23
$CHO + O + 5H$	-120.87	-135.82	-129.12	-119.83	-140.29	-131.59
$COH + O + 5H$	-136.72	-146.57	-130.97	-127.68	-139.93	-141.37
$CO + OH + 5H$	-146.27	-139.91	-149.50	-159.95	-143.86	-139.16
$COOH + 5H$	-163.18	-160.91	-160.09	-156.97	-168.33	-157.57
$CO + O + 6H$	-141.64	-154.51	-150.68	-161.23	-157.38	-155.45
$[CO_2]_g + 6H$	-158.98	-158.98	-158.98	-158.98	-158.98	-158.98

[a] $\Delta H_f[(HCOOH)_{ads}]$ is -140.41, -136.72, and 142.17 kcal/mol for carbonyl oxygen bound to on-top Pt, Ir and Rh.

Table 4-11. Combined heat of formation values (kcal/mol) on all six metals.

Adsorbate on Ir_8	Spin & site	Absolute energy (hartree)	Binding energy (kcal/mol)	Selected bond distances (Å)
CH_3OH	S=7; top	-953.14230	9.08	Ir-O 2.50; C-O 1.43
OCH_3	S=15/2; top	-952.51087	32.50	Ir-O 1.98; C-O 1.40
CH_2OH	S=13/2; top	-952.54707	55.98	Ir-C 2.09; C-O 1.40
CH_2O	S=6; bridge	-951.94014	19.39	Ir-C 2.06; C-O 1.43; Ir-O 2.01
CHOH	S=6; bridge	-951.95167	81.50	Ir-C 2.10; C-O 1.35
CHO	S=13/2; top	-951.35307	60.55	Ir-C 2.00; C=O 1.20
COH	S=13/2;cap	-951.37020	113.89	Ir-C 1.97; C-O 1.34
CO	S=7; bridge	-950.77545	37.63	Ir-C 2.01; C=O 1.18
OH_2	S=7; top	-913.84164	9.98	Ir-O 2.44
OH	S=15/2; top	-913.20367	44.26	Ir-O 1.98
O	S=7; cap	-912.61059	91.66	Ir-O 1.96
HCOOH	S=7; top	-1027.17460	3.96	Ir-O 2.47
$C(OH)_2$	S=13; top	-1027.20829	71.03	Ir-C 1.95
COOH	S=13/2; top	-1026.60092	63.28	Ir-C 1.99; C=O 1.22; C-O 1.33

Table 4-12. Calculated energies, spin states, and structural information for CH_xO_y and OH_x on Ir_8.

Adsorbate on Os_8	Spin & site	Absolute energy (hartree)	Binding energy (kcal/mol)	Selected bond distances (Å)
CH_3OH	S=11; top	-843.73641	3.25	Os-O 2.64; C-O 1.43
OCH_3	S=21/2; top	-843.12011	36.16	Os-O 1.99; C-O 1.41
CH_2OH	S=13/2; top	-843.14226	50.83	Os-C 2.12; C-O 1.41
CH_2O	S=10;bridge	-842.53790	15.85	Os-C 2.11; C-O 1.43; Os-O 2.03
CHOH	S=10;bridge	-842.54126	72.83	Os-C 2.12; C-O 1.36
CHO	S=21/2; top	-841.94694	54.57	Os-C 2.00; C=O 1.23
COH	S=21/2; cap	-841.94989	99.01	Os-C 2.02; C-O 1.35
CO	S=9; top	-841.37389	34.53	Os-C 1.84; C=O 1.16
OH_2	S=11; top	-804.43832	5.76	Os-O 2.52
OH	S=21/2; top	-803.81837	51.35	Os-O 2.00
O	S=10; cap	-803.21285	90.94	Os-O 1.99
$C(OH)_2$	S=10	-917.80565	67.24	Os-C 1.99
COOH	S=21/2; top	-917.19973	60.40	Os-C 2.03; C=O 1.23; C-O 1.34

Table 4-13. Calculated energies, spin states, and structural information for CH_xO_y and OH_x on Os_8.

Adsorbate on Pd_8	Spin & Site	Absolute Energy (hartree)	Binding Energy (kcal/mol)	Selected Bond Distances (Å)
CH_3OH	S=1; top	-1129.71756	6.32	Pd-O 2.35; C-O 1.44
OCH_3	S=3/2; cap	-1129.10213	39.78	Pd-O 2.12; C-O 1.43
CH_2OH	S=1/2; top	-1129.11862	50.89	Pd-C 2.04; C-O 1.38
CH_2O	S=1; bridge	-1128.50777	11.84	Pd-C 2.07; C-O 1.34; Pd-O 2.00
CHOH	S=1; bridge	-1128.53366	82.97	Pd-C 2.05; C-O 1.34
CHO	S=1/2; top	-1127.91536	49.65	Pd-C 1.95; C=O 1.20
COH	S=3/2; cap	-1127.95006	114.02	Pd-C 1.95; C-O 1.32
CO	S=1; cap	-1127.37392	49.45	Pd-C 2.05; C=O 1.18
OH_2	S=1; top	-1090.41864	8.31	Pd-O 2.30
OH	S=3/2; top	-1089.78751	46.89	Pd-O 1.92
O	S=1; cap	-1089.18215	86.58	Pd-O 1.95
$C(OH)_2$	S=1; top	-1203.77017	59.88	Pd-C 1.90
COOH	S=1/2; top	-1203.17102	57.29	Pd-C 1.94; C=O 1.22; C-O 1.33

Table 4-14. Calculated energies, spin states, and structural information for CH_xO_y and OH_x on Pd_8.

Adsorbate on Rh_8	Spin & Site	Absolute Energy (hartree)	Binding Energy (kcal/mol)	Selected Bond Distances (Å)
CH_3OH	S=7; top	-991.73339	15.28	Rh-O 2.51; C-O 1.43
OCH_3	S=15/2; top	-991.09636	35.18	Rh-O 2.05; C-O 1.40
CH_2OH	S=13/2; top	-991.12899	56.42	Rh-C 2.03; C-O 1.43
CH_2O	S=6; bridge	-990.52555	22.02	Rh-C 2.05; C-O 1.39; Rh-O 1.99
CHOH	S=6; bridge	-990.50788	65.82	Rh-C 2.03; C-O 1.36
CHO	S=13/2; top	-989.94052	64.67	Rh-C 1.91; C=O 1.23
COH	S=13/2; cap	-989.93994	106.69	Rh-C 1.96; C-O 1.34
CO	S=7; cap	-989.36035	39.96	Rh-C 2.06; C=O 1.19
OH_2	S=6; top	-951.42555	11.67	Rh-O 2.49
OH	S=15/2; top	-951.77857	40.30	Rh-O 2.02
O	S=6; cap	-951.19270	92.23	Rh-O 1.95
$C(OH)_2$	S=6; top	-1065.77179	59.91	Rh-C 1.91
COOH	S=13/2; top	-1065.19068	68.85	Rh-C 1.94; C=O 1.24; C-O 1.34

Table 4-15. Calculated energies, spin states, and structural information for CH_xO_y and OH_x on Rh_8.

Adsorbate on Ru_8	Spin & Site	Absolute Energy (hartree)	Binding Energy (kcal/mol)	Selected Bond Distances (Å)
CH_3OH	S=11; top	-866.56537	5.59	Ru-O 2.73; C-O 1.43
OCH_3	S=21/2; top	-865.94035	33.03	Ru-O 1.94; C-O 1.41
CH_2OH	S=21/2; top	-865.96155	47.10	Ru-C 2.08; C-O 1.43
CH_2O	S=10;bridge	-865.35726	12.16	Ru-C 2.12; C-O 1.39; Ru-O 1.95
CHOH	S=10;bridge	-865.35357	64.72	Ru-C 2.09; C-O 1.36
CHO	S=21/2; top	-864.75542	44.06	Ru-C 1.98; C=O 1.22
COH	S=21/2; cap	-864.77091	96.37	Ru-C 1.99; C-O 1.35
CO	S=10; cap	-864.18593	26.25	Ru-C 2.10; C=O 1.20
OH_2	S=11; top	-827.26060	3.91	Ru-O 2.75
OH	S=23/2; top	-826.64033	49.30	Ru-O 2.00
O	S=10; cap	-826.05888	104.00	Ru-O 1.96
$C(OH)_2$	S=10; top	-940.61125	54.92	Ru-C 1.97
COOH	S=21/2; top	-940.02096	57.89	Ru-C 1.99; C=O 1.24; C-O 1.34

Table 4-16. Calculated energies, spin states, and structural information for CH_xO_y and OH_x on Ru_8.

4-4-1. Methanol Dehydrogenation

The heat of formation chart of methanol dehydrogenation for all six metals is shown in Figure 4-8. Only the most stable isomers are shown. Quantitative details are shown in Table 4-9. Overall, Pt is the most favorable for methanol dehydrogenation since its intermediate adsorbed species are generally more stable than for the other metals. The least favorable pathway is for Ru, which has a roughly flat energy curve for the initial dehydrogenation and goes downhill only to lose the third and fourth hydrogen. This suggests that Ru is a poor metal for stripping hydrogens off the carbon in methanol. Thus it is not surprising that pure Ru leads to a dead catalyst for methanol oxidation. Intermediate to Pt and Ru for methanol dehydrogenation are Ir, Pd and Rh. All three follow a basic downhill trend for methanol dehydrogenation with a similar general pathway. Notable differences are that Rh prefers $(CH_2O)_{ads}$ over $(CHOH)_{ads}$, Pd makes

$(CHO)_{ads}$ to be uphill from $(CHOH)_{ads}$, while $(COH)_{ads}$ follows the general downhill trend, and Os has a rather shallow curve for initial dehydrogenation (similar to Ru) but still goes downhill.

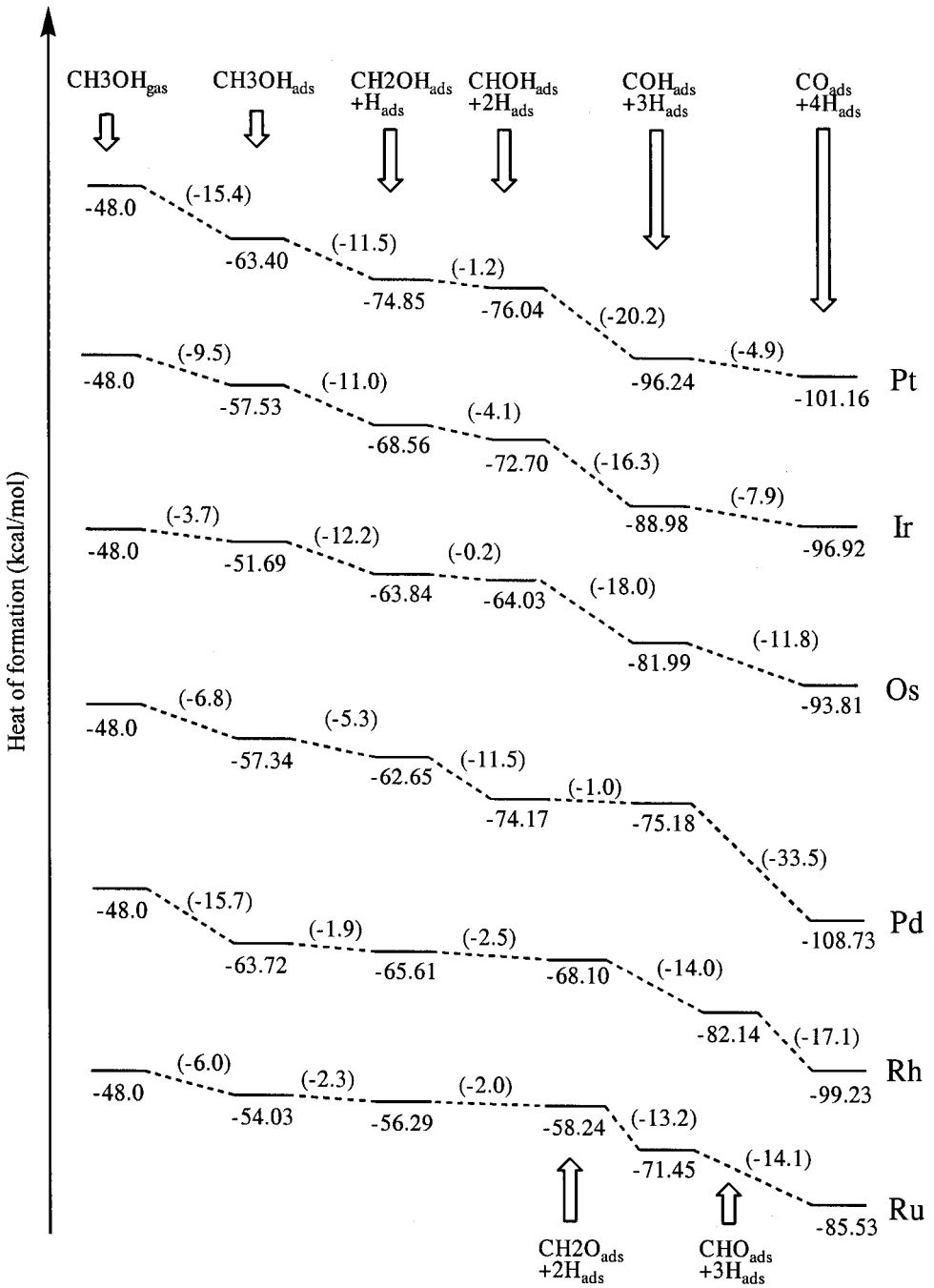

Figure 4-8. Heat of formation chart for comparing methanol dehydrogenation on Pt, Ir, Os, Pd, Rh, and Ru showing only the most stable isomers.

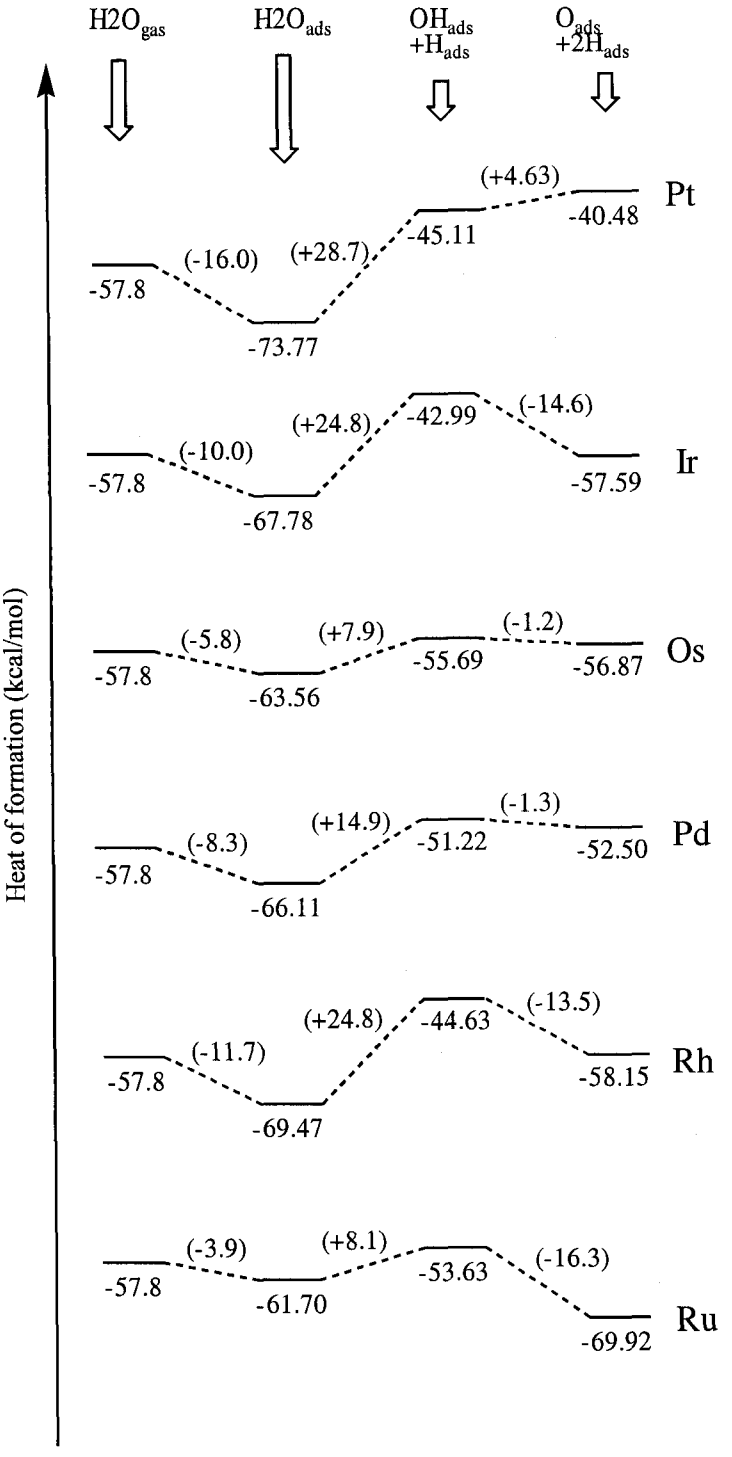

Figure 4-9. Heat of formation chart for comparing water dehydrogenation on Pt, Ir, Os, Pd, Rh, and Ru.

4-4-2. Water Dehydrogenation

For water dehydrogenation, the trends are opposite to that observed for CH_3OH. The heat of formation chart for all six metals is shown in Figure 4-9. Quantitative details are given in Table 4-10. In this case, Pt is poorest for dehydrogenation while Ru is the most facile. Ru is observed to have a much smaller potential (0.2 V versus RHE) for water decomposition and it is possible that atomic oxygen is the activated species for oxidation. For both Ir and Rh the first dehydrogenation is significantly uphill, followed by a downhill second dehydrogenation to form atomic O_{ads}. Pd and Os follow a similar trend with much shallower curves, Os being less steep.

These results support the bifunctional mechanism of Pt-Ru for methanol oxidation. Of the six metals, Pt is the most facile for methanol dehydrogenation because of its ability to easily strip hydrogens from the carbon. Dehydrogenating water, however, is more facile on Ru than the other five metals. Hence, the binary combination yielding the best overall activity for methanol oxidation is Pt-Ru.

4-4-3. Combined Results

Quantitative details for the combined heat of formation values are given in Table 4-11. Except for Os, none of the *pure* metals favor the complete methanol oxidation reaction. Pt, Ir, Pd, and Rh are favorable for methanol dehydrogenation (Pt is the best) but are poor for water dehydrogenation. Ru favorably dehydrogenates water but does poorly for methanol.

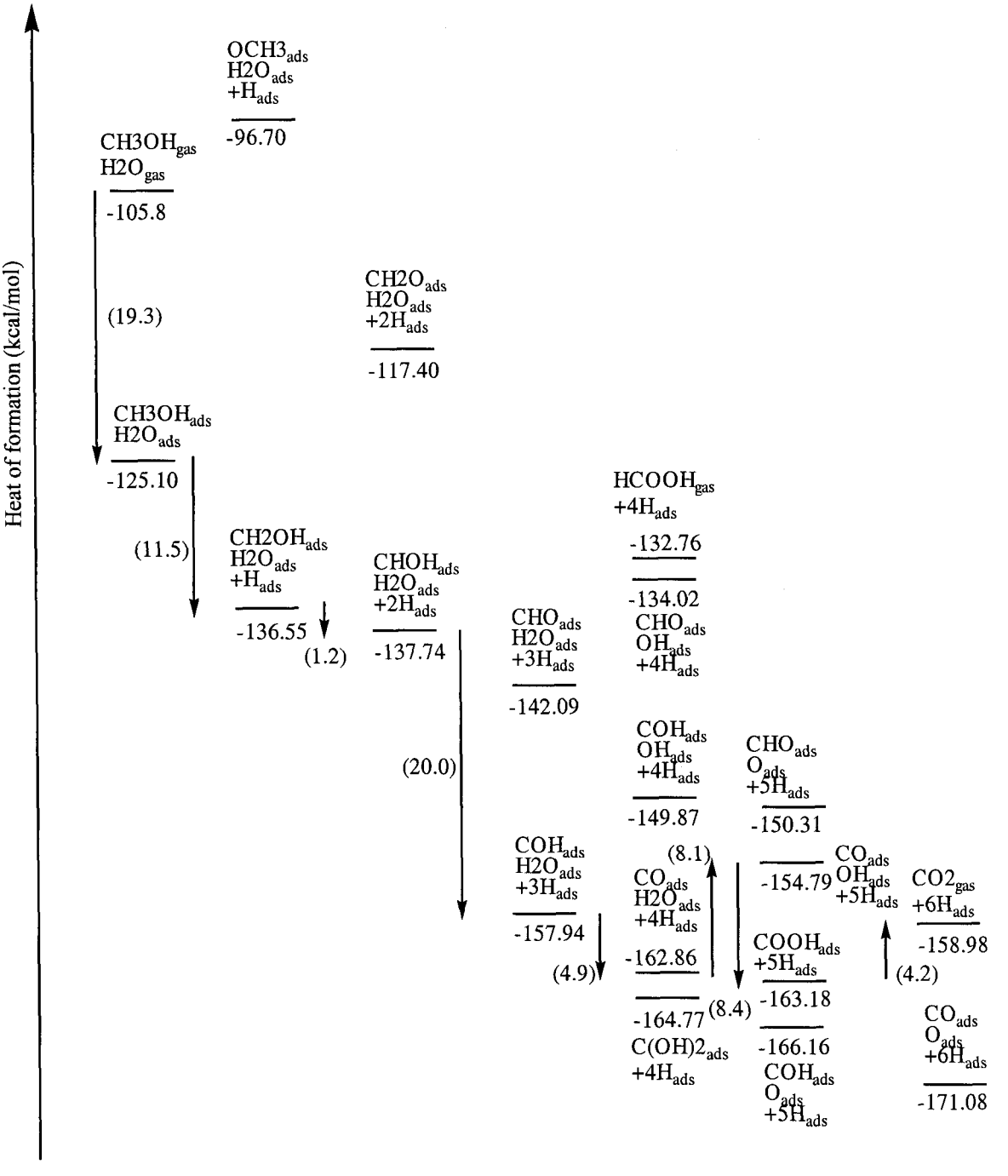

Figure 4-10. Combined heat of formation chart for methanol oxidation on Pt-Ru.

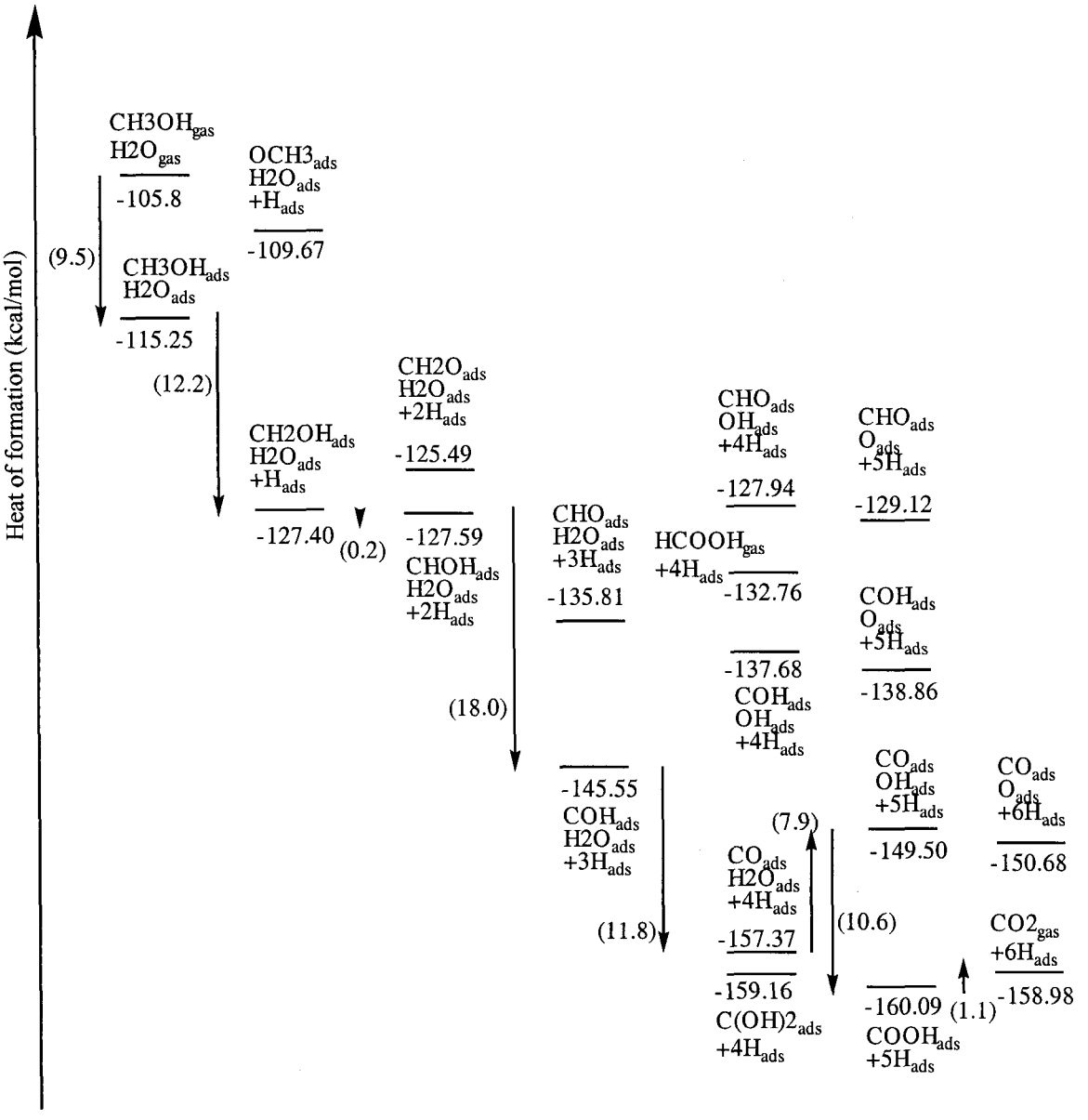

Figure 4-11. Combined heat of formation chart for methanol oxidation on Os.

4-4-4. Pt + Ru

To analyze the effect of a Pt-Ru alloy, we combine the data for methanol dehydrogenation using Pt (first column of Table 4-9) with the data for water dehydrogenation using Ru (sixth column of Table 4-10). From Figure 4-10, we see that

dehydrogenation still proceeds downhill (left half). However, the ability of Ru to decompose water changes the thermodynamics to form the second C-O bond.

Comparing Figure 4-10 with the combined data for pure Pt (Figure 4-6), we find that in Pt-Ru, the formation of $(COOH)_{ads}$ (ΔH_f = -163.18 kcal/mol) directly from $(CO)_{ads}$ + $(H_2O)_{ads}$ + $5H_{ads}$ (ΔH_f = -162.86 kcal/mol) is downhill by 0.3 kcal/mol. Were this to proceed sequentially by dehydrogenating water first to form $(CO)_{ads}$ + $(OH)_{ads}$ + $5H_{ads}$ (ΔH_f = -154.79 kcal/mol), it would have an initial uphill step of only 8.1 kcal/mol compared to 28.7 kcal/mol for pure Pt. A more probable pathway is via the formation of $(COH)_{ads}$ + O_{ads} + $5H_{ads}$ (ΔH_f = -166.16 kcal/mol). This is more stable than $(CO)_{ads}$ + $(H_2O)_{ads}$ + $5H_{ads}$ by 3.30 kcal/mol, and forming $(COOH)_{ads}$ from $(CO)_{ads}$ + $(OH)_{ads}$ is only 3.0 kcal/mol uphill. Thus the most favorable pathway goes through different intermediates suggesting a different reaction mechanism for Pt-Ru than for pure Pt. Once again the last dehydrogenation step converting $(COOH)_{ads}$ to desorbed CO_2 is expected to have a low activation barrier. Although this chart indicates that $(CO)_{ads}$ + O_{ads} is the thermodynamic sink, we see that oxidation can occur before methanol is fully dehydrogenated. Thus because Ru does so well at activating water to $(OH)_{ads}$ (or O_{ads}), the $(CO)_{ads}$ + O_{ads} state need not be accessed.

4-4-5. Pure Os

Finally, pure Os provides an interesting balance of the two dehydrogenations. Although less capable of dehydrogenating methanol than Pt and of dehydrogenating water than Ru, Os can do both processes favorably. Figure 4-11 shows the combined heats of formation for Os. The reaction is downhill practically all the way to form

desorbed CO_2. Forming $(COOH)_{ads} + 5H_{ads}$ (ΔH_f = -160,09 kcal/mol) directly from $(CO)_{ads} + (H_2O)_{ads} + 4H_{ads}$ (ΔH_f = -157.37 kcal/mol) is downhill 3.3 kcal/mol. If this step proceeds sequentially by first forming $(CO)_{ads} + (OH)_{ads} + 5H_{ads}$ (ΔH_f = -149.50 kcal/mol), then this initial step is only 7.9 kcal/mol uphill. This is much more favorable than Pt (28.7 kcal/mol uphill) and even slightly more favorable than Pt-Ru (8.1 kcal/mol uphill). Once again the last dehydrogenation step converting $(COOH)_{ads}$ to desorbed CO_2 is expected to have a low activation barrier, and the reaction is only 1.1 kcal/mol uphill. The mechanism goes through intermediates similar to pure Pt (but different than Pt-Ru).

These results suggest that the role of Os as a promoter in the quaternary system may be 2-fold: (1) it can contribute to dehydrogenation of methanol, but so can Pt and Ir (also a promoter), and (2) it can activate the oxygen species (water or its dehydrogenated counterparts), which can be done by Ru but not by Pt or Ir.

4-4-6. Kinetics

We have neglected the barriers for the various reaction steps. This is a serious limitation since the barriers dominate the rates. However, we expect somewhat similar results for the barriers for the same reaction steps on different metals. Thus, we believe that the energetics and structures allow us to reason about the various mechanistic steps.

4-5. Conclusions

We examined the intermediates involved in the methanol oxidation reaction in DMFCs on the second and third row Group VIII transition metals. The overall reaction can be considered in three stages: (1) dehydrogenation of methanol, (2) dehydrogenation

of water, and (3) formation of the second C-O bond. For pure Pt, we find that $(CO)_{ads}$ is the thermodynamic sink in the reaction, in agreement with experimental evidence that this species poisons catalytic activity if not actively removed from the surface. We also find that of the six metals, methanol dehydrogenation is most facile on Pt, while Ir is also favorable for this reaction. The mechanism of methanol dehydrogenation proceeds via stripping of the hydrogens from the carbon end before the oxygen end.

For water dehydrogenation, Ru is the most active while Pt performs very poorly. These results support the bifunctional mechanism of Pt-Ru whereby Pt is responsible for the dehydrogenation of methanol, and Ru for the dehydrogenation of water.

Our studies also suggest that Os, although poorer than Pt and Ru in their separate steps, combines both capabilities of the bifunctional mechanism. It is able to dehydrogenate both methanol and water favorably from a thermodynamic standpoint. This suggests that pure Os be examined as a potential DMFC catalyst. Although expensive it may lead to favorable kinetics even at very high dispersion and may have more favorable barriers (lower overpotential).

Our results suggest that $(COOH)_{ads}$ is likely the primary species obtained from forming the second C-O bond. In pure Pt, this species is formed via the reaction of CO_{ads} with $(OH)_{ads}$ [or $(H_2O)_{ads}$]. Pure Os follows this same pathway but it is more favorable thermodynamically. In Pt-Ru, a more favorable pathway can take place via the reaction $(COH)_{ads} + O_{ads}$. In either case the final step in the pathway is the dehydrogenation of $(COOH)_{ads}$ to desorb CO_2 from the surface.

4-6. Computational Strategy

In order to provide a more detailed understanding of the basic mechanistic issues, we separately considered three aspects of the catalytic reaction: (1) dehydrogenation of methanol, (2) dehydrogenation of water, and (3) formation of oxidized species to finally yield desorbed CO_2. We examined these reaction steps for the second and third row Group VIII transition metals. This includes Pt and Ru, the two basic ingredients established to exhibit the bifunctional mechanism, and includes Ir and Os, which have been demonstrated to act as promoters in Pt-Ru catalysts.[22] We compared the activity of each of these metals by examining the thermodynamics for each intermediate involved in the reaction.

Our strategy here is to use a consistent accurate level of theory on all plausible reaction intermediates (we considered over 13) at all plausible surface sites (we considered top, bridge, and cap sites) on all 6 transition metals. This sort of comprehensive data at a consistent level of accuracy has never before been available. Using this data we have considered the plausible reaction mechanisms. We have examined the reaction path to estimate the magnitude of the likely barriers, but we have not done systematic studies of the barriers. Instead we focus on comparing data that could be useful in discovering new candidates for catalysts and for designing experimental studies.

4-6-1. The M_8 Cluster Model

Based on the IEM, we chose the Pt_8 cluster (see Chapters 1 and 2) as the most economical choice satisfying these two properties. This M_8 model cluster was used to

study the thermodynamics of the dehydrogenation of methane and the chemistry of ethylene on Pt(111). In both cases the results were consistent with available experimental data.

We applied the same methodology to study the DMFC chemistry on six metals (Pt, Ir, Os, Pd, Rh, and Ru). Pt, Ir, Pd, and Rh are face-center-cubic (fcc) metals, so that the M_8 cluster models the (111) surface. Os and Ru are both hexagonal-closed-packed (hcp), so that the M_8 cluster models the (0001) surface. This is a reasonable choice since X-ray diffraction (XRD) suggests that the platinum alloys active in methanol oxidation are all in the fcc phase[13] and that the closed-packed surface (111) dominates.

4-6-2. Details for QM Computations

Calculations were carried out with the nonlocal DFT (generalized gradient approximation) including exact exchange. Specifically we use the B3LYP method which combines the exact Hartree-Fock (HF) exchange operators with the Slater local exchange functional[60] using the parameters referred to as Becke3.[61] In addition, we used the Becke nonlocal gradient correction,[62] the Vosko-Wilk-Nusair exchange functional,[63] and the Lee-Yang-Parr local and nonlocal correlation functional.[64]

All calculations were carried out using the Jaguar program.[65-66] The metals were described using the Hay and Wadt core-valence relativistic effective-core potential (ECP) with 18 explicit electrons for Pt, Pd; 17 electrons for Ir, Rh; and 16 electrons for Os, Ru (denoted LACVP in Jaguar).[67] This is a nonlocal ECP using angular momentum projection operators to enforce the Pauli principle.[68-71] All electrons were considered for carbon, oxygen and hydrogen using the 6-31G** basis set.

4-6-3. Spin States

The various spin states were calculated as pure spin states (restricted). The optimum spin of the metal-adsorbate complex is determined by separate calculations of all low-lying spins, where in each case the geometric structure for each adsorbate on the metal surface was fully optimized. However, the M-M bonds in each cluster were frozen at their bulk distances (Pt, 2.775; Ir, 2.714; Os, 2.734; Pd, 2.750; Rh, 2.689; Ru, 2.706 Å). This is because we consider that the real catalyst particles are sufficiently large to enforce this structure.

For the various M_8 clusters we calculated the various low-lying spin states and base all energetics on the calculated ground spin states, S_M (Table 4-1). In each case except Pd the electronic structure is consistent with the IEM, which suggests s^1d^{n-1} character in the surface atoms. The IEM suggests that the maximum spin of the cluster is given by

$$S = 8[10 - (n - 1)]/2 \qquad (4\text{-}15)$$

where n is the number of valence electrons. This predicts spins of S=12, 8, and 4 for columns 8, 9, and 10. Indeed for Ir the ground state has S=8. For the other metals, there is sufficient d-d overlap that some electrons in the high-lying d-orbitals spin pair, leading to lower net spins. For example, the ground state of Pt_8 is the S=3 state, 1.4 kcal/mol lower in energy than S=4. Pd_8 is anomalous in that the Pd_8 cluster has almost all d-electrons spin paired. This is because the ground state of Pd atom is d^{10}, whereas the other metals have s^1d^{n-1} atomic ground states.

For the metal-adsorbate clusters, we also calculated the various low-lying spin states and base all energetics on the ground spin state S_{a+M}. The previous results on C_xH_y/Pt_8

showed that each unpaired electron of the C_xH_y forms a localized covalent bond to an unpaired d-orbital of the Pt_8. Thus we expect the ground spin state to satisfy the formula $S_{a+M} = S_M - b/2$, where b is the number of bonds formed between the adsorbate and the surface. Occasionally (especially in 3-fold cap sites, and for some oxygen-based adsorbates) bonding the adsorbate leads to unpairing of a spin-paired d-orbital, resulting in $S_{a+M} = S_M - b/2 + 1$. Formally this corresponds to forming a covalent bond to the excited state of M_8 having a spin higher by 1.

Acknowledgement

The content of this chapter was adapted from reference 72. We thank Professor Eugene Smotkin for helpful comments. This research was initiated with funding from NSF (CHE 95-22179) and continued with funding from ARO (in collaboration with Illinois Institute of Technology and Schrodinger, Inc.).

References

1. Hogarth, M.; Christensen, P.; Hamnett, A.; Shukla, A. *J. Power Sources*, **1997**, *69*, 113.
2. Scherer, G. G. *Ber. Bunsenges. Phys. Chem.*, **1990**, *94*, 1008.
3. Leger, J.-M.; Lamy, C. *Ber. Bunsenges. Phys. Chem.*, **1990**, *94*, 1021.
4. Hamnett, A. *Catalysis Today*, **1997**, *38*, 445.
5. Parsons, R.; VanderNoot, T. *J. Electroanal. Chem.*, **1988**, *257*, 9.
6. Lin, W. F.; Wang, J. T.; Savinell, R. F. *J. Electrochem. Soc.*, **1997**, *144*, 1917.
7. Bockris, J. O.; Wroblowa, H. *J. Electroanal. Chem.*, **1964**, *7*, 428.
8. Petry, O. A.; Podlovchenko, B. I.; Frumkin, A. N.; Hira, L. *J. Electroanal. Chem.* **1965**, *10*, 253.
9. Wasmus, S.; Wang, J.-T.; Savinell, R. F. J. Electrochem. Soc. **1995**, *142,* 3825.

10. Yamanaka, I.; Otsuka, K. *Electrochim. Acta*, **1989**, *34*, 211

11. Gasteiger, H. A.; Markovic, N.; Ross, P. N., Jr.; Cairns, E. J. *J. Phys. Chem.*, **1994**, *98*, 617.

12. Gasteiger, H. A.; Markovic, N.; Ross, P. N., Jr.; Cairns, E. J. *J. Electrochem. Soc.*, **1994**, *141*, 1795.

13. McBreen, J.; Mukerjee, S. *J. Electrochem. Soc.*, **1995**, *142*, 3399 (1995).

14. Krausa, M.; Vielstich, W. *J. Electroanal. Chem.*, **1994**, *379*, 307.

15. Xia, X. H.; Iwasita, T.; Ge, F.; Vielstich, W. *Electrochim. Acta*, **1996**, *41*, 711

16. Munk, J.; Christensen, P. A.; Hamnett, A.; Skou, E. *J. Electroanal. Chem.*, **1996**, *401*, 215.

17. Lamy, C.; Leger, J.-M.; Clavilier, J.; Parsons, R. *J. Electroanal. Chem.*, **1983**, *150*, 71.

18. Kennedy, B. J.; Hamnett, A. *J. Electroanal. Chem.*, **1990**, *283*, 271.

19. Watanabe, M.; Saegusa, S.; Stonehart, P. *J. Electroanal. Chem.*, **1989**, *271*, 213.

20. Beden, B.; Lamy, C.; Bewick, A.; Kunimatsu, K. *J. Electroanal. Chem.*, **1981**, *121*, 343.

21. Beden, B.; Lamy, C. *Electrochim. Acta*, **1990**, *35*, 691.

22. Reddington, E.; Sapienza, A.; Gurau, B.; Viswanathan, R.; Saragapani, S.; Smotkin, E. S.; Mallouk, T. E. *Science*, **1998**, *280*, 1735.

23. Watanabe, M.; Motoo, S. *J. Electroanal. Chem.*, **1975**, *60*, 275.

24. Iwasita, T.; Nart, F. C.; Vielstich, W. *Ber. Bunsenges. Phys. Chem.*, **1990**, *94*, 1030.

25. Anderson, A. B.; Grantscharova, E. *J. Phys. Chem.*, **1995**, *99*, 9143.

26. Thiel, P. A.; Madey, T. E. *Surf. Sci. Rep.*, **1987**, *7*, 211.

27. Yeo, Y. Y.; Vattuone, L.; King, D. A. *J. Chem. Phys.*, **1997**, *106*, 392.

28. Williams, W. R.; Marks, C. M.; Schmidt, L. D. *J. Phys. Chem.*, **1992**, *96*, 5922.

29. Anderson, A. B.; Grantscharova, E. *J. Phys. Chem.*, **1995**, *99*, 9149.

30. Anderson, A. B.; Grantscharova, E.; Seong, S. *J. Electrochem. Soc.*, **1996**, *143*, 2075.

31. Mitchell, P. C. H.; Wolohan, P.; Thompsett, D.; Cooper, S. J. *J. Mol. Cat. A*, **1997**, *119*, 223.

32. Illas, F.; Zurita, S.; Marquez, A. M.; Rubio, J. *Surf. Sci.*, **1997**, *376*, 379.

33. Watwe, R. M.; Spiewak, B. E.; Cortright, R. D.; Dumesic, J. A. *Catal. Lett.*, **1998**, *51*, 139.

34. Hammer, B.; Nielsen, O. H.; Norksov, J. K. *Catal. Lett.*, **1997**, *46*, 31.

35. Chase, M. W., Jr.; Davies, C. A.; Downey, J. R., Jr.; Frurip, D. J.; McDonald, R. A.; Syverud, A. N. *J. Phys. Chem. Ref. Data, Suppl. 1*, **1985**, *14*, 1.

36. Christmann, K.; Ertl, G.; Pignet, T. *Surf. Sci.*, **1976**, *54*, 365.

37. Engstrom, J. R.; Tsai, W.; Weinberg, W. H. *J. Chem. Phys.*, **1987**, *87*, 3104.

38. Conrad, H.; Ertl, G.; Latta, E.E. *Surf. Sci.*, **1974**, *41*, 435.

39. Yates Jr., J. T.; Thiel, P. A.; Weinberg, W. H. *Surf. Sci.*, **1979**, *84*, 427.

40. Feulner, R.; Menzel, D. *Surf. Sci.*, **1985**, *154*, 465.

41. Low, J. J.; Goddard, W. A., III. *Organometallics*, **1986**, *5*, 609.

42. Szulczewski, G.; Levis, R. J. *J. Am. Chem. Soc.*, **1996**, *118*, 325.

43. Yeo, Y. Y.; Stuck, A.; Wartnaby, C. E.; King, D. A. *Chem. Phys. Lett.*, **1996**, *259*, 28.

44. Steininger, H.; Lehwald, S.; Ibach, H. *Surf. Sci.*, **1982**, *123*, 264.

45. Voogt, E. H.; Coulier, L.; Gijzeman, O. L. J.; Geus, J. W. *J. Catal.* , **1997**, *169*, 359.

46. Conrad, H.; Ertl, G.; Kuppers, J. *Surf. Sci.*, **1978**, *76*, 323.

47. Castner, D. G.; Sexton, B. A.; Somorjai, G. A. *Surf. Sci.*, **1978**, *71*, 519.

48. Loffreda, D.; Simon, D.; Sautet, P. *Surf. Sci.*, **1999**, *425*, 680.

49. Zhang, C. J.; Hu, P.; Lee, M.-H. *Surf. Sci.*, **1999**, *432*, 305.

50. Thiel, P. A.; Williams, E. D.; Yates, J. T., Jr.; Weinberg, W. H. *Surf. Sci.*, **1979**, *84*, 54.

51. Pfnur, H.; Feulner, P.; Menzel, D. *J. Chem. Phys.*, **1983**, *79*, 4613.

52. Ogletree, D. F.; Van Hove, M. A.; Somorjai, G. A. *Surf. Sci.* **1986**, *173*, 351.

53. Leung, L.-W. H.; Wieckowski, A.; Weaver, M. J. *J. Phys. Chem.*, **1988**, *92*, 6985.

54. Yau, S. L.; Gao, X.; Chang, S. C.; Schadt, B. C.; Weaver, M. J. *J. Am. Chem. Soc.*, **1991**, *113*, 6049.

55. Klunker, C.; Balden, M.; Lehwald, S.; Daum, W. *Surf. Sci.*, **1996**, *360*, 104.

56. Gland, J. L.; Sexton, J. L.; Fisher, G. B. *Surf. Sci.*, **1980**, *95*, 587.

57. Harding, L. B.; Goddard III, W. A. *Ann. Rev. Phys. Chem.* **1978**, *29*, 363.

58. Fahmi, A.; van Santen, R. A. *Z. Phys. Chem.*, **1996**, *197*, 203.

59. Chen, M.; Bates, S. P.; van Santen, R. A.; Friend, C. M. *J. Phys. Chem. B*, **1997**, *101*, 10051.

60. Slater, J. C. *Quantum Theory of Molecules and Solids*, Vol. 4: *The Self-Consistent Field for Molecules and Solids*, McGraw-Hill; New York, 1974.

61. Becke, A. D. *J. Chem. Phys.*, **1993**, *98*, 5648.

62. Becke, A. D. *Phys. Rev. A*, **1988**, *38*, 3098.

63. Vosko, S. H.; Wilk, L.; Nusair, M. *Can. J. Phys.*, **1980**, *58*, 1200.

64. Lee, C.; Yang, W.; Parr, R. G. *Phys. Rev. B*, **1988**, *37*, 785.

65. Jaguar 3.0, Schrodinger, Inc.; Portland, Oregon, 1997.

66. Greeley, B. H.; Russo, T. V.; Mainz, D. T.; Friesner, R. A.; Langlois, J.-M.; Goddard III, W. A.; Honig, B. *J. Am. Chem. Soc.*, **1994**, *116*, 11875.

67. Hay, P. J.; Wadt, W. R. *J. Phys. Chem.*, **1985**, *82*, 299.

68. Goddard III, W. A. *Phys. Rev.*, **1968**, *174*, 659.

69. Kahn, L. R.; Goddard III, W. A. *J. Chem. Phys.*, **1972**, *56*, 2685.

70. Melius, C. F.; Goddard III, W. A. *Phys. Rev. A*, **1974**, *10*, 1528.

71. Melius, C. F.; Olafson, B. O.; Goddard III, W. A. *Chem. Phys. Lett.*, **1974**, *28*, 457.

72. Kua, J.; Goddard III, W. A. *J. Am. Chem. Soc.*, **1999**, *121*, 10928.

Chapter 5: Stability and Thermodynamics of the Catalytica $PtCl_2$ Type Catalyst for Activating Methane to Methanol

Abstract

Stimulated by the recent experiments of Periana *et al.* (*Science*, **1998**, *280*, 560), we have studied the relative stability and reaction mechanism of the $Pt(NH_3)_2Cl_2$ and $Pt(bpym)Cl_2$ complexes in concentrated sulfuric acid, involved in the high-yield catalytic conversion of methane to methylbisulfate. We find that the mechanism involves a series of steps beginning with C-H activation to form an intermediate ion-pair Pt(II)-CH_4 methane complex prior to forming a Pt(II)-CH_3 complex. Our calculated relative activation barriers for C-H activation are in good agreement with experimentally observed H/D ratios. Subsequent oxidation to a Pt(IV) complex occurs with reduction of SO_3. Release of methylbisulfate regenerates the Pt(II) catalyst.

We find that the ammine complex is unstable in sulfuric acid suggesting that the active catalyst in this case has bisulfate ligands. We find that the bisulfate form favors precipitation of $PtCl_2$ which led to catalyst death. On the other hand we find that the bipyrimidine catalyst is stable in solution. Our calculations suggest that both the C-H activation and oxidation steps are more favorable for the bisulfate catalyst suggesting higher activity. We find that bipyrimidine acts as a "proton sink" which allows the protonated form of the ligand to remain bound to Pt in concentrated sulfuric acid. These results are consistent with observed behavior of the catalysts.

5-1. Introduction

The direct catalytic conversion of methane to methanol via a low temperature route could provide an economic advantage over the current high temperature processes involving the formation of syngas. The most promising route for low-temperature alkane activation has been the use of transition metal complexes in solution, as indicated by the significant research activity in this area since the 1970s.[1-9] However, the low yields of these processes for methane activation has prolonged commercialization. Methane is the most unreactive of the alkanes and its oxidized products are typically more reactive, making selective oxidation a great challenge. The homogeneous catalysis of methane oxidation using platinum salts was first reported by Shilov *et al.*[10] Mercuric salts in concentrated sulfuric acid were shown by the Catalytica group to produce a 43% one-pass yield.[11]

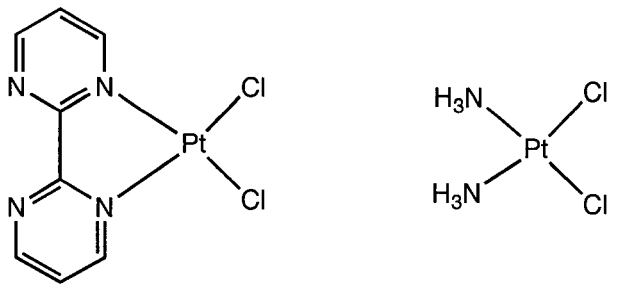

Figure 5-1. The (bpym)$PtCl_2$ and $(NH_3)_2PtCl_2$ catalysts for methane activation.

In 1998, Periana *et al.*[12] of Catalytica Inc. reported a significant breakthrough in developing an effective catalyst for high yield selective oxidation of CH_4 to CH_3OH. This catalyst was formed from $PtCl_2$(bpym), Figure 5-1. In well-dried sulfuric acid (80 ml at 102%) they found that 72% of 115 mmol CH_4 at 3.4 MPa (~34 atm) was converted

by 50 mmol of catalyst to product (mixture of CH_3OSO_3H + CH_3OH) in 2.5 hours at 220°C. They suggested that the reaction involved three processes:

a. CH_4 activation: $CH_4 + H_2SO_4 + SO_3 \rightarrow CH_3OSO_3H + H_2O + SO_2$ (5.1a)

b. CH_3OH conversion: $CH_3OSO_3H + H_2O \rightarrow CH_3OH + H_2SO_4$ (5.1b)

c. S reoxidation: $SO_2 + 1/2\ O_2 \rightarrow SO_3$ (5.1c)

leading to the net reaction

$$CH_4 + 1/2\ O_2 \rightarrow CH_3OH \quad (5.2)$$

This process is very promising since it provides high yield at relatively low temperatures. On the other hand the requirement of very dry sulfuric acid and the necessity of separating CH_3OSO_3H from the catalyst prior to converting to CH_3OH creates both materials and separations problems. As a result this promising process has not yet been commercialized by Catalytica.

Some experimental observations relevant to the mechanism of the bipyrimidine catalyst are:

- under conditions in which oxidized product is not made (< 150°C), H/D exchange is observed with CH_4 in D_2SO_4, and that
- addition of Pt(IV) salt as $H_2Pt(OH)_6$ to the catalyst results in the formation of product.

From these results, it is concluded that the C-H activation at 150°C is via Pt(II) and the oxidation step is rate-determining.

Consequently, we have embarked on a project to elucidate the fundamental mechanism. Our objective is to obtain an improved understanding of how the current catalyst works in order that we might suggest possible modifications that could improve the catalyst sufficiently that it would become commercially viable.

Periana *et al.* found that the ammine catalyst, $Pt(NH_3)_2Cl_2$, had higher initial activity than the bipyrimidine catalyst, $Pt(bpym)Cl_2$. [The extrapolated turnover frequency (TOF) is of the order of 10^{-2} s^{-1}, an order of magnitude higher than for the bipyrimidine catalyst (TOF ~ 10^{-3} s^{-1}).] However, after only several turnovers, $PtCl_2$ (solid) was precipitated, halting the reaction ($\tau_{1/2}$ ~ 15 min), whereas the bipyrimidine catalyst is stable over millions of turnovers. Our calculations (*vide infra*) suggest that the ammine complex is indeed short-lived, quickly converting to the predominant bisulfate form of the catalyst, $Pt(OSO_3H)_2Cl_2$, after being added to concentrated sulfuric acid. We find that it is thermodynamically favorable for the bisulfate form to aggregate forming dimers and trimers. On the other hand, we find the bipyrimidine catalyst does not convert to the bisulfate form and does not favorably form dimers and trimers.

In this paper we report thermodynamics of many possible stable species and intermediates in solution. Our calculations will only focus on methane activation, (5.1a), of the three processes in (5.1). Our calculated relative barriers for the C-H activation step with the bipyrimidine catalyst are in good agreement with observed ratios from H/D isotope exchange experiments. We also suggest mechanistic steps involved in oxidation and functionalization based on preliminary calculations. The calculated overall thermodynamics of the reaction suggests that the bisulfate form is more reactive than the bipyrimidine form, as observed.

5-2. Computational Details

All quantum mechanical calculations were carried out using the B3LYP flavor of density functional theory (DFT). This includes non-local gradient corrections to the Slater

local exchange functional[13] and includes exact Hartree-Fock (HF) exchange. We use the parameters referred to as Becke3[14] with the Becke nonlocal gradient correction,[15] the Vosko-Wilk-Nusair exchange functional,[16] and the Lee-Yang-Parr local and nonlocal correlation functional.[17]

The core electrons of the Pt were treated with a non-local ECP using angular momentum projection operators to enforce the Pauli Principle.[18-19] To do this we used the Hay and Wadt[20] core-valence effective core potential (ECP), which treats explicitly the outer 18 electrons of Pt (5s,5p,5d,6s,6p). This basis set is denoted as LACVP** in the Jaguar QM software[21-22] and treats H, C, N, O, S at the level of 6-31G** (valence double zeta plus polarization).

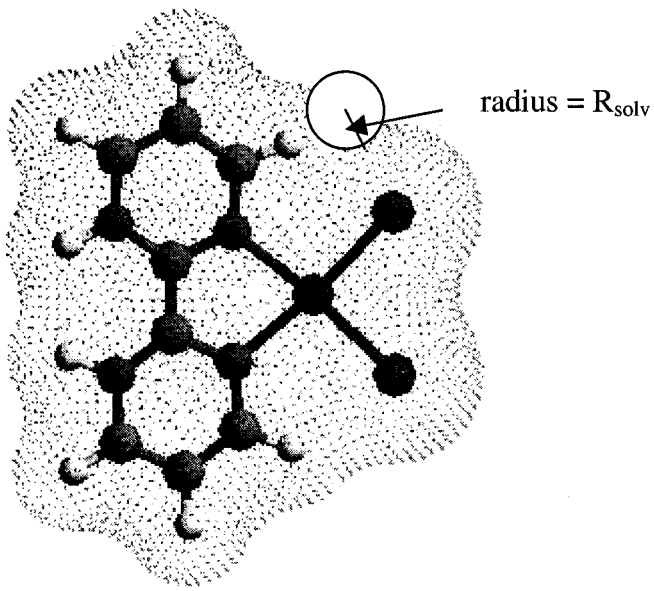

Figure 2. Illustration of calculated solvent accessible surface of $[(bpymH_2)PtCl_2]^{2+}$.

All calculations used the Poisson-Boltzmann continuum approximation (PBF) to describe the effect of solvent.[23-24] In this approximation, the solvent accessible surface of the solute is calculated as illustrated in Figure 5-2 (using van der Waals radii for the atoms and then rolling a sphere of radius R_{solv} over this surface to obtain a smooth

surface). Then at each self-consistent field (SCF) step, we calculate the reaction field in the solvent due to the electrostatic field of the solute wavefunction using the experimental dielectric constant {$\varepsilon = 98$ for 99% H_2SO_4 [ref 25] and radius $R_{solv} = 2.205$ Å [ref 26]}. This reaction field is then included in the Fock operator (Kohn-Sham Hamiltonian) to calculate the orbitals of the DFT wavefunction of the solute. This calculation uses a numerical grid to describe the solvent region of space. For a fixed geometry, this process is continued until self-consistent. The total energy then includes the QM energy (which includes rearrangement effects due to the solvent) and the solute-solvent interactions. The forces on the QM atoms due to the solvent are also calculated so that the geometry can be calculated in the presence of the solvent.

After calculating the self-consistent DFT wavefunction in solvent, we calculated the vibrational frequencies from the Hessian in solution and used this to correct the DFT energy for zero point vibrations. In addition we used the vibrational frequencies to calculate the enthalpy and entropy as a function of temperature to obtain the total free energy. For the reaction energies (Figures 5-4, 5-8; Table 5-3), we report two numbers.

- The first number, ΔH_{0K}, is the sum of the electronic energy, solvation energy and zero point energy with *no temperature corrections*. This corresponds to a zero Kelvin enthalpy change.
- The second number, ΔG_{453K} (in parentheses in Figure 5-4), adds the free energy correction at 453 K to the first number. *Note that we do not correct the free energy for concentration differentials among reacting species to obtain the chemical potential.* Such concentration corrections can be significant since some

of the reactions studied include ligand exchange with the solvent (sulfuric acid) present in much higher concentration than the other species in solution.

The various discussions in the text will use ΔH_{0K}. The calculated free energy corrections do not change the conclusions and are included in all the energy schemes.

5-3. Results on Catalyst Stability in Sulfuric Acid

5-3-1. Ammine Ligand

We calculate that, in sulfuric acid, the ammine ligands in $Pt(NH_3)_2Cl_2$ are favorably displaced by bisulfate ligands.

$$Pt(NH_3)_2Cl_2 + 2\ H_2SO_4 \rightarrow [Pt(OSO_3H)_2Cl_2]^{2-} + 2\ [NH_4]^+ \qquad (5.3)$$

$$\Delta H_{0K} = -40.8 \text{ kcal/mol}, \Delta G_{453K} = -28.4 \text{ kcal/mol}$$

The driving force for this reaction is the favorable protonation of the ammine ligands to form NH_4^+, which goes into solution.

In fact, we find that the bidentate form of bisulfate is the thermodynamically favored species.

$$[Pt(OSO_3H)_2Cl_2]^{2-} \rightarrow [Pt(\eta^2\text{-}OSO_3H)Cl_2]^- + [OSO_3H]^- \qquad (5.4a)$$

$$\Delta H_{0K} = -4.5 \text{ kcal/mol}, \Delta G_{453K} = -28.5 \text{ kcal/mol}$$

The protonated form of bisulfate ligands is highly unfavorable.

$$[Pt(OSO_3H)_2Cl_2]^{2-} + 2\ H_2SO_4 \rightarrow [Pt(OSO_3H_2)_2Cl_2]^0 + 2\ [OSO_3H]^- \qquad (5.4b)$$

$$\Delta H_{0K} = +42.1 \text{ kcal/mol}, \Delta G_{453K} = +38.1 \text{ kcal/mol}$$

Structures and relevant bond distances of these Pt complexes are shown in Figure 5-3a.

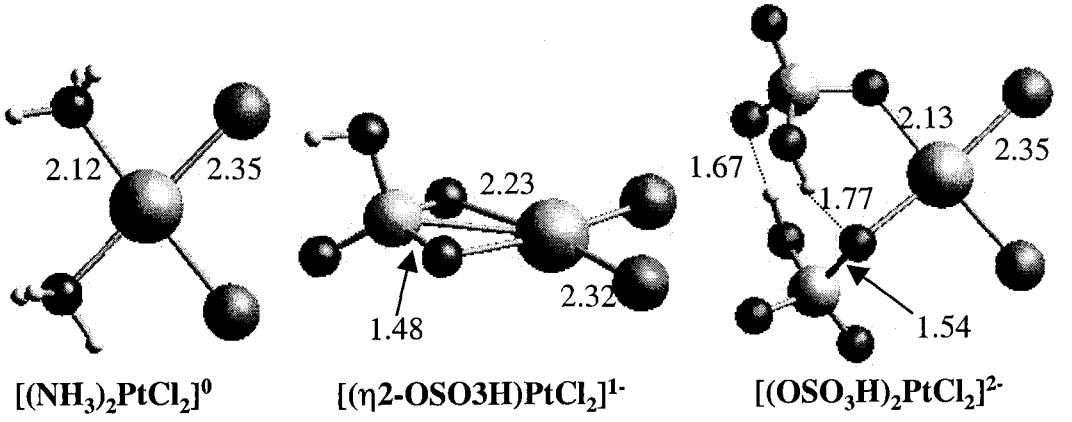

Figure 5-3a. Ammine and bisulfate forms of the catalyst [distances in Å].

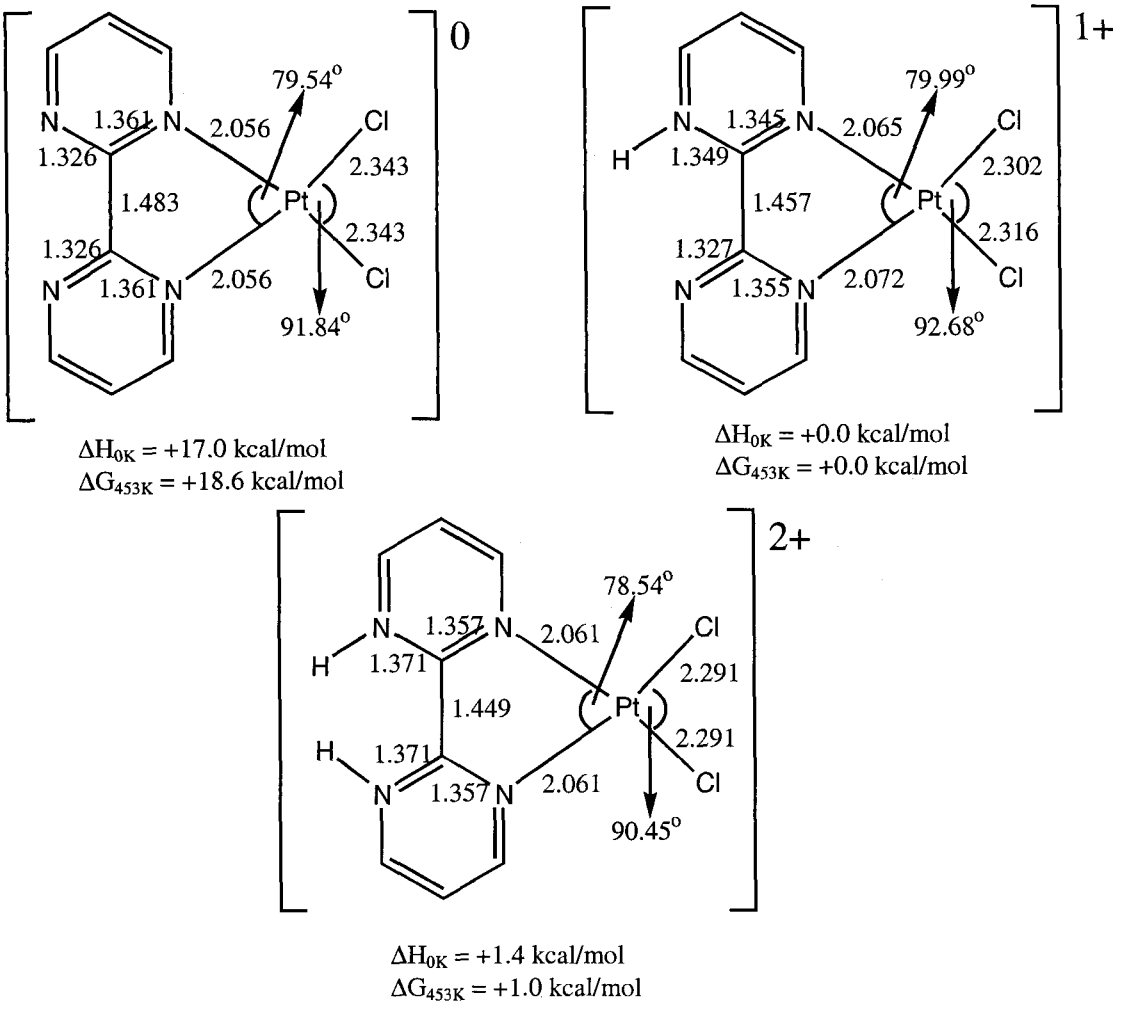

Figure 5-3b. Unprotonated, singly and doubly protonated forms of the bipyrimidine catalyst [distances in Å].

Compound	Electronic E (hartree)	Solvation E (kcal/mol)	Zero point energy (kcal/mol)	$G_{453\ K}$ correction (kcal/mol)
$[(NH_3)_2PtCl_2]^0$	-1152.79834	-31.0	56.1	-36.0
$[(OSO_3H)_2PtCl_2]^{2-}$	-2439.05690	-158.8	55.0	-45.8
$[(\eta^2\text{–}OSO_3H)PtCl_2]^{1-}$	-1739.36251	-56.1	21.4	-39.0
$[(H_2SO_4)_2PtCl_2]^{2-}$	-2440.02110	-17.6	76.6	-45.5
$[(bpymH_2)PtCl_2]^{2+}$	-1567.65087	-221.3	123.6	-41.4
$[(bpymH)PtCl_2]^{1+}$	-1567.46874	-80.1	108.5	-42.7
$[(bpym)PtCl_2]^0$	-2966.30428	-33.5	139.2	-44.0
$[(bpy)PtCl_2]^0$	-1535.06174	-22.7	113.8	-43.9
$[(OSO_3H)_2Pt_2Cl_4]^{2-}$	-3478.72490	-140.4	62.9	-53.7
$[(\eta^2\text{–}OSO_3H)Pt_2Cl_4]^{1-}$	-2778.99919	-53.0	25.4	-47.6
$[(bpymH_2)Pt_2Cl_4]^{2+}$	-2607.25089	-230.6	127.1	-51.8
$[(bpymH)Pt_2Cl_4]^{1+}$	-2607.05281	-102.8	110.9	-53.0
$[(OSO_3H)_2Pt_3Cl_6]^{2-}$	-4518.37874	-126.9	66.8	-62.9
$[(\eta^2\text{–}OSO_3H)Pt_3Cl_6]^{1-}$	-3818.63190	-52.1	28.6	-54.2
$[(bpymH_2)Pt_3Cl_6]^{2+}$	-3646.87746	-226.6	130.2	-58.1
$[(bpymH)Pt_3Cl_6]^{1+}$	-3646.66137	-114.7	114.0	-60.5
$[NH_4]^{1+}$	-56.90595	-89.3	31.9	-18.0
$[bpymH_2]^{2+}$	-528.04721	-197.3	116.0	-35.0
$[bpymH]^{1+}$	-527.84689	-55.4	102.0	-35.6
bpym (bipyrimidine)	-527.46143	-14.2	90.6	-35.5
$[bpyH_2]^{2+}$	-496.00982	-187.3	132.7	-34.4
H_2SO_4	-700.21440	-13.6	24.6	-29.1
$[OSO_3H]^{1-}$	-699.73051	-67.4	16.5	-30.8
CH_4	-40.52405	+1.7	29.2	-18.0
HCl	-460.80081	-0.8	4.3	-18.4
SO_3	-623.75933	-5.1	7.2	-25.6
SO_2	-548.58755	-3.5	4.1	-24.8
H_2O	-76.41963	-6.9	13.3	-18.3
CH_3OSO_3H	-739.54004	-9.6	42.7	-32.2

Table 5-1. Energetics of $L_2Pt_nCl_{2n}$ complexes and other reacting species.

5-3-2. Bipyrimidine Ligand

For the bipyrmidine ligand, we considered three cases (unprotonated, singly protonated and doubly protonated). We find that:

- the singly protonated form, $[Pt(bpymH)Cl_2]^+$ is the most stable.
- the doubly protonated form, $[Pt(bpymH_2)Cl_2]^{2+}$ is only 1.4 kcal/mol higher in energy.
- the neutral unprotonated form, $[Pt(bpym)Cl_2]$, which would be the most stable in the gas phase, is significantly less stable (17.0 kcal/mol) in solution.

Thus,

$$[Pt(bpym)Cl_2] + H_2SO_4 \rightarrow [Pt(bpymH)Cl_2]^+ + [OSO_3H]^- \quad (5.5a)$$

$$\Delta H_{0K} = -17.0 \text{ kcal/mol}, \Delta G_{453K} = -18.6 \text{ kcal/mol}$$

$$[Pt(bpymH)Cl_2]^+ + H_2SO_4 \rightarrow [Pt(bpymH_2)Cl_2]^{2+} + [OSO_3H]^- \quad (5.5b)$$

$$\Delta H_{0K} = +1.4 \text{ kcal/mol}, \Delta G_{453K} = +1.0 \text{ kcal/mol}$$

The geometries of these complexes are given in Figure 5-3b. A somewhat surprising result from these calculations is that the structure of $[Pt(bpym)Cl_2]$ hardly changes upon adding the protons. Thus, the Pt-N bond distance remains unchanged (2.06 Å), while the central C-C bond connecting the two pyrimidine units changes very little from 1.48 to 1.45 Å. The pyrimidine groups in all three cases are parallel when bound to the $PtCl_2$ complex.[28] Thus the bipyrimidine ligand functions as a proton reservoir. Our calculations suggest that both the singly and doubly protonated forms of the catalyst are present and in equilibrium in sulfuric acid. The consequences of this similar stability of (bpymH)Pt(II) and $(bpymH_2)$Pt(II) complexes suggests a shuttling mechanism for the oxidation step (discussed in Section 5-6-4).

Both these forms are more stable than the bisulfate forms. For example,

$$[Pt(bpymH_2)Cl_2]^{2+} + 2\ [OSO_3H]^- \rightarrow [Pt(OSO_3H)_2Cl_2]^{2-} + [bpymH_2]^{2+} \qquad (5.6)$$

$$\Delta H_{0K} = +19.3 \text{ kcal/mol}, \Delta G_{453K} = +42.2 \text{ kcal/mol}$$

This contrasts dramatically with the ammine case in (5.3).

A summary of the relative stability of these forms is given in Figure 5-4. The most stable form of free bipyrimidine in solution is the doubly protonated form. Adding the third proton is uphill 3.8 kcal/mol. Thus, bipyrimidine retains two unprotonated N sites that can form a complex with $PtCl_2$ even in concentrated sulfuric acid.

5-3-3. Precipitation of $PtCl_2$

To study the first steps towards precipitation of $PtCl_2$ we calculated the relative energetics for dimerization and trimerization of the two main forms of the catalyst. Recall from (5.3) that the ammine catalyst exists essentially in the bisulfate form while the bipyrimidine catalyst favorably retains the bpym ligand. We find that both bisulfate forms (two bisulfate ligands or one η^2-bound bisulfate ligand) favorably form dimers and trimers. Thus,

$$2\ [Pt(OSO_3H)_2Cl_2]^{2-} \rightarrow [(OSO_3H)_2Pt_2Cl_4]^{2-} + 2\ OSO_3H^- \qquad (5.7a)$$

$$\Delta H_{0K} = -17.0 \text{ kcal/mol}, \Delta G_{453K} = -40.7 \text{ kcal/mol}$$

$$2\ [Pt(\eta^2\text{-}OSO_3H)Cl_2]^{2-} \rightarrow [(\eta^2\text{-}OSO_3H)Pt_2Cl_4]^{2-} + OSO_3H^- \qquad (5.7b)$$

$$\Delta H_{0K} = -12.0 \text{ kcal/mol}, \Delta G_{453K} = -12.4 \text{ kcal/mol}$$

On the other hand, it is unfavorable for the bipyrimidine catalysts to form dimers and trimers. Thus,

$$2\ [Pt(bpymH_2)Cl_2]^{2+} \rightarrow [(bpymH_2)Pt_2Cl_4]^{2+} + [bpymH_2]^{2+} \qquad (5.8)$$

ΔH_{0K} = +12.9 kcal/mol, ΔG_{453K} = +9.6 kcal/mol

The energetics for these reactions are summarized in Figure 5-4b. *This explains the experimental observation that the ammine catalyst quickly forms $PtCl_2$ precipitate thus killing activity only after several turnovers while the bipyrimidine catalyst is long-lived.*[11]

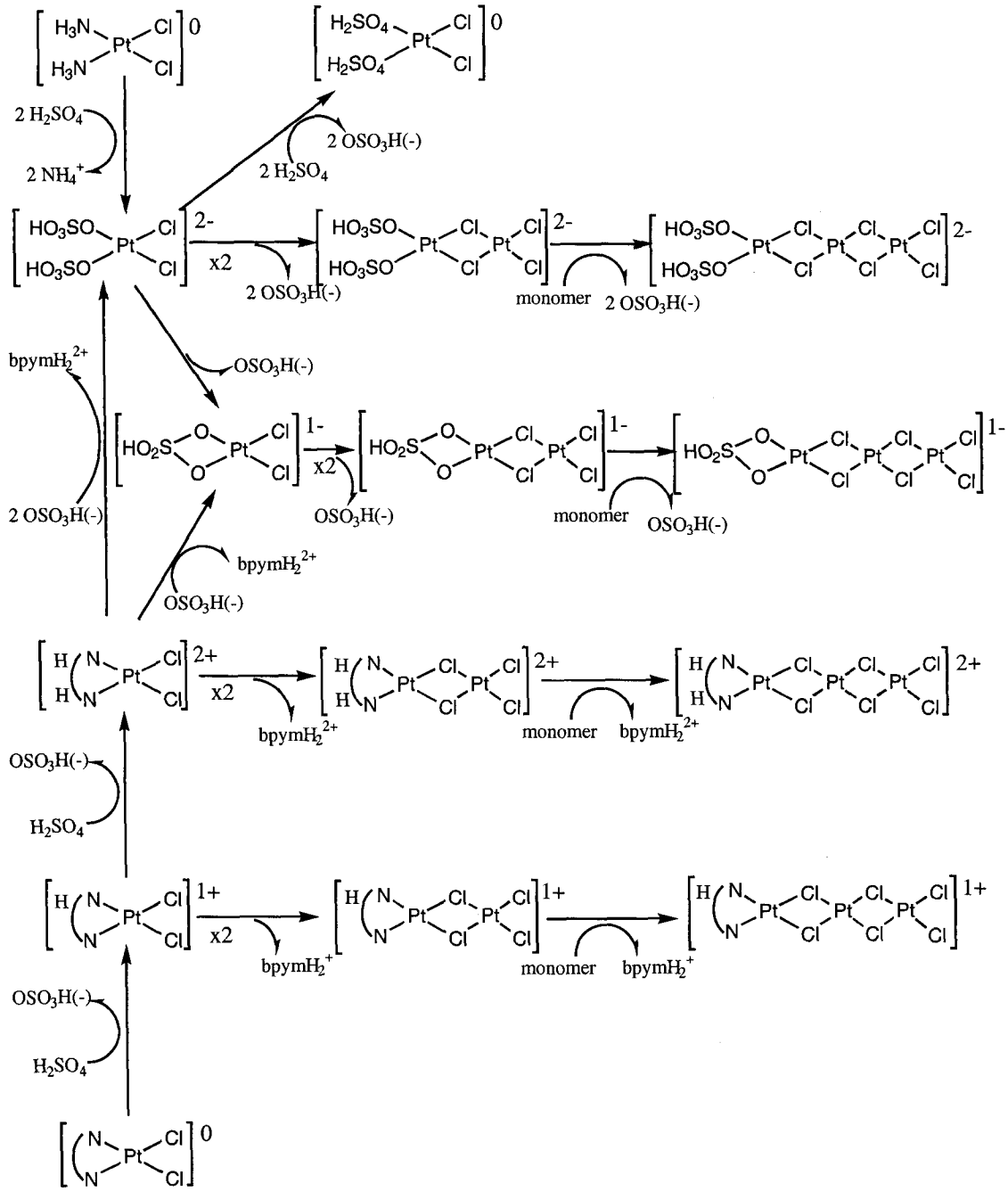

Figure 5-4a. Relative stability of L_2PtCl_2 complexes in sulfuric acid: Reactions.

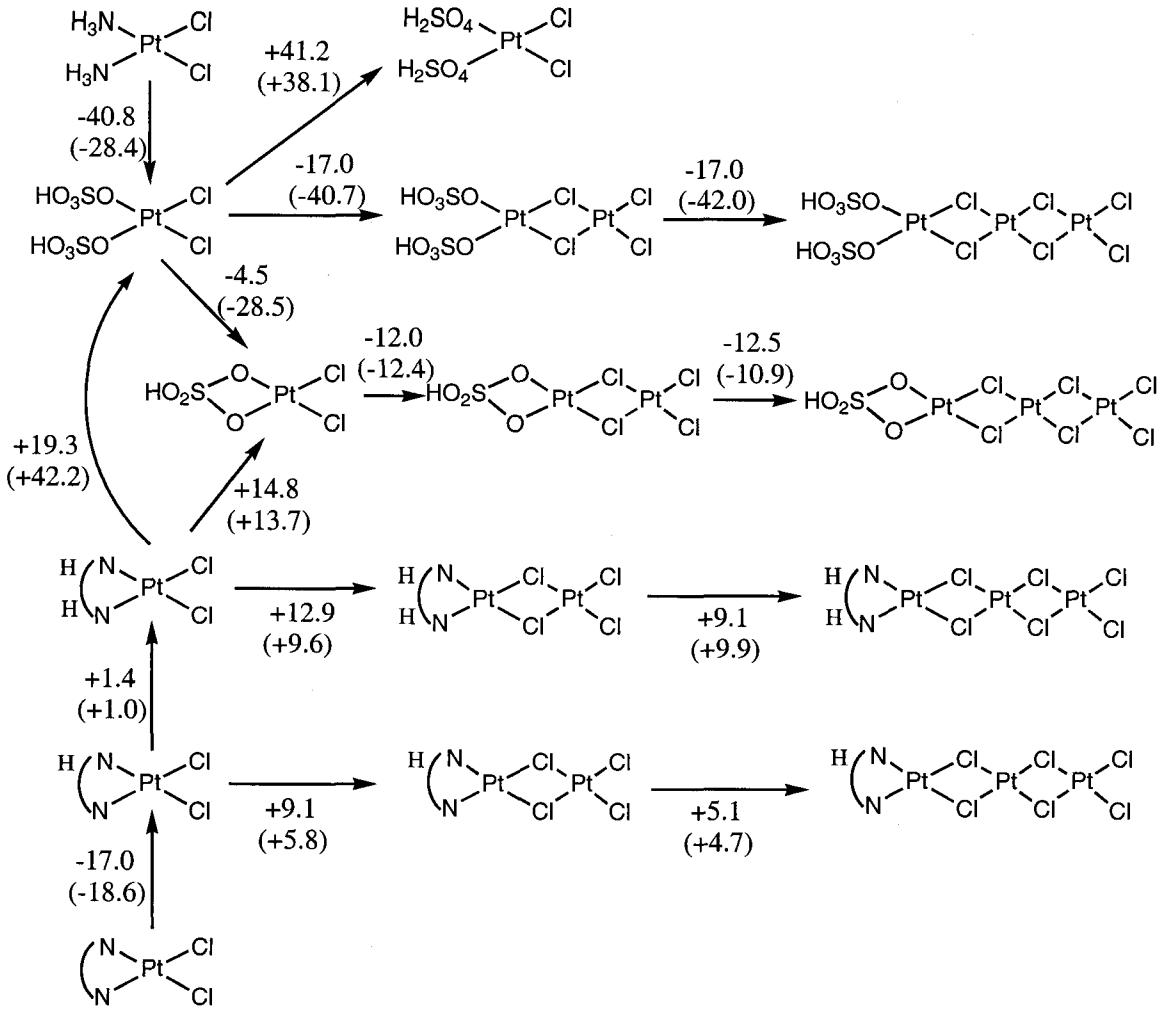

Figure 5-4b. Relative stability of L_2PtCl_2 complexes in sulfuric acid: Energetics.

5-3-4. Modified Ligands

Our calculations suggest that N-based π-acid ligands with *at least three N-sites* will stabilize $PtCl_2$ complexes in a solution of concentrated sulfuric acid. Two of these sites should be on the same side to form a complex with the Pt. The third site should be available for protonation.

In order to test our conclusion, we calculated the relative stability of the bipyridine (bpy) complex (only two N-sites for protonation) with respect to the bisulfate form of the catalyst. As with bipyrimidine, the doubly protonated form of free bipyridine is the most

stable. The corresponding ligand exchange reaction to form the bisulfate complex is exothermic.

$$[Pt(bpyH_2)Cl_2]^{2+} + 2\ H_2SO_4 \rightarrow [Pt(OSO_3H)_2Cl_2]^{2-} + [bpyH_2]^{2+} \qquad (5.9)$$

$$\Delta H_{0K} = -14.5 \text{ kcal/mol}, \Delta G_{453K} = -37.2 \text{ kcal/mol}$$

Hence, *we predict that while the bipyrimidine complex is stable with respect to forming $PtCl_2$ precipitate, the bipyridine complex would favorably convert to the bisulfate form leading to precipitate.* This is consistent with the lack of activity found for $Pt(bpy)_2Cl_2$ experimentally.

Since $[(bpymH)PtCl_2]^+$ is marginally more stable than $[(bpymH_2)PtCl_2]^{2+}$ (see Section 5-3-2), our calculations suggest that the analogous three nitrogen ligand (one pyridine and one pyrimidine) should not favorably convert to bisulfate and subsequently form $PtCl_2$ precipitate.

5-4. Mechanistic Issues of CH_4 to CH_3OSO_3H Conversion

5-4-1. Mechanism Proposed by Current Calculations

Our calculations support a reaction mechanism with three basic steps (see Figure 5-5a):

- Methane activation is via a square planar Pt(II) complex to produce a CH_3-Pt(II) complex via an intermediate ion-pair methane complex, $[L_2Pt(II)X(CH_4)]^{(m-1)+}Cl^-$.

$$[L_2Pt(II)\ Cl_2]^{m+} + CH_4 \rightarrow [L_2Pt(II)Cl(CH_4)]^{(m-1)+}Cl^- \qquad (5.10a)$$

$$[L_2Pt(II)Cl(CH_4)]^{(m-1)+}Cl^- \rightarrow [L_2Pt(II)Cl(CH_3)]^{m+} + HCl \qquad (5.10b)$$

- Oxidation of CH_3-Pt(II) to an octahedral CH_3-Pt(IV) complex by adding bisulfate ligands in the axial positions with reduction of SO_3.

$$[L_2Pt(II)Cl(CH_3)]^{m+} + 2\,H_2SO_4 + SO_3 \rightarrow$$

$$[L_2Pt(IV)Cl(CH_3)(OSO_3H)_2]^{m+} + SO_2 + H_2O \qquad (5.11)$$

- Functionalization via reductive elimination of CH_3OSO_3H.

$$[L_2Pt(IV)Cl(CH_3)(OSO_3H)_2]^{m+} \rightarrow$$

$$[L_2Pt(II)Cl(OSO_3H)]^{m+} + CH_3OSO_3H \qquad (5.12)$$

Since $[L_2Pt(II)Cl(OSO_3H)]$ is formed (5.11), the catalytic cycle proceeds with $[L_2Pt(II)Cl(OSO_3H)]$ and does not need to further involve the $[L_2Pt(II)Cl_2]$ species. Hence, (5.10a) can be replaced by (5.10a') for subsequent catalytic cycles.

$$[L_2Pt(II)Cl(OSO_3H)]^{m+} + CH_4 \rightarrow [L_2Pt(II)Cl(CH_4)]^{(m-1)+} + OSO_3H^- \qquad (5.10a')$$

This mechanism shares similarities to both the aqueous Pt(II)/Pt(IV) system proposed by Shilov[10,29-30] and the Periana mechanism[12] (Figure 5-5b) as discussed below.

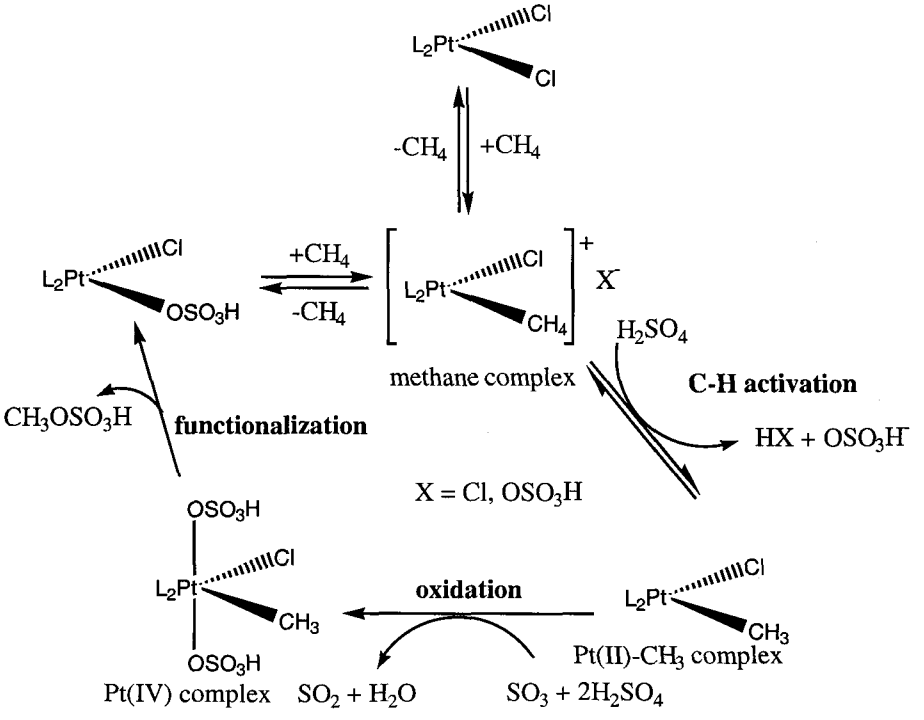

Figure 5-5a. Mechanism of catalytic cycle from current calculations.

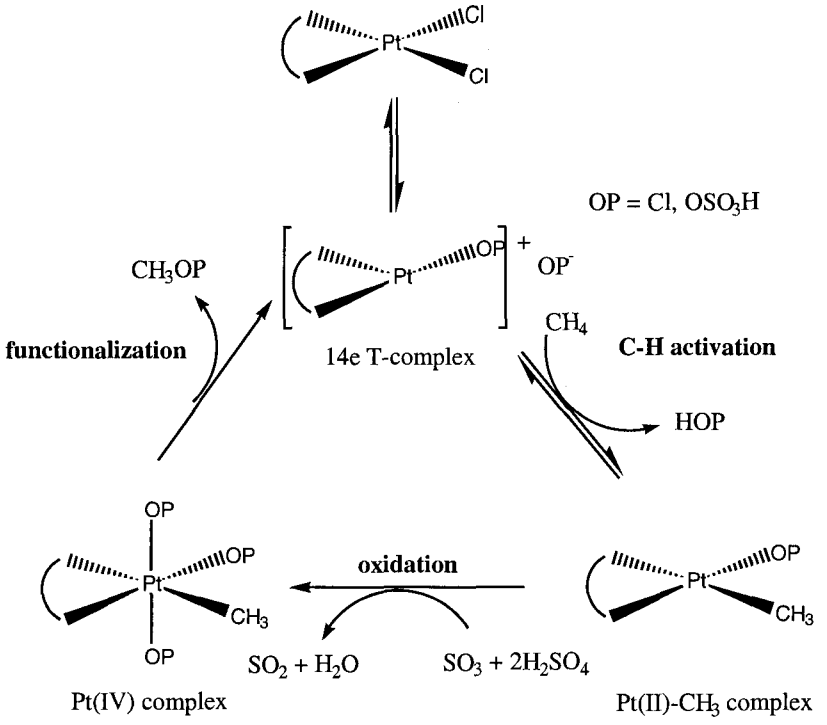

Figure 5-5b. Mechanism of catalytic cycle proposed by Periana *et al.*

5-4-2. Comparison with Experiment

Periana *et al.* suggested that C-H activation takes place via electrophilic substitution going through a 14-electron T-complex, $[(bpym)Pt(II)Cl]^{m+}$ (see Figure 5-5b). This first step is dissociative. Subsequent reaction with methane (5.13b) leads to the CH_3-Pt(II) intermediate.

$$[(bpym)Pt(II)Cl_2]^{m+} \rightarrow [(bpym)Pt(II)Cl]^{m+}\ldots Cl^- \qquad (5.13a)$$

$$[(bpym)Pt(II)Cl]^{m+}\ldots Cl^- + CH_4 \rightarrow [(bpym)Pt(II)Cl(CH_3)]^{m+} + HCl \qquad (5.13b)$$

The suggested T-complex (5.13a) is very similar to our proposed methane complex intermediate in (5.10a). We find that it is favorable for CH_4 to occupy the open coordination site once one Cl^- is removed. Hence, our mechanism goes through a methane complex intermediate rather than the T-complex.

The most significant mechanistic information comes from H/D exchange experiments with D_2SO_4 at temperatures below 150°C (no oxidized product is made) where significant amounts of highly deuterated species, CD_4, CD_3H, and CD_2H_2, are observed. This suggests that the activation barrier of the reverse reaction (5.10a and 5.13a) is higher than the forward reaction (5.10b and 5.13b). Since neither the 14-electron T-complex nor the methane complex have been directly observed experimentally, if such an intermediate species was formed, its conversion to the CH_3-Pt(II) species (5.10b and 5.13b) should be exothermic.

The large pool of H_2SO_4 in solution favors the formation of HCl as Cl^- goes into solution.

$$H_2SO_4 + Cl^- \rightarrow HCl + OSO_3H^- \qquad (5.14)$$

The proposed oxidation (5.11) and functionalization (5.12) steps are similar to those in our calculations.

5-4-3. Comparison with Previous Calculations

Hush and co-workers have reported the thermodynamics for the ammine complex.[31] The level of DFT and basis set used are similar to our work except that diffuse functions were not used and the Stoll ECP[32-33] was used instead of the Hay & Wadt ECP. The treatment of solvation is different. In their Isodensity Polarizable Continuum Model (IPCM), the cavity is defined from an isosurface of the total electron density calculated at the level of theory being applied.[34] The cavity is not fixed; the isodensity surface is varied at each iteration. As the solute density is updated, the cavity is relaxed to the new isodensity surface. It should be noted that since terms that couple the isodensity to the

solute Hamiltonian are missing, this process is not fully self-consistent with respect to the isodensity surface. For comparison, our method is described in Section 5-2.

They find that C-H activation via oxidative addition or via a Pt(IV) intermediate are less favorable compared to electrophilic addition, in agreement with our calculations and the mechanism suggested by Periana *et al.* They conclude that the reaction proceeds first by electrophilic attack by methane on an analog of the T-shaped complex, $[Pt(NH_3)_2(OSO_3H)(H_2SO_4)]^+$, to form the CH_3-Pt(II) species

$$[(NH_3)_2PtCl_2] + 3\ H_2SO_4 \rightarrow$$

$$[(NH_3)_2Pt(OSO_3H)(H_2SO_4)]^+ + 2\ HCl + OSO_3H^- \qquad (5\text{-}15a)$$

$$[(NH_3)_2Pt(OSO_3H)(H_2SO_4)]^+ + CH_4 + OSO_3H \rightarrow$$

$$[(NH_3)_2Pt(II)(OSO_3H)(CH_3)] + 2\ H_2SO_4 \qquad (5\text{-}15b)$$

They find that ligand exchange results in the exchange of the two chlorides with a bisulfate and a sulfuric acid molecule. The CH_3-Pt(II) complex then goes through similar oxidation and functionalization steps as proposed by Periana *et al.*[12] We find that replacement of chloride with bisulfate is not thermodynamically favorable. This is discussed in Section 5-6-2.

5-5. Calculated Kinetics of C-H Activation

5-5-1. (bpym)$PtCl_2$

Figure 5-6 shows the C-H activation reaction energy profile of (bpym)$PtCl_2$.[35] We find a distinct stable intermediate **B**. If the reverse barrier **B** → **A** is larger than the forward barrier **B** → **C**, and subsequent reactions of **C** are not favorable (low

temperature, <150°C), one might get multiple exchanges with deuterium in D_2SO_4 before desorption of methane.

We calculate the overall reaction **A** → **C** to be endothermic by 22.5 kcal/mol. We find that the first step to C-H activation involves the breaking of one Pt-Cl bond. Methane occupies the open coordination site forming the methane complex, **B**. Cl^- remains very closely associated as an ion-pair and can be involved in breaking the C-H bond to form **C**. The estimated barrier of **B** → **C** is small, ~7 kcal/mol (going through transition state **T2**), which may explain why **B** is transient. We find that the reverse reaction **B** → **A** indeed has a larger barrier (~14 kcal/mol).

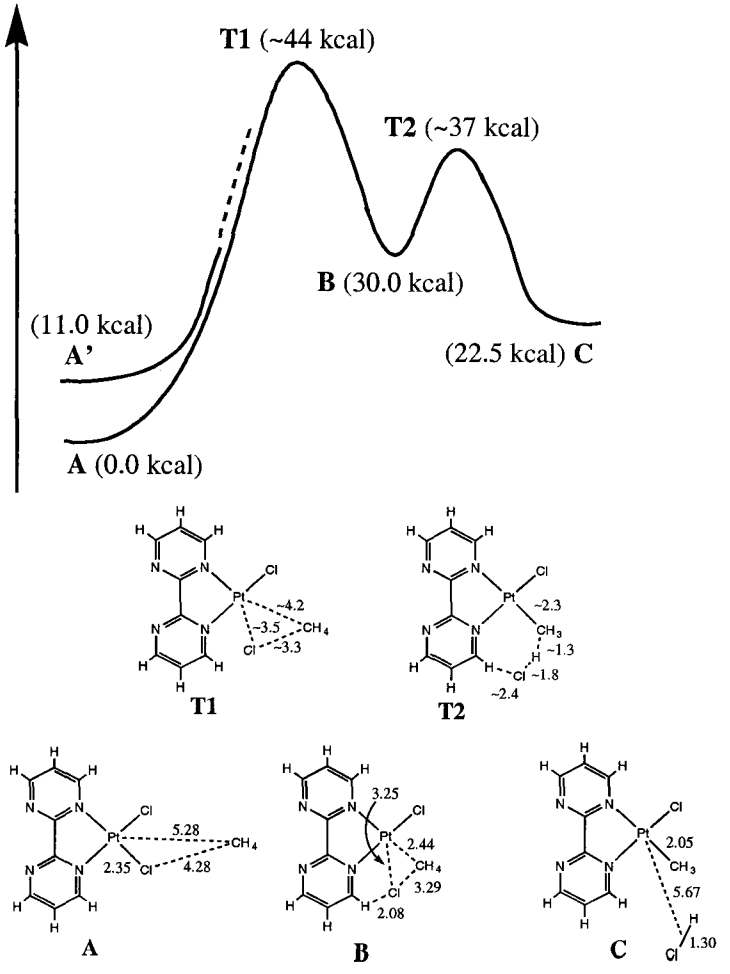

Figure 5-6. C-H activation reaction energy profile of $(bpym)PtCl_2$.

The highest barrier for the overall reaction **A** → **C** is estimated to be ~44 kcal/mol. As discussed in Section 5-4-1, although (bpym)$PtCl_2$ is the initial species in solution, after one turn of the catalytic cycle, the reacting species is (bpym)Pt(Cl)(OSO_3H). We find that exchanging a Cl^- ligand for a OSO_3H^- ligand is endothermic by 11 kcal/mol. Hence we expect the effective overall barrier to be less than 33 kcal/mol (since the Pt-O bond in Pt-OSO_3H is weaker than the Pt-Cl bond). Similarly, the relative energetics of the analogous **B**, **T2**, and **C** with respect to (bpym)Pt(Cl)(OSO_3H), **A'**, are 19, 26 and 12 kcal/mol instead of 30, 37 and 23 kcal/mol.

These results are completely consistent with experimental observations providing strong confirmation of our mechanism for C-H activation, in particular, that an ion-pair methane complex intermediate, **B**, is involved (as opposed to a single step reaction).

5-5-2. $(NH_3)_2PtCl_2$

H/D exchange experimental data is not available for the ammine catalyst because it is unstable in sulfuric acid, i.e., it forms precipitate leading to catalyst death (as discussed in Section 5-3). Our calculations for the kinetics of C-H activation suggest that, if the ammine catalyst was stable in solution, it would have a different reaction profile compared to the bipyrimidine catalyst.

Figure 5-7 shows the reaction energy profile of $(NH_3)PtCl_2$. The overall reaction **A** → **C** is endothermic by 18.7 kcal/mol. Methane occupies the open coordination site forming a distinct intermediate methane complex, **B**, only 17.3 kcal/mol uphill from **A**. Cl^- remains very closely associated as an ion-pair and is involved in breaking the C-H bond

to form **C**. The relative barrier heights are opposite to those found for (bpym)$PtCl_2$. The forward reaction **B** → **C** is ~19 kcal/mol (going through transition state **T2**), while the reverse reaction **B** → **A** has a smaller barrier (~12 kcal/mol).

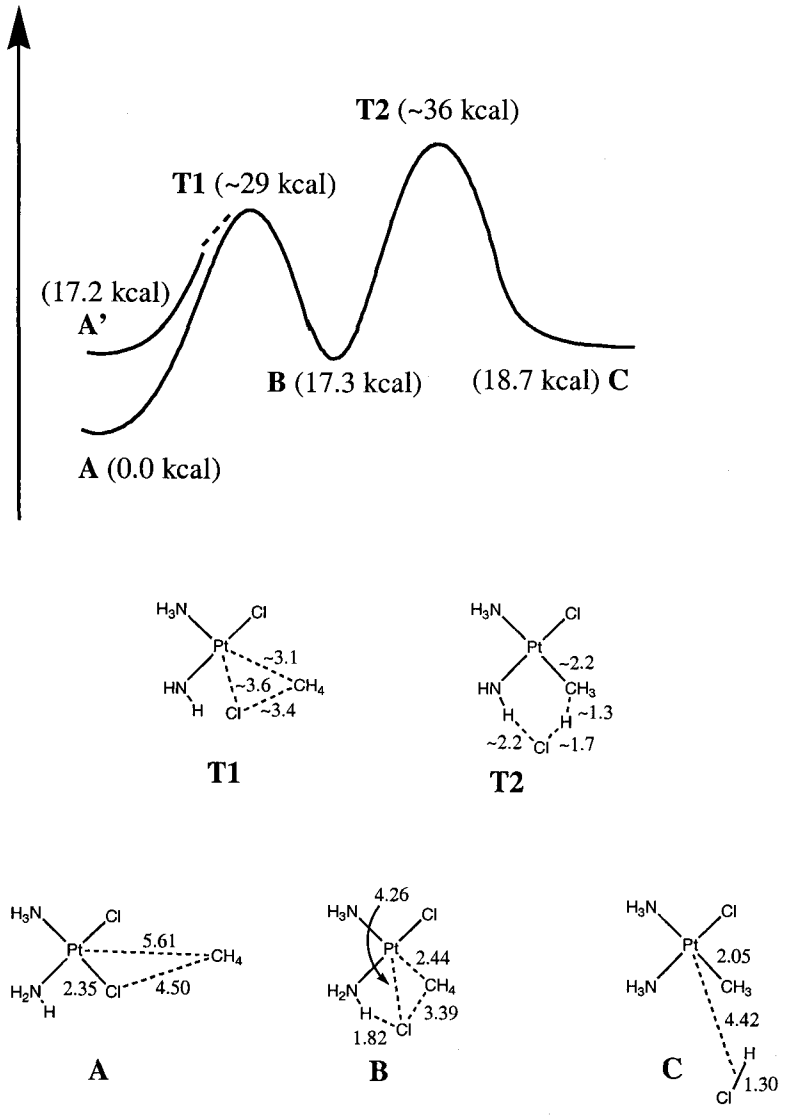

Figure 5-7. C-H activation reaction energy profile of $(NH_3)_2PtCl_2$.

The highest barrier for the overall reaction **A** → **C** is now ~36 kcal/mol. Comparing the magnitudes of the barriers for both (bpym)$PtCl_2$ and $(NH_3)_2PtCl_2$ suggests that the first barrier (**T1**) is controlled by the relative stability of the methane complex, **B**, with

respect to **A**. The relative endothermicity of **A** → **B** drops by 30.0 – 17.3 = 12.7 kcal/mol and the corresponding barrier for the forward reaction (**T1**) drops by 44 – 29 = 15 kcal/mol. On the other hand, the second barrier (**T2**) shows no significant change. Although the relative energetics of **B** → **C** are quite different for L_2 = bpym (-7.5 kcal/mol) and L = NH_3 (+1.4 kcal/mol), the overall endothermicity of **A** → **C** shows less change (+22.5 kcal/mol for L_2 = bpym and +18.7 kcal/mol for L = NH_3).

As discussed in Section 5-4-1, although $(NH_3)_2PtCl_2$ is the initial species in solution, after one turn of the catalytic cycle, the reacting species is $(NH_3)_2Pt(Cl)(OSO_3H)$. We find that exchanging a Cl^- ligand for a OSO_3H^- ligand is endothermic by 17 kcal/mol. Hence we expect the effective overall barrier to be ~19 kcal/mol. Similarly, the relative energetics of the analogous **T1**, **B**, and **C** with respect to $(NH_3)_2Pt(Cl)(OSO_3H)$, **A'**, are 12, 0 and 2 kcal/mol instead of 29, 17 and 19 kcal/mol.

5-6. Calculated Thermodynamics of CH_4 to CH_3OSO_3H Conversion

5-6-1. Overall Thermodynamics

The reactions involved in the overall thermodynamics are shown in Figure 5-8a. We calculated the overall energetics for six different cases (L = NH_3, L = OSO_3H, L_2 = η^2-OSO_3H, L_2 = $bpymH_2$, L_2 = bpymH, L_2 = bpym). We also examined a pathway where formation of the Pt-CH_3 bond occurs without displacing the Cl^- ligands. This involves only the left side of Figure 5-8 where L = Cl.

Energetics for the reaction intermediates are in Table 5-2 while energy differences of the reactions (ΔH_{0K} and ΔG_{453K}) are in Table 5-3. The alphanumeric labels for each reaction are shown in Figure 5-8b. For convenience in comparing the two major types of

ligands, we present the results for L = OSO_3H and L_2 = bpymH in Figures 5-8c and 5-8d. The reactions can be divided into three groups. The first group involves the reactions in the top half of Figures 5-8a and 5-8b (reactions **6**, **7**, **8**, and **9**). These are the overall thermodynamics of the species in solution due to ligand exchange between Cl^- and OSO_3H^-. Chloride from the complex goes into solution as HCl in fuming sulfuric acid.

The second group is the (lower right) catalytic cycle involving the L_2PtXCH_3 intermediates where X = Cl. Formation of Pt(II)-CH_3 via C-H activation is given by reactions **10a** and **11a**. The oxidation step is reaction **3a**. The functionalization step is reaction **4a**. Reactions **1a**, **2a** and **5a** involve the methane complex (L_2PtXCH_4 species) as an intermediate to C-H activation. The methane complex may be transient in a two-step C-H activation and has not been detected by experiment; however, we calculate the complex to be a stable structure.

The third group is the (lower left) catalytic cycle involving the L_2PtXCH_3 intermediates where X = OSO_3H. Formation of Pt(II)-CH_3 via C-H activation is given by reactions **10b** and **11b**. The oxidation step is reaction **3b**. The functionalization step is reaction **4b**. Reactions **1b**, **2b** and **5b** involve the methane complex (L_2PtXCH_4 species) as an intermediate to C-H activation. The methane complex is also calculated to be a stable structure.

For C-H activation to occur in a single step, simultaneous breaking of the C-H bond and Pt-X bond with formation of the H-X bond is required. We have not been able to locate a transition state for single step C-H activation.

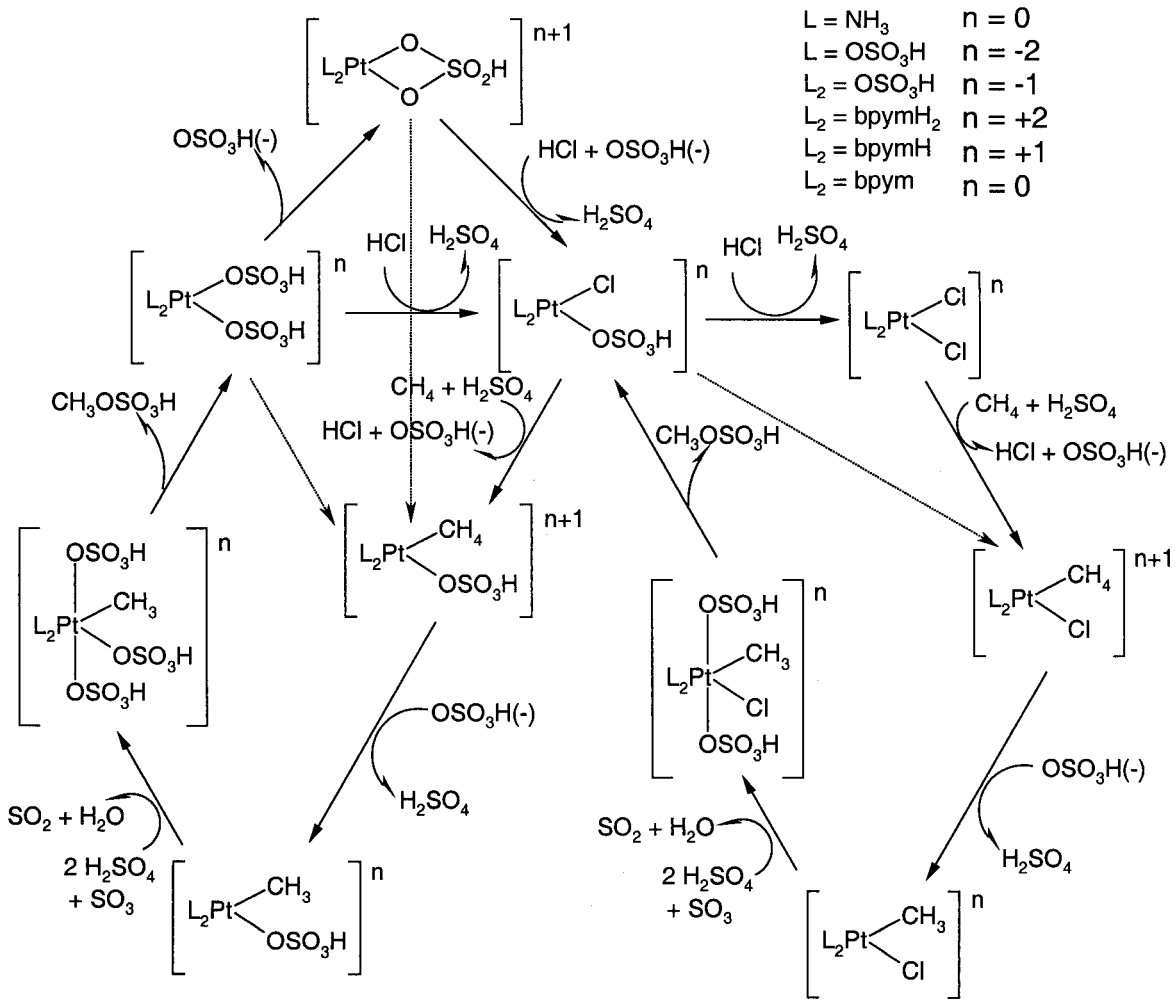

Figure 5-8a. Calculated overall thermodynamics of the catalytic cycle: Reactions.

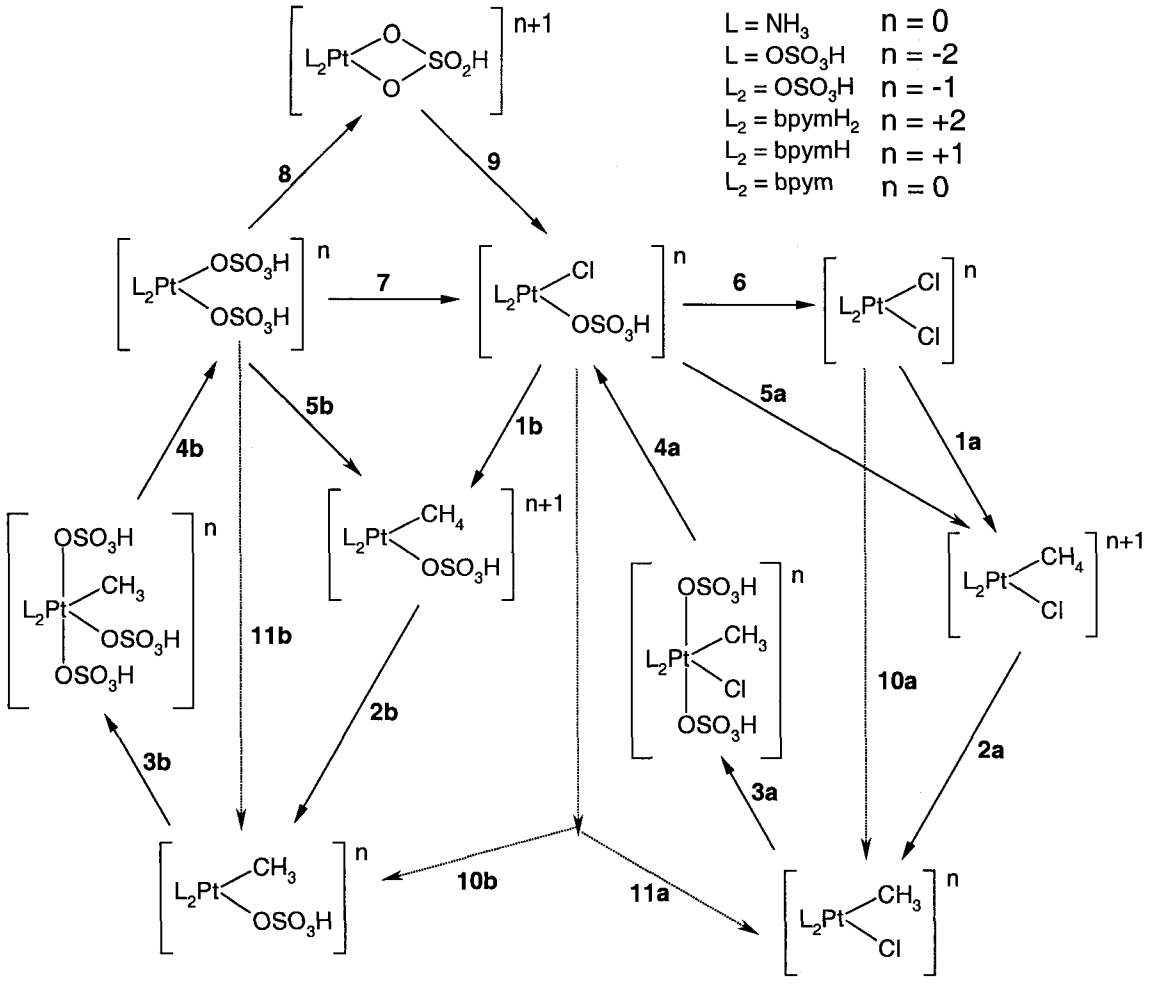

Figure 5-8b. Calculated overall thermodynamics of the catalytic cycle: Energetics.

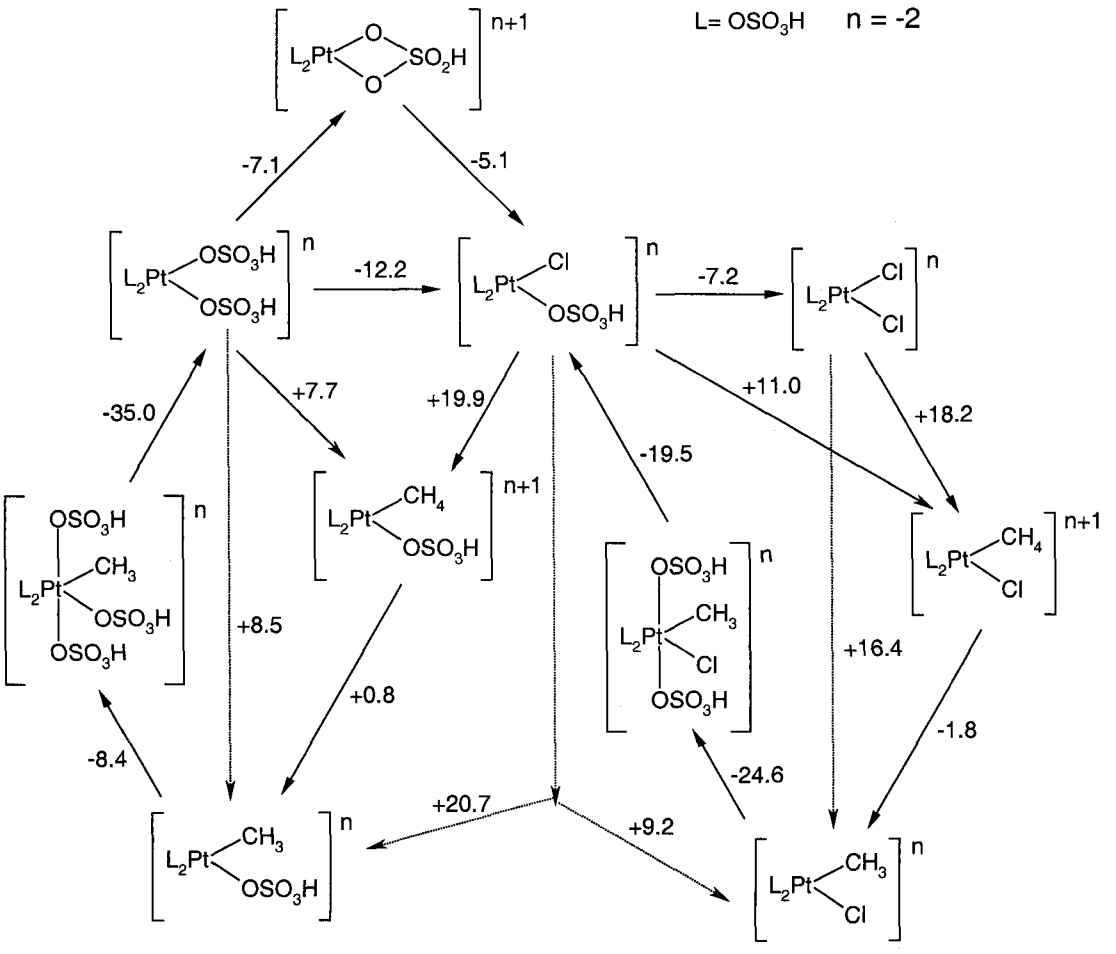

Figure 5-8c. Calculated overall thermodynamics of the catalytic cycle: Energetics for L = OSO_3H.

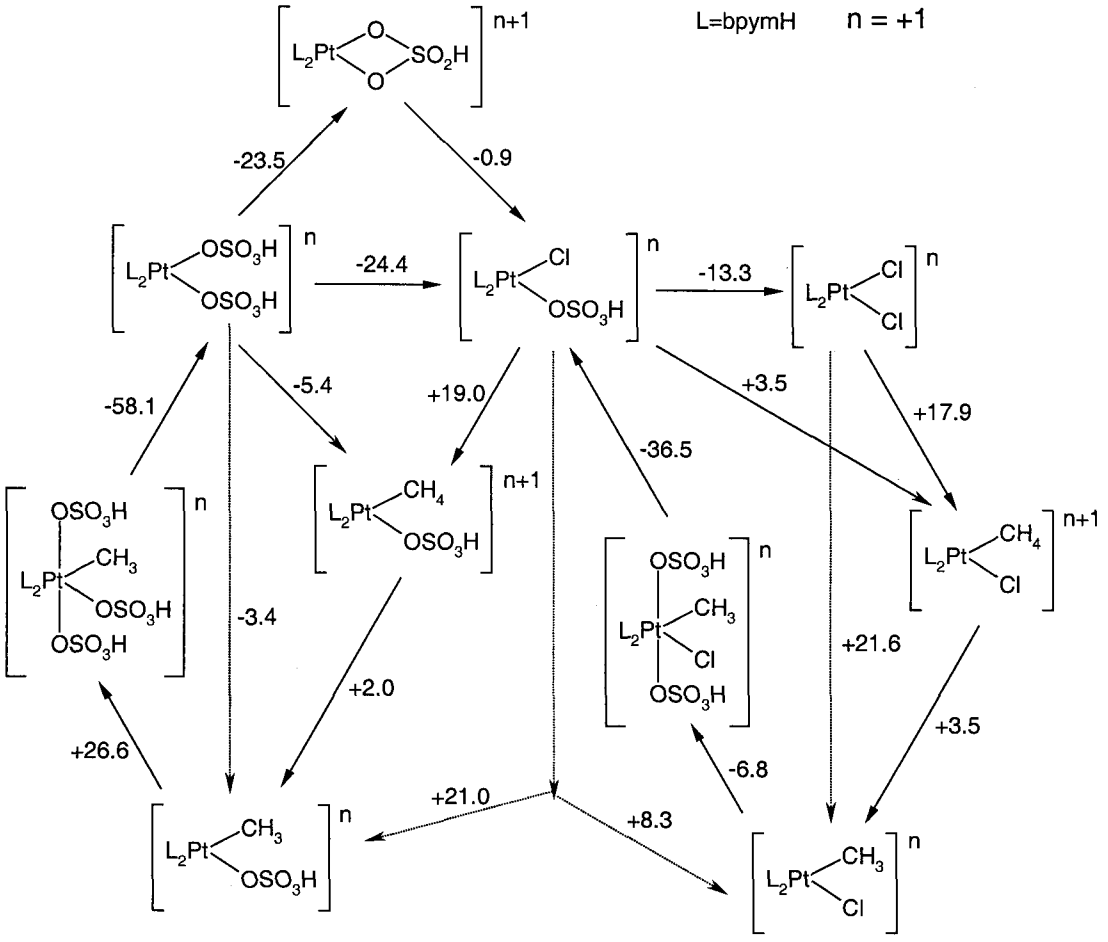

Figure 5-8d. Calculated overall thermodynamics of the catalytic cycle: Energetics for L = bpymH.

Compound	Electronic E (hartree)	Solvation E (kcal/mol)	Zero point energy (kcal/mol)	$G_{453\ K}$ correction (kcal/mol)
$[L_2Pt(Cl)_2]^n$	-1152.79834	-31.0	56.1	-36.0
$[L_2Pt(Cl)(CH_4)]^{n+1}$	-732.83854	-73.4	88.9	-36.7
$[L_2Pt(Cl)(CH_3)]^n$	-732.48401	-24.1	79.0	-36.3
$[L_2Pt(Cl)(CH_3)(OSO_3H)_2]^n$	-2131.71621	-33.8	134.5	-48.6
$[L_2Pt(Cl)(OSO_3H)]^n$	-1392.20934	-33.9	82.1	-41.7
$[L_2Pt(OSO_3H)(CH_4)]^{n+1}$	-972.23914	-81.4	115.5	-42.0
$[L_2Pt(OSO_3H)(CH_3)]^n$	-971.88549	-33.3	102.8	-42.5
$[L_2Pt(OSO_3H)_3(CH_3)]^n$	-2371.12277	-37.8	167.9	-49.5
$[L_2Pt(OSO_3H)_2]^n$	-1631.62783	-38.8	116.1	-43.7
$[L_2Pt(\eta^2\text{-}OSO_3H)]^{n+1}$	-931.72965	-78.9	76.6	-38.2

Table 5-2a. Energetics of L_2PtXY complexes: L = NH_3, n = 0.

Compound	Electronic E (hartree)	Solvation E (kcal/mol)	Zero point energy (kcal/mol)	$G_{453\ K}$ correction (kcal/mol)
$[L_2Pt(Cl)_2]^n$	-2439.05690	-158.8	55.0	-45.8
$[L_2Pt(Cl)(CH_4)]^{n+1}$	-2019.32413	-49.5	90.9	-44.9
$[L_2Pt(Cl)(CH_3)]^n$	-2018.74539	-162.1	80.3	-45.5
$[L_2Pt(Cl)(CH_3)(OSO_3H)_2]^n$	-3418.04043	-146.8	129.1	-57.6
$[L_2Pt(Cl)(OSO_3H)]^n$	-2678.50181	-152.1	82.7	-48.5
$[L_2Pt(OSO_3H)(CH_4)]^{n+1}$	-2258.75044	-54.2	120.0	-48.6
$[L_2Pt(OSO_3H)(CH_3)]^n$	-2258.19476	-152.3	111.9	-48.6
$[L_2Pt(OSO_3H)_3(CH_3)]^n$	-3657.46731	-141.6	167.4	-59.2
$[L_2Pt(OSO_3H)_2]^n$	-2917.94522	-144.4	113.4	-51.8
$[L_2Pt(\eta^2\text{-}OSO_3H)]^{n+1}$	-2218.22471	-57.1	76.2	-45.2

Table 5-2b. Energetics of L_2PtXY complexes: L = OSO_3H, n = -2.

Compound	Electronic E (hartree)	Solvation E (kcal/mol)	Zero point energy (kcal/mol)	$G_{453\ K}$ correction (kcal/mol)
$[L_2Pt(Cl)_2]^n$	-1739.36251	-56.1	21.4	-39.0
$[L_2Pt(Cl)(CH_4)]^{n+1}$	-1319.49845	-12.9	51.9	-37.9
$[L_2Pt(Cl)(CH_3)]^n$	-1319.06352	-57.7	44.5	-41.8
$[L_2Pt(Cl)(CH_3)(OSO_3H)_2]^n$	-2718.33944	-52.7	88.1	-55.9
$[L_2Pt(Cl)(OSO_3H)]^n$	-1978.78562	-61.2	51.8	-41.7
$[L_2Pt(OSO_3H)(CH_4)]^{n+1}$	-1158.89367	-23.3	79.8	-42.7
$[L_2Pt(OSO_3H)(CH_3)]^n$	-1558.48775	-56.1	66.4	-45.8
$[L_2Pt(OSO_3H)_3(CH_3)]^n$	-2957.77452	-46.9	144.2	-52.9
$[L_2Pt(OSO_3H)_2]^n$	-2218.22471	-57.1	76.2	-45.2
$[L_2Pt(\eta^2\text{-}OSO_3H)]^{n+1}$	-1518.39336	-18.6	41.3	-39.4

Table 5-2c. Energetics of L_2PtXY complexes: L_2 = η^2-OSO_3H, n = -1.

Compound	Electronic E (hartree)	Solvation E (kcal/mol)	Zero point energy (kcal/mol)	$G_{453\ K}$ correction (kcal/mol)
$[L_2Pt(Cl)_2]^n$	-1567.65087	-221.3	123.6	-41.4
$[L_2Pt(Cl)(CH_4)]^{n+1}$	-1147.46093	-396.6	158.7	-42.5
$[L_2Pt(Cl)(CH_3)]^n$	-1147.36156	-205.0	146.2	-42.7
$[L_2Pt(Cl)(CH_3)(OSO_3H)_2]^n$	-2546.56342	-209.8	185.1	-55.4
$[L_2Pt(Cl)(OSO_3H)]^n$	-1807.04458	-225.7	139.8	-46.7
$[L_2Pt(OSO_3H)(CH_4)]^{n+1}$	-1386.86445	-392.8	175.8	-48.1
$[L_2Pt(OSO_3H)(CH_3)]^n$	-1386.76132	-207.9	164.0	-49.9
$[L_2Pt(OSO_3H)_3(CH_3)]^n$	-2785.94709	-210.6	233.4	-57.7
$[L_2Pt(OSO_3H)_2]^n$	-2046.44506	-237.4	161.7	-54.8
$[L_2Pt(\eta^2\text{-}OSO_3H)]^{n+1}$	-1346.36094	-399.1	141.7	-45.0

Table 5-2d. Energetics of L_2PtXY complexes: L_2 = $bpymH_2$, n = +2.

Compound	Electronic E (hartree)	Solvation E (kcal/mol)	Zero point energy (kcal/mol)	$G_{453\ K}$ correction (kcal/mol)
$[L_2Pt(Cl)_2]^n$	-1567.46874	-80.1	108.5	-42.7
$[L_2Pt(Cl)(CH_4)]^{n+1}$	-1147.40010	-181.1	143.7	-43.1
$[L_2Pt(Cl)(CH_3)]^n$	-1147.16954	-68.4	131.7	-43.1
$[L_2Pt(Cl)(CH_3)(OSO_3H)_2]^n$	-2546.38003	-80.2	172.4	-59.6
$[L_2Pt(Cl)(OSO_3H)]^n$	-1806.86454	-87.8	125.8	-50.0
$[L_2Pt(OSO_3H)(CH_4)]^{n+1}$	-1386.79880	-186.3	161.3	-49.1
$[L_2Pt(OSO_3H)(CH_3)]^n$	-1386.56403	-78.5	149.9	-50.4
$[L_2Pt(OSO_3H)_3(CH_3)]^n$	-2785.76805	-87.9	217.5	-59.1
$[L_2Pt(OSO_3H)_2]^n$	-2046.27340	-93.4	160.3	-51.3
$[L_2Pt(\eta^2\text{-}OSO_3H)]^{n+1}$	-1346.29621	-187.9	127.4	-44.0

Table 5-2e. Energetics of L_2PtXY complexes: L_2 = bpymH, n = +1.

Compound	Electronic E (hartree)	Solvation E (kcal/mol)	Zero point energy (kcal/mol)	$G_{453\ K}$ correction (kcal/mol)
$[L_2Pt(Cl)_2]^n$	-1567.12764	-23.3	96.4	-42.8
$[L_2Pt(Cl)(CH_4)]^{n+1}$	-1147.17452	-55.7	129.5	-44.7
$[L_2Pt(Cl)(CH_3)]^n$	-1146.81247	-17.2	120.5	-43.5
$[L_2Pt(Cl)(CH_3)(OSO_3H)_2]^n$	-2546.02852	-30.0	161.4	-58.9
$[L_2Pt(Cl)(OSO_3H)]^n$	-1806.53339	-29.1	115.6	-50.2
$[L_2Pt(OSO_3H)(CH_4)]^{n+1}$	-1386.57032	-65.1	147.3	-51.7
$[L_2Pt(OSO_3H)(CH_3)]^n$	-1386.21570	-25.1	140.9	-51.2
$[L_2Pt(OSO_3H)_3(CH_3)]^n$	-2785.43128	-33.5	203.3	-58.7
$[L_2Pt(OSO_3H)_2]^n$	-2045.95022	-30.8	153.9	-51.2
$[L_2Pt(\eta^2\text{-}OSO_3H)]^{n+1}$	-1346.07185	-62.5	115.3	-45.0

Table 5-2f. Energetics of L_2PtXY complexes: L_2 = bpym, n = 0.

Compound	Electronic E (hartree)	Solvation E (kcal/mol)	Zero point energy (kcal/mol)	$G_{453\ K}$ correction (kcal/mol)
$[L_2Pt(OSO_3H)(CH_4)]^{n+1}$	-1779.88304	-50.6	63.2	-41.2
$[L_2Pt(OSO_3H)(CH_3)]^n$	-1779.28266	-172.5	49.0	-41.0
$[L_2Pt(OSO_3H)_3(CH_3)]^n$	-3178.59560	-146.5	112.2	-52.5
$[L_2Pt(OSO_3H)_2]^n$	-2439.05690	-158.8	55.0	-45.8
$[L_2Pt(\eta^2\text{-}OSO_3H)]^{n+1}$	-1739.36251	-56.1	21.4	-39.0

Table 5-2g. Energetics of L_2PtXY complexes: L = Cl, n = -2.

Rxn	L=NH_3	L=OSO_3H	L_2=OSO_3H	L_2=bpymH_2	L=bpymH	L=bpym	L=Cl
1a	+5.9	+18.2	+29.1	+19.7	+17.9	+12.0	
2a	+20.1	-1.8	-21.0	-0.3	+3.5	+13.2	
3a	-3.5	-24.6	-28.1	+3.9	-6.8	-11.0	
4a	-40.2	-19.5	-3.1	-38.4	-36.5	-40.0	
5a	-11.3	+11.0	+17.3	-0.1	+4.6	+1.2	
10a	+26.0	+16.4	+8.1	+19.4	+21.6	+25.2	
11a	+8.8	+9.2	-3.7	-0.4	+8.3	+14.4	
1b	+7.9	+19.9	+38.8	+19.6	+19.0	+13.2	
2b	+15.5	+0.8	-33.2	-4.0	+2.0	+14.5	-1.1
3b	+8.2	-8.4	+3.5	+46.6	+26.6	+15.2	-10.7
4b	-48.0	-35.0	-39.0	-89.3	-58.1	-50.6	-37.2
5b	-10.6	+7.7	+33.8	+11.7	-5.4	-13.9	+14.1
10b	+23.4	+20.7	+5.6	+15.6	+21.0	+27.7	
11b	+4.9	+8.5	+0.6	+7.7	-3.4	+0.6	+13.0
6	-17.2	-7.2	-11.8	-19.8	-13.3	-10.8	
7	-18.5	-12.2	-5.0	-7.9	-24.4	-27.1	
8	-25.3	-7.1	+16.0	-10.7	-23.5	-28.4	-4.5
9	+6.8	-5.1	-21.0	+2.8	-0.9	+1.3	

Table 5-3a. Reaction Enthalpies at 0 K in kcal/mol (solvation and ZPE included).

Rxn	L=NH_3	L=OSO_3H	L_2=OSO_3H	L_2=bpymH_2	L=bpymH	L=bpym	L=Cl
1a	+3.5	+17.0	+28.1	+16.5	+15.4	+8.0	
2a	+22.2	-0.7	-23.2	+1.2	+5.3	+17.9	
3a	+24.9	+4.0	-1.5	+31.9	+17.4	+14.3	
4a	-65.5	-42.6	-21.1	-61.9	-59.1	-63.5	
5a	-18.7	+1.8	+8.3	-8.7	-1.3	-6.1	
10a	+25.7	+16.3	+4.9	+17.7	+20.7	+25.9	
11a	+3.5	+1.1	-14.9	-7.8	+4.0	+11.8	
1b	+5.5	+17.7	+35.7	+16.1	+17.8	+15.1	
2b	+16.7	+2.5	-34.6	-4.1	+2.4	+15.7	+0.8
3b	+41.9	+21.7	+37.1	+79.5	+58.6	+48.4	+18.5
4b	-74.4	-59.8	-63.5	-118.6	-82.5	-75.3	-62.7
5b	-21.7	-1.9	+23.5	+5.6	-16.0	-21.7	+5.9
10b	+23.4	+20.2	+1.1	+12.0	+20.2	+31.8	
11b	+4.9	+0.6	-11.1	+1.5	-13.6	-5.0	+6.7
6	-22.2	-15.2	-19.8	-25.2	-16.7	-14.1	
7	-27.2	-19.6	-12.2	-10.5	-33.8	-36.8	
8	-50.6	-31.3	-9.0	-31.7	-47.0	-53.0	-28.5
9	+23.4	+11.7	-3.2	+21.2	+13.2	+16.2	

Table 5-3b. Free energy corrections to 453 K in kcal/mol (solvation and ZPE included).

5-6-2. Stable Species in Solution Before Reacting with CH_4

Before reaction with methane, among the four species involved in reactions **6-9**, the most thermodynamically stable species in solution is L_2PtCl_2 for all ligands. The least favored species is $L_2Pt(OSO_3H)_2$, with the exception of $Pt(\eta^2\text{-}OSO_3H)_2$. For {$L_2$ = bpym, $bpymH_2$; L = NH_3}, $L_2Pt(\eta^2\text{-}OSO_3H)$ is slightly favored over $L_2Pt(Cl)(OSO_3H)$ in solution. However, given that the concentration of sulfuric acid (the solvent) is ~10^4 times greater than any of the other species in solution, it is expected that there is a small but non-negligible amount of $L_2Pt(Cl)(OSO_3H)$ and $L_2Pt(\eta^2\text{-}OSO_3H)$ in solution. The exothermicity for reaction **6** from most to least exothermic is

$$bpymH_2 > 2\ NH_3 > bpymH > 2\ OSO_3H > bpym > \eta^2\text{-}OSO_3H$$

ranging from –19.8 to –7.2 kcal/mol. The exothermicity for reactions **6+9** from most to least exothermic is

$$\eta^2\text{-}OSO_3H > bpymH_2 > bpymH > 2\ NH_3 \sim 2\ OSO_3H > bpym$$

ranging from –32.8 to –8.5 kcal/mol. $Pt(\eta^2\text{-}OSO_3H)_2$ is particularly unfavorable.

5-6-3. Thermodynamics of C-H Activation

We will start with L_2PtCl_2 since it is the most stable species in solution. The formation of $L_2Pt(Cl)(CH_3)$ from L_2PtCl_2 (reaction **10a**) is endothermic for all ligands. The bisulfate ligands are the least endothermic (+8.1 and +16.4 kcal/mol). The bpym ligands lead to +19.4, +21.6, and +25.2 kcal/mol with decreasing protonation. The NH_3 ligands are most endothermic (+26.0 kcal/mol).

Starting from $L_2Pt(Cl)(OSO_3H)$ going to $L_2Pt(Cl)(CH_3)$ (reaction **11a**), the $\eta^2\text{-}OSO_3H$ ligand is actually exothermic (-3.7 kcal/mol). The trend is not as clear-cut because this

reaction is now a balance of reactions **6** and **10a**. For reaction **6**, the trend is opposite to that of **10a**; the NH_3 and bpym ligands are more exothermic than the bisulfate ligands.

Since we find that C-H activation step includes the preliminary formation of the methane complex $L_2Pt(Cl)(CH_4)$, then starting from L_2PtCl_2, this reaction (**1a**) is least endothermic for NH_3 ligands, moderately endothermic for bpym ligands, and most endothermic for bisulfate ligands. Reaction **5a** shows a similar trend with less overlap among the three classes of ligands.

For ease in comparing the thermodynamics of several different ligands, note that we have chosen to dissociate Cl^- completely in the form of HCl infinitely separated from the CH_4-Pt(II) complex. Thus, for purposes of comparing thermodynamics, we use (5.16a) and (5.16b), which correspond to steps **1a** and **2a**, instead of (5.10a) and (5.10b).

$$[L_2Pt(II)Cl_2]^{m+} + CH_4 + H_2SO_4 \rightarrow$$

$$[L_2Pt(II)Cl(CH_4)]^{(m-1)+} + HCl + OSO_3H^- \qquad (5.16a)$$

$$[L_2Pt(II)Cl(CH_4)]^{(m-1)+} + OSO_3H^- \rightarrow$$

$$[L_2Pt(II)Cl(CH_3)]^{m+} + H_2SO_4 \qquad (5.16b)$$

Combining the relative energetics of **1a** to **10a** (and analogously **5a** to **11a**), we find that for the NH_3 ligands, preliminary formation of $L_2Pt(Cl)(CH_4)$ is significantly less endothermic than forming $L_2Pt(Cl)(CH_3)$, +5.9 to +26.0 kcal/mol, leading to an endothermic step **2a** of +20.1 kcal/mol. This is reversed for the bisulfate ligands; reaction **2a** is –1.8 and –21.0 kcal/mol for two and one bisulfate ligand respectively. The bpym ligands are intermediate. Reaction **2a** is marginally exothermic (-0.3 kcal/mol) for $bpymH_2$ and increasing in endothermicity with deprotonation (+3.5 and +13.2 for bpymH and bpym respectively).

Note that our calculations investigating the kinetics of C-H activation for L_2 = bpym (Section 5-5-1, Figure 6), where Cl^- remains associated with the complex in an ion-pair, rather than separated at infinity, find the reaction corresponding to **2a** (**B** → **C**) to be exothermic (-7.5 kcal/mol).

Considering the bipyrimidine complexes, the singly protonated $[(bpymH)PtCl_2]^+$ is only marginally more stable (by 1.4 kcal/mol) than the doubly protonated $[(bpymH_2)PtCl_2]^{2+}$. Hence, we expect both species to be present in significant amounts. For L_2 = bpymH, reaction **10a** is endothermic by +21.6 kcal/mol. However, for L_2 = $bpymH_2$, reaction **10a** is less endothermic (+19.4 kcal/mol). Hence, the doubly protonated $[(bpymH_2)Pt(Cl)(CH_3)]^{2+}$ is now marginally more stable (by 0.8 kcal/mol) than the singly protonated $[(bpymH)Pt(Cl)(CH_3)]^+$.

The catalytic cycle on the left (reactions **1b**, **2b**, **5b**, **10b**, **11b**) where X = OSO_3H show similar trends to the cycle on the right (X = Cl) although this cycle would be thermodynamically less accessible since reactions **6** and **7** are exothermic.

Hush and co-workers[31] find instead that replacement of X = Cl with X = OSO_3H is thermodynamically favorable, hence the cycle on the left is accessed. For example, they calculate the reaction **10+6b**,

$$[(NH_3)_2PtCl_2]^0 + 2\ H_2SO_4 + CH_4 \rightarrow$$
$$[(NH_3)Pt(CH_3)(OSO_3H)]^0 + 2\ HCl + [OSO_3H]^- \qquad (5.17)$$

to be exothermic (ΔH_{0K} = -6.2 kcal/mol). Our calculations suggest the reaction is endothermic (ΔH_{0K} = +40.6 kcal/mol) and the large difference is mainly due to the relative solvation energies of the two Pt complexes. Whereas we find that the solvation energies of $[(NH_3)_2PtCl_2]^0$ and $[(NH_3)Pt(CH_3)(OSO_3H)]^0$ are close in energy (-31.0 and -

33.3 kcal/mol respectively), Hush and co-workers calculate a large difference (-9.5 and -50.4 kcal/mol respectively).

5-6-4. Thermodynamics of Oxidation

The oxidation step (**3a**) involves a two-electron redox reaction: oxidation of Pt(II) to Pt(IV) coupled to reduction of S(VI) in the form of SO_3 to S(IV) in the form of SO_2 (5.11). Experimentally, the oxidation step is rate-determining. Formation of the Pt(IV) octahedral complex is most exothermic for the bisulfate ligands (-24.6 and -28.1 kcal/mol). It is mildly exothermic (-3.5 kcal/mol) for the NH_3 ligands. For the bpym ligands, this step ranges from +3.9 kcal/mol (doubly protonated) to -11.0 kcal/mol (unprotonated). If the activation barrier to oxidation follows this same trend, the bisulfate ligand complexes would be the most active, having the lowest barriers. In our study of the stability of complexes in solution (Section 5-3-1), we found that for the ammine catalyst, the bisulfate form predominates because of the exothermicity for ligand exchange from NH_3 to bisulfate ligands. *We propose that the bisulfate form is the active catalyst in solution, exhibiting the observed higher initial activity* (based on the exothermicity of the rate-determining oxidation step) before the catalyst dies via precipitation of $PtCl_2$.

The analogous reaction on the left side of the catalytic cycle (**3b**) follows the same general trend (comparing the different ligands) except all these reactions are significantly more endothermic than the reaction **3a**. Thus, we conclude that retention of one Cl^- leads to the most active form of the catalyst. This is in good agreement with experimental

evidence that Cl is important for the oxidation step. When the $L_2Pt(OSO_3H)_2$ complex was used as the starting material instead of L_2PtCl_2, activity was drastically reduced.[36]

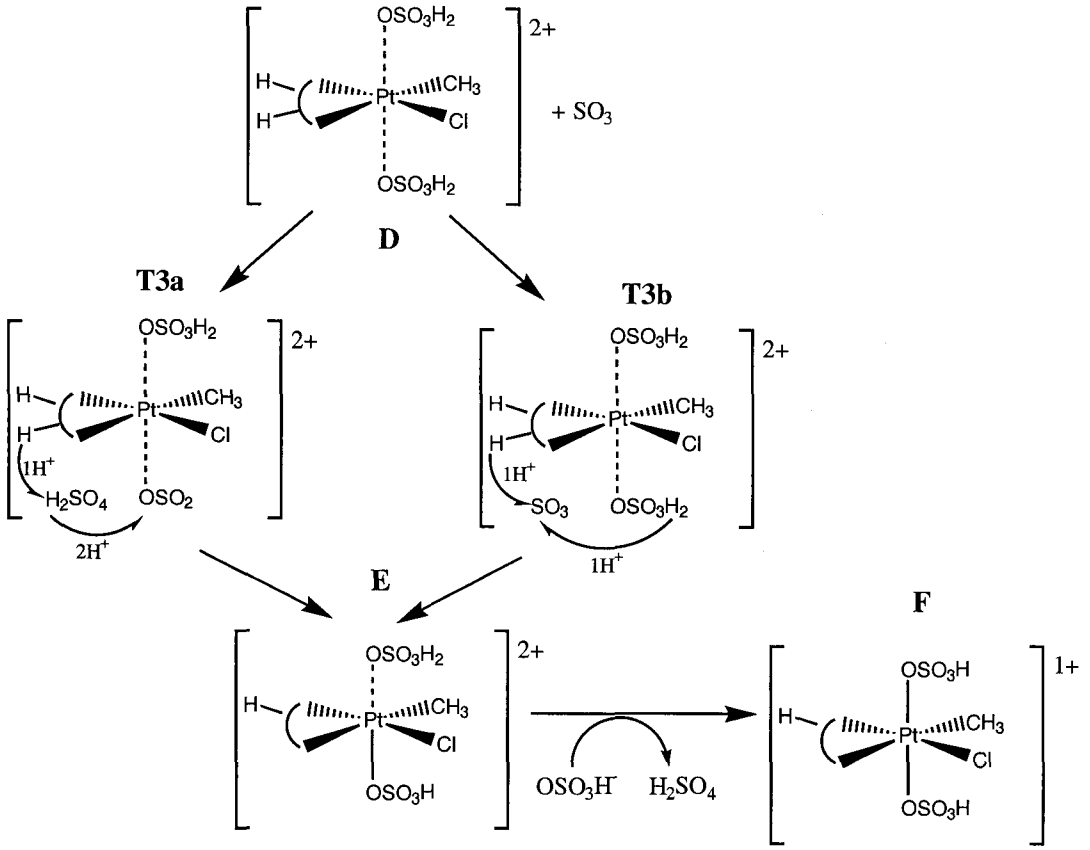

Figure 5-9. Suggested mechanism for oxidation step.

Based on preliminary calculations of the intermediates involved in the oxidation step our suggested mechanism for oxidation is shown in Figure 5-9, illustrated with L_2 = $bpymH_2$ (which is marginally more stable than L_2 = bpymH). Structure **D** is the Pt(II)-CH_3 intermediate with two additional H_2SO_4 solvent molecules loosely associated with the axial positions. Since oxidation of Pt(II) to Pt(IV) requires the simultaneous reduction of SO_3 to SO_2, we have added one SO_3 molecule to the system. SO_3 may displace one of the axial H_2SO_4 molecules, the latter moving to a position that bridges the protons of the bpym ligand and SO_3. The bpym ligand rotates slightly and one of the protons points

towards the bridging H_2SO_4 molecule to form a hydrogen bonding network (see Figure 5-10). Simultaneous proton transfer across this bridge (concurrent with electron transfer from Pt to SO_3) can take place to transform SO_3 to reduced H_2SO_3 (illustrated by **T3a**). H_2SO_3 goes into solution, favorably dissociating into SO_2 and H_2O. The remaining bisulfate ion can form a strong Pt-O bond (~2 Å) giving rise to structure **E**. Subsequent proton transfer between sulfuric acid (in the opposite axial position) and bisulfate in solution leads to structure **F**.

An alternate route (illustrated by **T3b**) keeps the H_2SO_4 molecules associated with the axial positions of the complex and utilizes SO_3 as the bridge. As before, to form H_2SO_3, one proton leaves the bpymH_2 ligand and the other comes from the axial H_2SO_4 molecule. This route also leads to structures **E** and **F**.

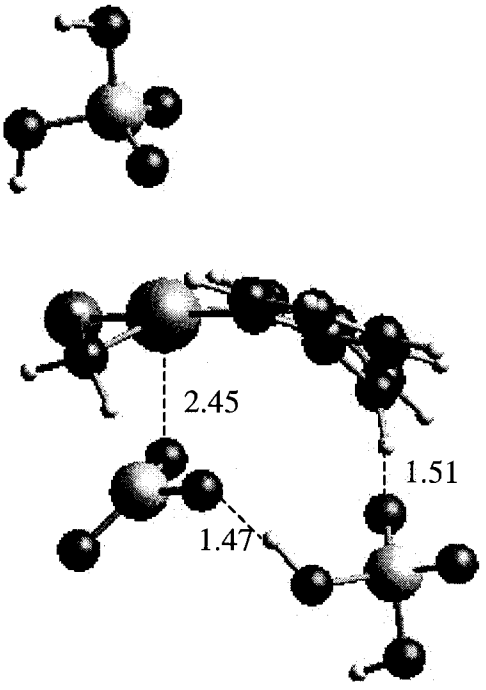

Figure 5-10. Structure of $[(bpymH_2)Pt(Cl)(CH_3)\ldots(SO_3)(H_2SO_4)_2]^{2+}$.

The key to the oxidation step therefore is to transfer two protons and two electrons from the Pt(II) complex to an SO_3 molecule leading to the oxidized Pt(IV) complex. Formally, **D** has a $bpymH_2$ (+2), a chloride (-1) and a bisulfate (-1) ligand. Since the net overall charge of the complex is +2, this leads to Pt(II). On the other hand, **E** formally has a bpymH (+1), a chloride (-1) and two bisulfate (-1 each) ligands. Since the net overall charge of the complex is still +2, this leads to Pt(IV). Proton transfer from **E** to **F** reduces the net charge, hence **F** is still formally Pt(IV).

The proton transfer from $bpymH_2$ is made possible by the similarity in stability of the (bpymH)Pt(II) and ($bpymH_2$)Pt(II) complexes in solution as discussed in the previous section.

5-6-5. Thermodynamics of Functionalization

The functionalization step involves removal of CH_3OSO_3H from the Pt(IV) complex via reductive elimination to regenerate a Pt(II) complex (5.12). We find this step (**4a**) to be exothermic for all ligands. Experimental evidence suggests that this is a fast step.[12] Methanol is then formed from the hydrolysis of CH_3OSO_3H, regenerating H_2SO_4.

$$CH_3OSO_3H + H_2O \rightarrow CH_3OH + H_2SO_4 \qquad (5.18)$$

Preliminary calculations suggest (see Figure 5-11) that the equatorial methyl is transferred to an axial bisulfate to form CH_3OSO_3H, which then easily leaves the complex. The bisulfate ligand in the opposite axial position rotates to occupy the vacated equatorial position.

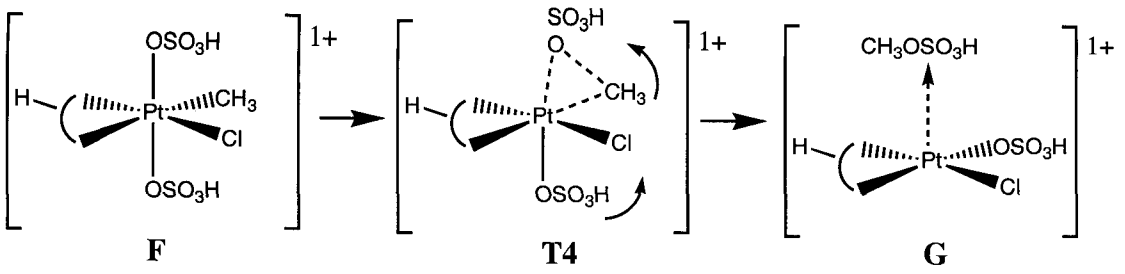

Figure 5-11. Suggested mechanism for functionalization step.

5-7. Discussion

We find that critical to stability of the catalytic complex in concentrated sulfuric acid is having a ligand that in its protonated state (at low pH) still can bind strongly to the Pt center. The bipyrimidine ligand (doubly protonated in solution) still has two N centers to bind to the complex. On the other hand, N-based ligands that have all N centers protonated in solution favorably undergo ligand exchange to form the bisulfate complex, e.g., the bipyridine ligand will have both its N centers protonated in highly acidic conditions leading to loss of the ligand. Simple amines would not be favorable in acidic media for the same reasons since they favorably form free RNH_2^+ in solution. We expect a three-N π-acid ligand to be stable in strong acid, provided at least two of the nitrogens are in the right positions to act as a bidentate ligand to the Pt complex.

Our calculations show that the bisulfate complex favorably forms dimers and trimers leading to $PtCl_2$ precipitate and catalyst death. This explains the short-lived nature of the ammine catalyst. The bipyrimidine catalyst on the other hand retains the bpym ligand and does not favorably form dimers and trimers, and hence remains stable in sulfuric acid.

In studying the thermodynamics of the catalytic cycle, we find both the C-H activation and oxidation steps to be most favorable for the bisulfate ligands. Since the

oxidation step is rate-determining, this suggests that the bisulfate form of the catalyst may be responsible for the short-lived higher catalytic activity before precipitation occurs.

Although L_2PtCl_2 is the starting catalyst, our mechanism suggests that one Cl^- is irreversibly lost as HCl. After the functionalization step, $L_2Pt(Cl)(OSO_3H)$ is regenerated, and becomes the starting point for subsequent catalytic cycles.

We find that weaker binding ligands enhance C-H activation by stabilizing the formation of a stronger Pt-C bond in the Pt(II)-CH_3 intermediate. We calculated the enthalpy of C-H activation to be less endothermic for the weaker binding O-based bisulfate ligands than the N-based ligands (reactions **10** and **11** in Table 5-3a).

Our calculated relative activation barriers (Section 5-5-1) of the intermediate methane complex formed, strongly associated in an ion-pair, are in good agreement with H/D exchange experiments. Our calculations also suggest that the reaction pathway involving the close association of X^- (X = Cl, OSO_3H) keeps the intermediate methane complex reactive to forming the Pt(II)-CH_3 species.

We also find that more electronegative ligands (O-based) stabilize the Pt(IV) intermediate and hence enhance the oxidation step (reaction **3**). Noteworthy is the trend where decreasing protonation of bpym favors the oxidation step. This is not surprising since one would expect that a less positive ligand would stabilize the Pt(IV) complex. Hence, we expect that having too many protonation sites on L may not be as favorable for stabilizing the oxidation complex. In addition, we expect that as the solvent is changed to one that is less acidic, the oxidation step should be increasingly favorable. The oxidation step is also favored by more electronegative X ligands in L_2PtX_2. From our calculations it is clear that step **3a** is much more favorable than **3b**, i.e., retention of one

Cl^- ligand leads to the most active form of the catalyst. The similar stability of (bpymH)Pt(II) and ($bpymH_2$)Pt(II) complexes allows for a simple shuttling mechanism for the oxidation step.

Taking these factors into account, we believe that the use of O-based L or L_2 ligands, possibly attached to a surface, that have a sufficient number of acidic sites is one way to prevent catalyst death while enhancing catalytic activity.

Although water is involved in the hydrolysis to convert methylbisulfate to methanol (5.18), the presence of water in the catalytic cycle has deleterious effects on activity. As more water is generated from the decomposition of H_2SO_3 to SO_2 and H_2O (by-product of the oxidation step), the equilibrium of H_2SO_4 and SO_3 (direct oxidant) shifts to reduce the concentration of SO_3, and hence inhibit the oxidation step. Preliminary calculations also suggest that water can bind to the axial positions to block the oxidation step, or compete with methane at the equatorial position to block C-H activation.

5-8. Conclusions

Modern DFT methods with solvation can elucidate reactions even in very acidic media. Our studies suggest that in order to prevent catalyst death via precipitation of $PtCl_2$ in highly concentrated acidic conditions, suitable ligands require multiple protonation sites. The protonated free ligand should have open electron donor sites to form a complex with $PtCl_2$. This explains the observed stability of the bipyrimidine catalyst, which does not favorably undergo ligand exchange with bisulfate. In contrast, the ammine catalyst favorably undergoes ligand exchange to form the bisulfate complex in sulfuric acid. The bisulfate complex favorably forms dimers and trimers leading to

$PtCl_2$. The bipyrimidine catalyst retains the bpym ligand, does not favorably form dimers and trimers, and hence remains stable in sulfuric acid.

We calculate the thermodynamics of the C-H activation step to be most favorable for the weaker-binding bisulfate ligands. Mechanistically, we find that the methane complex is more stable than the 14-electron T-complex. Our calculated relative barriers for a two-step C-H activation mechanism are in good agreement with observed experimental results. We find that the thermodynamics of the rate-determining oxidation step is also most favorable for the bisulfate ligands, suggesting that the bisulfate form of the catalyst may be responsible for the short-lived higher catalytic activity before precipitation of $PtCl_2$ occurs. This is in good agreement with the experimentally observed higher activity of the ammine catalyst (which converts to the bisulfate form) over the bipyrimidine catalyst.

Acknowledgement

We thank Professor Roy Periana for helpful comments. This research was initiated with funding from BP and the NSF (CHE 95-22179) and completed with funding from Chevron.

References

1. Arnstden, B. A.; Bergman, R. G.; Mobley, T. A.; Peterson, T. H. *Acc. Chem. Res.*, **1995**, *28*, 154.
2. Bromberg, S. E.; Yang, H.; Asplund, C. M.; Lian, T.; McNamara, K. B.; Kotz, K. T.; Yeston, J. S.; Wilkens, M.; Frei, H.; Bergman, R. G.; Harris, C. B. *Science*, **1997**, *278*, 260.

3. Davies, J. A.; Watson, P. L.; Liebman, J. L.; Greenberg, A., Eds. *Selective Hydrocarbon Activation*, Wiley-VCH, New York, 1990.

4. Hall, C.; Perutz, R. N. *Chem. Rev.*, **1996**, *96*, 3125.

5. Hill, C. L. *Activation and Functionalization of Alkanes*, Wiley-Interscience, New York, 1989.

6. Sen, A. *Acc. Chem. Res.*, **1988**, *21*, 421.

7. Shilov, A. E.; Shul'pin, G. B. *Chem. Rev.*, **1997**, *97*, 2879.

8. Sommer, J.; Bukala, J. *Acc. Chem. Res.*, **1993**, *26*, 370.

9. Walktz, K. M.; Hartwig, J. F. *Science*, **1997**, *277*, 211.

10. Shilov, A. E. *Activation of Saturated Hydrocarbons by Transition Metal Complexes;* D. Riedel Publishing Co., Dordrecht, The Netherlands, 1984.

11. Periana, R. A.; Taube, D. J.; Gamble, S.; Taube, H.; Satoh, T.; Fujii, H. *Science*, **1998**, *280*, 560.

12. Periana, R. A.; Taube, D. J.; Evitt, E. R.; Loffler, D. G.; Wentrcek, P. R.; Voss, G.; Masuda, T. *Science*, **1993**, *259*, 340.

13. Slater, J. C. *Quantum Theory of Molecules and Solids*, Vol. 4: *The Self-Consistent Field for Molecules and Solids*, Mc-Graw Hill, New York, 1974.

14. Becke, A. D. *J. Chem. Phys.*, **1993**, *98*, 5648.

15. Becke, A. D. *Phys. Rev. A*, **1988**, *38*, 3098.

16. Vosko, S. H.; Wilk, L.; Nusair, M. *Can. J. Phys*, **1980**, *58*, 1200.

17. Lee, C.; Yang, W.; Parr, R. G. *Phys. Rev. B*, **1988**, *37*, 785.

18. Goddard III, W. A. *Phys. Rev.*, **1968**, *174*, 659.

19. Melius, C. F.; Olafson, B. O.; Goddard III, W. A. *Chem. Phys. Lett.*, **1974**, *28*, 457.

20. Hay, P. J.; Wadt, W. R. *J. Phys. Chem.*, **1985**, *82*, 299.

21. Jaguar 3.5, Schrodinger, Inc., Portland, Oregon, 1998.

22. Greeley, B. H.; Russo, T. V.; Mainz, D. T.; Friesner, R. A.; Langlois, J.-M.; Goddard III, W. A.; Honig, B. *J. Am. Chem. Soc.*, **1994**, *116*, 11875.

23. Tannor, D. J.; Marten, B.; Murphy, R.; Friesner, R. A.; Sitkoff, D.; Nicholls, A.; Ringnalda, M.; Goddard III, W. A.; Honig, B. *J. Am. Chem. Soc.*, **1994**, *116*, 11875.

24. Marten, B.; Kim, K.; Cortis, C.; Friesner, R. A.; Murphy, R. B.; Ringnalda, M. N.; Sitkoff, D.; Honig, B. *J. Phys. Chem.*, **1996**, *100*, 11775.

25. Klassen, J. K.; Fiehrer, K. M.; Nathanson, G. M. *J. Phys. Chem B*, **1997**, *101*, 9098.

26. Probe radius is calculated from $r^3 = 3m\Delta / 4\pi\rho$ where r is the solvent probe radius in Å, m is the molecular mass obtained by dividing the molecular weight given in ref 27 in g/mol by Avogadro's number 6.023×10^{23}, Δ is the packing density (assumed to be 0.5) and ρ is the density given in g/cm^3 at 20 deg. C obtained from ref 27.

27. Lide, D. R. *Handbook of Chemistry and Physics*, 74th ed.; CRC Press: Boca Raton, 1993-1994.

28. In free bipyrimidine the calculated angle between the pyrimidine planes was 28.4°. The energy required to twist the planes parallel was calculated to be –2.7 kcal/mol including solvation and zero point energy corrections.

29. Siegbahn, P. E. M.; Crabtree, R. H. *J. Am. Chem. Soc.*, **1996**, *118*, 4442.

30. Holtcamp, M. W.; Labinger, J. A.; Bercaw, J. E. *J. Am. Chem. Soc.*, **1997**, *119*, 848.

31. Mylavaganam, K.; Backsay, G. B.; Hush, N. S., *J. Am. Chem. Soc.*, **1999**, *121*, 4633.

32. Igel-Mann, G.; Stoll, H.; Preuss, H. *Mol. Phys.*, **1988**, *65*, 1321.

33. Andrae, D.; Haussermann, U.; Dolg, M.; Stoll, H.; Preuss, H. *Theor. Chim. Acta*, **1990**, *77*, 123.

34. Foresman, J. B.; Keith, T. A.; Wiberg, K. B.; Snoonian, J.; Frisch, M. J. *J. Phys. Chem.*, **1996**, *100*, 16098.

35. Note that in calculating the kinetics, all species are included, i.e., we do not calculate reactant fragments as separated species at infinity.

36. Periana, R. A. *unpublished results.*